The Higgs from A_μ to Z_μ: Higgs boson cross section measurements using diphoton and four lepton decays at 13 TeV

Bijan Perry Berton Haney IV

a dissertation

in

Physics and Astronomy

Presented to the Faculties of the University of Pennsylvania

in Partial Fulfillment of the Requirements for the Degree of Doctor of Philosophy

2018

Hugh "Brig" Williams, Mary Amanda Wood Professor of Physics

Supervisor of Dissertation

Joshua Klein, Professor, Physics

Graduate Group Chairperson

Dissertation Committee

Justin Khoury, Professor, Physics

Elliot Lipeles, Associate Professor, Physics

Christopher M. Mauger, Associate Professor, Physics

Burt Ovrut, Professor, Physics

CERN-THESIS-2018-265
13/11/2018

The Higgs from A_μ to Z_μ: Higgs boson cross section measurements using diphoton and four lepton decays at 13 TeV

COPYRIGHT
2018
Bijan Perry Berton Haney IV

This work is licensed under a Creative Commons
Attribution-NonCommercial-ShareAlike 3.0 Unported License.

To view a copy of this license, visit
http://creativecommons.org/licenses/by-nc-sa/3.0

or send a letter to:

Creative Commons
PO Box 1866
Mountain View, CA 94042
USA

Acknowledgements

Thank you to Paul Tipton for inspiring me to pursue physics, and to Tobias Golling and Hong Ma for their mentorship in my formative years. A big thank you to Brig Williams for being a great adviser and always providing useful insight and clarity to any question I brought him. Thank you to Sarah Heim and Christopher Meyer for their patience, mentorship, intelligence and friendship. This would not have been possible without you.

Thank you to the Penn HEP faculty: Brig Williams, Evelyn Thomson, Joe Kroll, and Elliot Lipeles for fostering a great environment for physics research. Thank you to the TRT Operations group: Anatoli, Dominik, Andrea B, Jola, Elzbieta, Zbyszek, and Kostya for being an amazing and competent team always there to help and ensure the TRT stayed green and awesome. Andrey, you introduced me to the TRT and were always there during my first year guiding me through the stressful 2am calls to fix the TRT. I learned so much about the detector from you and miss you. Thank you to the TRT DAQ team over the years: Jamie, Jon, Ximo, Sarah, Chris, Zoltan, Khilesh, Elodie, Vincent, Daniil, Keisuke, Shion, and Ian for being amazing at preparing the DAQ for Run 2. Thank you to the entire ATLAS collaboration for getting this large and complex detector to work and collect data. Thank you and congratulations to the members of the Higgs group for the achievement of measuring the Higgs boson cross section in Run 2. I'd like to specifically thank Sarah, Chris, Florian, Dag, Haider, Xiangyang, RD, Roberto, Giacomo, Eleni, Andrea G, Antonio, Gaetano, Hannah, Rosy and Arthur for all their help, collaboration, and training in the Higgs cross section analysis.

I would not have made it through grad school without all the friends I made while in Philadelphia and Geneva. If I were transported back in time and asked if I wanted to do this all again, I would say yes, if only to ensure I'd meet all of you again. In Philadelphia, I'd like to thank Khilesh, Ben Elder, Charlotte, and Josh for making the first years of grad school full of good memories and good food.

I'd like to thank those in the HEP group for a full five years of enjoyment and for everything they've taught me: Joana, Jeff, Keisuke, Shion, Will, Billy, Khilesh, Leigh, Joey, Eric (honorary), Christian, Elodie, Rachael, Tony, Ian, Lucas, Ben, Joe, and James. I will always look back fondly on our great lunch conversations. In Geneva, I had a wonderful time living with my roommates Alex, Ryan, and Kurt, and with the exquisite Marigold Memory Palace of Leigh, Rob, and Jake. You three made Geneva feel like home to me. Thank you Dan for introducing me to the LTA, and to everyone there for the great kebabs, beers, hikes, and laughs. Thanks Murdo, Iwan, and Sergio for our runs around Geneva and great conversations. Thanks Fenton, Rob, Will M, Liam, Xanthe, Cameron, Anna, Adam, Tim, Iwan, Sun, and Ellis for our stimulating walks through vineyards, museums, and parks. Thank you Philipp, Kelvin, Ryan, Mallorie, Rohan, Jack, Stoyan, Ben, Konstantin, David, Duncan, Rose, Harry, Greg, Savvas, Alison, Amal, Soph, Leo, Crystal and Sofia for being an unforgettable part of my time in Europe.

And there are those who have been there from the very beginning, before CERN. Thank you to Josh Baker, you've been an amazing friend and roommate and I'm so glad we got to spend even more years living together after college. Thank you Brandon Jackson for always being there to talk. Thank you to my boyfriend Sebastian Rowland for always being so full of patience, understanding, and love. And thank you to my parents Annahita and Trey, and my brother Piruz, for always being a loving and supportive family to me.

And finally thank you to all those butterflies in Brazil for having flapped their wings in that specific way to have brought my life to this point. It's been an amazing ride.

ABSTRACT

The Higgs from A_μ to Z_μ: Higgs boson cross section measurements using diphoton and four lepton decays at 13 TeV

Bijan Perry Berton Haney IV

H.H. Williams

This thesis presents measurements of the Higgs boson inclusive and differential cross sections with 36.1 fb^{-1} of proton-proton collision data from the Large Hadron Collider at a center of mass energy of 13 TeV recorded with the ATLAS detector. The cross sections are measured in the fiducial phase space of the $H \to ZZ^* \to 4\ell$ (four lepton) decay channel as well as in the total Higgs phase space, combining data from the $H \to ZZ^* \to 4\ell$ and $H \to \gamma\gamma$ (diphoton) decay channels. These two channels have high sensitivity to the Higgs signal and allow for full reconstruction of the Higgs boson kinematics. Unfolding techniques are used to correct for detector effects in the measurements, and comparisons are made to various state-of-the-art Standard Model theory predictions such as the predicted gluon-gluon fusion total cross section at N3LO and the Higgs differential transverse momentum spectrum at NNLO. These precision measurements are used to set limits on anomalous Higgs boson couplings beyond the Standard Model within the framework of pseudo-observables. In the $H \to ZZ^* \to 4\ell$ analysis, the inclusive fiducial Higgs boson cross section is measured to be 3.62 ± 0.50 (stat) +0.25/-0.20 (sys) fb, in agreement with the Standard Model prediction of 2.91 ± 0.13 fb. In the combined analysis, the inclusive total cross section is measured to be 57.0 +6.0/-5.9 (stat.) +4.0/-3.3 (syst.) pb, in agreement with the Standard Model prediction of of 55.6 ± 2.5 pb. Measured differential cross sections are also presented for the Higgs transverse momentum, Higgs rapidity, number of associated jets, leading jet transverse momentum, and other kinematic variables.

Contents

Acknowledgements iii

Abstract v

Contents vi

List of Tables xi

List of Figures xiii

Preface xviii

1 Introduction 1

2 Theoretical Framework 5

2.1 Introduction to the Standard Model 5

2.2 The Higgs Field and Electroweak Symmetry Breaking 8

2.3 The Higgs Cross Section 11

2.3.1 Parton Distribution Functions 12

2.3.2 Perturbative QCD 13

2.3.3 Higgs Production Modes 13

2.3.4 Higgs Decay Channels 17

2.4 Monte Carlo Simulations 18

2.4.1 Signal Event Generators 19

2.4.2 Background Event Generators 20

3 LHC and the ATLAS Detector **21**
3.1 The Large Hadron Collider . . . 21
3.2 Luminosity . . . 22
3.2.1 Pile-up . . . 23
3.3 The ATLAS Detector . . . 23
3.3.1 ATLAS Coordinate System . . . 24
3.4 The Inner Detector . . . 27
3.4.1 Pixel Detector . . . 27
3.4.2 Semiconductor Tracker . . . 27
3.4.3 Transition Radiation Tracker . . . 28
3.5 The Calorimeters . . . 30
3.5.1 Liquid Argon Calorimeters . . . 31
3.5.2 Tile Calorimeters . . . 31
3.6 The Muon System . . . 32
3.6.1 Muon System Barrel . . . 32
3.6.2 Muon System End-cap . . . 32

4 Trigger and Reconstruction **34**
4.1 The ATLAS Trigger . . . 34
4.1.1 Trigger Efficiency for $H \to 4\ell$ . . . 35
4.2 Electron Reconstruction and Identification . . . 36
4.2.1 Electron Reconstruction . . . 36
4.2.2 Electron Identification . . . 39
4.3 Muon Reconstruction and Identification . . . 40
4.3.1 Muon Reconstruction . . . 40
4.3.2 Muon identification . . . 42
4.4 Jet Reconstruction and Identification . . . 43
4.4.1 Jet Reconstruction . . . 43
4.4.2 Jet Identification . . . 44

5 Higgs Event Selection **45**
5.1 $H \to ZZ^* \to 4\ell$ . . . 45
5.2 Analysis Event Selection . . . 47

5.2.1 Lepton Selection . . . 47
5.2.2 Jet Selection . . . 48
5.2.3 Background Rejection . . . 48
5.2.4 Quadruplet formation . . . 49
5.2.5 Final State Radiation Recovery . . . 50
5.2.6 Mass Window . . . 50
5.3 Truth Fiducial Selection . . . 51
5.3.1 Lepton Selection . . . 52
5.3.2 Dressed leptons definition . . . 52
5.3.3 Jet Selection . . . 53
5.3.4 Quadruplet Formation . . . 53
5.3.5 Study: Truth lepton definition comparisons . . . 54
5.4 Variable Definitions . . . 55
5.4.1 Higgs Invariant Mass . . . 56
5.4.2 Kinematic Variables . . . 56
5.4.3 Jet variables . . . 58
5.5 Optimized Binning . . . 59

6 Backgrounds **68**
6.1 Irreducible Background . . . 68
6.2 Reducible Background . . . 70
6.3 Reducible $\ell\ell + \mu\mu$ Background . . . 71
6.3.1 $\ell\ell\mu\mu$ Control Regions . . . 71
6.3.2 Step 1. Fit for $Z + bb$ and $t\bar{t}$ . . . 73
6.3.3 Step 2. Fit for Z+light . . . 74
6.3.4 $\ell\ell\mu\mu$ Results . . . 75
6.4 Reducible $\ell\ell + ee$ Background . . . 76
6.4.1 $\ell\ell ee$ Control Regions . . . 77
6.4.2 The n_{InnerPix} fit in $3\ell + X$ . . . 78
6.4.2.1 Events in the CR, $N^{3\ell+X}_{\text{data},ijk}$ . . . 79
6.4.2.2 Efficiency, ε_{ijk} . . . 79
6.4.2.3 Scale Factor, $\mathcal{S}_{ij}$ . . . 80
6.4.3 $\ell\ell ee$ Result . . . 81

7 Unfolding **83**
7.1 Introduction . . . 83
7.2 Acceptance factors . . . 84
7.3 Correction factors . . . 87
7.3.1 Bin-by-bin correction factors . . . 89
7.4 Fiducial Leakage and Purity . . . 91
7.5 Alternative Models . . . 92

8 Systematic Uncertainties **95**
8.1 Event Systematics . . . 95
8.1.1 Electron uncertainties . . . 96
8.1.2 Muon uncertainties . . . 96
8.1.3 Jet uncertainties . . . 97
8.2 Background Systematics . . . 100
8.3 Unfolding Systematics . . . 102

9 Statistical Methods **108**
9.1 Simple Example . . . 109
9.2 Signal Extraction with Backgrounds and Nuisance Parameters . . . 110
9.2.1 Adding Systematic Uncertainties . . . 112
9.3 Inclusive Cross Section Measurement . . . 112
9.3.1 The Likelihood function . . . 113
9.3.2 Parameter Estimation . . . 114
9.4 Differential Cross Section Measurement . . . 115
9.5 Tests on Asimov Data . . . 115
9.6 Combination with $H \to \gamma\gamma$ . . . 125
9.6.1 Acceptance Factors for Full Phase Space . . . 125
9.6.2 Combination Likelihood Function . . . 126

10 Cross Section Results **129**
10.1 Events Measured . . . 129
10.2 Fiducial Cross Sections . . . 134
10.2.1 Inclusive Cross Section . . . 134
10.2.2 Differential Cross Section . . . 134

10.3 Total Cross Sections 139
10.3.1 Inclusive Cross Section 139
10.3.2 Differential Cross Section 139
10.4 Limits on Beyond the Standard Model Physics 142
10.4.1 Brief Introduction to Effective Field Theories 142
10.4.2 Parameterizing a BSM model 143
10.4.3 Settings limits on Pseudo Observables 145

11 Conclusion **147**

Bibliography **150**

List of Tables

21 Standard Model Higgs boson production cross sections for gluon fusion, vector-boson fusion and associated production with a W or Z boson or with a $b\bar{b}$ or $t\bar{t}$ pair in pp collisions at $\sqrt{s} = 13$ TeV. 15

41 Efficiencies of various triggers and their combinations, used in 2015, for 125 GeV ggF Higgs signals in the four decay channels. The uncertainties are from MC statistics. . . 37
42 Efficiencies of various triggers and their combinations, used in 2016, for 125 GeV ggF Higgs signals in the four decay channels. The uncertainties are from MC statistics. . . 38

51 The percent difference of born to dressed fiducial events on a $m_H = 125$ GeV ggF sample using different definitions of the dressing. 55
52 Binning chosen for Higgs kinematic variables Jet variables of interest. 61

61 Transfer factor calculated from Monte Carlo simulations in SR and Relaxed CR. The shown errors on the transfer factors are statistical only. 73
62 Estimate of the reducible $\ell\ell\mu\mu$ event yields. 76
63 Data/MC scale factors for f and γ calculated from their respective enriched $Z + X$ CR. Errors shown are statistical only. 81
64 Estimate of the reducible $\ell\ell ee$ event yields. 82

71 The fiducial leakage on a $m_H = 125$ GeV ggF sample using the born, dressed, and bare truth lepton defintions. 92

81 Summary of the systematic uncertainties on the inclusive irreducible and reducible backgrounds. 102
82 Summary of the systematic uncertainties on the inclusive $\mathcal{A}$ and $\mathcal{C}$ factors for the fiducial analysis. 107

91 Expected and fitted cross sections in each category of p_T using the Asimov dataset (top) without systematics and (bottom) with systematics. 121
92 Expected and fitted cross sections in each category of N_{jets} using the Asimov dataset (left) without systematics and (right) with systematics. 121

93 Summary of particle level fiducial definitions in the $H \to \gamma\gamma$ analysis. The particle photon isolation $p_{\mathrm{T}}^{\mathrm{iso},0.2}$ is defined analogously to the track isolation of reconstructed objects as the transverse momentum of the system of charge truth particles within $\Delta R < 0.2$ of the photon. 126
94 Acceptance factors and total systematic errors for the $H \to ZZ^* \to 4\ell$ channels. 126
95 Acceptance factors and total systematic errors for the $H \to \gamma\gamma$ channels. 126

101 The number of events expected and observed for a $m_H = 125\,\mathrm{GeV}$ hypothesis for the four lepton final states using the FSR-corrected $m_{4\ell}$. 130
102 p-values (in percent) indicating the compatibility of the measured differential cross sections and various theory predictions 135
103 p-values (in percent) indicating the compatibility of the measured differential cross sections and various theory predictions 140
104 Descriptions of the pseudo observables that affect the $H \to ZZ^* \to 4\ell$ channel. 144

List of Figures

11 Simplified cartoon of the expected differential cross section between the Thomson and Rutherford models of the atom as a function of scattering angle. 3

21 The Standard Model of Particle Physics info-schematic. 6
22 Illustration of the Higgs potential and spontaneous symmetry breaking. 9
23 NNLO PDFs with 68% confidence intervals for gluons, sea quarks, and valence quarks in the proton as calculated by MMHT at $Q^2 = 10\,\text{GeV}^2$ (left) and $Q^2 = 10^4\,\text{GeV}^2$ (right). 12
24 Calculated cross sections for a Standard Model Higgs boson with a mass of 125 GeV in pp collisions as a function of the center of mass energy $\sqrt{s}$. 15
25 Lowest order Feynman diagrams for gluon-gluon fusion ($gg \to H$) (left) and vector boson fusion ($qq' \to Hqq'$) (right). 16
26 Feynman diagrams of the Higgs production modes where the Higgs couples to vector bosons. 16
27 Feynman diagrams of the Higgs production modes where the Higgs couples directly to fermions. 16
28 Calculated branching fractions for some decay channels of the Higgs boson as a function of Higgs mass. 17
29 Illustration of a $t\bar{t}H$ simulation using the SHERPA Monte Carlo generator. 18

31 A schematic of the CERN accelerator complex. 22
32 Luminosity-weighted distribution of the mean number of interactions per bunch crossing for 2015 and 2016 (left) and integrated luminosity recorded by ATLAS during stable beams over Run 1 and Run 2 (right). 24
33 General cut-away view of the ATLAS detector. 25
34 Picture representing how ATLAS detects different kinds of particles. 26
35 Cut away view of the ATLAS Inner Detector. 28
36 The probability to exceed the high threshold for electrons and muons from J/ψ and Z decays as a function of the Lorentz factor. 29
37 Cut away view of the ATLAS Calorimeters. 30
38 Cut away view of the ATLAS Muon System. 33
39 Side view in the yz plane of one-fourth of the ATLAS Muon System. 33

41 Schematic of the ATLAS Trigger and Data Acquisition system in Run 2 showing expected event rates and data rates through each decision step. . . . 35
42 All trigger efficiency in the combined final state and in each of the four final states as a function of the Higgs p_{T}. . . . 36
43 Measured electron reconstruction efficiencies as a function of E_{T} (left) and as a function of $|\eta|$ (right) for the 2015 dataset. . . . 39
44 Combined electron reconstruction and identification efficiencies in $Z \to ee$ events as a function of the transverse energy E_{T} and pseudorapidity η 41
45 Combined muon reconstruction and identification efficiencies in $J/\psi \to \mu\mu$ and $Z \to \mu\mu$ events as a function of the transverse momentum p_{T} (left) and as a function of pseudorapidity η (right) for the *Loose* selection. . . . 43

51 Feynman diagram of the $H \to ZZ^* \to 4\ell$ decay channel. . . . 46
52 $m_{4\ell}$ before FSR recovery and $m_{4\ell}$ after FSR recovery. Only events with an identified FSR are shown in this plot. . . . 51
53 Plots show born vs. dressed distributions using a ggF $m_H = 125\,\mathrm{GeV}$ MC sample to compare the inclusive distributions (before any fiducial cuts) of m_{12}, m_{34}, and p_T^H. . . . 54
54 Diagram of decay angles for the $H \to ZZ^* \to 4\ell$ decay. . . . 57
55 Proportion of production modes for N_{jets}. A SM Higgs with $m_H = 125.0\,\mathrm{GeV}$ has been assumed. . . . 58
56 m_{12} versus m_{34} distribution and bin edges illustration. . . . 62
57 Expected signal and background events at $36.1\mathrm{fb}^{-1}$ for $p_T^{4\ell}$. For each bin, S/B and expected significance values are listed. . . . 62
58 Expected signal and background events at $36.1\mathrm{fb}^{-1}$ for $|y^{4\ell}|$. For each bin, S/B and expected significance values are listed. . . . 63
59 Expected signal and background events at $36.1\mathrm{fb}^{-1}$ for $|\cos\theta^*|$. For each bin, S/B and expected significance values are listed. . . . 63
510 Expected signal and background events at $36.1\mathrm{fb}^{-1}$ for m_{12}. For each bin, S/B and expected significance values are listed. . . . 64
511 Expected signal and background events at $36.1\mathrm{fb}^{-1}$ for m_{34}. For each bin, S/B and expected significance values are listed. . . . 64
512 Expected signal and background events at $36.1\mathrm{fb}^{-1}$ for m_{12}vs.m_{34}. For each bin, S/B and expected significance values are listed. . . . 65
513 Expected signal and background events at $36.1\mathrm{fb}^{-1}$ for N_{jets}. For each bin, S/B and expected significance values are listed. . . . 65
514 Expected signal and background events at $36.1\mathrm{fb}^{-1}$ for $p_T^{\text{lead. jet}}$. For each bin, S/B and expected significance values are listed. . . . 66
515 Expected signal and background events at $36.1\mathrm{fb}^{-1}$ for m_{jj}. For each bin, S/B and expected significance values are listed. . . . 66
516 Expected signal and background events at $36.1\mathrm{fb}^{-1}$ for $\Delta\eta_{jj}$. For each bin, S/B and expected significance values are listed. . . . 67
517 Expected signal and background events at $36.1\mathrm{fb}^{-1}$ for $\Delta\phi_{jj}$. For each bin, S/B and expected significance values are listed. . . . 67

61 Expected Higgs and expected irreducible background events (obtained from MC) at $36.1\mathrm{fb}^{-1}$. $q\bar{q}ZZ$ contributes the most. Next is $ggZZ$ at less than 4% of $q\bar{q}ZZ$. Triboson (ZZW,WWZ,ZZZ) and $V + t\bar{t}$ all-leptonic all together are minor. . . . 69
62 Irreducible background contributions. $q\bar{q}ZZ$ contributes the most. Next is $ggZZ$. Triboson (ZZW,WWZ,ZZZ) and $V + t\bar{t}$ all-leptonic are minor irreducible backgrounds. . 69

63 Reco data events compared to Monte Carlo truth reco events in an irreducible background control region. Defined by an event selection where the mass window cut is replaced by $m_{4\ell} < 115$ GeV or 130 GeV$< m_{4\ell} <$ 170 GeV. 70
64 Expected Higgs and expected reducible background events (gotten from MC) at 36.1fb^{-1}. Z+jets contributes the most. $t\bar{t}$ and WZ are minor. 70
65 Reducible background contributions. Z+jets contributes the most, through both heavy and light quark jets. Others include WZ and $t\bar{t}$ (where the b-jets semileptonically decay). 71
66 The m_{12} distributions for data and MC-simulated events in the inverted d_0 CR (left) and the $e\mu$+$\mu\mu$ CR (right). 74
67 Distributions of m_{12} in the CRs. The data are fitted simultaneously in the the inverted d_0 (left) and the $e\mu$+$\mu\mu$ (right) CRs and the result of the fit is shown with the continuous line. The dashed lines correspond to the $Z + bb$ and $t\bar{t}$ components of the fit. 75
68 The left plot shows the m_{12} distributions for data and MC-simulated events from different background sources in the inverted isolation control region. The right plot shows the m_{12} distributions for data and the final fit to different background sources in the inverted isolation control region. The fits use the analytic functions of the background shapes. No Z+light background yield is found from the fit. 76
69 $\ell\ell + \mu\mu$ Relaxed CR plots for $p_T^{4\ell}$ (left) and N_{jets} (right). Background yields are taken from the data driven method for Z+jets and $t\bar{t}$ while ZZ^*,WZ, and Triboson are taken from Monte Carlo. 77
610 (Left) Templates used in the 3ℓ+X fit to n_{InnerPix} for the γ and f backgrounds, obtained from MC simulation in the Z+X control sample. q is very similar in shape to f and f is used for both when needed. (Right) Data 3ℓ+X events and result of the fit to n_{InnerPix} with q estimated from MC and subtracted out. 80

71 Acceptance factors for $\sqrt{s} = 13\,\text{TeV}$ and 125.0 GeV. 86
72 Values of $\mathcal{A}$ as a function of $p_T^{4\ell}$ and N_{jets}. 86
73 Response matrices evaluated using signal MC at $m_H = 125\,\text{GeV}$ (summing over all production modes) for $p_T^{4\ell}$ (a) and N_{jets} (b). Only the events that pass both fiducial and reco selection cuts have been included. 88
74 Correction factors for $\sqrt{s} = 13\,\text{TeV}$ and 125.0 GeV. 89
75 Values of $\mathcal{C}$ as a function of $p_T^{4\ell}$ and N_{jets}. 90
76 Purity of production modes for variables $p_T^{4\ell}$ (a) and N_{jets} (b) in each bin. A SM Higgs with $m_H = 125.0\,\text{GeV}$ has been assumed. 93
77 ggF values of $\mathcal{A}$ and $\mathcal{C}$ as a function of $p_T^{4\ell}$ for Powheg (nominal) and MadGraph SM and EFT samples. 93
78 ggF values of $\mathcal{A}$ and $\mathcal{C}$ as a function of N_{jets} for Powheg (nominal) and MadGraph SM and EFT samples. 94

81 Effect of the electron systematics on the (left) $p_T^{4\ell}$ and (right) N_{jets} yields. The nominal distribution (black) is compared with up (red) and down (blue) variations. 97
82 Effect of the muon systematics on the (left) $p_T^{4\ell}$ and (right) N_{jets} yields. The nominal distribution (black) is compared with up (red) and down (blue) variations. 98
83 Effect of the jet systematics on the (left) $p_T^{4\ell}$ and (right) N_{jets} yields. The nominal distribution (black) is compared with up (red) and down (blue) variations. 99
84 $p_T^{4\ell}$ (left) and N_{jets} (right) scale uncertainties due to missing higher terms in the ZZ^* Monte Carlo. The envelope of the scale variations determines the final uncertaintity. . . 100

85 $p_T^{4\ell}$ (left) and N_{jets} (right) PDF theory variations due to alternative choices of Parton Distribution Function in the Monte Carlo. The envelope of the variations determines the final uncertaintity. . . . 101
86 Comparison of scaled efficiencies $\mathcal{S}_{ij} \cdot \varepsilon_{ij}$ obtained from Sherpa 2.2.1 and MadGraph for the f (left) and γ (right) background components. The blue band around Sherpa represents uncertainty from q contamination. . . . 102
87 Renormalization (stylized `muR` in the plots) and Factorization (`muF`) scale uncertainties on the Acceptance (left) and Correction (right) factor are shown for variable $p_T^{4\ell}$. The envelope of the 8 scale variations determines the final uncertaintity. . . . 103
88 Renormalization (stylized `muR` in the plots) and Factorization (`muF`) scale uncertainties on the Acceptance (left) and Correction (right) factor are shown for variable N_{jets}. The envelope of the 8 scale variations determines the final uncertaintity. . . . 104
89 Uncertainties due to the variation of the PDF sets on the Acceptance (left) and Correction (right) factor for variable $p_T^{4\ell}$. Each plot is one of the 32 PDF4LHC variations. . . . 104
810 Uncertainties due to the variation of PDF sets on the Acceptance (left) and Correction (right) factor for variable N_{jets}. Each plot is one of the 32 PDF4LHC variations. . . . 104

91 Higgs boson production mode fractions as a function of variables p_T (a), $|y|$ (b), $|cos(\theta^*)|$ (c), m_{12} (d), m_{34} (e), and m_{12}vs.m_{34} (f). A SM Higgs with $m_H = 125.0\,\text{GeV}$ has been assumed. . . . 116
92 Higgs boson production mode fractions as a function of variables N_{jets} (a), $p_T^{\text{lead. jet}}$ (b), $\Delta\eta_{jj}$ (c), $\Delta\phi_{jj}$ (d), m_{jj} (e). A SM Higgs with $m_H = 125.0\,\text{GeV}$ has been assumed. . . . 117
93 Differential $\mathcal{C}$ factors for variables p_T (a), $|y|$ (b), $|cos(\theta^*)|$ (c), m_{12} (d), m_{34} (e) and m_{12}vs.m_{34} (f) in each bin. A SM Higgs with $m_H = 125.0\,\text{GeV}$ has been assumed. . . . 118
94 Differential $\mathcal{C}$ factors for N_{jets} (a), $p_T^{\text{lead. jet}}$ (b), $\Delta\eta_{jj}$ (c), $\Delta\phi_{jj}$ (d), m_{jj} (e) in each bin. A SM Higgs with $m_H = 125.0\,\text{GeV}$ has been assumed. . . . 119
95 Expected and fitted cross section for the fiducial inclusive cross section using Asimov data and assuming an integrated luminosity of 36.1fb^{-1}. The table shows cross section uncertainty with and without systematics included. . . . 120
96 Cross sections fit in bins 0 through 5 of p_T distribution ($\sigma_{p_T,\,i}$) using the Asimov dataset. Systematic uncertainties are included. . . . 122
97 Cross sections fit in bins 6 through 9 of p_T distribution ($\sigma_{p_T,\,i}$) using the Asimov dataset. Systematic uncertainties are included. . . . 123
98 Cross sections fit in each bin of N_{jets} distribution ($\sigma_{N_{\text{jets}},\,i}$) using the Asimov dataset. Systematic uncertainties are included. . . . 124
99 Acceptance factors and total uncertainties for a 125.0 GeV Higgs at $\sqrt{s} = 13\,\text{TeV}$ in the $H \to ZZ^* \to 4\ell$ and $H \to \gamma\gamma$ channels. Plots show acceptance factors for p_T^H, $|y^H|$, N_{jets}, and $p_T^{\text{lead. jet}}$. The first bin of $p_T^{\text{lead. jet}}$ is the same as the 0-jet bin in N_{jets}, as indicated by the black vertical line . . . 127

101 Invariant mass of the four lepton system ($m_{4\ell}$) comparing data and expected events from MC simulation. . . . 130
102 Distribution of p_T (top left), $|y|$ (top right), m_{12} (bottom left) and m_{34} (bottom right) when comparing data and MC simulation. . . . 131
103 Distribution of $|\cos(\theta^*)|$ (top left), N_{jets} (top right), $p_T^{\text{lead. jet}}$ (bottom left) and m_{jj} (bottom right) when comparing data and MC simulation. . . . 132
104 Distribution of $\Delta\eta_{jj}$ (left), $\Delta\phi_{jj}$ (right), and m_{12}vs.m_{34} (bottom) when comparing data and MC simulation. . . . 133

105 Differential fiducial cross sections, for (top left) the transverse momentum $p_T^{4\ell}$ of the Higgs boson, (top right) the absolute value of the rapidity $|y^{4\ell}|$ of the Higgs boson, (bottom left) the invariant mass of the leading lepton pair m_{12}, (bottom right) the invariant mass of the subleading lepton pair m_{34}. 136
106 Differential fiducial cross sections, for (top left) the number of jets N_{jets}, (top right) the transverse momentum of the leading jet $p_T^{\text{lead. jet}}$, (bottom left) the magnitude of the cosine of the decay angle of the leading lepton pair in the four lepton rest frame with respect to the beam axis $|\cos\theta^*|$, and (bottom right) the invariant mass of the two leading jets m_{jj}. 137
107 Differential fiducial cross sections, for (top left) the angle between the two leading jets in the transverse plane $\Delta\phi_{jj}$, (top right) the difference in pseudorapidity between the two leading jets $\Delta\eta_{jj}$, and (bottom) the invariant mass of the leading lepton pair vs that of the subleading pair m_{12}vs.m_{34}. 138
108 Differential total cross sections, for (top left) the transverse momentum p_T^H of the Higgs boson, (top right) the absolute value of the rapidity $|y^H|$ of the Higgs boson, (bottom left) the number of jets N_{jets}, and (bottom right) the transverse momentum of the leading jet $p_T^{\text{lead. jet}}$. 141
109 The left diagram shows a $us \to du$ weak decay using the full Standard Model theory, while the right diagram shows the same diagram in Fermi's Theory, an EFT of the weak interaction. 142
1010 Limits on pseudo-observables in $H \to 4\ell$ decays. On the left plot, the limits are set for $\varepsilon_{Z\ell_L}$ and $\varepsilon_{Z\ell_R}$, which are contact terms between Higgs boson and Z+left/right-handed leptons. On the right, limits are set on a linear EFT inspired scenario expressed with $\varepsilon_{Z\ell_L}$ and κ_{ZZ}. κ_{ZZ} modifies the strength of the Higgs boson coupling to Z bosons. The 95% confidence contour is surrounded by the red solid line. It is shifted with respect to the Standard Model (the black star and the black dotted line) but there are no significant deviations. The colors indicates the values of $-2\ln\lambda$. 146

Preface

In 2013 I joined the University of Pennsylvania ATLAS group after an internship at Brookhaven National Lab working on LAr calorimeter trigger upgrades for ATLAS Phase-I. I was very curious about hardware on ATLAS, and decided to join Penn in part for their involvement in the development and maintenance of the TRT subdetector. I began learning about the TRT during my first summer before starting classes by going to CERN and meeting the Penn group there. I had an amazing time in Geneva and enjoyed working with my future colleagues, all extremely smart and kind. When I returned to Philadelphia in the Fall, I began classes while continuing to learn about the TRT and thinking about what to do for my authorship task.

In 2014 while still taking classes, I would often return to Geneva for a few weeks at a time to help out with Run 2 upgrades of the TRT. CERN was in the middle of its Long Shutdown period, so I got to spend a lot of time using the detector and learning about the ATLAS data acquisition (DAQ) system. I will never forget the first time I ever went down to the ATLAS cavern and got to crawl around inside the detector and see it all for myself. During this time of upgrades, I also developed a High Threshold Calibration program as a way to correct for the effects of radiation damage the team had measured on the front-end boards over Run 1. I presented my program at the TRT Workshop in Krakow, Poland in June. At this point I also began learning about Higgs cross sections and began working with the Higgs combination "HComb" group to combine the data from $H \to ZZ^* \to 4\ell$ and $H \to \gamma\gamma$ analyses at 8 TeV to measure the Higgs boson differential cross section. My responsibilities involved calculating the acceptance and correction factors for the analysis.

I finished my classes in April of 2015, around the same time the HComb differential cross section paper was being submitted for publication. I moved to Geneva in May, where I began to work full time as part of the TRT DAQ operations team. We worked on upgrading the TRT DAQ to run at a 100 kHz trigger rate for Run 2, which would start later that year. At this time, I also became

involved with the HZZ group, specifically in the four lepton group. I began studying and optimizing new cuts for the Higgs boson signal selection, and began writing the framework for the fiducial analysis. As for the HComb analysis, in June I was able travel to Vienna in Austria to present a poster at EPS-HEP on the combined differential cross section results. In August, the paper was published in Physics Review Letters [1].

At the start of 2016, while visiting the USA, I chose my dissertation topic to be the measurement of the Higgs boson fiducial differential cross section in the four lepton channel using the new 13 TeV data. When I returned to Geneva, I helped upgrade the HOLA cards on the TRT back-end computers to increase the data throughput rate of the TRT by 20%. I also began working on multiple aspects of the four lepton analysis. I continued developing the fiducial framework for the group in order to study the unfolding of the signal from the reconstructed to fiducial phase space, I calculated the acceptance and correction factors for the cross section analysis, and also calculated the theory systematics for the analysis. The framework was also useful for testing alternative models where certain EFT couplings were included. During this year I also became the trigger contact person for the HZZ group and calculated the Higgs to four lepton trigger rates for different luminosity scenarios in 2016. I was also the editor for the 2016 ICHEP supporting note for the four lepton inclusive cross section measurement. During the year I continued to be involved in TRT DAQ and gained more responsibility on the team.

In 2017, I became TRT DAQ coordinator. In addition to the standard responsibilities of detector calibration, maintenance, and upgrades, one of my goals was to make the running of the operations more efficient. I began a campaign to move the TRT DAQ code base from SVN to Git, change the compilation scheme from cmt to CMake, add continuous integration and basic testing of the code base, and also create a better documentation service that was searchable (dubbed DAQ-docs) to replace the Twiki service. In terms of research, I also began calculating expected cross sections for the four lepton analysis using a maximum likelihood method with simulated Asimov data while continuing the calculation of systematic uncertainties for the analysis. I presented the four lepton fiducial differential cross section results at the Rencontres de Blois Conference in June. In August we were able to submit the paper for publication, and it was published in the Journal of High Energy Physics in October [2]. At this point I began working on the HComb differential cross section analysis, the same analysis as in my first year, but for 13 TeV data.

In 2018 I moved back to Philadelphia. I continued to work in the HZZ group by providing updates to the fiducial framework and also in the HComb cross section analysis by providing the acceptance and correction factors as well as systematic theory uncertainties. The combined $H \to ZZ^* \to 4\ell$ and

$H \to \gamma\gamma$ differential cross section results were submitted for publication in May, and were published in Physics Letters B recently this November [3]. Since the summer I have also been working on completing this document. In the interest of length and time, I have focused on the 13 TeV analyses and results rather than the 8 TeV analysis and TRT upgrades. As with any long piece of writing, the most important thing is an engaging and gripping title. There were many other titles for this thesis I workshoped before settling on the current one. Some of the alternatives include:

- Cross sections at the crossroads of the Standard Model and New Physics.
- Two Z or not two Z, that is the question.
- Catching some ZZs: The dream of New Physics measurements with ATLAS (credit to Leigh)
- Spontaneous Symmetry Breakin' in Run 2: Electron Boogaloo.
- ATLASt, a new Higgs cross section measurement!
- 4 Leptons 4 Furious: Charged, prompt, and vevving the engine.
- The 7 distributions of highly effective field theories: Powerful lessons from Higgs cross section measurements.
- How to BULK UP this epoch with tips from Peter Higgs!
- Golden Channels and Parton Showers: The UNCENSORED TRUTH about the GOD Boson.

Working on ATLAS has been an amazing experience. The sense of teamwork and collaboration is unparalleled to any other kind of work I've done, and the scope of the questions ATLAS is trying to answer is both grand and humbling. In this thesis, I present a very small part of the entire program of ATLAS, a measurement of the Higgs boson cross section. I begin by explaining the theory behind cross sections and what they are used for, how to select for Higgs boson events out of billions of collisions, how to estimate backgrounds and systematics, and how to extract a result that can be compared to other experiments and exclude alternative models. This thesis is largely silent on the work I did to maintain and upgrade the TRT, though it is probably the thing I spent the most time doing. There are so many hidden parts that go into making a giant endeavor like ATLAS a success. Nothing written here would have been possible without the work of my colleagues in all of ATLAS operations, Combined Performance, and in Higgs Physics. The work presented in this thesis is a mix of my own work and theirs. I am thankful for everyone I met and worked with for making this period of my life so memorable and meaningful.

Bijan Haney

Philadelphia, November 2018

Chapter 1

Introduction

On July 4, 2012, ATLAS and CMS announced the discovery of a new particle with a measured mass of 126.0 GeV and 125.3 GeV respectively [4, 5]. Its mass, charge, spin, couplings and other properties were consistent with the Standard Model's Higgs boson, introduced in 1964 to explain how the W and Z gauge bosons gained mass without ruining the Standard Model's gauge symmetries [6, 7, 8]. As a result of this monumental discovery, the 2013 Nobel Prize in Physics was awarded to Peter Higgs and François Englert for their contributions to the theory. It would have surely been awarded to Robert Brout as well, Englert's collaborator and coauthor, if he had not passed away at the age of 82 only a year before the new particle was discovered.

Between 2013-2015 the LHC shut down to increase the center of mass energy of its collisions from 7 TeV to 13 TeV as well as to increase its collision rate from every 50 ns to every 25 ns. ATLAS and CMS also did upgrade work to handle the future increase in data throughput and improve their detector electronics. They were preparing for a new era of particle physics research with collision energies more powerful than ever before, with a completed Standard Model, a culmination of more than 50 years of theory and experiment. But a completed Standard Model does not a mean a total model of particle physics. There are many questions in particle physics still open that the Standard Model cannot answer. What is dark matter? Why is there more matter than anti-matter in the universe even though the theory predicts them to be created at almost equal rates? What is the Quantum Field Theory of gravity? Besides completing the Standard Model, a large program at CERN and the LHC has always been to find anomalies and inconsistencies with the theory in hopes of answering these open questions.

Since beginning Run 2 at the LHC in 2015, ATLAS has been measuring the new scalar boson (now established as a Higgs boson) as precisely as possible to see if there are any hints of physics beyond

the Standard Model. Research with new Run 2 data has improved the Higgs mass measurement [9], width measurement [10], coupling measurement [11, 12], as well as the cross section measurement [12, 2, 3]. This thesis will describe the Higgs cross section measurement as published in [2] and [3], both inclusively and differentially, using $\mathcal{L}_{\text{int}} = 36.1\,\text{fb}^{-1}$ worth of data from 2015 and 2016 at the LHC.

What is a cross section? In broad terms, it is quantity with units of area that is proportional to the probability of particles scattering off of each other in a collider experiment[1]. In an elastic scattering experiment, the outgoing particles of the scatter are the same as the incoming ones, but in inelastic scattering events like the ones of interest at the LHC, the outgoing particles can be completely different than the incoming ones. Therefore a cross section can be thought of as being a probability of a scattering experiment going from known incoming particles like protons, to new outgoing particles, like a Higgs boson. A *differential* cross section is a cross section as a function of some observable, such as the angle of at which the outgoing particle scatters.

To give a better idea of why measuring a cross section is a powerful method of investigating the unknown properties of particles, we can look at history. The most well-known differential cross section experiment in particle physics might be the Rutherford gold foil experiment done in 1909 [13]. The electron had been discovered in 1897 but the structure of the atom was still an open question. J.J. Thompson had proposed that the atom was a uniform sphere of positive charge and electrons were embedded evenly throughout the diffuse charge, like negative plums in a positive plum pudding [14]. Rutherford's experiment, carried out by his students Hans Geiger and Ernest Marsden, was designed to gain insight into the structure of the atom by conducting a scattering experiment by colliding α-particles against the atoms of gold in a foil and measuring the differential cross section of the scattering angle of the rebounding α's.

In the experiment, α-particles were accelerated towards a stationary gold foil and the angle of scattering of the rebounding α's was measured. This was expressed as a differential cross section measurement $\frac{\mathrm{d}\sigma}{\mathrm{d}\Omega}$, where σ denotes the cross section and Ω is the solid angle of scattering. As this was an elastic scattering experiment, the incoming and outgoing α's were the same. The experiment showed the differential cross section to be proportional to $\frac{1}{\sin^4(\theta/2)}$ i.e. $\frac{\mathrm{d}\sigma}{\mathrm{d}\Omega} \propto \frac{1}{\sin^4(\theta/2)}$, where θ is the angle relative to the initial motion of the α particles. $\theta = 0$ is the α continuing straight ahead, and $\theta = 180°$ is the α rebounding right back towards the emitter. The differential distribution showed that most particles passed right through the gold foil (as the Thomson model predicted), but that there was also a non-negligible chance of the α rebounding at very large angles, even right back at 180 degrees! This result gave huge insight into the structure of the atom, revealing a small positive

[1] More details about Higgs cross section in Section 2.3

nucleus at the center of the atom, and refuting Thomson's idea of a "plum-pudding" model of the atom as an evenly distributed positive charge. See Figure 11 for an illustration of the differential cross section as predicted by both models.

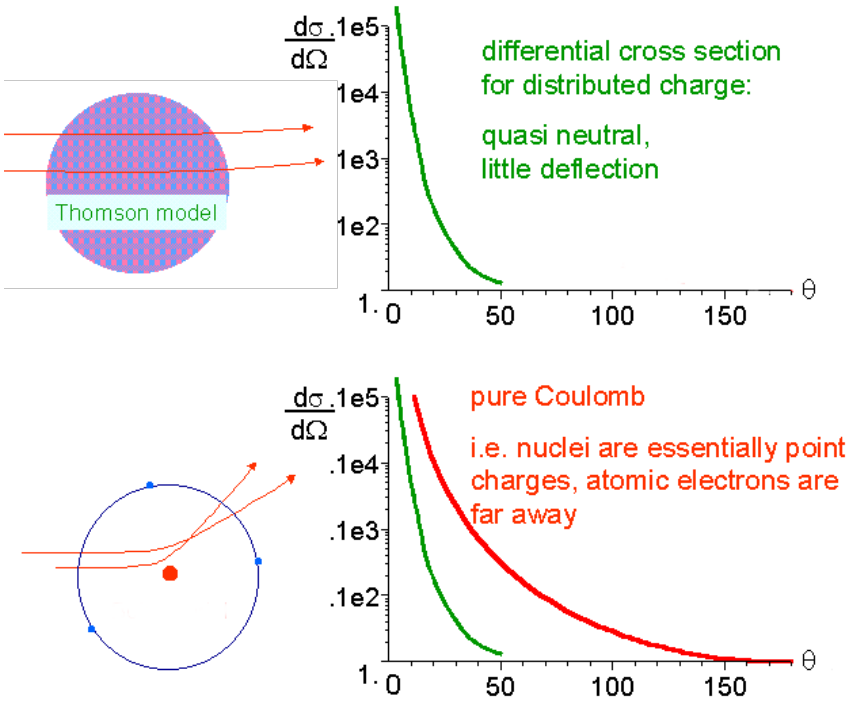

Figure 11: Simplified cartoon of the expected differential cross section between two models of the atom as a function of scattering angle. The Thomson "plum pudding" expected differential cross section is shown in green while the Rutherford expected differential cross section is shown in red. The scattering angles seen in the experiment are too large on average to be explained by an evenly distributed positive charge in the entire atom, but fit well for a model generated by assuming a concentrated point positive charge interacting through the Coulomb force [15].

Coming back to the modern day, our current understanding of particle physics in encoded in the Standard Model and the predictions it makes. By probing the cross section of the Higgs, we can test the predicted properties of the new boson as well as discover unexpected physics by measuring deviations from those predictions. Properties like the strength of the coupling of the Higgs to other bosons and fermions will affect how often a Higgs boson is created in proton-proton collisions, as well as how often it will decay to final states like two photons or four leptons. The structure of the proton and the effects of higher order terms in perturbative QCD can be measured by studying the

number and distributions of jets produced in association with the Higgs boson.

The differential cross section of the Higgs is also measured as a function of much more than just the scattering angle. It can be measured as a function of variables such as its transverse momentum p_T^H, rapidity $|y^H|$, number of associated jets in the event, N_{jets}, and many more, each which can be sensitive to different properties such as the Higgs spin, parity, production mode, and proton structure. All the measured differential variables are explained in Section 5.4. Any beyond-the-Standard-Model theories that add new terms to the Higgs interaction, undiscovered particles that have mass, or any anomalous modifications of the Higgs couplings to Standard Model particles will also show up in the measurements of the Higgs inclusive and differential cross section.

The theory behind the Higgs boson and how to measure its cross section is explained in Chapter 2, while the ATLAS detector itself is described in Chapter 3, and Chapter 4 describes the methods for reconstructing the measured particles. Chapter 5 describes how to select Higgs boson events from collisions in ATLAS using a very sensitive decay channel, the $H \to ZZ^* \to 4\ell$ channel, and how to optimize the signal significance in this channel. Chapter 6 describes the common backgrounds of the Higgs selection and the use of control regions to constrain the uncertainty on the background events. Chapter 7 describes the methods for unfolding the number of measured Higgs events to a more detector independent phase space. Chapter 8 describes the systematic uncertainties on the cross section measurements. Chapter 9 describes the maximum likelihood method used to extract the Higgs inclusive and differential cross sections from the measured events. Finally Chapter 10 summarizes the cross section results.

Chapter 2

Theoretical Framework

2.1 Introduction to the Standard Model

The Standard Model (SM) of particle physics describes the fundamental particles as well as three of the four fundamental forces of nature (i.e. strong, electromagnetic, and weak force). It successfully predicts their interactions down to the current smallest measurable scale of around 10^{-19} m.[2] It is a Quantum Field Theory (QFT) where the particles that make up matter are described as the excitations of spin-1/2 fermion fields, and the forces between them are described by the exchange of excitations of spin-1 gauge boson fields. There is also a spin-0 boson field, known as the Higgs field, which is responsible for electroweak symmetry breaking (EWSB)[3] and giving some bosons and fermions their mass.

The fermion fields can be split into two families, quarks and leptons, where quarks have color charge and interact with the strong force, while leptons do not. The gauge boson fields (after EWSB) are each associated with one of three fundamental force:

1. The eight gluon fields, G_μ, are associated with the strong force and couple to fields with color charge C. The strength of the coupling is denoted by α_s and is of order 1.

2. The photon field, A_μ, is associated with the electromagnetic force and couples to fields with electric charge Q. The strength of its coupling is the fine structure constant, $\alpha = 1/137$.

3. The $W^\pm_\mu$ and Z_μ are three fields that are associated with the weak force and couple to fields with a weak isospin charge I. The strength of its coupling is denoted by α_w and is of order $\sim 10^{-6}$.

[2] $\frac{\hbar c}{1\,\mathrm{TeV}} = 2.0 \times 10^{-19}\,\mathrm{m}$
[3] Explained in Section 2.2.

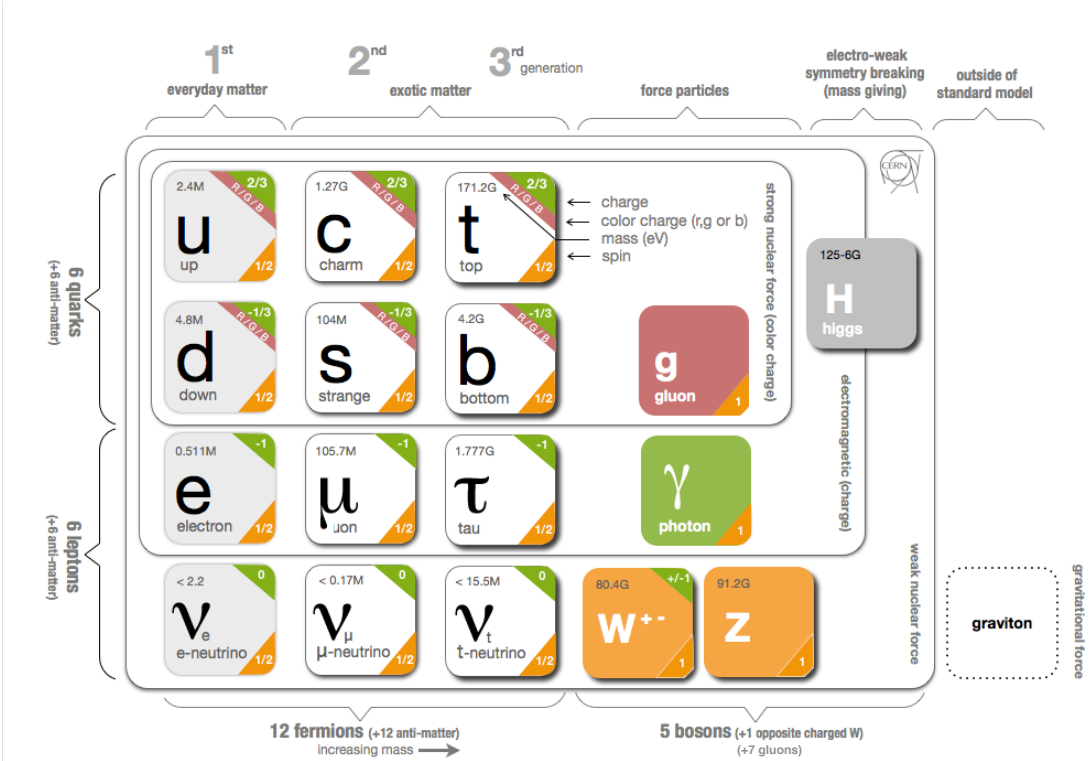

Figure 21: The Standard Model of Particle Physics. There are 12 fermions, 6 of which are quarks and 6 of which are leptons. The 6 quarks interact with all three forces, and have a color charge of r, g, or b in addition to an electric charge of either $+2/3$ or $-1/3$. The 6 leptons do not have color charge and so do not interact with the strong force. Three of the leptons, the neutrinos, do not have electrical charge and so in addition do not interact with the electromagnetic force. The gauge bosons mediate the forces, with the gluon mediating the strong force, the photon mediating the electromagnetic force, and the W and Z bosons mediating the weak force. Since the W bosons have electric charge, they also interact with the photon. The Higgs boson interacts with any particle that has mass. There is not yet a Quantum Field Theory for gravity, so it is not included in the Standard Model. [16].

A diagram displaying the masses and relevant quantum numbers of all the known particles of the SM is shown in Figure 21. The Standard Model makes predictions about the dynamics and kinematics of particle interactions, which can be empirically tested by collider experiments.

The dynamics of the boson and fermion fields are described mathematically with a Lagrangian.

The coupling constants appear in the interaction terms between fields and determine how strongly the fields interact with each other. One can derive the equations of motion of the fields from the Lagrangian using the Euler-Lagrange equation, but other methods of calculating observables are often used instead [17].

The Lagrangian of the Standard Model is consistent with special relativity and so is manifestly invariant under Lorentz transformations. This means that the equations do not change under "boosts" i.e. they do not depend on the frame of reference of the observer. The equations are also gauge invariant, meaning that they do not change under certain "internal symmetries" which are the local Lie group transformations of the $SU(3)_C \otimes SU(2)_L \otimes U(1)_Y$ product group [18]. Another feature of the SM is that the interactions in the Lagrangian are all renormalizable [19].

The strong force and $SU(3)_C$

$SU(3)_C$ is the "internal symmetry" and Lie group that describes the strong force, also known as the theory of Quantum Chromodynamics (QCD). $SU(3)_C$ has a symmetry under color charge permutations C, and has eight generators, which corresponds to eight gauge bosons which are the gluons G^i_μ (where i is 1 through 8) [20]. $SU(3)_C$ is also a Non-Abelian Lie group, which in this context means the gluons can interact with themselves. Since the gluons are also massless, this leads to a phenomenon known as "color confinement" [21], where color-charged particles cannot form free states. The quarks are the only fermions that have a color charge (which are denoted as r, g, and b and their anti-colors) and therefore are never observed by themselves, but always as bound color-neutral triplets of rgb or $\bar{r}\bar{g}\bar{b}$ (known as baryons) or bound color-neutral pairs of $C\bar{C}$ (known as mesons). Another important phenomenon in QCD is known as "asymptotic freedom" [22, 23]. The coupling constant α_s is order 1 at low energy scales, which is non-perturbative, but at high energies such as those at the LHC, due to renormalization effects, α_s becomes weaker, and therefore perturbative.

The electroweak force and $SU(2)_L \otimes U(1)_Y$

$SU(2)_L \otimes U(1)_Y$ is the Lie product group that describes the electroweak force, a unification of the weak and electromagnetic force, described by the Glashow-Weinberg-Salam (GWS) theory [24, 25, 26]. $SU(2)_L$ is the symmetry of isospin (I) for left-handed particles, and has three generators which correspond to the W bosons W^1_μ, W^2_μ, and W^3_μ (which are not the same $W^\pm$ bosons mentioned before). $U(1)_Y$ has a hypercharge (Y) symmetry, which is related to electric charge Q through the

equation $Q = Y/2 + I_3$ (I_3 is the third component of isospin) and has one generator, corresponding to the B boson B_μ. To preserve the gauge symmetry, the gauge bosons cannot have explicit mass terms in the Lagrangian, but we know from experimental observations that the W and Z bosons have a mass. The process known as the Higgs mechanism (see Section 2.2) explains how the electroweak symmetry spontaneously breaks as $SU(2)_L \otimes U(1)_Y \rightarrow U(1)_Q$. The Higgs mechanism causes the four massless electroweak states to mix and form the two charged $W^\pm$ bosons, neutral Z^0, and neutral photon, A_μ. The W and Z bosons also acquire a mass and the photon remains massless and has an unbroken $U(1)$ gauge symmetry for the electric charge, Q, described by Quantum Electrodynamics (QED) [27].

2.2 The Higgs Field and Electroweak Symmetry Breaking

According to the gauge theory described by Yang and Mills [28] that is the basis for the GWS electroweak theory, all of the electroweak bosons are predicted to be massless. This is due to the fact that any mass term in the Lagrangian would have to contain the product of gauge fields $W_\mu W^\mu$ or $B_\mu B^\mu$ explicitly, which would violate the gauge symmetry. However, the W and Z bosons were experimentally observed to have masses. A way to generate masses without having to sacrifice the idea of a gauge symmetry was to add, in an ad hoc way, a complex scalar field with a potential that would "spontaneously break" it instead. This idea was developed in 1964 by Higgs, Brout, Englert, Guralnik, Hagen, and Kibble [6, 7, 29, 8], and now is commonly referred to as just the "Higgs Mechanism."

The complex scalar field that needs to be added to the electroweak theory is an $SU(2)_L$ isospin doublet of the form

$$\phi = \frac{1}{\sqrt{2}} \begin{pmatrix} \phi^+ \\ \phi^0 \end{pmatrix}_L \tag{2.1}$$

called the Higgs field. The Y hypercharge of both components is 1, and the $I_3 = +1/2$ upper component has a charge of $Q = +1$ and the $I_3 = -1/2$ lower has a charge of $Q = 0$. This field is added to the electroweak Lagrangian in the following way

$$\mathcal{L}_\phi = T_\phi - V_\phi = |(\partial_\mu - i\frac{g}{2} W_\mu^a \sigma^a - i\frac{g'}{2} B_\mu Y)\phi|^2 + \mu^2 \phi^\dagger \phi + \lambda(\phi^\dagger \phi)^2 \tag{2.2}$$

Where $T_\phi = |(\partial_\mu - i\frac{g}{2} W_\mu^a \sigma^a - i\frac{g'}{2} B_\mu Y)\phi|^2$ is the kinetic term and the expression of the covariant derivative. g and g' are the coupling constants of the W_μ^a and B_μ fields respectively, σ^a are the Pauli

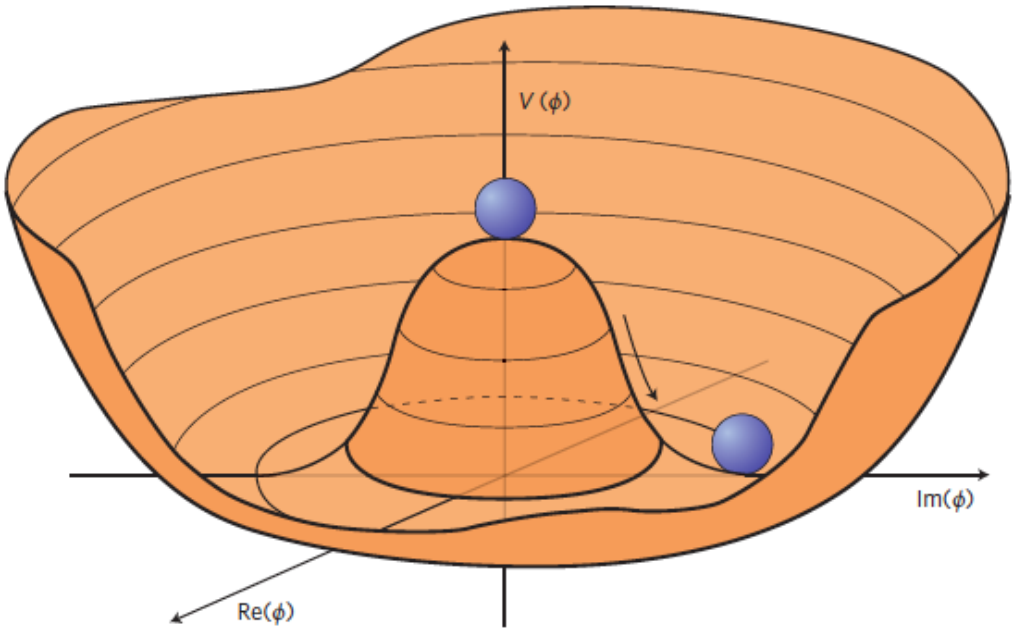

Figure 22: Illustration of the Higgs potential $V(\phi)$ and spontaneous symmetry breaking. When $\mu^2 < 0$, the potential of the Higgs field takes the shape of "Mexican Hat" and the minimum of the field is no longer at 0. The magnitude of the displaced minimum is known as the vacuum expectation value, and is not a point, but a ring of possible ϕ. The ball represents the ground state of the field. When it moves to the new equilibrium, choosing a specific ϕ breaks the $U(1)$ rotational symmetry, but it is done "spontaneously" and with no bias to any one ϕ value [30].

matrices of $SU(2)$, and Y is the hypercharge of $U(1)$ (which is just 1 here). $V_\phi = -\mu^2\phi^\dagger\phi - \lambda(\phi^\dagger\phi)^2$ on the other hand is the Higgs potential, chosen as the simplest and most general potential that can generate symmetry breaking. μ^2 and λ are free parameters, though μ has units of mass, and is the only free parameter of the SM that has units. For illustrative purposes, we can write the potential and its minima (with $\Phi = \phi^\dagger\phi$) as

$$V_\phi = -\mu^2\Phi - \lambda\Phi^2 \qquad \Phi_{\min} = \frac{-\mu^2}{2\lambda} \tag{2.3}$$

λ must be greater than 0 in order to bound the potential from below. Since Φ is a non-negative magnitude, if $\mu^2 > 0$ then the minimum of the potential would be $\Phi = 0$, and $(\phi^+, \phi^0) = (0, 0)$. But if $\mu^2 < 0$, then the Higgs potential obtains a non-zero minimum of $v = \frac{-\mu^2}{2\lambda}$, known as the vacuum expectation value or vev. The vev has a ring of allowed values in (ϕ^+, ϕ^0) such that

$\sqrt{|\phi^+|^2 + |\phi^0|^2} = v$, but as only one set can be chosen (though the choice is arbitrary) the symmetry is "spontaneously broken" when the field moves to the new ground state. This is shown pictorially in Figure 22. As the universe is electrically neutral, it is consistent to choose $\phi^+ = 0$, which leaves $\langle \phi^0 \rangle = v$. After EWSB, we now have

$$\phi = \begin{pmatrix} 0 \\ v + \frac{H}{\sqrt{2}} \end{pmatrix} \qquad \text{and} \qquad \langle \phi \rangle = \begin{pmatrix} 0 \\ v \end{pmatrix} \tag{2.4}$$

Where H is a real scalar field now. Perturbatively expanding around this new ground state, one can plug ϕ back into the kinetic T_ϕ term in Equation 2.2 and see that

$$T_\phi \approx \frac{1}{2}[\partial_\mu H]^2 + \frac{v^2 g^2}{4} W^1_\mu W^{1\mu} + \frac{v^2 g^2}{4} W^2_\mu W^{2\mu} + \frac{v^2}{4}[(g W^3_\mu - g' B_\mu)^2] \tag{2.5}$$

Three gauge boson mass terms, which includes a mixed $W^a_\mu W^{a\mu}$ and $B_\mu B^\mu$ term, have now appeared! The two $W^{1,2}$ terms correspond to the $W^\pm$ boson, while the mixed state of W^3 and B corresponds to the Z boson. The masses are expressed in terms of the coupling constants and the vev, so $M_W = \frac{vg}{2}$ and $M_Z = \frac{v}{2}\sqrt{g^2 + g'^2}$. There is another fourth term that is another mixture of the W^3 and B field, but has no mass. This is the photon. While the overall $SU(2)$ symmetry of the theory has been preserved, the expansion around the vev has broken the symmetry.

The symmetry breaking also implies the existence of a massive excitation of the H field, coming from the new $\mu^2 H^2$ term in the potential. This implies the existence of a scalar boson with mass $M_H = \sqrt{\mu^2} = \sqrt{2\lambda v^2}$, called the Higgs boson. Since we have measured the masses of the W,Z, and Higgs to be $M_W = 80.3\,\text{GeV}$ [31, 32], $M_Z = 91.2\,\text{GeV}$ [33, 34], and $M_H = 125.1\,\text{GeV}$ [35] respectively, we know the vev is around $v = 246\,\text{GeV}$.

The Higgs field also gives fermions their mass through Yukawa couplings [36]. These appear in the Lagrangian as terms of the form

$$\mathcal{L}_{\text{yukawa}} = -\lambda_\psi(\bar{\psi}_L \phi \psi_R + \bar{\psi}_R \phi^\dagger \psi_L) \tag{2.6}$$

Where ψ is a fermion field, either right handed or left handed, and λ_ψ is its Yukawa coupling, a unit-less free parameter in the SM that must be measured experimentally (just like μ^2 and λ). After spontaneous symmetry breaking, this term in the Lagrangian becomes

$$\mathcal{L}_{\text{yukawa}} = -\lambda_\psi(\bar{\psi}_L \left(v + \frac{H}{\sqrt{2}}\right) \psi_R + \bar{\psi}_R \left(v + \frac{H}{\sqrt{2}}\right) \psi_L) \tag{2.7}$$

$$= -\lambda_\psi v \left(\bar{\psi}_L \psi_R + \bar{\psi}_R \psi_L\right) - \lambda_\psi \left(\bar{\psi}_L \frac{H}{\sqrt{2}} \psi_R + \bar{\psi}_R \frac{H}{\sqrt{2}} \psi_L\right) \tag{2.8}$$

The first term corresponds to the mass of the fermion, $m_\psi = \lambda_\psi v$. The second term is the coupling of the Higgs to the fermion. Since the coupling is proportional to the Yukawa coupling, which is proportional to the mass, fermions with larger masses interact more strongly with the Higgs.

2.3 The Higgs Cross Section

At the LHC, we conduct scattering experiments by colliding two beams of known particles (in this case protons) at a known center of mass energy (in this case 13 TeV) every 25 ns. These repeated scattering experiments collect a very large independent and identically distributed sample of physics statistics regarding particle production and kinematics. The parameters governing these statistics can can be calculated from the theoretical cross sections of the particles, where cross section is a property intrinsic to the incoming and outgoing particles and a function of their momenta [37].

The Higgs cross section can be calculated from theory, which makes measuring them a perfect test of the Standard Model. Different experiments with different beam luminosities are able to independently verify the same cross section. With the QCD factorization theorem [38], the hadronic cross section calculation for the production of a Higgs boson at LHC can be split into a perturbatively calculable part and a non-perturbatively calculable part:

$$\sigma(pp \to H) = \int \mathrm{d}x_1 \, \mathrm{d}x_2 \, f_{\text{pdf}}(x_1, \mu_F^2) \, f_{\text{pdf}}(x_2, \mu_F^2) \, \hat{\sigma}(x_1 x_2 s, \mu_R^2, \mu_F^2) \tag{2.9}$$

Where σ is the cross section, s is the center of mass energy of the collision, x_1 and x_2 are the momentum fractions of the colliding quarks or gluons in the first and second proton, f_{pdf} is the "soft" non-perturbative part governed by a parton distribution function (PDF) (see Section 2.3.1), and $\hat{\sigma}$ is the "hard" perturbative part that can be calculated with an expansion in Feynman diagrams thanks to the asymptotic freedom of QCD (see Section 2.3.2).

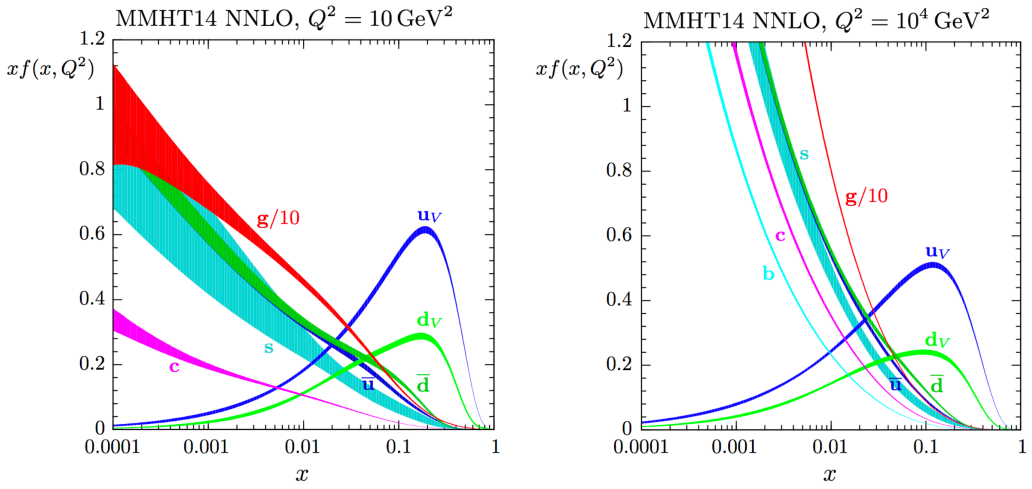

Figure 23: NNLO PDFs 68% confidence intervals for gluons, sea quarks, and valence quarks in the proton as calculated by MMHT at $Q^2 = 10\,\mathrm{GeV}^2$ (left) and $Q^2 = 10^4\,\mathrm{GeV}^2$ (right) [39]. Q^2 is also sometimes written as μ_F^2.

2.3.1 Parton Distribution Functions

Protons are not fundamental particles, and are described as bound states of quarks and gluons (known collectively as partons) interacting through a color charge described by QCD [37]. Since the protons have substructure, the collisions are actually between the partons, which carry fractions of the total momentum of the proton. The density of partons at a certain energy scale μ_F^2 (the momentum transfer between the partons) and momentum fraction x of the total proton momentum is described by what are known as Parton Distribution Functions (PDFs), $f_{\mathrm{pdf}}(x, \mu_F^2)$, for each kind of parton. μ_F^2 is also known as the factorization scale.

The PDFs cannot be calculated with perturbation theory and are determined empirically through deep inelastic scattering experiments at detectors like H1 at HERA [40]. The PDFs are measured at specific μ_F^2 values which can be extrapolated to LHC interaction energies using QCD evolution equations known as DGLAP equations, named after the people that developed the method [41, 42]. The PDF4LHC [43] group has gathered PDF-sets calculated by the CT [44], MMHT [39] and NNPDF [45] collaborations and combined them for theoretical calculations of the Higgs cross section. Figure 23 shows PDFs at $\mu_F^2 = 10\,\mathrm{GeV}^2$ and $\mu_F^2 = 10^4\,\mathrm{GeV}^2$ (called Q^2 in the plots) from MMHT for quarks and gluons of the proton. The gluon and sea quark [4] PDFs are large at low x and rapidly

[4] Sea quarks are due to gluons in the proton splitting into virtual quark-antiquark pairs, which then quickly re-annihilate.

decrease, while the valence u and d quark PDFs peak at around $x \sim 0.3$, about a third of the proton's momentum.

2.3.2 Perturbative QCD

The "hard" part of the cross section equation is the part that can be calculated perturbatively and essentially is a measure of the probability of particles with momentum $\boldsymbol{p}_a$ and $\boldsymbol{p}_b$ scattering to a particle with momentum $\boldsymbol{p}_f$, i.e.

$$\mathrm{d}\hat{\sigma} \propto \left(\frac{\mathrm{d}^3 p_f}{(2\pi)^3} \frac{1}{2E_f} \right) |\mathcal{M}(\boldsymbol{p}_a, \boldsymbol{p}_b \to \boldsymbol{p}_f)|^2 (2\pi)^4 \delta(\boldsymbol{p}_a + \boldsymbol{p}_b - \boldsymbol{p}_f) \tag{2.10}$$

The matrix element $\mathcal{M}$ encodes the interesting physics of the process of going from two partons to a Higgs, and is essentially a sum of Feynman diagrams. The diagrams that begin with partons and end with a Higgs are known as "production modes" of the Higgs. The most important production modes of the Higgs, as well illustrations of their leading-order Feynman diagrams, are explained in the next section, Section 2.3.3.

Higher order loop diagrams in the perturbation series of $|\mathcal{M}|^2$ are proportional to momentum p^n or $\ln p$, which diverge as p goes to infinity. These loop divergences are usually resolved by saying that p is not actually integrated to infinity, but to some upper momentum cut-off Λ. This cut-off is also known as the renormalization scale, $\Lambda = \mu_R^2$. This scale can be used to renormalize QCD by adding counter terms to the Lagrangian that eliminate μ_R^2 and shift the strong coupling constant $\alpha_S(\mu_R^2)$ to lower values (making it a "running" constant). At leading-order (LO) and next-to-leading-order (NLO) in the perturbative expansion, the cross section result significantly depend on μ_R^2, but it becomes less important at higher orders. If one could fully sum the perturbation series, μ_R^2 would drop out completely [37]. As we reduce statistical error in our measurements with more data, the theoretical uncertainties become much more important. The higher order one can calculate in perturbation theory, the less the answer depends on μ_R^2, which reduces the theory uncertainty. The process of taking into account theory uncertainties in the final measurement is described in Section 8.3.

2.3.3 Higgs Production Modes

The cross sections of the Higgs are calculated perturbatively to different orders according to methods outlined in the LHC Higgs Cross Section Working Group Yellow Report 4 (LHCHXSWGYR4) [17]. Figure 24 shows the calculated cross sections for a Standard Model Higgs boson with a mass of

125 GeV in pp collisions as a function of the center of mass energy $\sqrt{s}$. The most important production mode of the Higgs is gluon-gluon fusion (ggF), since 87% of Higgs bosons at the LHC will be produced this way. Next is vector boson fusion (VBF) with the production of 6.9% of all Higgs bosons. These production modes as well as smaller production modes like associated production with a W or Z boson (VH) or with a $b\bar{b}$ or $t\bar{t}$ pair are described below and the calculated cross sections are listed in Table 21.

Each of these production modes provide rich information to study the Higgs with. Since gluons do not have mass there is no tree-level diagram coupling the Higgs directly to gluons, making the triangle loop diagram the lowest order diagram in the ggF production mode (See Figure 25). Despite no tree-level coupling, ggF is the still the most abundant production mode due to the large gluon density in the proton at the typical momentum fraction of the partons. ggF is more sensitive to higher order QCD effects, therefore the cross section has been calculated to next-to-next-to-next-to-leading order (N3LO) in QCD corrections [17], next-to-leading order (NLO) in electroweak corrections [46], and is further improved with a next-to-next-to-next-to-leading logarithmic (N3LL) threshold resummation of soft, virtual and collinear gluon effects [47, 48].

VBF and VH probe the Higgs's coupling to vector bosons (See Figure 25 and 26), and the $t\bar{t}H$ and $b\bar{b}H$ production modes probe the Higgs's coupling to quarks at the tree level (See Figure 27). Calculations of the VBF and VH cross section have QCD corrections up to NNLO, and electroweak corrections up to NLO, while $t\bar{t}H$ and $b\bar{b}H$ have QCD+EW corrections up to NLO [17]. All of these final states are also produced in association with other jets or leptons, which have distinct kinematic properties that can be observed in data to distinguish between the production modes.

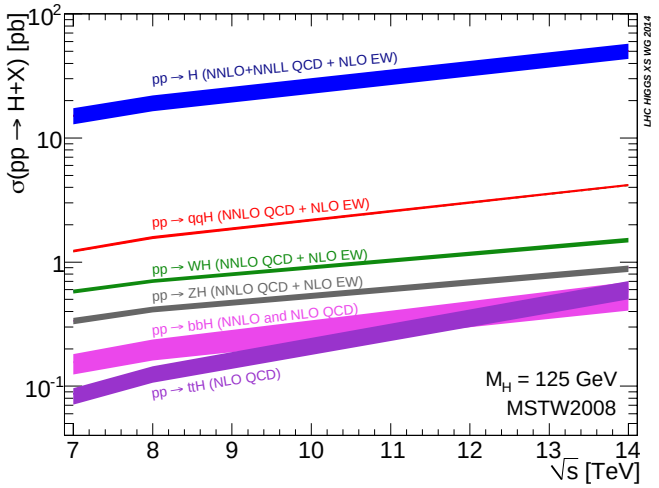

Figure 24: Calculated cross sections for a Standard Model Higgs boson with a mass of 125 GeV in pp collisions as a function of the center of mass energy $\sqrt{s}$. The uncertainty bands are from QCD scale and PDF uncertainties. The data during 2015 and 2016 was collected at an energy of $\sqrt{s} = 13$ TeV [17].

Table 21: Standard Model Higgs boson production cross sections for gluon fusion, vector-boson fusion and associated production with a W or Z boson or with a $b\bar{b}$ or $t\bar{t}$ pair in pp collisions at $\sqrt{s} = 13$ TeV. The first and second quoted uncertainties correspond to the theoretical systematic uncertainties calculated by adding in quadrature the perturbative QCD scale and PDF uncertainties, respectively. The branching ratio for $H \to 4\ell$ with $\ell = e, \mu$, is shown in the last column [17].

m_H [GeV]	$\sigma(gg \to H)$ [pb]	$\sigma(qq' \to Hqq')$ [pb]	$\sigma(q\bar{q}' \to WH)$ [pb]	$\sigma(q\bar{q} \to ZH)$ [pb]
124.5	$48.92\ ^{+4.6\%}_{-6.7\%}\ ^{+3.2\%}_{-3.2\%}$	$3.798\ ^{+0.4\%}_{-0.3\%}\ ^{+2.1\%}_{-2.1\%}$	$1.390\ ^{+0.6\%}_{-0.6\%}\ ^{+1.9\%}_{-1.9\%}$	$0.8943\ ^{+3.8\%}_{-3.0\%}\ ^{+1.6\%}_{-1.6\%}$
125.0	$48.58\ ^{+4.6\%}_{-6.7\%}\ ^{+3.2\%}_{-3.2\%}$	$3.782\ ^{+0.4\%}_{-0.3\%}\ ^{+2.1\%}_{-2.1\%}$	$1.373\ ^{+0.5\%}_{-0.7\%}\ ^{+1.9\%}_{-1.9\%}$	$0.8839\ ^{+3.8\%}_{-3.1\%}\ ^{+1.6\%}_{-1.6\%}$
125.09	$48.52\ ^{+4.6\%}_{-6.7\%}\ ^{+3.2\%}_{-3.2\%}$	$3.779\ ^{+0.4\%}_{-0.3\%}\ ^{+2.1\%}_{-2.1\%}$	$1.369\ ^{+0.5\%}_{-0.7\%}\ ^{+1.9\%}_{-1.9\%}$	$0.8824\ ^{+3.8\%}_{-3.0\%}\ ^{+1.6\%}_{-1.6\%}$
125.5	$48.23\ ^{+4.6\%}_{-6.7\%}\ ^{+3.2\%}_{-3.2\%}$	$3.767\ ^{+0.4\%}_{-0.3\%}\ ^{+2.1\%}_{-2.1\%}$	$1.355\ ^{+0.5\%}_{-0.7\%}\ ^{+1.9\%}_{-1.9\%}$	$0.8744\ ^{+3.7\%}_{-3.1\%}\ ^{+1.6\%}_{-1.6\%}$

m_H [GeV]	$\sigma(gg \to ZH)$ [pb]	$\sigma(q\bar{q}/gg \to t\bar{t}H)$ [pb]	$\sigma(q\bar{q}/gg \to b\bar{b}H)$ [pb]	BR$(H \to 4\ell)$ [10^{-3}]
124.5	$0.1235\ ^{+25.1\%}_{-18.9\%}\ ^{+2.4\%}_{-2.4\%}$	$0.5132\ ^{+5.8\%}_{-9.2\%}\ ^{+3.6\%}_{-3.6\%}$	$0.4930\ ^{+20.0\%}_{-23.9\%}$	$0.1185\ \pm 2.21\%$
125.0	$0.1227\ ^{+25.1\%}_{-18.9\%}\ ^{+2.4\%}_{-2.4\%}$	$0.5071\ ^{+5.8\%}_{-9.2\%}\ ^{+3.6\%}_{-3.6\%}$	$0.4880\ ^{+20.2\%}_{-23.9\%}$	$0.1240\ \pm 2.18\%$
125.09	$0.1227\ ^{+25.1\%}_{-18.9\%}\ ^{+2.4\%}_{-2.4\%}$	$0.5065\ ^{+5.7\%}_{-9.3\%}\ ^{+3.6\%}_{-3.6\%}$	$0.4863\ ^{+20.1\%}_{-23.9\%}$	$0.1251\ \pm 2.16\%$
125.5	$0.1221\ ^{+25.1\%}_{-18.9\%}\ ^{+2.4\%}_{-2.4\%}$	$0.5023\ ^{+5.7\%}_{-9.3\%}\ ^{+3.6\%}_{-3.6\%}$	$0.4809\ ^{+20.1\%}_{-23.8\%}$	$0.1297\ \pm 2.14\%$

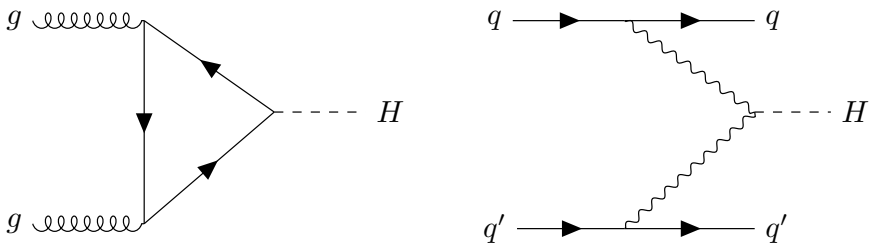

Figure 25: Lowest order Feynman diagrams for gluon-gluon fusion ($gg \to H$) (left) and vector boson fusion ($qq' \to Hqq'$) (right). These production modes are the two most likely ways to produce a 125 GeV Higgs boson at $\sqrt{s} = 13$ TeV, with 87% produced by ggF and 6.9% produced by VBF.

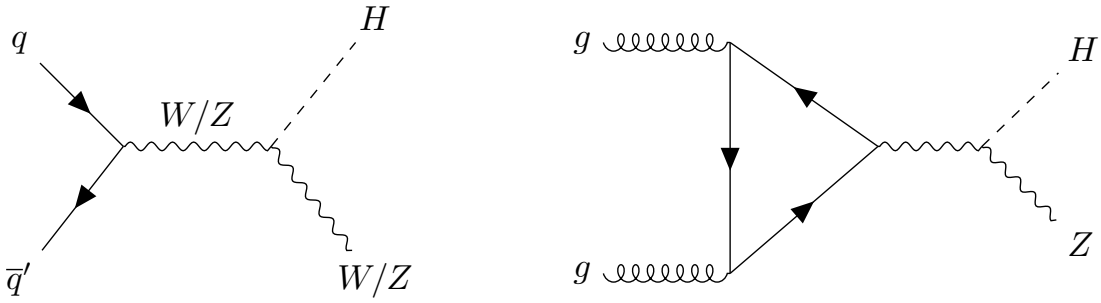

Figure 26: Feynman diagrams of the Higgs production modes where the Higgs couples to vector bosons. Diagrams show the $q\bar{q}' \to WH$ (left) production mode, $q\bar{q} \to ZH$ (middle, quark initialized) and $gg \to ZH$ (right, gluon initialized). All together, these production modes are how 125 GeV Higgs bosons at $\sqrt{s} = 13$ TeV are produced 4.3% of the time.

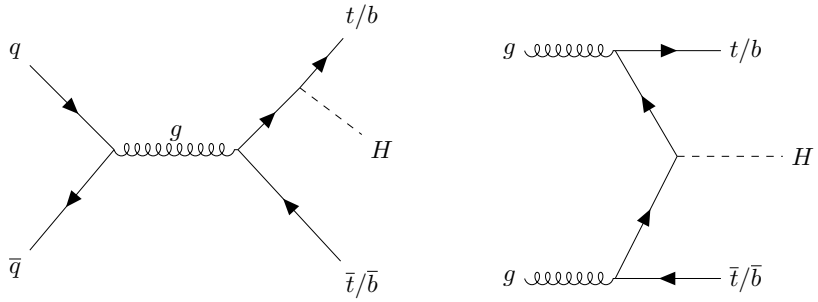

Figure 27: Feynman diagrams of the Higgs production modes where the Higgs couples directly to fermions. Since Higgs coupling strength is proportion to fermion mass, t and b are the most important diagrams, but they happen for all other quarks too. Diagrams show $q\bar{q} \to t\bar{t}H/b\bar{b}H$ (left) and $gg \to t\bar{t}H/b\bar{b}H$ (right). All together, these production modes are how 125 GeV Higgs bosons at $\sqrt{s} = 13$ TeV are produced 1.8% of the time.

2.3.4 Higgs Decay Channels

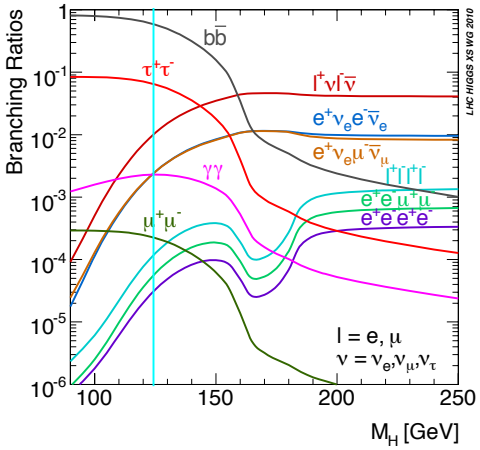

Decay Channel	Branching Fraction [%]	
$b\bar{b}$	57.7	+3.2% -3.3%
$\tau\bar{\tau}$	6.32	+5.7% -5.7%
$WW^* \to \ell^+\nu\ell^-\bar{\nu}$	1.06	+4.3% -4.3%
$WW^* \to e^+\nu_e e^-\bar{\nu}_e$	0.252	+4.3% -4.3%
$WW^* \to e^+\nu_e \mu^-\bar{\nu}_\mu$	0.252	+4.3% -4.3%
$\gamma\gamma$	0.228	+5.0% -4.9%
$\mu^+\mu^-$	0.0219	+6.0% -5.9%
$ZZ^* \to \ell^+\ell^-\ell^+\ell^-$	0.0125	+4.3% -4.3%
$ZZ^* \to e^+e^-\mu^+\mu^-$	0.00593	+4.3% -4.3%
$ZZ^* \to e^+e^-e^+e^-$	0.00327	+4.3% -4.3%

Figure 28: Calculated branching fractions for some decay channels of the Higgs boson as a function of Higgs mass. A cyan line is drawn at a Higgs mass of 125 GeV [17].

The Higgs boson is not a stable particle and will quickly decay with a predicted mean lifetime of 1.56×10^{-22} s, given by $\hbar/\Gamma$, where Γ is the predicted total width of 4.07 MeV [17]. Limits from ATLAS have excluded widths above 14.4 MeV at the 95% confidence level [10]. The decay of the Higgs to a specific final state is determined by the coupling of the Higgs to those particles. The Higgs coupling to fermions is linear in the fermion mass, while the coupling to vector bosons is proportional to the square of the boson mass. If the Higgs were greater than double the mass of the W or Z boson, then the Higgs would predominantly decay to the vector bosons, but since the Higgs is around 125 GeV, one of the W or Z must necessarily be off-shell, making the decay to two Ws or two Zs much less likely.

As it stands, the heaviest particle the Higgs can decay to on-shell is two b-quarks, making $H \to b\bar{b}$ 58% of all Higgs decays. Figure 28 shows the branching fractions for some decay channels of the Higgs boson as a function of Higgs mass. While $H \to b\bar{b}$ is the most abundant decay, it also suffers from some of the worst backgrounds, given that the LHC is a hadron collider and there is huge amount of QCD noise in every event as the proton is broken up. Final states with charged leptons and photons do a good job of cutting through the QCD background, and so the channels where the Higgs decays to electroweak bosons, despite having a small branching fraction, are some of the most sensitive channels for measuring the Higgs. When the Higgs was discovered in 2012, it was the $H \to ZZ^* \to 4\ell$ and $H \to \gamma\gamma$ decays that drove the result [4]. It is also why this thesis focuses on

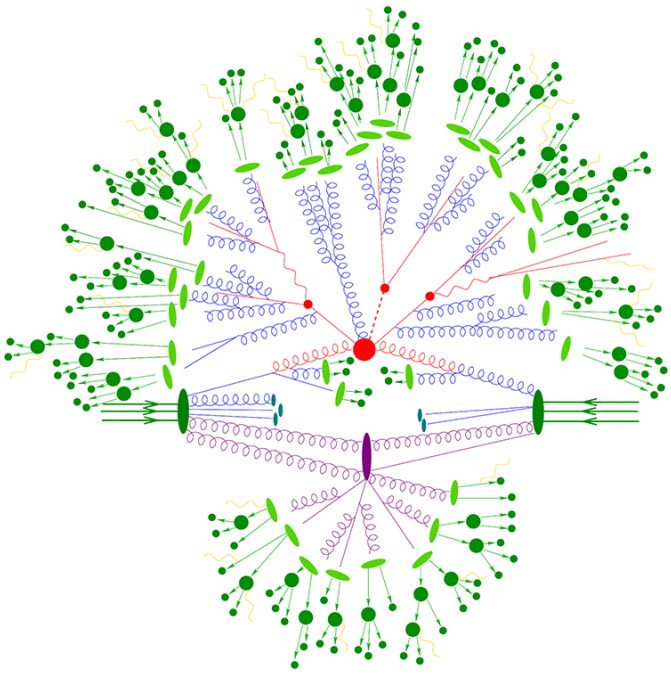

Figure 29: Illustration of a $t\bar{t}H$ simulation [49]. The big red circle is the hard scatter while the three smaller red circles are the two top quarks and the Higgs. Hard QCD radiation before hadronization is in red, the parton shower is in blue, while hadronization is the light-green. The decay of the hadrons is the dark green. A secondary interaction is shown in purple, and the yellow QED processes can happen at any stage.

Higgs decays to Z bosons and photons.

2.4 Monte Carlo Simulations

The Monte Carlo method is a way of simulating experimental data. A random number generator is used to create a sample from a given probability distribution, which in our case is the scattering angle from two protons forming a Higgs boson. With the scattering angle, the event generator calculates a matrix element that could have led to that scattering, and generates the four-vector of the outgoing Higgs boson (and any other four-vector of associated particles also produced in the hard scatter). We then use these four-vectors and associated weights to populate the differential distribution for any observable of our choice. Each Higgs production mode is simulated with its own event generator, and the backgrounds have their own generators as well. The four-vector produced by the event generators can be input into other Monte Carlo simulators to model the decay of the Higgs to four

leptons (or any other decay channel) as well as perform the showering and hadronization steps. An illustration of this process in shown in Figure 29.

Next, these simulated particles are passed through a detector simulation program of ATLAS made with GEANT4 [50]. This program simulates interactions of the particles with the detector material to mimic things like multiple Coulomb scattering as well as the detector response in general. The process of turning the simulated particles into simulated detector hits is called digitization. The addition of pile-up[5] is done at this step by overlaying simulated minimum bias events over the event. Finally, the event reconstruction algorithms are run on the detector hits, in the exact same way as data.

2.4.1 Signal Event Generators

The Powheg-Box v2 MC event generator [51, 52, 53] is used to simulate ggF [54], VBF [55] and WH/ZH [56] production modes, using the PDF4LHC_NLO PDF set [43].

- While the ggF inclusive cross section calculation is accurate to N3LO, The ggF Higgs boson production mode sample from Powheg is accurate to NNLO in QCD. It uses the MiNLO method [57] to merge the NLO Higgs plus jets cross section to the parton shower, and then reweights the distribution using the HNNLO program [58, 59] to achieve full NNLO accuracy. This sample is referred to as NNLOPS and is the baseline ggF sample. Since ggF is an important process with 87% of the Higgs production, other theory prediction samples have been produced. One alternative sample is generated using MadGraph5_aMC@NLO[60] at NLO in QCD for Higgs plus zero, one and two jets, merged using the FxFx scheme [61]. The third sample is generated using HRes v2.3 [62, 63] with the MSTW2008 NNLO PDF set [64]. This sample is accurate to NNLO in QCD, and takes into account top and bottom quark-mass dependence up to NLL+NLO in QCD. At NNLL+NNLO only the top quark contribution is considered.

- The VBF, WH, and ZH samples are produced at NLO accuracy in QCD. For WH and ZH, the MiNLO method is used to merge Higgs plus zero and one-jet events [65].

- The $t\bar{t}H$ and $b\bar{b}H$ samples are simulated at NLO accuracy in QCD with MadGraph5_aMC@NLO (v.2.2.3 for $t\bar{t}H$ and v.2.3.3 for $b\bar{b}H$) [60], using the CT10nlo PDF set [66] for $t\bar{t}H$ and the NNPDF23 PDF set [67] for $b\bar{b}H$.

[5] Explained in Section 3.2.

For the ggF, VBF, WH/ZH, and $t\bar{t}H$ production modes, Pythia 8 [68] is used for the $H \to ZZ^* \to 4\ell$ decay as well as for parton showering, hadronization, and multiple partonic interactions using the AZNLO parameter set [69]. For the $t\bar{t}H$ production mode, Herwig++ [70] is used with the UEEE5 parameter set [71]. The partial width for the Higgs decay into four leptons has been calculated using PROPHECY4F [72, 73] which takes into account NLO QCD and EW corrections. PROPHECY4F also includes interference effects among the diagrams containing identical final-state leptons ($4e$ and 4μ).

2.4.2 Background Event Generators

- The $q\bar{q}ZZ^*$ background is simulated with Sherpa 2.2.2 [49], using the NNPDF3.0 NNLO PDF set. It is accurate to NLO in QCD for zero and one jet final states, and accurate to LO for two and three jet final states. It uses the MePs@NLO method [74] to do the merging to the Sherpa parton shower [75]. NLO EW corrections are applied as a function of the invariant mass m_{ZZ^*} [76, 77].

- The $ggZZ^*$ process is modeled at high m_{ZZ^*} by Sherpa 2.1, which includes the Higgs-ZZ^* interference. At low m_{ZZ^*}, gg2VV [78] is used instead. Higher-order QCD effects for the $ggZZ^*$ process have been calculated for massless quark loops [79, 80] in the heavy top-quark approximation [81].

- The Z+jets background is simulated using Sherpa at NLO in QCD for zero, one and two jets and at LO for three and four jets. It uses Comix [82] and OpenLoop [83] for matrix elements, and is merged to the parton shower using the Sherpa MePs@NLO method [74]. Alternative samples of the Z+jets background are made with Powheg-Box v2 and MadGraph [84]. Both of them are interfaced to Pythia 8 for parton shower and hadronization. The POWHEG samples also use Photos++ [85] for the QED emissions from electroweak vertices and charged leptons.

- The $t\bar{t}$ background is modeled using Powheg-Box v2 interfaced to Pythia 6 [86] for parton shower and hadronization, to Photos [87] for quantum electrodynamics (QED) radiative corrections, and to Tauola [88, 89] for the simulation of τ lepton decays.

- The WZ background is modeled using Powheg-Box v2 interfaced to Pythia 8 for parton shower and hadronization. The tribosons backgrounds ZZZ, WZZ, WWZ, and all leptonic $t\bar{t} + Z$ with four or more actual leptons are modeled using Sherpa.

Chapter 3

LHC and the ATLAS Detector

3.1 The Large Hadron Collider

The Large Hadron Collider (LHC) [90] is a particle accelerator located in Geneva, Switzerland at the European Organization for Nuclear Physics (CERN). The accelerator is a circular ring 27 km in circumference and 100 m underground. Using superconducting magnets cooled with liquid helium to a temperature of 1.9 K, it accelerates bunches of protons to energies of 6.5 TeV in order to collide them at a center of mass energy of 13 TeV. This collision energy is characteristic of a time very close to the Big Bang when the electromagnetic and weak force had not yet separated, and is optimal for studying properties of the Higgs boson. Physicists hope collisions at this energy scale will also lead to insights about open questions in fundamental physics, from the nature of dark matter to the reason for the matter-antimatter asymmetry we see in the universe.

The protons used in these collisions originate from a small tank of hydrogen gas in the CERN accelerator complex. The gas is ionized and the separated protons are sent down a linear accelerator (LINAC2) and accelerated to a momentum of 50 MeV. Next, the protons are sent to a circular accelerator, the Proton Synchrotron Booster (PSB), to increase to an energy of 1.4 GeV. Next they enter the Proton Synchrotron (PS) and then the Super Proton Synchrotron (SPS) which accelerate the protons to 25 and 450 GeV respectively. Finally the protons are injected into two separate, oppositely circulating beams in the LHC, each with energies of 6.5 TeV. Figure 31 shows a schematic of the CERN accelerator complex and the various acceleration stages the proton must traverse.

The protons are made to collide at four interaction points around the LHC ring where four experiments are located: ATLAS [92], CMS [93], ALICE [94], and LHCb [95]. ALICE is designed to observe heavy ion collisions and study the physics of quark-gluon plasma. LHCb is designed to

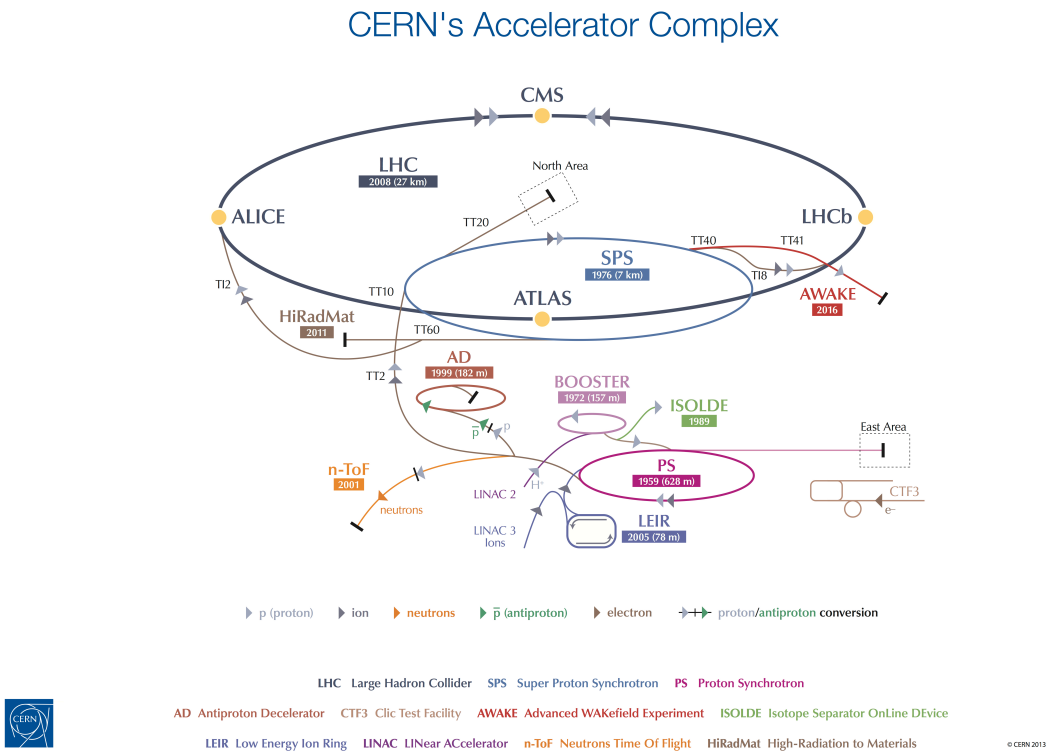

Figure 31: A schematic of the CERN accelerator complex. [91]

observe the decay of b-hadron and study the physics of matter-antimatter asymmetry. ATLAS and CMS are general purpose particle detector experiments built for studying the Standard Model as well as physics Beyond the Standard Model.

3.2 Luminosity

The rate of collisions at the LHC is measured by a quantity known as the luminosity. For two head-on colliding beams of particles with k bunches of protons per revolution, the formula for the instantaneous luminosity $\mathcal{L}$ is

$$\mathcal{L} = \frac{fkN_1N_2}{4\pi a_h a_v} \tag{3.1}$$

where f is the frequency of the collisions, N_1 and N_2 are the number of particles in each of

the bunches of the beam, and a_h and a_v are the RMS of the horizontal and vertical dimensions of the beam [96, 97]. Under nominal operating conditions, $f = 40\,\text{MHz}$, $k = 2808$ bunches, and $N = 10^{11}$ protons per bunch. The LHC was designed to achieve an instantaneous luminosity of $\sim 1 \times 10^{34}\,\text{cm}^{-2}\,\text{s}^{-1}$ or $0.01\,\text{pb}^{-1}\,\text{s}^{-1}$. The instantaneous luminosity is not constant over a fill of protons, but follows an exponential decay curve. This decay of beam intensity with time is caused by the growth of the transverse emittance, increase of the bunch length, and other factors.

The amount of data available for analysis is determined by the integrated luminosity, which is simply the integral of the instantaneous luminosity over time, $\mathcal{L}_{\text{int}} = \int \mathcal{L}\ \text{d}t$. Over the course of 2015 and 2016, a total of $\mathcal{L}_{\text{int}} = 36.1\,\text{fb}^{-1}$ was collected by ATLAS for physics analysis.

3.2.1 Pile-up

Over time, the LHC has increased its instantaneous luminosity in order to deliver more data at a faster rate to the experiments. This comes at the cost of increased pile-up, μ,

$$\mu = \frac{\mathcal{L}\sigma_{\text{inel.}}}{kf} \tag{3.2}$$

Where $\sigma_{\text{inel.}}$ is the cross section for inelastic collisions, and the rest of the variables have the same definition as in Equation 3.1. μ is the average number of inelastic events per bunch crossing, i.e. the number of pp collisions per bunch crossing.

There are two kinds of pile-up, in-time pile-up, which is more than one interaction in the same bunch crossing, and out-of-time pile-up, which is the signals from previous collisions still present in the current bunch crossing. During 2015 and 2016, μ has ranged from 10 to 45 as shown in Figure 32. A large μ can negatively affect the energy resolution of measured particles, or can cause track mis-reconstruction due to extra noise. Techniques in particle reconstruction and triggering (described in Chapter 4) aim to mitigate these issues with pile-up in order to reap the benefits of a higher instantaneous luminosity with minimal draw backs.

3.3 The ATLAS Detector

ATLAS [92] is a general-purpose particle detector built to discover the Higgs Boson and other physics beyond the Standard Model. It has a forward-backward symmetric cylindrical geometry and has a nearly 4π coverage in solid angle. Figure 33 shows a detailed picture of ATLAS. It is 25 m in diameter and has a length of 44 m. ATLAS can roughly be segmented into four distinct parts, each specializing in measuring different properties of the particles from the collisions.

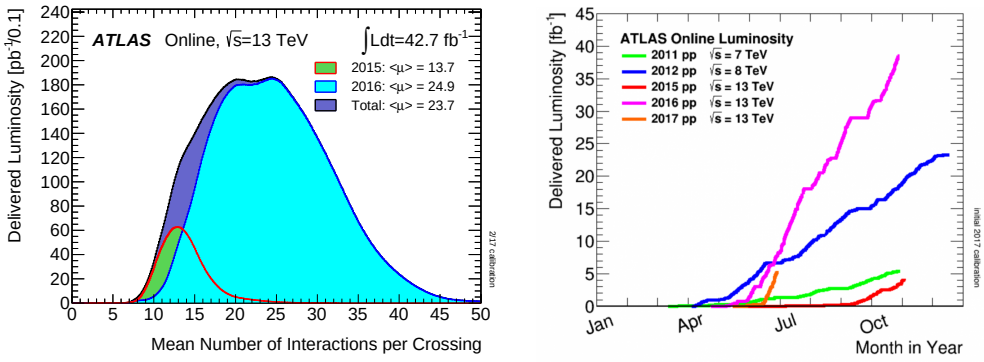

Figure 32: Luminosity-weighted distribution of the mean number of interactions per bunch crossing for 2015 and 2016 (left) and integrated luminosity recorded by ATLAS during stable beams over Run 1 and Run 2 (right).

The innermost part of ATLAS is the Inner Detector (Section 3.4) and is used to reconstruct charged particle tracks as well as to identify electrons. The Solenoid and Toroid Magnets surrounding the Inner Detector bend the charged particle tracks, giving information about particle momentum and charge. The Electromagnetic and Hadronic Calorimeters (Section 3.5) are the middle layer of ATLAS and measure the energy deposits and shower shapes of the particles. The outermost layer of ATLAS is the Muon Spectrometer/System (Section 3.6) which provides more tracking information for muons specifically, since they are not stopped by the calorimeters. Figure 34 show how different species of particles interact with ATLAS and roughly illustrates how they are identified.

3.3.1 ATLAS Coordinate System

ATLAS uses a right-handed coordinate system, where the z-axis is the beam axis and the positive direction is counterclockwise along the LHC ring, the positive x-axis points towards the center of the LHC ring, and the positive y-axis points vertically up towards the surface. Since ATLAS is cylindrical, it is easier to describe using modified cylindrical coordinates. The z-axis is the same, the azimuthal angle ϕ is the angle around the beam axis where $\phi = 0$ is along the x-axis towards the ring center and $\phi = \pi/2$ is along the y-axis pointing upwards, and the polar angle θ from the beam axis has $\theta = 0$ along the beam axis and $\theta = \pi/2$ along the y-axis pointing upwards.

A particle moving through ATLAS is naturally described with its momentum 4-vector, expressed in the basis of $[E, p_{\mathrm{T}}, \eta, \phi]$. The three spatial coordinates are a bit different from the modified cylindrical coordinates. ϕ is the same as in cylindrical coordinates, but the other coordinates of the momentum vector are defined in the following way

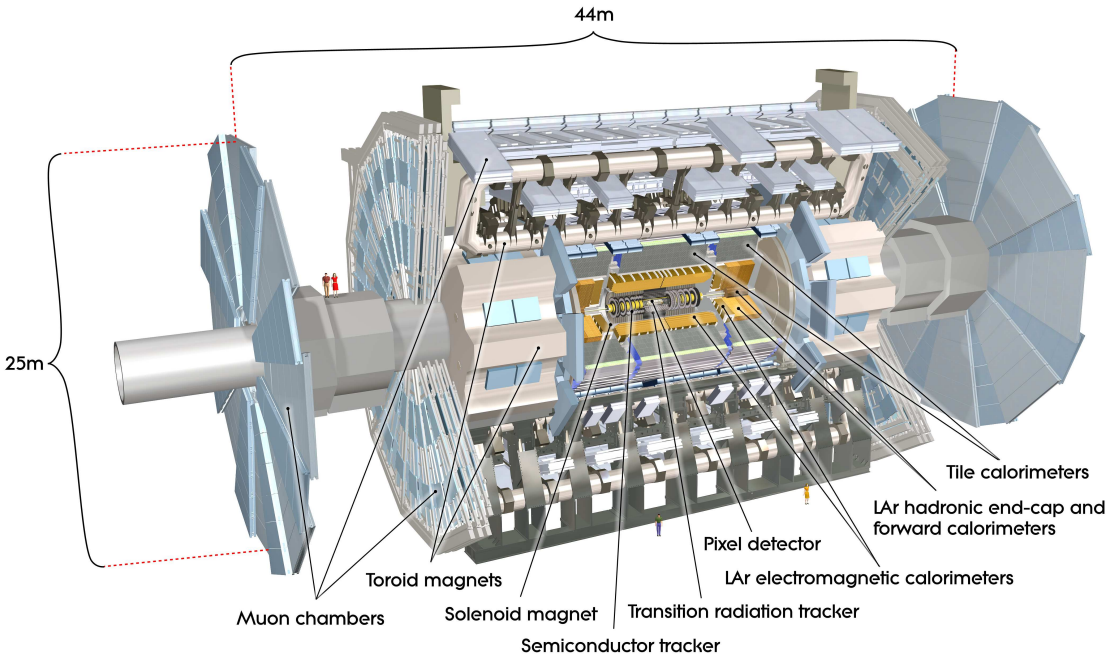

Figure 33: General cut-away view of the ATLAS detector [92].

Transverse momentum, p_{T}

The transverse momentum p_{T} is the projection of the momentum $\vec{p}$ vector in the xy plane:

$$p_{\mathrm{T}} = |\vec{p}| \cdot \sin\theta \tag{3.3}$$

Rapidity and Pseudorapidity, y and η

The rapidity y or pseudorapidity η is the substitute for the polar angle θ and is defined as

$$y = \frac{1}{2} \ln \frac{E + p_z}{E - p_z} \qquad \eta = -\ln \tan \frac{\theta}{2} \tag{3.4}$$

For particles that are massless or that have very high momentum relative to their mass, y and η are interchangeable. A particle close to $\theta = 0$ will have a very large η that approaches infinity, while at $\theta = \pi/2$, $\eta = 0$. The difference in η between particles is invariant under Lorentz boosts along the z-axis, which is why it is used over θ.

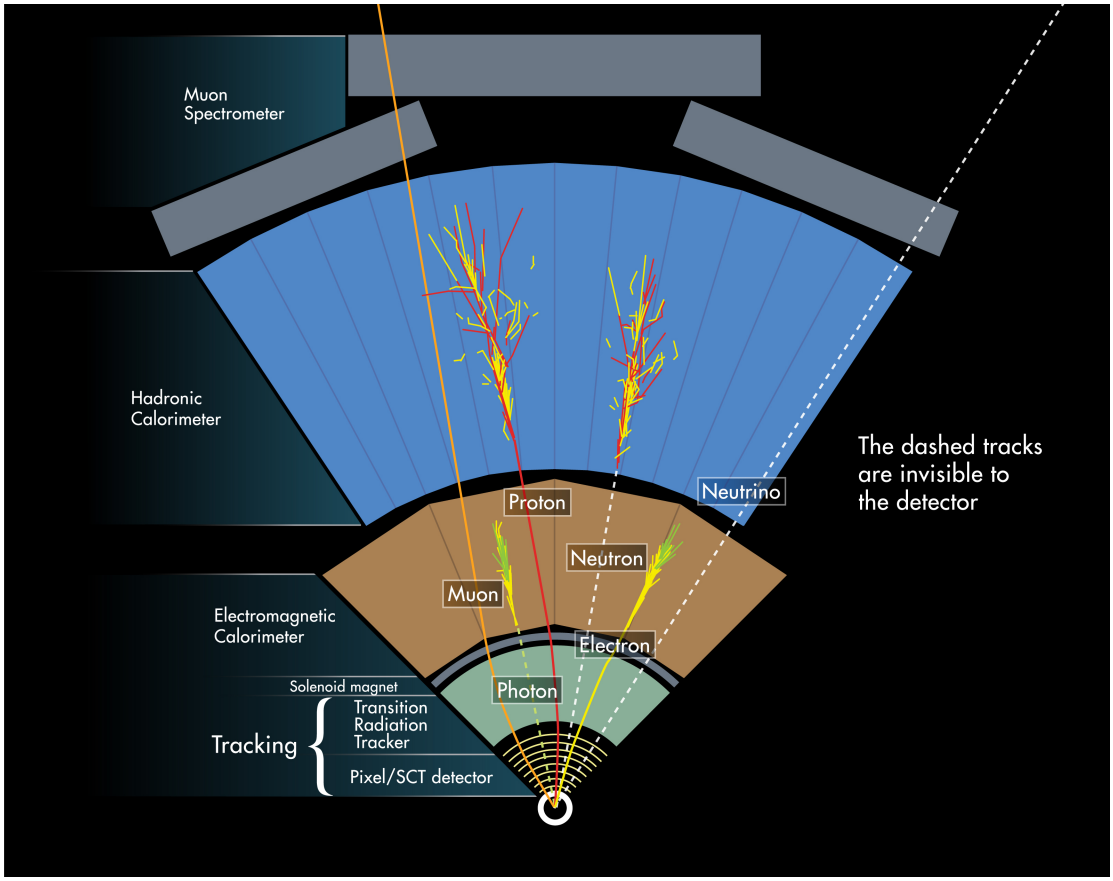

Figure 34: Picture representing how ATLAS detects different kinds of particles [98].

Distances ΔR, d_0, and z_0

Other quantities used to define particle distances within ATLAS are

- ΔR, the angular distance between two particles. It is defined as $\sqrt{\Delta\eta^2 + \Delta\phi^2}$, where $\Delta\eta = \eta_2 - \eta_1$ and $\Delta\phi = \phi_2 - \phi_1$.
- d_0, the impact parameter. It is defined as the distance between the beam axis and the point of closest approach of a particle, i.e. $\sqrt{x^2 + y^2}$ from the z-axis to the point of closest approach. It can be used to calculate the transverse distance from the closest approach a particle track to an interaction point or vertex.
- z_0, the longitudinal impact parameter. It is defined as the the z-coordinate of the point of closest approach, i.e. the distance between the origin and the projection of the point of closest

approach onto the z-axis. It can be used to calculate the distance in z from the closest approach of a particle track to an interaction point or vertex.

3.4 The Inner Detector

The Inner Detector (ID) [99] measures the paths of charged particles in ATLAS and covers scattering angles up to $|\eta| = 2.5$. Particle tracks that pass through the Inner Detector bend under the influence of a 2 T solenoid magnet, which provides information about the particle's charge, momentum, and decay vertices. A vertex is a point in the inner detector where particle tracks originate, either from the pp interaction or a subsequent particle decay (such as B-hadrons, which have a long lifetime and will move to a secondary vertex before they decay). The primary vertex is the location of the pp collision where all of the tracks from the hard scatter originate. Due to pile-up, there can be multiple vertices in an event, but the primary vertex is identified as the one with the largest scalar sum of the transverse momentum of at least two associated tracks, $\sum p_{\mathrm{T}}^2$ [100]. Figure 35 shows a picture of the shape and dimension of the Inner Detector and labels all of its subdetectors.

3.4.1 Pixel Detector

The Pixel detector [102] is the innermost component of the ID and consists of four cylindrical barrel layers and three disk-shaped endcap layers. It is made up of silicon semiconductor material, and each pixel sensor is a $50\,\mu\mathrm{m} \times 400\,\mu\mathrm{m}$ rectangle. There are 1744 total pixel sensors with a total of 80 million readout channels. Each pixel sensor has a spatial resolution of $10\,\mu\mathrm{m}$ in the xy plane, and $115\,\mu\mathrm{m}$ in the z direction of the barrel.

The innermost Pixel layer is called the Insertable B-Layer (IBL) [103] and was added in 2014 between the end of Run 1 and the beginning of Run 2 for better vertex and d_0 resolution in the face of increased pile-up. The IBL provides additional 8 million readout channels close to the beam line, with each sensor providing a spatial resolution of $8\,\mu\mathrm{m}$ in the xy plane and $40\,\mu\mathrm{m}$ in the z direction.

3.4.2 Semiconductor Tracker

The Semiconductor Tracker (SCT) [104] is the middle component of the Inner Detector, and uses the same basic technology as the Pixels, but its sensors are organized into strips rather than pixels. It consists of four cylindrical barrel layers and nine disk shaped endcap layers. A hit along a strip has a resolution of $17\,\mu\mathrm{m}$ in the xy plane and $580\,\mu\mathrm{m}$ in the z direction, with a total of 6.3 million readout channels.

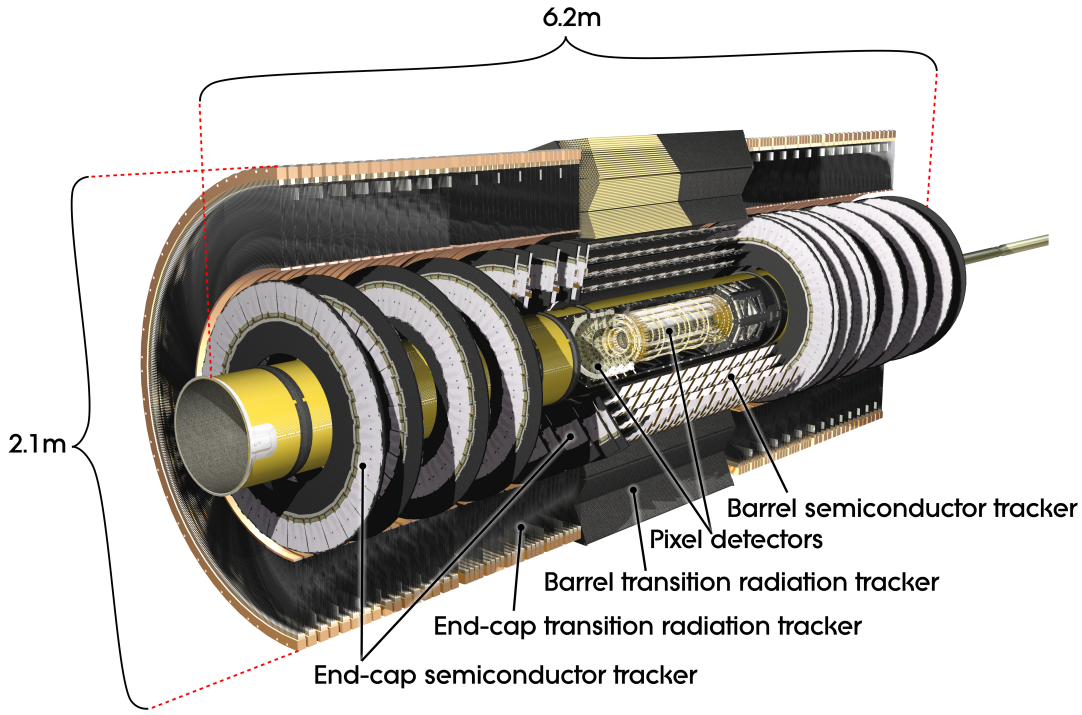

Figure 35: Cut away view of the ATLAS Inner Detector showing the Pixel, SCT, and TRT subdetectors [101].

3.4.3 Transition Radiation Tracker

The Transition Radiation Tracker (TRT) [105, 106] is the outermost component of the ID used to reconstruct charged particle tracks and identify electrons. The TRT at the most granular level is made up of 352,256 gas-filled straws. There are 106,496 straws in the barrel and 245,760 straws in the endcap, each with a diameter of about 4 mm. When a sufficiently energetic charged particle travels through the Xenon or Argon gas in the straw, the gas atoms are ionized. A wire down the middle of the straw acts as an anode while the straw walls act as a cathode, and a high voltage difference of around 1.4 to 2 kV is set between them. The ionized electrons will be attracted to the central wire while the heavier ions will drift towards the straw wall.

The TRT also has polypropylene-polyethylene fiber mats about 3 mm thick between every straw.

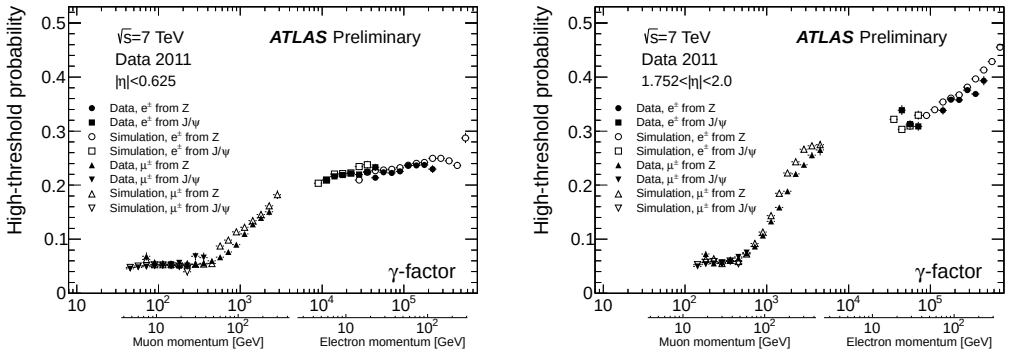

Figure 36: The probability to exceed the high threshold for electrons and muons from J/ψ and Z decays as a function of the Lorentz factor for the TRT barrel (left) and TRT endcap (right) [108].

A charged particle moving through this material will have a probability of emitting transition radiation photons. Transition radiation is caused by a charged particle moving between media with different indices of refraction. Particles with a higher Lorentz factor (γ) have a higher probability of emitting transition radiation when they pass through the material than those with lower γ. These transition radiation photons will also pass through the straws and ionize the noble gases alongside the charged particle, creating a much larger pulse in the straw. Since high energy electrons have a higher Lorentz factors than muons or charged pions on average, the presence of transition radiation can be used for electron identification.

The resulting current in the straw from the ionized gas can be detected by an analog ASIC chip called the Amplification, Shaping, and Baseline Restoration (ASBDBLR) Chip at the end of the straw [107]. Besides amplifying and shaping the current pulse, ASDBLRs apply two thresholds to the resulting pulse, one for tracking and one for the detection of transition radiation. The signal is digitized when passed to the Drift Time Measurement/Read Out Chip (DTMROC) [107]. When a central trigger decides to save an event, the digitized threshold hits associated with the event are sent to the TRT back-end. Saved events are processed offline and the hits are reconstructed as charged particle tracks that may have passed a high threshold for electrons. The TRT provides 35 hits per track on average. Figure 36 shows the high threshold probability for electrons and muons at different energies.

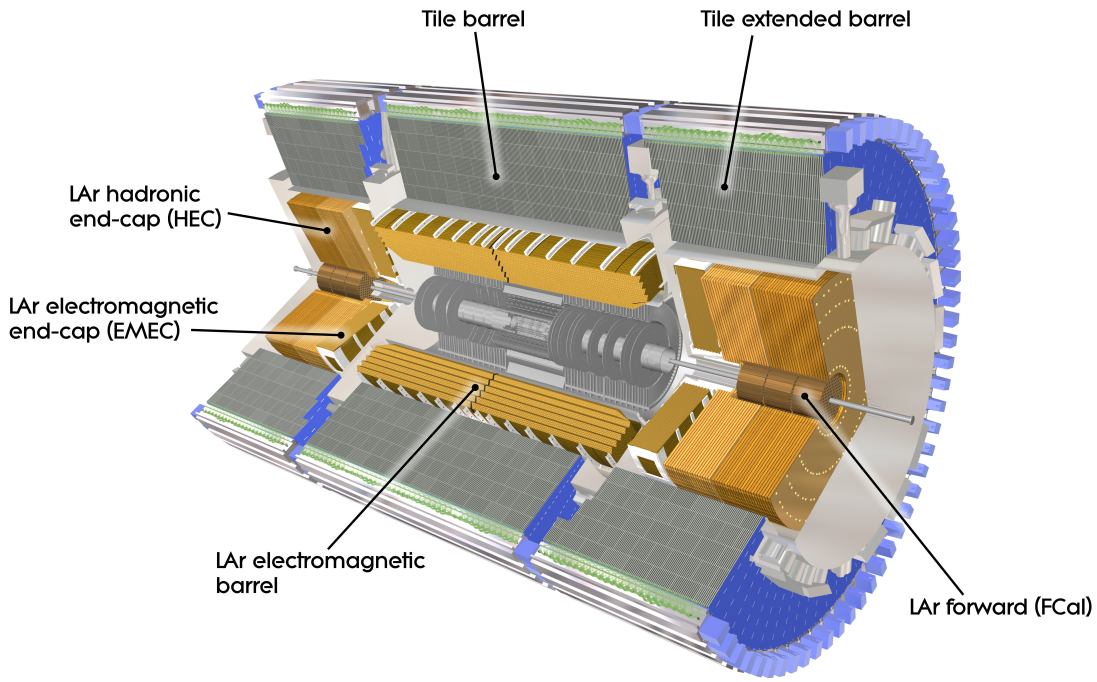

Figure 37: Cut away view of the ATLAS Calorimeters, showing the Liquid Argon electromagnetic calorimeter and the Tile hadronic calorimeter [109].

3.5 The Calorimeters

ATLAS includes two types of calorimeter systems for measuring the energies of electromagnetic and hadronic showers. These are the Liquid Argon (LAr) calorimeters and the Tile calorimeters. Together, these cover a region with $|\eta| < 4.9$. Both are sampling calorimeters, consisting of a layer of absorber material which induces the particles to shower, followed by active layers which measure the energy of the particle showers. Figure 37 shows a cutout of the calorimeters in ATLAS and labels the two subdetectors.

3.5.1 Liquid Argon Calorimeters

The Liquid Argon system [110] is used to detect electrons and photons in the region of $|\eta| < 3.2$. Lead is used as the absorber material because of its heavy nucleus. Electrons will electromagnetically interact with the lead and emit bremsstrahlung photon radiation, while the the photons will create e^+/e^- pairs, and together they will create a thin shower shape in the calorimeter (thanks to the relatively small Molière radius of 10 cm). The Liquid Argon is the active material used to measure the energy of the shower, selected for its linear response and its radiation hardness.

The typical distance in a material for which an electron will lose $1/e$ of its energy is called the radiation length X_0. The radiation length through the calorimeter is about 0.5 cm which allows the electromagnetic calorimeter to be rather compact while still having a depth of about $22X_0$, ensuring the photons and electrons will not leak much into the hadronic calorimeter. Most of the active material is in the middle of calorimeter, placed after initial layers meant to account for the energy losses in the material in front of the calorimeter and measure accurate position information about the showers. The active layer in the barrel has a granularity of 0.025×0.025 in $\Delta\eta \times \Delta\phi$ and the end caps have a granularity of 0.025×0.1 in $\Delta\eta \times \Delta\phi$.

3.5.2 Tile Calorimeters

The Tile calorimeter [111] is used to detect jet energies in the region of $|\eta| < 4.9$. It uses plastic scintillating tiles as the active material and steel plates as the absorber in the barrel region ($|\eta| < 1.5$), LAr active and copper absorber in the end-cap ($1.5 < |\eta| < 3.2$) and LAr active and copper/tungsten absorber in the FCal forward region ($3.1 < |\eta| < 4.9$). Hadrons shower mostly through strong interactions, so will produce showers of pions, of which about a third will decay electromagnetically. The scintillators in the active materials read the energy of the showers using photomultiplier tubes.

The typical distance for which the numbers of relativistic charged particles will be reduced by a factor of $1/e$ is called the interaction length, λ. The hadronic calorimeters have a depth of about 9.7λ in the barrel and 10λ in the end-caps. This helps ensure that most all of the hadron's energies are being sampled and that only muons will enter the Muon Spectrometer. The active layer in the barrel region have a granularity of 0.1×0.1 in $\Delta\eta \times \Delta\phi$ in the first two layers and 0.2×0.1 in $\Delta\eta \times \Delta\phi$ in the third layer. The end-cap regions have a granularity of 0.1×0.1 in $\Delta\eta \times \Delta\phi$ in the first wheel and 0.2×0.2 in $\Delta\eta \times \Delta\phi$ in the second.

3.6 The Muon System

The Muon Spectrometer or Muon System (MS) [112] is the outermost layer of ATLAS and the largest amount (by volume) of material. Neutrinos and muons are the only Standard Model particles that pass through the calorimeter system, and since neutrinos don't interact at all with the detector, muons are the only particle that interact with the Muon System. The subdetector is designed to cover a region of $|\eta| < 2.7$ and uses the magnetic field from the toroid magnet to measure muon momentum with high precision, giving a resolution of 3% for muons at 100 GeV. The Muon System is divided into a barrel region with $|\eta| < 1.05$ and an end-cap region between $1.05 < |\eta| < 2.7$. Figure 38 shows a cutout of the MS in ATLAS and labels the subdetectors, and Figure 39 shows a detailed schematic of the subdetectors that make up the barrel and end-cap regions.

3.6.1 Muon System Barrel

The barrel region has three cylindrical layers made out of precision measurement chambers called Resistive Plate Chambers (RPCs) and Monitored Drift Tubes (MDTs). RPCs are plane capacitors with a 2 mm gap, at a operation voltage of 9.8 kV, filled with $C_2H_2F_4$ gas. The high voltage difference between the plates allows for a timing resolution of of better than 2 ns. They are used for triggering on muons in the barrel. The MDTs are 3 cm diameter drift tubes filled with Argon gas and with a Tungsten wire down the middle held at a voltage of 3 kV. Muons passing through the MDTs ionize the Argon gas and the drift time of the ions is measured providing a hit resolution of 80 µm. The MDTs of layer two and three of the barrel are equipped with RPCs surrounding them.

3.6.2 Muon System End-cap

The end-cap region has four wheels, made up of MDTs, as well as Cathode Strip Chambers (CSC) and Thin-gap Chambers (TGCs). The first wheel closest to the interaction point is made out of MDTs and CSC. A CSC is like a higher precision version of the MDT, with strips rather than tubes, with many wires arranged in a plane. The CSC is only in the region of $2 < |\eta| < 2.7$. The anode wires are held 2.5 mm away from the cathode wires and are held at a potential difference of 1.9 kV. The CSC detector has a hit resolution of 60 µm. It is used rather an MDT due to having better radiation hardness as well as better background rejection for the increased rate of background closer to the interaction point. The third wheel in the end-cap has three TGCs close together which extend to $|\eta| = 2.4$. The TGCs are multi-wire plane chambers like the CSC, but The anode wires are held

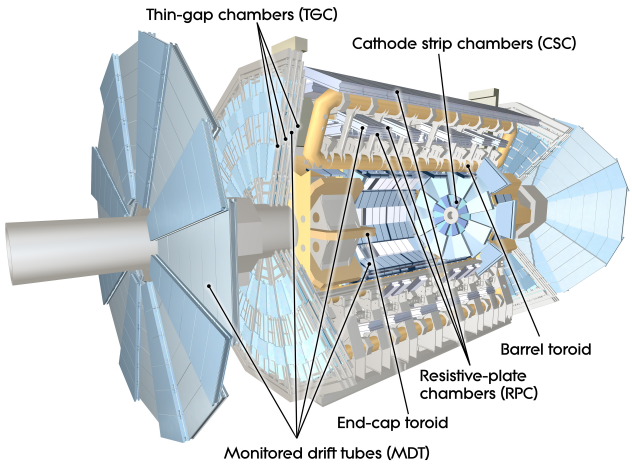

Figure 38: Cut away view of the ATLAS Muon System, showing the subdetectors and the toroid magnet [113].

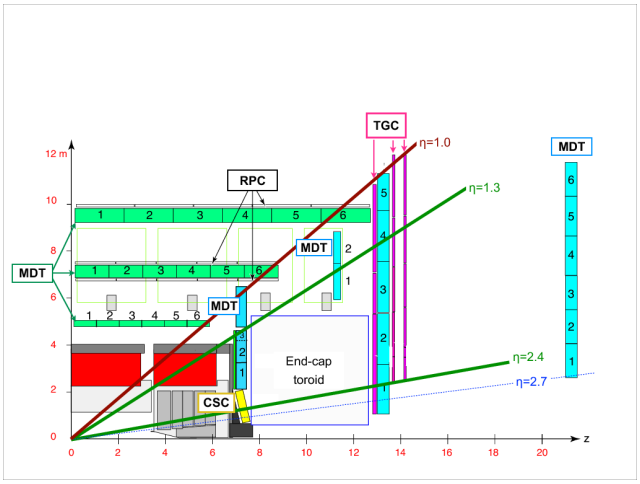

Figure 39: Side view in the yz plane of one-fourth of the ATLAS Muon System. Monitor Drift Tubes are shown in green and blue. Resistive Plate Chambers are in white, and Thin-Gap Chambers are in purple. the Cathode Strip Chambers are shown in yellow [114].

1.4 mm away from the cathode wires and the potential difference between them is 2.9 kV, giving a timing resolution of 4 ns. They are used for triggering on muons in the end-caps.

Chapter 4

Trigger and Reconstruction

Of utmost importance to the measurement of the Higgs cross section is the ability to reconstruct and identify the particles of its decay in ATLAS. We choose to measure the Higgs decay to the electroweak bosons $ZZ*$ as a way to decrease noise from the QCD background, and also choose the subsequent decay of $ZZ*$ to either muon or electron pairs in order to measure the full kinematic information of the original Higgs. It is necessary that any electrons or muons that could possibly have come from a Higgs boson are recorded for analysis, and that their momentum and energy are reconstructed with high fidelity. The trigger system decides which collisions are saved for full reconstruction, and is explained in Section 4.1. The high fidelity reconstruction and identification of the electrons and muons in saved events is explained in Sections 4.2 and 4.3 respectively. The reconstruction of jets is also important as they are often produced in association with the Higgs and give information about which production mode the Higgs came from, as well as information about higher order QCD effects in ggF. Jets are explained in Section 4.4.

4.1 The ATLAS Trigger

The LHC collides bunches of protons every 25 ns for an event rate of 40 MHz. The size of an unprocessed event is about 1.5 MB worth of data, which means that if every event were saved, at the end of the day there would be about 5 million TB worth of data to store. It is not possible to save and process the data from every collision, nor desirable, as many of the events are quark-quark or gluon-gluon scattering events where nothing "interesting" happens. What is known as a "trigger" is implemented to quickly filter events such that only interesting events, as chosen by a trigger menu, are saved and sent to CERN's computing center for full reconstruction [115].

This filtering is done in two steps. The first step is the Level 1 (L1) trigger, which is implemented in hardware and uses coarse reconstruction algorithms programmed into FPGAs to reduce the event rate from 40 MHz to 100 kHz. These algorithms only use calorimeter energy towers and muon system hits (no ID tracking hits) gathered from the ATLAS data acquisition system (DAQ) to make their decision [116]. The second step in the filtering is the High Level Trigger (HLT) which is implemented in software and uses less coarse reconstruction with track information to reduce the event rate further from 100 kHz to 1.5 kHz. Figure 41 shows a schematic of how data passes between the trigger system and the DAQ to filter the total number of events.

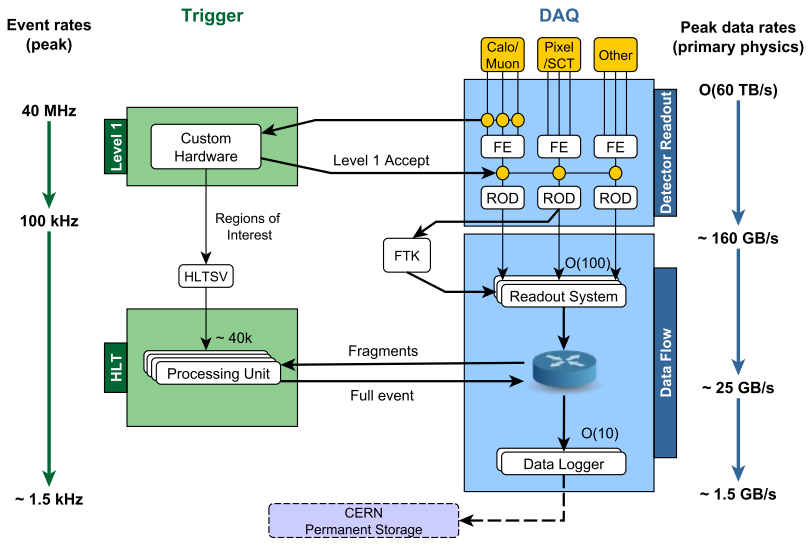

Figure 41: Schematic of the ATLAS Trigger and Data Acquisition system in Run 2 showing expected event rates and data rates through each decision step. [117].

4.1.1 Trigger Efficiency for $H \to 4\ell$

Even though the LHC collides protons 40 million times a second, given the running conditions over 2015 and 2016, we only expect an average of 5 collisions every week to produce a Higgs that decays to four leptons. Since this is such a rare occurrence, it is important that the trigger not filter away any of our signal events when they happen. The $H \to 4\ell$ trigger efficiency must be as close as possible to 100%. This can be a challenge due to increasing instantaneous luminosity.

The triggers for 4ℓ consist of single lepton, di-lepton, and tri-lepton triggers. Di-lepton and tri-lepton triggers include combinations of electron and muon triggers. As instantaneous luminosities increased between 2015 and 2016, certain single lepton triggers had to increase their p_{T} thresholds, thus decreasing the 4ℓ event efficiency. For example single muon triggers increased from 18 GeV to 24 GeV. To compensate for this loss of efficiency, more tri-lepton triggers and mixed-flavored triggers were introduced, like `3mu4`, which required hits in the Muon System consistent with 3 muons above 4 GeV.

Efficiencies of various triggers and their combinations for 125 GeV ggF Higgs signals in the four lepton decay channel are shown in Table 41 (for the 2015 data taking) and Table 42 (for the 2016 data taking). The trigger efficiencies split into the different flavor 4ℓ final states as a function of the Higgs p_{T} for the full 2015 + 2016 dataset are shown in Figure 42. The inclusive trigger efficiencies are 99.51%($4e$), 98.59%(4μ), 99.52%($2e2\mu$) and 96.84%($2\mu2e$).

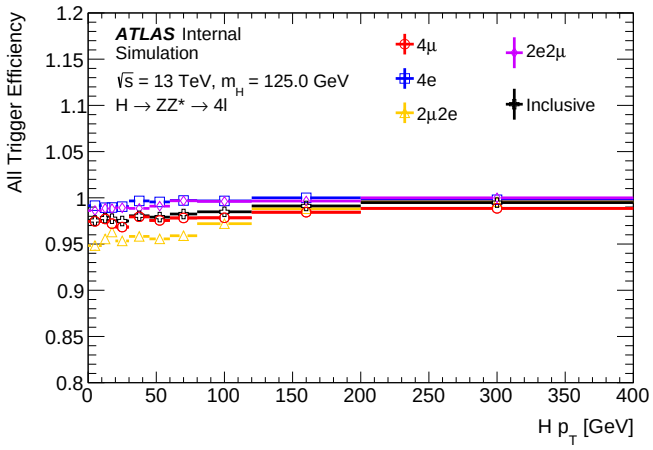

Figure 42: All trigger efficiency in the combined final state and in each of the four final states as a function of the Higgs p_{T}. Efficiencies are stable over the range of the variable, except for the $2\mu2e$ channel which shows variations up to 5%. The variation for this channel is caused by electron triggers gaining hugely in efficiency as the Higgs p_{T} increases.

4.2 Electron Reconstruction and Identification

4.2.1 Electron Reconstruction

A prompt electron is an electron that is a a product of the hard scatter, i.e. it is a decay of a Z or associated W boson from the Higgs production. As a prompt electron moves through ATLAS, it will

Table 41: Efficiencies of various triggers and their combinations, used in 2015, for 125 GeV ggF Higgs signals in the four decay channels. The uncertainties are from MC statistics.

trigger	$4e$	4μ	$2e2\mu$	$2\mu2e$
e24_lhmedium_L1EM18VH	0.9726 ± 0.0056		0.9577 ± 0.0064	0.2915 ± 0.0150
e60_lhmedium	0.2332 ± 0.0145		0.2096 ± 0.0129	0.0244 ± 0.0054
e120_lhloose	0.0234 ± 0.0048		0.0196 ± 0.0047	0.0006 ± 0.0006
mu20_iloose_L1MU15		0.9658 ± 0.0048	0.4447 ± 0.0156	0.9360 ± 0.0080
mu50		0.4958 ± 0.0132	0.0431 ± 0.0065	0.5012 ± 0.0166
mu60_0eta105_msonly		0.1693 ± 0.0100	0.0122 ± 0.0035	0.1694 ± 0.0126
2e12_lhloose_L12EM10VH	0.9826 ± 0.0044		0.8839 ± 0.0101	0.3837 ± 0.0161
2mu10		0.9599 ± 0.0053	0.4513 ± 0.0157	0.6820 ± 0.0154
mu18_mu8noL1		0.9773 ± 0.0040	0.4610 ± 0.0157	0.8777 ± 0.0110
e17_lhloose_mu14			0.7967 ± 0.0127	0.5317 ± 0.0165
e7_medium_mu24			0.2792 ± 0.0141	0.8465 ± 0.0120
e24_medium_L1EM20VHI_mu8noL1			0.9050 ± 0.0094	0.2368 ± 0.0139
e17_lhloose_2e9_lhloose	0.9272 ± 0.0090			
3mu6		0.8568 ± 0.0094		
3mu6_msonly		0.8711 ± 0.0089		
mu18_2mu4noL1		0.9720 ± 0.0044		
2e12_lhloose_mu10			0.8293 ± 0.0119	0.4247 ± 0.0164
e12_lhloose_2mu10			0.4499 ± 0.0157	0.6315 ± 0.0160
single-e triggers	0.9737 ± 0.0055			
di-e triggers	0.9826 ± 0.0044			
tri-e triggers	0.9272 ± 0.0090			
single-μ triggers		0.9672 ± 0.0048		
di-μ triggers		0.9908 ± 0.0025		
tri-μ triggers		0.9802 ± 0.0037		
single OR di-e triggers	0.9941 ± 0.0027			
single OR tri-e triggers	0.9860 ± 0.0042			
di OR tri-e triggers	0.9855 ± 0.0041			
single OR di-μ triggers		0.9910 ± 0.0025		
single OR tri-μ triggers		0.9834 ± 0.0034		
di OR tri-μ triggers		0.9920 ± 0.0023		
e triggers			0.9789 ± 0.0045	0.5139 ± 0.0166
μ triggers			0.6940 ± 0.0145	0.9559 ± 0.0067
$e\mu$ triggers			0.9841 ± 0.0042	0.9550 ± 0.0069
e OR μ triggers			0.9982 ± 0.0012	0.9855 ± 0.0041
e OR $e\mu$ triggers			0.9942 ± 0.0025	0.9638 ± 0.0062
μ OR $e\mu$ triggers			0.9895 ± 0.0034	0.9801 ± 0.0047
all combined	0.9941 ± 0.0027	0.9921 ± 0.0023	0.9996 ± 0.0003	0.9889 ± 0.0035

Table 42: Efficiencies of various triggers and their combinations, used in 2016, for 125 GeV ggF Higgs signals in the four decay channels. The uncertainties are from MC statistics.

trigger	$4e$	4μ	$2e2\mu$	$2\mu2e$
single electron triggers:				
e24_lhtight_nod0_ivarloose	0.9374±0.0016		0.9116±0.0016	0.2676±0.0027
e60_lhmedium_nod0	0.2267±0.0027		0.2065±0.0022	0.0174±0.0008
e60_medium	0.2162±0.0027		0.1974±0.0022	0.0165±0.0008
e140_lhloose_nod0	0.0145±0.0008		0.0103±0.0006	0.0004±0.0001
e300_etcut	0.0000±0.0000		0.0000±0.0000	0.0000±0.0000
double electron triggers:				
2e15_lhvloose_nod0_L12EM13VH	0.9662±0.0012		0.8574±0.0019	0.1814±0.0023
triple electron triggers:				
e17_lhloose_nod0_2e9_lhloose_nod0	0.9415±0.0015			
single muon triggers:				
mu20_ivarloose_L1MU15		0.9597±0.0009	0.4285±0.0027	0.9184±0.0017
mu20_iloose_L1MU15		0.9587±0.0009	0.4277±0.0027	0.9178±0.0017
mu40		0.6704±0.0022	0.0565±0.0013	0.6409±0.0029
double muon triggers:				
2mu10		0.9525±0.0010	0.4201±0.0027	0.6558±0.0029
mu20_mu8noL1		0.9607±0.0009	0.3385±0.0026	0.8546±0.0021
triple muon triggers:				
3mu4		0.8702±0.0016		
mu6_2mu4		0.8750±0.0016		
mu20_2mu4noL1		0.9565±0.0010		
$e\mu$ triggers:				
e7_lhmedium_nod0_mu24			0.2745±0.0024	0.8673±0.0021
e17_lhloose_nod0_mu14			0.7661±0.0023	0.5485±0.0030
e24_lhmedium_nod0_L1EM20VHI_mu8noL1			0.9393±0.0013	0.2925±0.0028
e12_lhloose_nod0_2mu10			0.4188±0.0027	0.6057±0.0030
2e12_lhloose_nod0_mu10			0.8043±0.0022	0.4164±0.0030
all single-e triggers	0.9408±0.0015			
all di-e triggers	0.9662±0.0012			
all tri-e triggers	0.9415±0.0015			
all single-μ trigger		0.9614±0.0009		
all di-μ trigger		0.9840±0.0006		
all tri-μ trigger		0.9741±0.0008		
all single OR di-e triggers	0.9915±0.0006			
all single OR tri-e triggers	0.9905±0.0006			
all di OR tri-e triggers	0.9872±0.0007			
all single OR di-μ trigger		0.9844±0.0006		
all single OR tri-μ trigger		0.9775±0.0007		
all di OR tri-μ trigger		0.9855±0.0006		
all e triggers			0.9644±0.0010	0.3402±0.0029
all μ triggers			0.6237±0.0026	0.9275±0.0016
all $e\mu$ triggers			0.9848±0.0007	0.9483±0.0013
all $eOR\mu$ triggers			0.9892±0.0006	0.9565±0.0012
all $eORe\mu$ triggers			0.9934±0.0004	0.9512±0.0013
all $\mu ORe\mu$ triggers			0.9868±0.0006	0.9656±0.0011
all all combined	0.9951±0.0004	0.9859±0.0006	0.9952±0.0004	0.9684±0.0011

leave tracking hits in every layer of the inner detector. These detector hits are turned into a track using a Kalman filter algorithm [118] with three hits as a seed, and the curvature of the track due to the influence of the ATLAS solenoid will identify the lepton as either having a negative or positive

charge. The track will then terminate in the electromagnetic calorimeter where the electron will deposit all of its energy, making a thin shower shape that terminates before it reaches the hadronic calorimeter.

Electron candidates are then reconstructed by using a sliding window in the electromagnetic calorimeter to look for localized energy clusters that are also in proximity to inner detector tracks that in turn can be traced to the primary vertex[6]. As the electron moves through the inner detector, energy is lost due to Bremsstrahlung radiation. To improve reconstruction efficiency, the track associated to the calorimeter cluster is refitted using a Gaussian-Sum Filter [119]. The electron reconstruction efficiency as a function of the electron E_{T} and $|\eta|$ is shown in Figure 43.

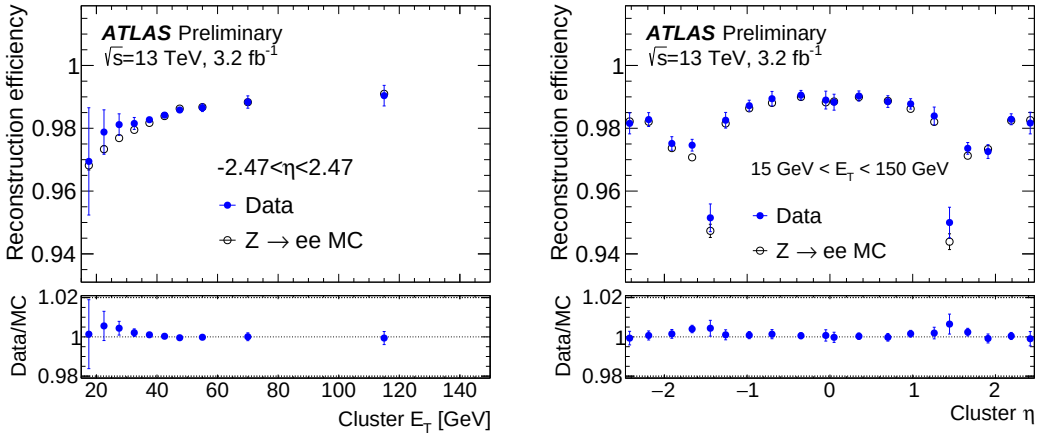

Figure 43: Measured electron reconstruction efficiencies as a function of E_{T} (left) and as a function of $|\eta|$ (right) for the 2015 dataset. The area between $1.37 < |\eta| < 1.52$ has lower efficiency as this is a "crack" region in the detector between measuring components, so electrons are not reconstructed there. [120]

4.2.2 Electron Identification

Not all objects built by the electron reconstruction algorithms are prompt electrons. Backgrounds of the reconstruction process include leptons from photon conversions, Dalitz decays, fake leptons that are actually charged light jets, and semi-leptonic decays from heavy-flavor jets.

An electron identification algorithm is applied after reconstruction to the candidates in order to reject these background objects. The algorithm uses the fact that the background objects can

[6]Primary vertices defined in the Inner Detector section, 3.4

be distinguished from real electrons using other variables besides track information. For example, calorimeter information is used to distinguish electrons from charged hadrons since the shower produced by electrons is predominately deposited in the electromagnetic calorimeter over the hadronic calorimeter. Another example is the high threshold activation of the TRT, which is activated by electrons emitting transition radiation due to their larger β factor, as explained in Section 3.4.3. Many variables like this are combined into a Naive Bayes Classifier [120], given by the formula in the following equation

$$d_L = \frac{L_S}{L_S + L_B} \qquad L_{S(B)}(\vec{x}) = \prod_{i=1}^{n} P_{s(b),i}(x_i) \tag{4.1}$$

d_L is the classifier, $L_{S(B)}$ is the likelihood function for the signal or background object, and $P_{s(b),i}(x_i)$ is the probability distribution for either the signal or background variable x_i. The likelihood functions used in the classifier are simply a product of probability density distributions for signal and background objects, which are obtained from Monte Carlo as well as from data-driven methods by using the Tag and Probe method [120].

The algorithm to reject background objects is implemented as a cut on the calculated d_L for each candidate. A larger cut threshold leads to a better probability of choosing a signal electron at the cost of lowering the overall electron efficiency. A cut threshold chosen to match a certain electron efficiency at $E_{\mathrm{T}} = 40\,\mathrm{GeV}$ defines the current working points, *Loose* (93% eff.), *Medium* (88% eff.), and *Tight* (80% eff.). The *Loose* working point is used in this analysis. The working point efficiencies in general depend on the $|\eta|$ and E_{T} of the electrons, which is shown in Figure 44.

4.3 Muon Reconstruction and Identification

4.3.1 Muon Reconstruction

A prompt muon is a muon that is a a product of the hard scatter, i.e. it is a decay of a Z or associated W boson from the Higgs production. As a prompt muon moves through ATLAS, it will leave tracking hits in every layer of the inner detector, be minimally ionizing in the calorimeter and leave little energy there, and then continue moving through the Muon System and leave tracking hits there before completely escaping ATLAS. Due to leaving little energy in the calorimeter, muons are reconstructed predominantly from tracking information and use calorimeter information in a limited way [121].

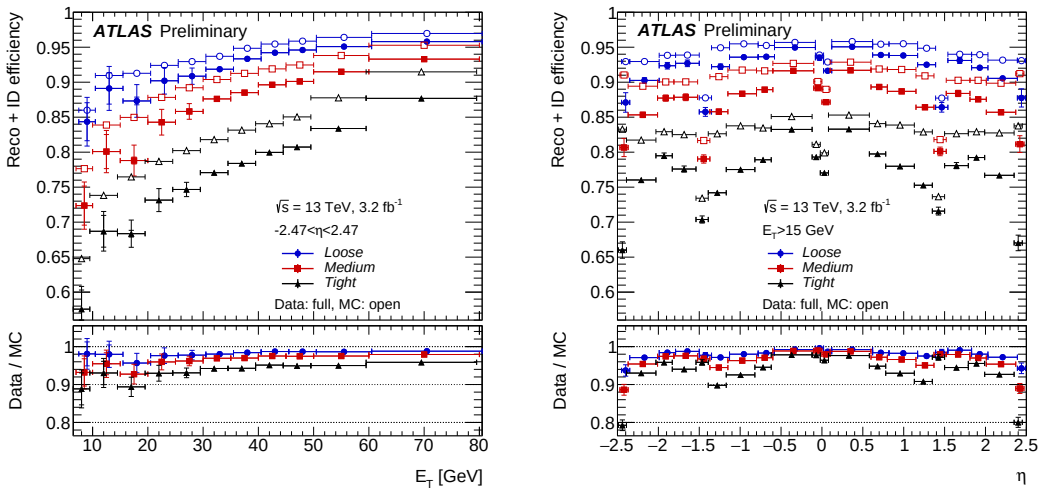

Figure 44: Combined electron reconstruction and identification efficiencies in $Z \to ee$ events as a function of the transverse energy E_{T} (left) and as a function of pseudorapidity η (right) [120].

The Muon System tracks are built in a segmented way from each of the muon subdetectors. Each subdetector builds track segments from its detector hits. A full track candidate is then built by taking combinations of these track segments and using a χ^2 fit to see if the track candidate is consistent with a full muon path. Track candidates that pass a χ^2 cut are then labeled as Muon System tracks. There are four methods to reconstruct muons using Inner Detector tracks and Muon System tracks in ATLAS:

1. **Combined (CB) Muons**

   A full detector track using tracks from both the Muon System and Inner Detector is formed with a global fit. The fit starts with tracks reconstructed in the Muon System and then extrapolates them back to the Inner Detector. The majority of muons are reconstructed this way.

2. **Segment Tagged (ST)**

   If there is not a high quality track in the Muon System, but a track from the Inner Detector can be extrapolated to the Muon System and be associated with a track segment from one of the subdetectors, the muon is Segment Tagged. The kinematics of the muon are taken from the Inner Detector track.

3. **Calorimeter Tagged (CT)**

There are no Muon System hits, but a trajectory in the Inner Detector is associated with energy deposits in the calorimeters that are consistent with a minimum ionizing particle. Their use in the analysis is to cover the region of $|\eta| < 0.1$ which is not equipped with muon chambers. This method has low muon purity and the analysis only uses CT muons with $p_{\mathrm{T}} > 15\,\mathrm{GeV}$.

4. **Standalone (SA)**

   A track is found only in the Muon System and not in the Inner Detector, but the track in the Muon System is compatible with originating from the primary vertex. Their use in the analysis is to cover the region of $2.5 < |\eta| < 2.7$ which is not covered well by the Inner Detector. The kinematics of the muon is reconstructed taking into account the estimated energy loss from deposited energy in the calorimeters.

When the same tracks in the Inner Detector are reconstructed by more than one method, the priority for reconstruction goes as Combined Muon, Segment Tagged, and then Calo Tagged [121].

4.3.2 Muon identification

Just like electron backgrounds, non-prompt muons are considered background. These muons primarily originate from pion and kaon decays. Background rejection is achieved through cuts of the quality of the tracks. Tracks from pion and kaon decays will have 'kinks' which will lead to worse fit quality. A variables used in muon identification to measure this is the q/p significance $\sigma_{q/p}$, the absolute value of the difference between the ratio of the charge and momentum of the muons measured in the ID and MS divided by the quadrature sum of their uncertainties [121]. i.e.

$$\frac{|q/p_{\mathrm{ID}} - q/p_{\mathrm{MS}}|}{\sqrt{\sigma^2_{\mathrm{ID}} + \sigma^2_{\mathrm{MS}}}} \tag{4.2}$$

We use the *Loose* working point in the $H \to 4\ell$ analysis, which allows the use of all muon types, though restricts the use of ST and CT muons to regions of $|\eta| < 0.1$, and restricts SA muons to regions of $2.5 < |\eta| < 2.7$. Background rejection cuts include requiring a q/p significance of $\sigma_{q/p} < 7$.

Muons with Inner Detector tracks (CB,ST,CT) are required to have a minimum number of hits from some inner subdetectors: at least 1 Pixel hit, 5 SCT hits, and less than 3 Pixel or SCT holes (which are active sensors with no hits in the path). In the $|\eta| > 2.5$ region, requirements are relaxed such that at least 1 Pixel hit and at least 3 SCT hits are required. CB muons are required to have ≥ 3 precision hits in at least two layers of the MDT. The efficiency for muon reconstruction and identification is shown in Figure 45.

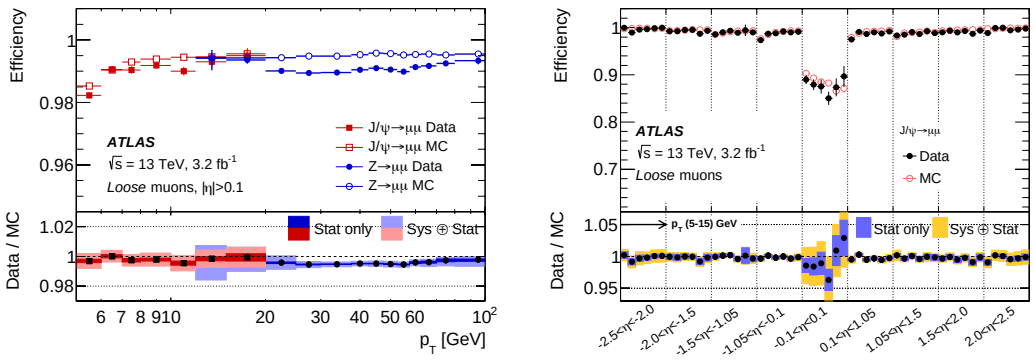

Figure 45: Combined muon reconstruction and identification efficiencies in $J/\psi \to \mu\mu$ and $Z \to \mu\mu$ events as a function of the transverse momentum p_{T} (left) and as a function of pseudorapidity η (right) for the *Loose* selection.

4.4 Jet Reconstruction and Identification

4.4.1 Jet Reconstruction

Jets are showers of hadrons that have a conical shape and originate from quarks and gluons. Jets can be charged or neutral, and so may or may not leave tracks in the Inner Detector. Jets interact less with the electromagnetic calorimeter and deposit most of their energy in the hadronic calorimeter. Their shower shape in the calorimeter is deep and broad compared to the shower shapes of electrons and photons. Energy deposits in the calorimeter are gathered into 3D topological clusters (topo-clusters) [122], which are topologically connected calorimeter cells that contain a significant amount of energy above a noise threshold. These topo-clusters are used as inputs to the anti-k_t algorithm [123] in order to reconstruct jets. The anti-k_t algorithm is implemented with a radius parameter of $R = 0.4$ using the `FastJet` software package [124]. Tracks can also be associated to a jet using spatial proximity to an energy cluster or using a technique known as ghost association [125, 126].

Jets need to be calibrated to a Jet Energy Scale (JES) that is the same as truth jets created using the same clustering algorithm from final-state particles in Monte Carlo. Calibration has to account for dead material in the detector, energy losses from the showers passing beyond the calorimeter edge, energy losses from particle deposits below the noise threshold that do not create clusters, and also contamination from pile-up jets from other pp collisions in the same bunch crossing [127]. The jet calibration procedure is the same as it was in Run 1 apart from updates that take into account the IBL detector, new beam conditions, changes and in the LAr sampling points [128, 129].

4.4.2 Jet Identification

Jet backgrounds mostly come from collisions from upstream of the interaction point, cosmic-rays, and calorimeter noise [130]. Just as in the case of electron and muon identification, algorithms are developed to reject background jets, and these algorithms are defined for different efficiency working points. The 4ℓ analysis uses the *BadLoose* working point which maintains a high real jet efficiency of 99.8% with a fake jet rejection of about 50% [131]. In addition, to help eliminate contributions from pile-up jets, jets are required to pass a Jet Vertex Tagger (JVT) [132], which is a 2D likelihood discriminator that uses the variables

1. $R_{p_{\mathrm{T}}}$,the scalar p_{T} sum of the tracks that are associated with the jet and originate from the primary vertex divided by the fully calibrated jet p_{T}, and
2. corrJVF, defined as the scalar p_{T} sum of the tracks that are associated with the jet and originate from the primary vertex divided by the scalar p_{T} sum of all associated tracks, including those from other vertices

in order to classify the jet as pile-up or not.

b-jets

B-hadrons have a special distinction of being long-lived particles, which means that they can travel up to 4 mm in the detector before decaying. So in addition to the primary vertex of the hard scatter that produced the B-hadron, the subsequent decay of the B-hadron and the formation of the jet creates a secondary vertex, which can be identified in tracking. These b-jets can be important in the 4ℓ analysis for identifying a Higgs boson from the $t\bar{t}H$ production mode, which will be associated with two b-jets from the top quark decays. b-jets are tagged in the analysis using the `MV2_c10` algorithm [133] at its 70% efficiency point.

Chapter 5

Higgs Event Selection

5.1 $H \to ZZ^* \to 4\ell$

Most collisions at the LHC will not produce a Higgs Boson. The cross section for inelastic collisions is around 79 mb [134], while the theoretical cross section for the Higgs Boson is around 55 pb [17]. That means for 36 fb^{-1} of integrated luminosity, there will be around 2.8×10^{15} inelastic pp collisions, of which only around 2.0×10^6 will produce a Higgs boson.

The Higgs has a short lifetime and will decay in the beam pipe before reaching the detector at all, as explained in Section 2.3.4. The $H \to ZZ^* \to 4\ell$ final state also has a small decay fraction of 0.0124%, meaning of the two million Higgs bosons produced, only around 250 will decay through this channel. Even with such small statistics, the channel consists of a distinctive signature which is relatively easy to detect. The four high p_{T} leptons form opposite sign, same flavor pairs i.e. $(\mu^+\mu^-)(\mu^+\mu^-)$,$(e^+e^-)(e^+e^-)$, or $(e^+e^-)(\mu^+\mu^-)$ from the decay of two Z bosons, and all together the leptons have an invariant mass equal to the Higgs mass of around 125 GeV. Figure 51 shows the Feynman diagram for this Higgs decay.

This signature is not common to many Standard Model backgrounds[7]. Optimizing our selection for Higgs bosons in this channel can achieve a signal to background ratio of greater than 2. Its high sensitivity made it the natural 'golden channel' for discovering the Higgs when the LHC first turned on. For doing differential cross section measurements of the Higgs, getting high sensitivity in every bin requires a large amount of statistics, so there is a great emphasis on trying to increase lepton efficiency (especially at low p_{T}) whenever possible to capture as many of the few Higgs bosons that decay to 4ℓ.

[7] see Chapter 6 for backgrounds of this channel.

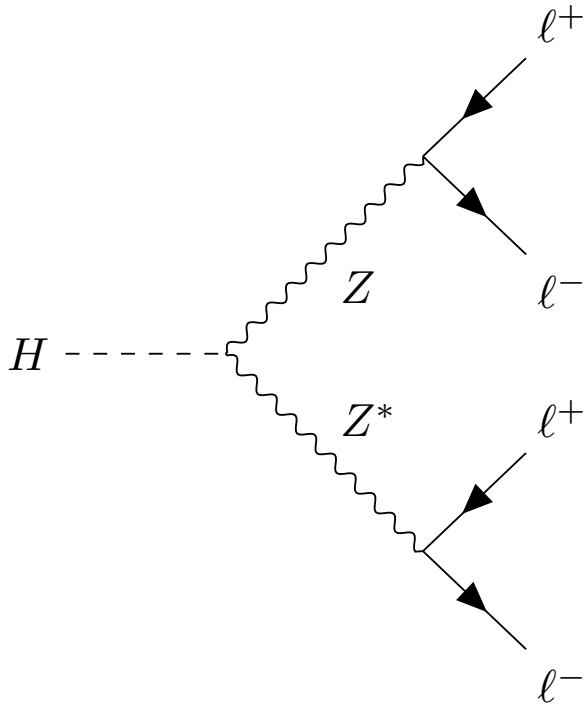

Figure 51: Feynman diagram of the $H \to ZZ^* \to 4\ell$ decay channel. One of the Z bosons is on-shell and has a mass near 91 GeV while the other Z is off-shell. The decay signal always consists of 2 same flavor, opposite sign pairs of leptons (e or μ).

The selection of the Higgs events in data is known as a 'reco' selection, for reconstructed, since we do not have the labels of the particles as they are produced and instead must reconstruct them from detector tracks and energy clusters. We can also define a 'truth reco' selection alongside this reco selection, where truth means that we are using simulated collisions where we do know the labels of the particles, and we pass these particles through a simulated ATLAS detector to turn them into tracks and calorimeter clusters before reconstructing them. Using 'truth reco' events is important for optimizing the selection criteria before applying it to real data to avoid bias, and also to calculate the expected sensitivity of our measurements.

Alongside the 'truth reco' selection, it is important to define a 'truth fiducial' selection as well. Since the ATLAS detector cannot measure the entire phase space of the Higgs decays due to limited acceptance and efficiency, we will not able to measure all of the predicted 250 Higgs events. There is no sensitivity to events outside the detector acceptance, so to make a model independent measurement of $H \to ZZ^* \to 4\ell$ events we expect to be able to detect in ATLAS, we define a fiducial phase space, which is the fraction of the phase space that we think we can confidently or 'fiducially'

measure with our detector. The fiducial selection is applied to the simulated events before reconstruction, and the events that pass the fiducial selection are used as the model we will compare our results to. The fiducial selection is necessary for the unfolding (described in Chapter 7) and also to be able to extrapolate the fiducial result to the full phase space. Section 5.2 describes the reco event selection, and Section 5.3 describes the fiducial selection.

5.2 Analysis Event Selection

5.2.1 Lepton Selection

After having reconstructed and identified possible electron and muon candidates in the event as described in Section 4.2 and Section 4.3, electrons and muons are chosen in such a way to balance high signal efficiency (e.g. selecting all the real electrons) and low background efficiency (e.g. rejecting light-flavor jets which fake electrons). Since we are looking specifically for a Higgs boson, we also know that the leptons must have emerged from a common vertex[8]. We select the primary vertex to be the vertex with the largest p_{T} sum in the event, and all the lepton candidate tracks are constrained to be close to this primary vertex.

Electrons. We select the electron candidates which pass the *Loose* Likelihood working point [9], which aims for a 95% signal efficiency overall, but decreases to 85% at $E_{\mathrm{T}} < 10\,\mathrm{GeV}$. Cuts on the electron at $E_{\mathrm{T}} > 7\,\mathrm{GeV}$ and $|\eta| < 2.47$ are also done, as efficiencies rapidly fall at low E_{T} and high η as seen in Figure 44. Inner detector tracks are extrapolated back to the interaction point and a further cut of $|z_0 \cdot \sin_\theta| < 0.5\,\mathrm{mm}$[10] is done to reject fakes or electrons that did not come from the Higgs.

Muons. We select the muon candidates which pass the *Loose* criteria, which includes muons from all the different reconstruction algorithms as described in Section 4.3. The calo-tagged muons are not optimized for $p_{\mathrm{T}} < 15\,\mathrm{GeV}$ and therefore are required to have $p_{\mathrm{T}} > 15\,\mathrm{GeV}$, while track-tagged muon are required to have $p_{\mathrm{T}} > 5\,\mathrm{GeV}$. Just like the electrons, if a track is present in the inner detector, it is extrapolated back to the interaction point and a cut on $|z_0 \cdot \sin_\theta| < 0.5\,\mathrm{mm}$ is done to reject fakes. A further cut on the impact parameter of $|d_0| < 1$ mm is imposed to reduce background muons from cosmic rays.

[8] Track vertices are discussed in the Inner Detector section, Section 3.4.
[9] Explained in the electron identification section, Section 4.2.
[10] See Section 3.3.1 for coordinate system and distance definitions.

5.2.2 Jet Selection

Jets are reconstructed from energy clusters in the hadronic calorimeter using the anti-k_T algorithm with a distance parameter of $R = 0.4$. They must pass the *BadLoose*[11] criteria and have $p_{\mathrm{T}} > 30\,\mathrm{GeV}$ and $|\eta| < 4.5$. Due to increased pile-up in Run 2, jets with $p_{\mathrm{T}} < 60\,\mathrm{GeV}$ and $|\eta| < 2.4$ must also pass Jet Vertex Tagger (JVT) with a score of > 0.59, which corresponds to a jet efficiency of 92%. Jets within $\Delta R < 0.2$ of an electron or $\Delta R < 0.1$ of a muon are removed. Finally, jets are tagged as b-jets by using the `MV2_c10` algorithm [133] at its 70% efficiency point.

5.2.3 Background Rejection

Once the electron and muons in the event have been selected, we apply cuts to the leptons in order to eliminate fake leptons and leptons not from the Higgs. These cuts include isolation requirements, impact parameter requirements, and vertex requirements.

Isolated leptons are leptons that have a low ratio of track or calorimeter p_{T} in a cone around them compared to their own measured p_{T}. They are more likely to be prompt leptons[12] and less likely to come from semileptonic decays of heavy jets or misidentified light jets. Isolation can be measured with track information, given by $p_T^{\mathrm{varcone}X}$ variables, which are the sum of the transverse momenta of all tracks that fall within a cone $\Delta R < 0.X$ of the lepton, and with calorimeter information, given by $E_T^{\mathrm{varcone}X}$ variables, which are the sum of the transverse energy in the calorimeter cells within a cone $\Delta R < 0.X$ around the lepton. Isolation cuts have been optimized for the 13 TeV conditions [135]. Related to isolation is overlap removal which cuts on the ΔR[13] distance between leptons in order to ensure that leptons are not sharing tracks or calorimeter clusters.

The impact parameter significance reduces contributions from backgrounds with long decay lifetimes, like leptons from semileptonic decays of b-jets, and is defined as the impact parameter d_0 divided by the estimated uncertainty σ_{d_0}.

Vertex requirements ensure that the leptons all came from the same primary vertex, and are not split between vertices, for example as from a $Z + b\bar{b}$ decay. The vertex cut is based on the fit quality of the vertex formed by the four tracks of the quadruplet leptons. The quality is measured by a $(\chi^2/N_{\mathrm{dof}})$ goodness of fit. The vertex cut is new for Run 2 and provides enough background rejection to allow the muon p_{T} cut to be relaxed from Run 1's 6 GeV to 5 GeV.

The background rejection cuts using isolation, impact parameter, and vertex cuts are as follows:

[11] Explained in the jet identification section, Section 4.4.
[12] Prompt leptons are those that are produced by the hard scatter and come from the primary vertex.
[13] See Section 3.3.1 for definition of ΔR.

- $\Delta R(\ell, \ell') > 0.10$ (0.20) for all same (different) flavor leptons in the quadruplet.
- Muon track isolation $p_T^{\text{varcone30}}/p_{\text{T}} < 0.15$.
- Muon calorimeter isolation $E_T^{\text{topocone20}}/p_{\text{T}} < 0.30$
- Electron track isolation $p_T^{\text{varcone20}}/E_{\text{T}} < 0.15$
- Electron calorimeter isolation $E_T^{\text{topocone20}}/E_T < 0.20$
- Impact parameter cuts, for electrons: $d_0/\sigma_{d_0} < 5$ for muons: $d_0/\sigma_{d_0} < 3$
- $\chi^2/N_{\text{dof}} < 6$ for 4μ and < 9 for others.

5.2.4 Quadruplet formation

Once we have a set of prompt and isolated leptons, they are passed through a cutflow in order to determine if they are consistent with coming from a Higgs decay. An event with a real Higgs decay can have more than four prompt leptons in it due to the decay of an associated W or Z boson. In order to discern the Higgs leptons from the other leptons, all possible sets of 4 leptons (of same-flavor, opposite sign pairs) are passed to the cutflow to select the quadruplet that most likely is a Higgs decay. The cutflow goes through each of the quadruplets one-by-one and applies the following kinematic cuts:

- The three leading leptons in the quadruplet must pass the p_{T} thresholds $20, 15$ and $10\,\text{GeV}$ respectively.
- There can be at most one calo-tagged or stand-alone muon or silicon-associated forward muon in the quadruplet.
- The leading pair of leptons (i.e. the on-shell Z boson) is chosen to be the pair with an invariant mass closest to the PDG Z mass ($91.1876\,\text{GeV}$).
- The leading pair invariant mass must be $50 < m_{12} < 106$ GeV.
- The subleading pair invariant mass must be $12 < m_{34} < 115\,\text{GeV}$.
- $m_{\ell,\ell'} > 5\,\text{GeV}$ is applied for all same flavor lepton pairs in order to reject J/ψ particles.

At the end of these quadruplet cuts, there may be multiple quadruplets that all pass. Within a channel (i.e. 4μ,$2e2\mu$,$2\mu2e$, or $4e$) we select the best quadruplet to be the one with the leading pair mass closest the Z mass. If the quadruplets have the same leading pair mass, then the subleading pair closest to the Z mass is used to decide the quadruplet.

5.2.5 Final State Radiation Recovery

Next we want to improve the estimation of the $m_{4\ell}$ of the signal events by recovering energy from final state radiation (FSR) photons. This recovery is done after all the kinematic cuts, but before the mass window cut. QED processes allow the leptons to radiate off low energy photons. FSR recovery attempts to identify these low energy photons and add their four vector back to the four lepton system. There are two methods of recovering the energies, one for collinear photons from $Z \to \mu\mu$ decays ($\Delta R_{\text{cluster},\mu} = \Delta\eta^2 + \Delta\phi^2 < 0.15$) and one for non-collinear photons ($\Delta R_{\text{cluster},\mu} = \Delta\eta^2 + \Delta\phi^2 > 0.15$) from both $Z \to \mu\mu$ and $Z \to ee$ decays. While many FSR candidates may be identified in an event, only one photon is allowed to be added back, with priority given to collinear photons, and then to the non collinear photon with the highest E_{T}.

Collinear photon candidates are obtained either from EM calorimeter clusters or from the standard reconstructed Egamma photon object, depending on the energy of the photon. If the transverse energy of the cluster is $1.5 < E_{\text{T}} < 3.5$ GeV, then calorimeter clusters are used, and the cone between the cluster and the muon must be $\Delta R_{\text{cluster},\mu} < 0.08$. If the transverse energy of the cluster is $E_{\text{T}} > 3.5$ GeV, then the standard Egamma photon objects are used, and the cone between the cluster and the muon must be $\Delta R_{\text{cluster},\mu} < 0.15$. If more than one cluster is found in the cone, then the cluster with the highest E_{T} is chosen.

Non-collinear photon candidates can come from $Z \to ee$ decays as well as $Z \to \mu\mu$ decays, and are obtained from the standard reconstructed Egamma photons that pass *Tight* identification. The transverse energy of the cluster must be $E_{\text{T}} > 10\,\text{GeV}$ and the cone between the cluster and the lepton must be $\Delta R_{\text{cluster}} > 0.15$.

5.2.6 Mass Window

Finally, for the cross section analysis, there is a mass window cut on the $m_{4\ell}$ of the quadruplet (taking into account the FSR recovery). Since we have knowledge of the Higgs Boson mass, and none of the backgrounds have a resonance close to the Higgs mass, this is a powerful cut to maximize our significance. We only keep events between $115 < m_{4\ell} < 130$ GeV.

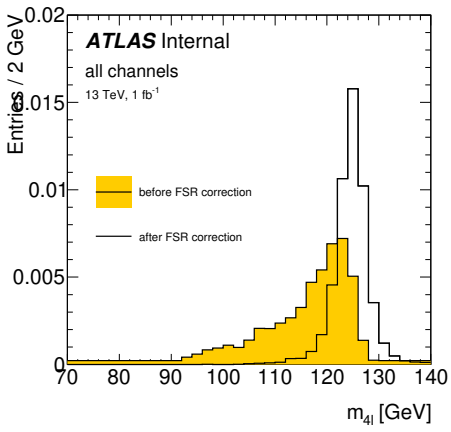

Figure 52: $m_{4\ell}$ before FSR recovery and $m_{4\ell}$ after FSR recovery. Only events with an identified FSR are shown in this plot.

If after all of these cuts, multiple channels still have a quadruplet, one channel is chosen from the follow order: 4μ, then $2e2\mu$, then $2\mu2e$, then finally $4e$. This is because muons usually have better resolution than electrons. Some events that pass all of these cuts will still come from background events, and predicting the rate of those background events is explained in Chapter 6. All quadruplets that pass the signal selection (after background subtraction) will be used in the cross section extraction as described in Chapter 9.

5.3 Truth Fiducial Selection

As explained in Section 5.1, the fiducial selection is the event selection on simulated truth events to go from the total phase space of $H \to ZZ^* \to 4\ell$ decays to the phase space that can be confidently measured by the ATLAS detector. The fiducial selection is meant to mirror the reco selection closely since the fiducial selection establishes the model that the results from the reco selection will be compared to. The selection is also meant to be generator independent, so that multiple generators and matrix element calculators can be used to produce different predictions. Since the selection is applied to truth events, we can use the known kinematics of the particles generated from Monte Carlo simulations in our cutflow. How to handle FSR recovery in the fiducial selection is explained in Section 5.3.2 and is known as "dressing" the leptons.

5.3.1 Lepton Selection

Each event in truth simulations has a collection of final state particles identified by their Particle Data Group Identification (PDGID) and whose history is stored in the High Energy Monte Carlo (HepMC) record. The truth p_{T}, η, ϕ, and mass of each particle is stored in the record as well.

Electrons. We select final state dressed electrons that have $p_{\mathrm{T}} > 7\,\mathrm{GeV}$ and $|\eta| < 2.47$. We require that their decay history include either a W or Z boson.

Muons. We select final state dressed muons that have $p_{\mathrm{T}} > 5\,\mathrm{GeV}$ and $|\eta| < 2.7$. We require that their decay history include either a W or Z boson.

5.3.2 Dressed leptons definition

Truth lepton definitions can be divided into three categories based on how QED radiation effects are handled: Bare, Born, and Dressed. Bare leptons are the stable, final state leptons after QED Final State Radiation (FSR). Born leptons are leptons before QED FSR, and are intermediate particles that often neglect interference effects between initial and final state QED radiation, and their behavior is often generator dependent. Dressed leptons attempt to define truth leptons before QED FSR in a generator independent way by mimicking partial QED FSR recovery. Beginning with final state leptons in the simulated sample, dressed leptons are defined by adding the four vectors from all final state photons in a ΔR cone around the lepton to the lepton. In the cross section analysis, we use dressed lepton to describe the truth lepton kinematics. The photons for clustering are selected by the following criteria:

- Final state (status 1) photons.
- They do not come from hadrons.
- Located $\Delta R < 0.1$ away from a bare lepton that itself comes from a W/Z Boson in the event.

Selected photons have their four-momentum added to the bare lepton and then removed from the truth list so they are not accidently added to any other lepton. In the case there is more than one bare lepton within $\Delta R < 0.1$ of a photon, the photon is assigned to the lepton with the smallest ΔR from the photon.

5.3.3 Jet Selection

To make our jets, we begin with the set of all final state particles in the event excluding electrons, muons, and neutrinos from W or Z decays. We also exclude photons within $\Delta R < 1.0$ around a lepton from a W or Z decay, as they are considered our dressing photons. These final state particles are clustered into jets using `FastJet` [124] anti-k_T algorithm with a distance parameter of $R = 0.4$ [123]. These jets are then required to have $p_{\mathrm{T}} > 30\,\mathrm{GeV}$ and $|y| < 4.4$. Jets within $\Delta R < 0.2$ of an electron or $\Delta R < 0.1$ of a muon are removed as well. Finally, jets are tagged as b-jets by using the `MV2_c10` algorithm [133] at its 70% efficiency point.

5.3.4 Quadruplet Formation

Once we have our set of electrons and muons, we apply what's essentially the reco selection to the truth leptons. We once again form all possible quadruplets out of the same-flavor, opposite sign pairs and pass these quadruplets through our kinematic cutflow:

- The three leading leptons in the quadruplet must pass the p_{T} thresholds $20, 15$ and $10\,\mathrm{GeV}$ respectively.
- The leading pair (i.e. the on-shell Z boson) is chosen to be the lepton pair with invariant mass closest to the PDG Z mass.
- The leading pair invariant mass must be $50 < m_{12} < 106\,\mathrm{GeV}$.
- The subleading pair invariant mass must be $12 < m_{34} < 115\,\mathrm{GeV}$.
- $m_{\ell,\ell'} > 5\,\mathrm{GeV}$ is applied for all same flavor lepton pairs in order to reject J/ψ particles.
- A mass window cut of $115 < m_{4\ell} < 130\,\mathrm{GeV}$ is applied to the quadruplet.

At the end of these quadruplet cuts, there may be multiple quadruplets that all pass. Within a channel (i.e. 4μ,$2e2\mu$,$2\mu2e$, or $4e$) we select the best quadruplet to be the one with the leading pair mass closest the Z mass. If the quadruplets have the same leading pair mass, then the subleading pair closest to the Z mass is used to decide the quadruplet. No isolation cuts are implemented since background rejection is not necessary in this truth analysis.

5.3.5 Study: Truth lepton definition comparisons

Comparing the variable distributions between the born and dressed lepton definitions, we see a skew towards lower 4ℓ mass and momentum in the distributions using dressed leptons. This is because the dressed leptons algorithm may not recover all the photons that were associated with the born lepton. This is similar to how FSR recovery may not recover everything in the reco selection. This decreases the momentum of the dressed leptons on average. This can be seen in the distributions in Figure 53.

Comparing the number of events that pass the fiducial cuts when using born versus dressed leptons, we see a decrease of around 5% from born to dressed.

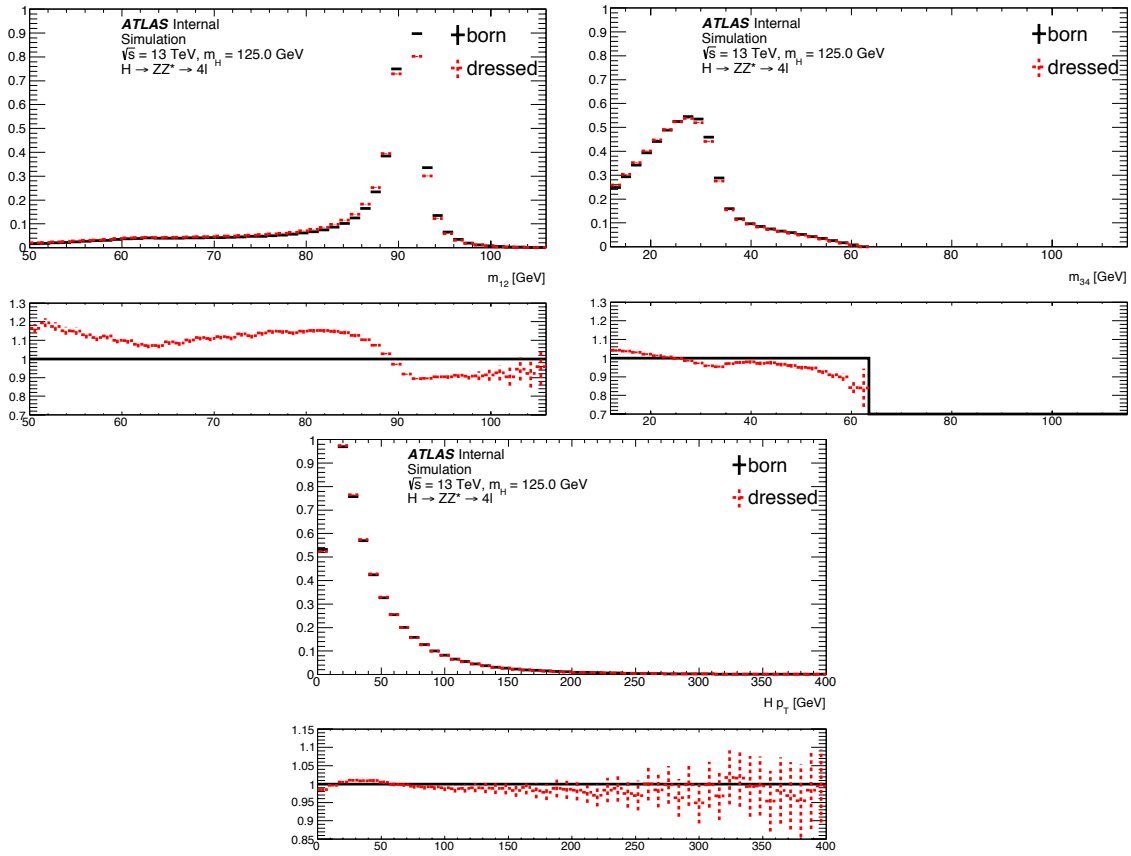

Figure 53: Born lepton (black) vs. dressed lepton (red) distributions of the leading lepton pair invariant mass m_{12} (top left), subleading lepton pair invariant mass m_{34} (top right), and four lepton transverse momentum $p_T^{4\ell}$ (bottom). Distributions were drawn using a ggF $m_H = 125\,\text{GeV}$ MC sample to compare the inclusive distributions (before any fiducial cuts) of three variables.

The 5% difference between the fiducial events of born and dressed leptons is caused by both the $m_{4\ell}$ mass window cut and the p_T from far-FSR photons that are not recovered by the dressing algorithm. The effect of the $m_{4\ell}$ window cut is seen in how the born lepton $m_{4\ell}$ distribution is peaked around 125 GeV for all events, while the dressed distribution has a tail at low $m_{4\ell}$ due to losing lepton momentum from FSR radiation.

Even removing the $m_{4\ell}$ cut does not remove all the differences between born and dressed leptons. There is still a 2.5% difference between the two definitions, as seen in (b) in Table 51. The large difference is probably caused by far-FSR not falling into the $\Delta R = 0.1$ cone around the lepton. To demonstrate this, the effect on enlarging the ΔR is shown in (a) in Table 51. As we make the cone bigger, the dressed number of events gets closer and closer to born, since more and more far-FSR is now falling into the cone. The $\Delta R = 0.1$ is chosen to remain close to the way FSR recovery is done in the reco analysis.

Change in Fiducial Events [%]	
ΔR cut	Born to Dressed
0.1	-5.38
0.2	-3.94
0.3	-3.36
0.5	-2.64
0.7	-2.28
1.0	-1.48
2.0	-0.94

Change in Fiducial Events [%]	
Fiducial Cuts	Born to Dressed
All fid cuts	-5.38
No m_{4l} cut	-2.46
Only lepton fid cuts	-1.50

Table 51: The percent difference of born to dressed fiducial events on a $m_H = 125$ GeV ggF sample using different definitions of the dressing. (a) changes the values for the ΔR cut in the lepton dressing algorithm. (b) compares the effect of the fiducial cuts, and the m_{4l} mass window cut in particular, on the change in events, using the $\Delta R < 0.1$ photon cut for all rows.

5.4 Variable Definitions

The $H \to ZZ^* \to 4\ell$ decay channel is useful not only for its high sensitivity to the Higgs signal, but also for the fact that the reconstructed events contain the full kinematic information of the Higgs since all four leptons can be measured. The fully reconstructed Higgs four-vectors can be used to calculate the differential cross section of the Higgs as a function of any variable of interest. Variables like the scattering angles are sensitive to properties like the Higgs spin, while a variable like the transverse momentum can be sensitive to various Beyond-the-Standard-Model properties of the Higgs, such as new particles that could be produced in association with the Higgs, or deviations in

Higgs production cross section due to new couplings or symmetries in the Higgs Lagrangian. The following sections describe the Higgs variables measured by the analysis and what their measurements could tell us about the Higgs boson and the Standard Model.

5.4.1 Higgs Invariant Mass

The Higgs resonance at $125.09 \pm 0.24\,\text{GeV}$ is a definite peak in the $m_{4\ell}$ spectrum, and is the most powerful variable for separating signal from background. A fit to the mass peak can be used to extract the signal events in the analysis. The number of signal events will be proportional to the inclusive cross section of the Higgs Boson. In the ggF production mode, the Higgs does not couple directly to gluons, but is produced through a loop of quarks at tree level. A Beyond-the-Standard-Model QCD particle that has mass could couple to the Higgs and would be present in this loop, thus increasing the inclusive cross section. The inclusive cross section would also increase if the Higgs were produced in association with a new particle. Once we have extracted the events that we consider to be Higgs Bosons with this $m_{4\ell}$ variable, we can also begin to study the properties of those events and measure the differential cross sections of the Higgs.

5.4.2 Kinematic Variables

To specify the four vector of the Higgs boson, we can use the invariant mass $m_{4\ell}$, the transverse momentum p_T^H, the azimuthal angle ϕ_H, and the rapidity $|y^H|$. The decay to four leptons is described by the invariant mass of the leading lepton pair m_{12}, the invariant mass of the sub-leading lepton pair m_{34}, and five decay angles (ϕ_H, ϕ_1, θ^*, θ_1, θ_2) between the leptons as shown in Fig. 54. The Z boson masses and decay angles are sensitive to the spin and CP properties of the Higgs boson.

Transverse Momentum, p_T^H. This is momentum of the Higgs transverse to the beampipe. At leading order, ggF has 0 transverse momentum, so any observed transverse momentum in ggF is due to higher order Feynman diagrams. Cross section derivations for ggF also often treat the top mass as infinite within an effective field theory, creating an effective coupling directly between gluons and the Higgs. The real finite masses of the top and bottom quark can affect the p_T of the Higgs in data to deviate away from this assumption. The tail of the p_T^H spectrum can also be changed by new particles produced in association with the Higgs.

Rapidity, $|y^H|$. Since the partons in the protons collide with different momentum fractions, x, the entire system may be boosted either forward or backwards down the beampipe. If partons collide with equal x and create a Higgs with no other associated particle, it will have $y = 0$, while a

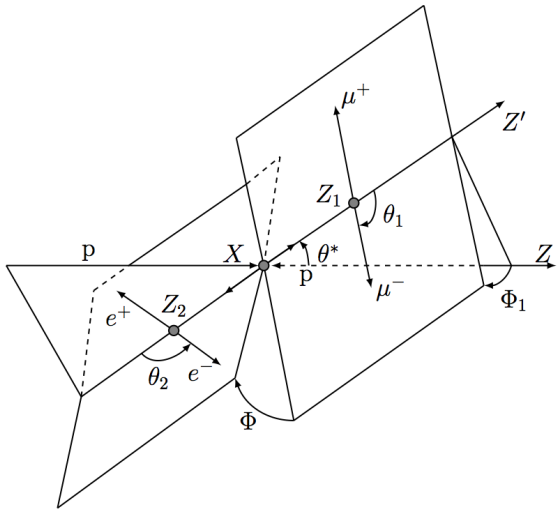

Figure 54: Diagram of decay angles for the $H \to ZZ^* \to 4\ell$ decay.

very boosted system where there is a large difference in momentum fraction will create a Higgs with large y. y is essentially a measure of the relativistic angle between the x-y plane and the direction of the emitted Higgs boson[14]. The rapidity of the Higgs can be used as a constraint for gluon Parton Distribution Functions[15] (again in the ggF production mode) at high x.

Helicity Angle, $|\cos\theta^*|$. Refer to Figure 54. The helicity angle is defined as the production angle of the on-shell Z defined in the four lepton rest frame. It is sensitive to the spin and parity of the Higgs boson. In the case of a spin zero boson, the cross section does not depend on $|\cos\theta^*|$ since the Higgs has no spin axis to define the angle on.

Mass of leading lepton pair, m_{12}. The leading lepton pair invariant mass should reconstruct to an on-shell Z boson with a peak around 91 GeV. Enhancements in number of events in m_{12} distributions could be sensitive to modified couplings in the HZZ vertex, which could be visible in VBF and VH production modes besides just the Higgs decay to ZZ^*.

Mass of sub-leading lepton pair, m_{34}. The sub-leading lepton pair reconstructs to the off-shell Z boson in the Higgs decay. It may also be sensitive to any models that contain a light exotic gauge boson (Z-dark bosons). Like m_{12}, the number of events in m_{34} distributions could be sensitive to modified couplings in the HZZ vertex.

Leading lepton pair mass vs. Sub-leading lepton pair mass, m_{12}vs.m_{34}. A 2D variable that captures the correlations between the leading and subleading lepton pair invariant mass. In

[14]See Section on ATLAS coordinate system, Section 3.3.1
[15]See Section on Parton Functions, Section 2.3.1

a BSM Effective Field Theory framework with extra contact couplings between the Higgs and the final lepton pairs that modifies the HZZ vertex, m_{12}vs.m_{34} would be more sensitive than m_{12} or m_{34} on their own since the contact term affects both distributions.

5.4.3 Jet variables

A Higgs with measurable p_{T} is often produced with an associated jet in the event. These jets can provide information about the production mode of the Higgs, or if the jet is an ISR/FSR jet, about QCD interactions. Besides the SM effects, dimension-6 operators in a Higgs EFT Lagrangian will have the effect of increasing the momentum transfer through the VVH vertex. This momentum transfer is not directly observable, but the transverse momenta of the jets and the Higgs boson are strongly correlated with it. Observables like $p_T^{\text{lead. jet}}$ could be sensitive to such effects in the tail of their distribution. The rapidity and azimuthal difference between two jets in an event also could be sensitive to modifications of the vertex, especially in VBF.

Jet multiplicity, N_{jets}. The number of jets in an event is sensitive to the production mode. For example, ggF events at lowest order produce no associated jets, while VBF events at lowest order always are associated with two jets. See Figure 55 for a plot of production mode fractions in N_{jets}.

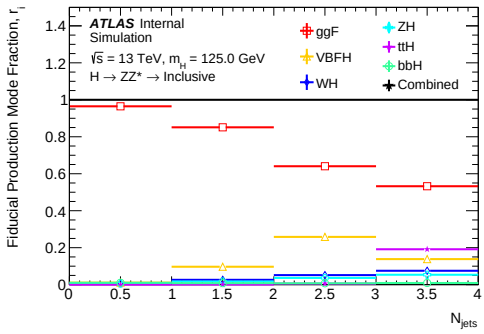

Figure 55: Proportion of production modes for N_{jets}. A SM Higgs with $m_H = 125.0\,\text{GeV}$ has been assumed.

Transverse momentum of the leading jet, $p_T^{\text{lead. jet}}$. Transverse momentum of the leading jet is a probe of QCD by being sensitive to the partonic radiation in higher order ggF. Is possibly sensitive to changes in the VVH vertex in the VBF and ZH/WH production modes due to modified couplings.

Dijet invariant mass, m_{jj}. Simply the invariant mass of the two four-vectors of the associated jets. Sensitive to new resonances that decay to jets produced in association with a Higgs boson.

Dijet separation in pseudorapidity, $\Delta\eta_{jj}$, and separation in azimuthal angle, $\Delta\phi_{jj}$. Sensitive to changes in the VVH coupling in the VBF production mode.

5.5 Optimized Binning

We now have our method of selecting Higgs boson candidates and have decided what differential observables to measure. Next we want to guarantee that we will be sensitive to measuring our Higgs events in the presence of background. The reco selection has been optimized for maximum significance, given by $Z = \frac{s}{\sqrt{s+b}}$, and reaches an expected $Z = 6$ for the inclusive analysis. Though the test statistic is Poisson and not Gaussian, we translate the expected sensitivity into the language of "sigma" (or Z-score) of a unit Gaussian. This translation is purely conventional, and doesn't imply that the underlying distribution is Gaussian.

For a differential analysis, the events must be binned, and each bin will have a small fraction of the total statistics. For the 4ℓ differential variables, we must balance fine binning (which gives shape information about the variable) with the available statistics expected in each bin. Using the expected signal and background yields from the truth reco selection at $\mathcal{L}_{\text{int}} = 36.1\text{fb}^{-1}$, the binning was chosen to allow a significant measurement at the 2σ level, i.e. in each bin $Z \geq 2$. When measuring significance, it is always measured given the assumption that a certain model is true. In our case, our assumed hypothesis is the signal+background hypothesis ($s_H + b$), since we have discovered the Higgs and are confident it exists. We choose our binning such that the probability of getting only background events in that bin is low, i.e. the probability of measuring only background events in this bin should be below 5%.

In the limit of a large number of events, due to the central limit theorem, we can assume that expected number of events in each bin follows a Gaussian probability distribution, where the mean is $\mu = s + b$ and the variance is also $\sigma^2 = s + b$. Significance for getting n events from a Gaussian is

$$Z = \frac{|\mu - n|}{\sigma} = \frac{|s + b - n|}{\sqrt{s + b}} \tag{5.1}$$

The sigma of getting only background events i.e. $n = b$, assuming the $s + b$ hypothesis is true, is then

$$Z = \frac{s + b - b}{\sqrt{s + b}} = \frac{s}{\sqrt{s + b}} \tag{5.2}$$

If the bin has a small number of events, sometimes the Gaussian approximation is not entirely justified. In that case, one can use the original Poisson distribution combined with a log-likelihood

test to determine the significance. The likelihood function of a Poisson distributed variable (as a function of the s number of signal events) is

$$L(s) = \frac{(s+b)^n}{n!} e^{-(s+b)} \tag{5.3}$$

And the test statistic, q_s, for the log-likelihood test is defined as

$$q_s = -2 \ln \frac{L(s)}{L(\hat{s})} = -2 \ln \frac{L(s)}{L(n-b)} \tag{5.4}$$

Where $\hat{s}$ is the best fit value of s given the data. If n is the measured number of events and b is the background known without error, then $\hat{s} = n - b$. Using Wilk's theorem [136] which says we can approximate the probability distribution of q_s as a χ^2 with one degree of freedom, we can then say that $\sqrt{q_s}$ will be the significance of a measurement n under the assumption of a model s.

So

$$q_s = -2 \ln \frac{\frac{(s+b)^n}{n!} e^{-(s+b)}}{\frac{(n)^n}{n!} e^{-(n)}} = -2 \left[n \ln(s+b) - s - b - n \ln n + n \right] \tag{5.5}$$

$$q_s = -2 \left[n \ln \left(\frac{s+b}{n} \right) - s - b + n \right] \tag{5.6}$$

$$\sqrt{q_s} = Z_s = \sqrt{2 \left[n \ln \left(\frac{n}{s+b} \right) + s + b - n \right]} \tag{5.7}$$

So when we were first discovering the Higgs Boson, we used the "discovery" significance, where we used a model that assumes $s = 0$

$$\text{"Discovery", assuming } s = 0, \qquad Z_0(n) = \sqrt{2 \left[n \ln \left(\frac{n}{b} \right) + b - n \right]} \tag{5.8}$$

So the expected significance of actually measuring a signal $n = s + b$ assuming a $s = 0$ model would be equal to

$$Z_0^{\text{exp}}(s+b) = \sqrt{2 \left[(s+b) \ln \left(1 + \frac{s}{b} \right) - s \right]} \tag{5.9}$$

On the other hand, now that we know the Higgs Boson exists, we should not be assuming an $s = 0$ hypothesis but an $s = s_H$ hypothesis. So now our significance is equal to

$$\text{"Measurement", assuming } s = s_H, \qquad Z_{s_H}(n) = \sqrt{2 \left[n \ln \left(\frac{n}{s_H + b} \right) + s_H + b - n \right]} \tag{5.10}$$

So the expected significance of measuring only background in a bin $n = b$ would be equal to

$$Z_{s_H}^{\exp}(b) = \sqrt{2\left[s_H - b\ln\left(1 + \frac{s_H}{b}\right)\right]} \tag{5.11}$$

When optimizing the binning, we used the Gaussian approximation of $Z = s/\sqrt{s+b}$, and cross-checked the significance with $Z = \sqrt{2\left[s - b\ln\left(1+\frac{s}{b}\right)\right]}$. In order to reduce the bias from using the bin-by-bin correction factors, another consideration in the binning choice was the extent to which events migrated between bins during reconstruction. More information of bin migration and bin purity is in Section 7.4. Table 52 show the final bin limits for each of the variables, and Figures 57 through 517 show expected signal and background events for each bin and their significance.

Variable	Bin Edges	N_{bins}
p_T	0, 10, 15, 20, 30, 45, 60, 80, 120, 200, 350 GeV	10
$\|y\|$	0, 0.3, 0.6, 0.9, 1.2, 1.6, 2, 2.5	7
$\|cos(\theta^*)\|$	0, 0.125, 0.25, 0.375, 0.5, 0.625, 0.75, 0.875, 1.0	8
m_{12}	50, 65, 74, 82, 88, 94, 106 GeV	6
m_{34}	12, 20, 24, 28, 32, 40, 55, 65 GeV	7
m_{12}vs.m_{34}	See Figure 56	5
N_{jets}	0, 1, 2, $\geq$3	4
$p_T^{\text{lead. jet}}$	30, 40, 55, 75, 120, 350 GeV	5
m_{jj}	0, 120, 3000 GeV	2
$\Delta\eta_{jj}$	0, 2, 10	2
$\Delta\phi_{jj}$	0, π, 2π	2

Table 52: Binning chosen for Higgs kinematic variables Jet variables of interest.

Figure 56: m_{12} versus m_{34} distribution and bin edges illustration.

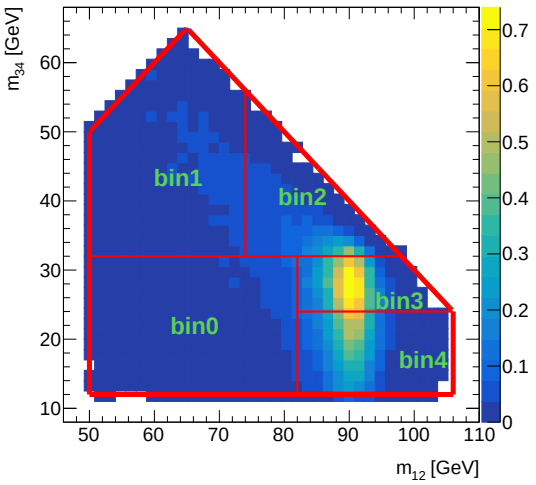

Bin	m_{12} and m_{34} values [GeV]
0	$m_{12} < 82$ and $m_{34} < 32$
1	$m_{12} < 74$ and $m_{34} > 32$
2	$m_{12} > 74$ and $m_{34} > 32$
3	$m_{12} > 82$ and $24 < m_{34} < 32$
4	$m_{12} > 82$ and $m_{34} < 24$

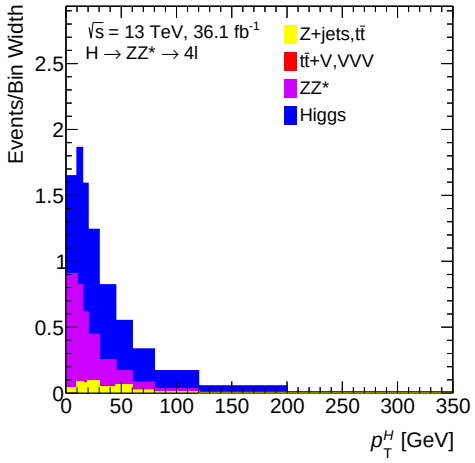

Bins	Higgs	Z+jets,$t\bar{t}$	$t\bar{t}+V$,VVV	ZZ^*	$\frac{S}{B}$	$\frac{S}{\sqrt{S+B}}$	Z_S
0	7.42	0.38	0.01	8.68	0.82	1.83	2.00
1	5.22	0.43	0.00	3.66	1.27	1.71	1.93
2	4.89	0.37	0.00	2.69	1.60	1.73	1.98
3	7.98	0.93	0.02	3.49	1.80	2.26	2.61
4	8.55	0.73	0.12	2.92	2.27	2.44	2.86
5	5.74	0.92	0.03	1.58	2.28	2.00	2.34
6	5.08	0.41	0.12	1.08	3.14	1.96	2.36
7	5.56	0.30	0.12	0.79	4.55	2.14	2.63
8	3.98	0.03	0.06	0.28	10.65	1.91	2.47
9	1.33	0.00	0.01	0.04	23.40	1.13	1.52

Figure 57: Expected signal and background events at 36.1fb^{-1} for $p_T^{4\ell}$. For each bin, S/B and expected significance values are listed.

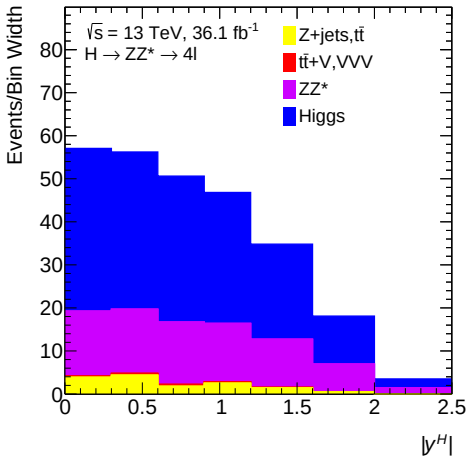

Bins	Higgs	Z+jets,$t\bar{t}$	$t\bar{t}+V$,VVV	ZZ^*	$\frac{S}{B}$	$\frac{S}{\sqrt{S+B}}$	Z_S
0	11.34	1.16	0.09	4.52	1.96	2.74	3.18
1	10.96	1.31	0.13	4.47	1.85	2.67	3.08
2	10.17	0.54	0.13	4.35	2.03	2.61	3.04
3	9.13	0.75	0.10	4.07	1.86	2.44	2.82
4	8.83	0.56	0.06	4.47	1.74	2.37	2.72
5	4.45	0.18	0.01	2.59	1.60	1.66	1.89
6	1.02	0.01	0.00	0.72	1.40	0.77	0.88

Figure 58: Expected signal and background events at 36.1fb^{-1} for $|y^{4\ell}|$. For each bin, S/B and expected significance values are listed.

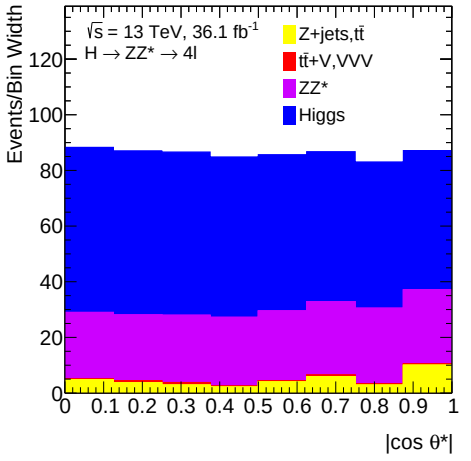

Bins	Higgs	Z+jets,$t\bar{t}$	$t\bar{t}+V$,VVV	ZZ^*	$\frac{S}{B}$	$\frac{S}{\sqrt{S+B}}$	Z_S
0	7.42	0.60	0.03	2.99	2.05	2.23	2.60
1	7.37	0.46	0.08	2.96	2.10	2.24	2.61
2	7.33	0.36	0.11	3.02	2.10	2.23	2.60
3	7.21	0.27	0.04	3.09	2.12	2.21	2.58
4	7.02	0.50	0.06	3.13	1.90	2.15	2.49
5	6.74	0.73	0.07	3.29	1.64	2.05	2.35
6	6.57	0.35	0.06	3.39	1.73	2.04	2.35
7	6.25	1.25	0.06	3.33	1.35	1.90	2.14

Figure 59: Expected signal and background events at 36.1fb^{-1} for $|\cos\theta^*|$. For each bin, S/B and expected significance values are listed.

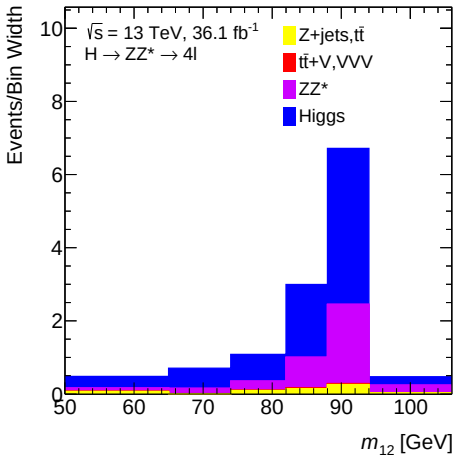

Bins	Higgs	Z+jets,$t\bar{t}$	$t\bar{t}+V$,VVV	ZZ^*	$\frac{S}{B}$	$\frac{S}{\sqrt{S+B}}$	Z_S
0	4.77	1.00	0.09	1.34	1.96	1.78	2.06
1	4.96	0.06	0.04	1.29	3.59	1.97	2.39
2	5.86	0.74	0.06	2.00	2.09	1.99	2.32
3	11.95	0.86	0.12	5.03	1.98	2.82	3.28
4	25.59	1.54	0.17	13.00	1.74	4.03	4.64
5	2.78	0.30	0.04	2.54	0.96	1.17	1.29

Figure 510: Expected signal and background events at 36.1fb^{-1} for m_{12}. For each bin, S/B and expected significance values are listed.

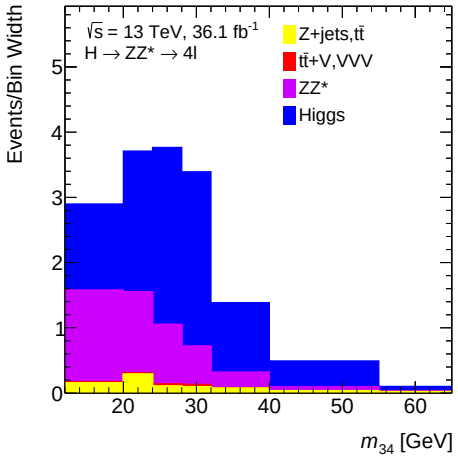

Bins	Higgs	Z+jets,$t\bar{t}$	$t\bar{t}+V$,VVV	ZZ^*	$\frac{S}{B}$	$\frac{S}{\sqrt{S+B}}$	Z_S
0	10.58	1.24	0.12	11.25	0.84	2.20	2.41
1	8.62	1.16	0.06	5.00	1.39	2.24	2.54
2	10.85	0.42	0.12	3.67	2.58	2.80	3.31
3	10.69	0.39	0.13	2.35	3.72	2.90	3.53
4	8.55	0.59	0.05	1.90	3.37	2.57	3.10
5	5.91	0.49	0.04	0.94	4.02	2.18	2.66
6	0.70	0.22	0.00	0.10	2.19	0.69	0.81

Figure 511: Expected signal and background events at 36.1fb^{-1} for m_{34}. For each bin, S/B and expected significance values are listed.

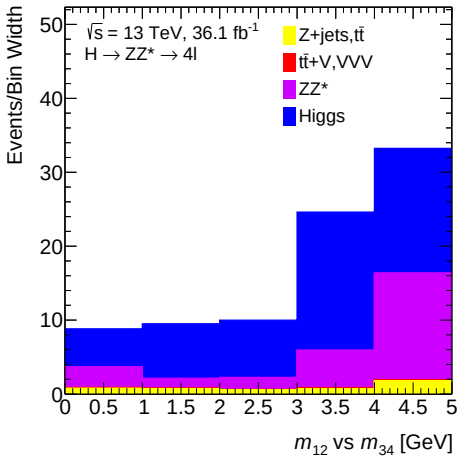

Bins	Higgs	Z+jets,$t\bar{t}$	$t\bar{t}+V$,VVV	ZZ^*	$\frac{S}{B}$	$\frac{S}{\sqrt{S+B}}$	Z_S
0	5.15	0.75	0.12	2.79	1.41	1.74	1.97
1	7.40	0.72	0.05	1.32	3.52	2.40	2.91
2	7.76	0.57	0.03	1.62	3.49	2.46	2.97
3	18.71	0.69	0.16	5.05	3.17	3.77	4.53
4	16.89	1.78	0.14	14.42	1.03	2.93	3.25

Figure 512: Expected signal and background events at 36.1fb^{-1} for m_{12}vs.m_{34}. For each bin, S/B and expected significance values are listed.

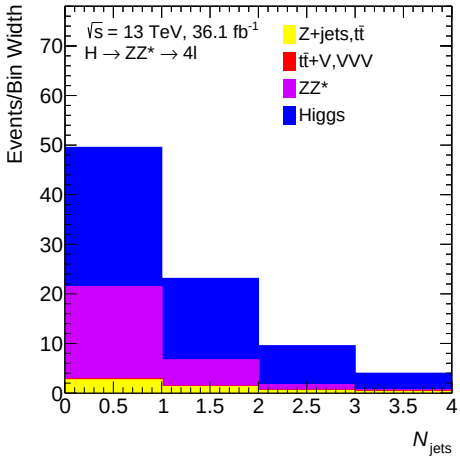

Bins	Higgs	Z+jets,$t\bar{t}$	$t\bar{t}+V$,VVV	ZZ^*	$\frac{S}{B}$	$\frac{S}{\sqrt{S+B}}$	Z_S
0	28.15	2.59	0.19	18.60	1.32	4.00	4.51
1	16.47	1.25	0.08	5.29	2.49	3.43	4.05
2	7.91	0.43	0.11	1.08	4.89	2.56	3.18
3	3.37	0.23	0.14	0.24	5.58	1.69	2.11

Figure 513: Expected signal and background events at 36.1fb^{-1} for N_{jets}. For each bin, S/B and expected significance values are listed.

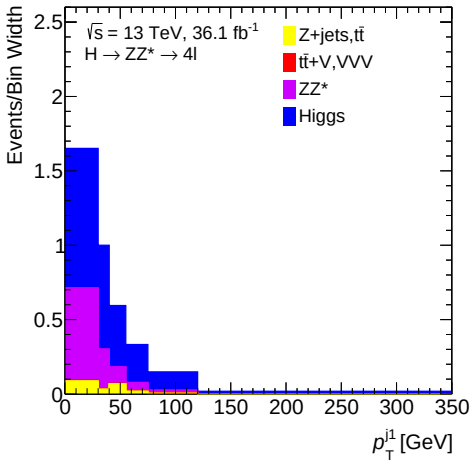

Bins	Higgs	Z+jets,$t\bar{t}$	$t\bar{t}+V$,VVV	ZZ^*	$\frac{S}{B}$	$\frac{S}{\sqrt{S+B}}$	Z_S
0	28.15	2.59	0.19	18.60	1.32	4.00	4.51
1	6.99	0.31	0.02	2.68	2.32	2.21	2.60
2	6.19	1.01	0.05	1.67	2.27	2.07	2.43
3	5.11	0.35	0.06	1.13	3.33	1.98	2.39
4	5.56	0.17	0.10	0.86	4.92	2.15	2.66
5	3.79	0.07	0.09	0.27	8.88	1.85	2.37

Figure 514: Expected signal and background events at 36.1fb^{-1} for $p_T^{\text{lead. jet}}$. For each bin, S/B and expected significance values are listed.

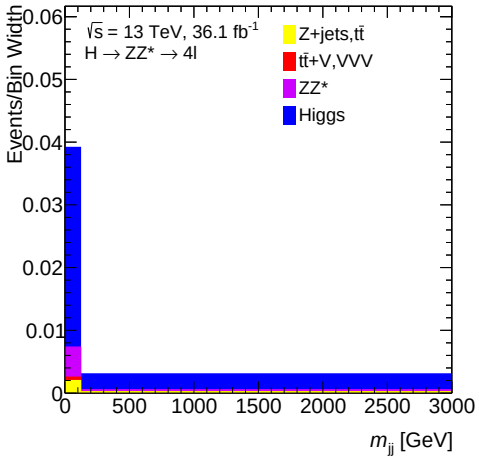

Bins	Higgs	Z+jets,$t\bar{t}$	$t\bar{t}+V$,VVV	ZZ^*	$\frac{S}{B}$	$\frac{S}{\sqrt{S+B}}$	Z_S
0	3.83	0.24	0.06	0.57	4.38	1.76	2.17
1	7.42	0.43	0.18	0.74	5.49	2.51	3.13

Figure 515: Expected signal and background events at 36.1fb^{-1} for m_{jj}. For each bin, S/B and expected significance values are listed.

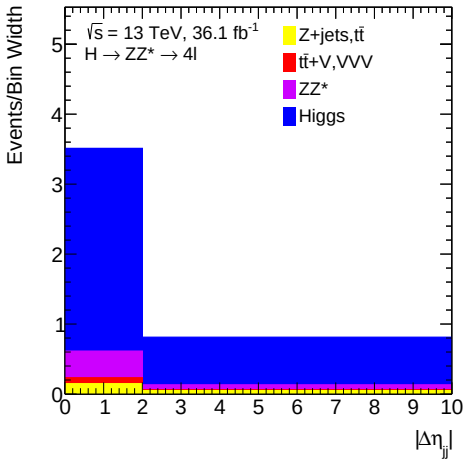

Bins	Higgs	Z+jets,$t\bar{t}$	$t\bar{t}+V$,VVV	ZZ^*	$\frac{S}{B}$	$\frac{S}{\sqrt{S+B}}$	Z_S
0	5.80	0.29	0.17	0.76	4.77	2.19	2.71
1	5.48	0.38	0.08	0.55	5.45	2.15	2.69

Figure 516: Expected signal and background events at 36.1fb^{-1} for $\Delta\eta_{jj}$. For each bin, S/B and expected significance values are listed.

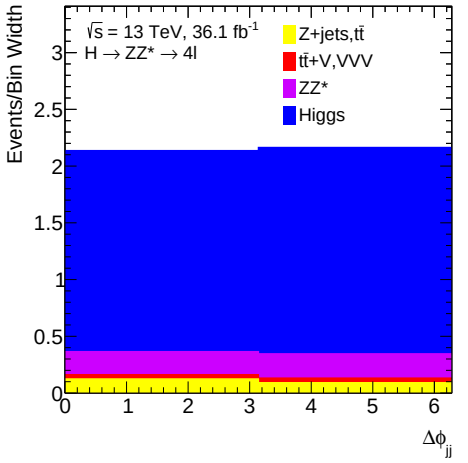

Bins	Higgs	Z+jets,$t\bar{t}$	$t\bar{t}+V$,VVV	ZZ^*	$\frac{S}{B}$	$\frac{S}{\sqrt{S+B}}$	Z_S
0	5.57	0.38	0.12	0.64	4.85	2.15	2.66
1	5.72	0.28	0.12	0.67	5.31	2.19	2.73

Figure 517: Expected signal and background events at 36.1fb^{-1} for $\Delta\phi_{jj}$. For each bin, S/B and expected significance values are listed.

Chapter 6

Backgrounds

Though the event selection described in Chapter 5 was optimized to find $H \to ZZ^* \to 4\ell$ events, it will select events that are not $H \to ZZ^* \to 4\ell$ around a third of the time. A cross section is a function of the signal events only, so the background events must be estimated and subtracted off the selected sample.

There are two types of backgrounds that can pass the event selection, called the reducible and irreducible background. The reducible background is made by fake leptons (e.g. light jets that get reconstructed as electrons), pair production from photons, and leptons from semi-leptonic decays of heavy jets. This background could possibly be reduced by better background rejection in the event selection, hence the name "reducible". The largest reducible background comes from $Z + \text{jets}$. The irreducible background is made from SM processes that also decay to four isolated leptons and look exactly like the $H \to 4\ell$ final state, apart from the resonance. The largest irreducible background is the SM $q\bar{q} \to ZZ^* \to 4\ell$ channel.

The following sections describe how the backgrounds are modeled and constrained through both Monte Carlo and data driven methods.

6.1 Irreducible Background

The biggest irreducible background is the Standard Model $q\bar{q} \to ZZ^* \to 4\ell$ process, making up about 80% of all the background events in the analysis. The next biggest irreducible process is $gg \to ZZ^* \to 4\ell$, at less than 4% of $q\bar{q}ZZ$. Both production channels produce four well-isolated leptons of good quality. Finally, triboson and $t\bar{t} + V$ events will produce four real leptons, though they are rarely produced, at less than 1 event expected in 36fb^{-1} of data all together. Table 61

shows the expected number of events that will pass the reco selection with 36.1fb^{-1} of data. Figure 62 shows the Feynman diagrams for the relevant irreducible backgrounds. The box diagram for $ggZZ$ interferes with the ggF diagram and so technically can't be separated from the Higgs signal, but the interference accounts for a less than 1% difference of events within the $m_{4\ell}$ mass window [137], and so is ignored in the modeling.

Higgs	$q\bar{q}ZZ$	$ggZZ$	triboson and $t\bar{t}+V$
55.91	24.32	0.88	0.35

Figure 61: Expected Higgs and expected irreducible background events (obtained from MC) at 36.1fb^{-1}. $q\bar{q}ZZ$ contributes the most. Next is $ggZZ$ at less than 4% of $q\bar{q}ZZ$. Triboson (ZZW,WWZ,ZZZ) and $V+t\bar{t}$ all-leptonic all together are minor.

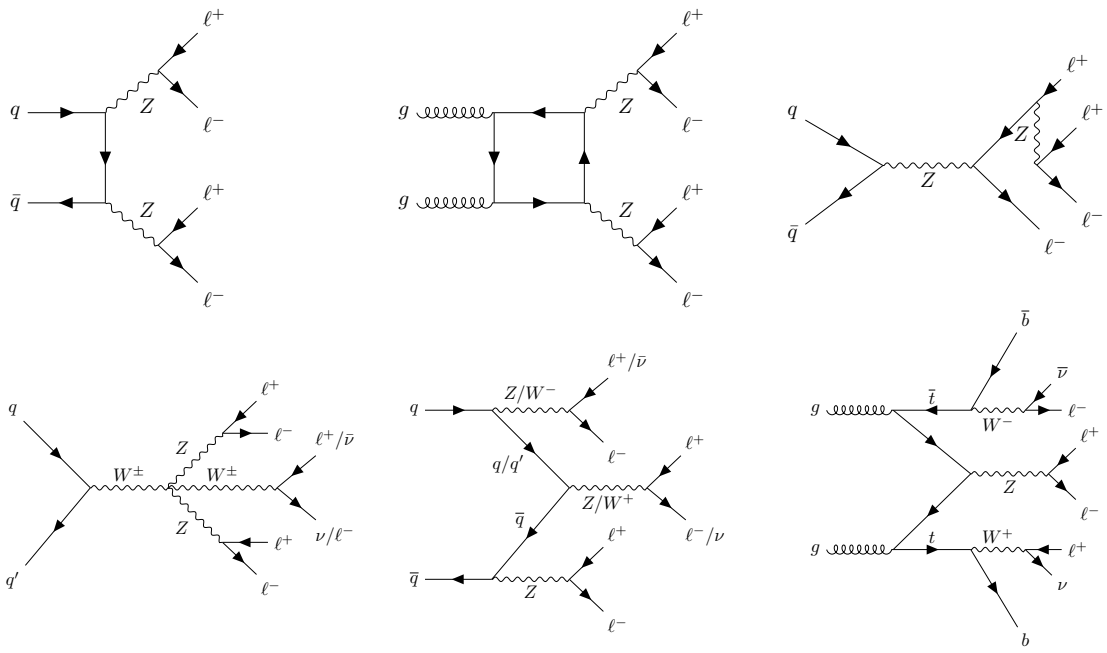

Figure 62: Irreducible background contributions to the 4ℓ signal selection. $q\bar{q}ZZ$ (top left) contributes the most. Next is $ggZZ$ (top middle) and single resonant $Z \to 4\ell$ (top right). Triboson (ZZW,WWZ,ZZZ) (bottom left and middle) and $V+t\bar{t}$ all-leptonic (bottom right) are minor irreducible backgrounds.

The normalization and modeling for these backgrounds is taken from the Monte Carlo theory prediction, described in Section 2.4.2. The simulations are verified with data by using control regions in which the Higgs mass window is inverted to be the region $m_{4\ell} < 115\,\text{GeV}$ and $130 < m_{4\ell} < 170\,\text{GeV}$. Figure 63 shows the comparison between data and Monte Carlo in these side bands,

demonstrating that the agreement is good.

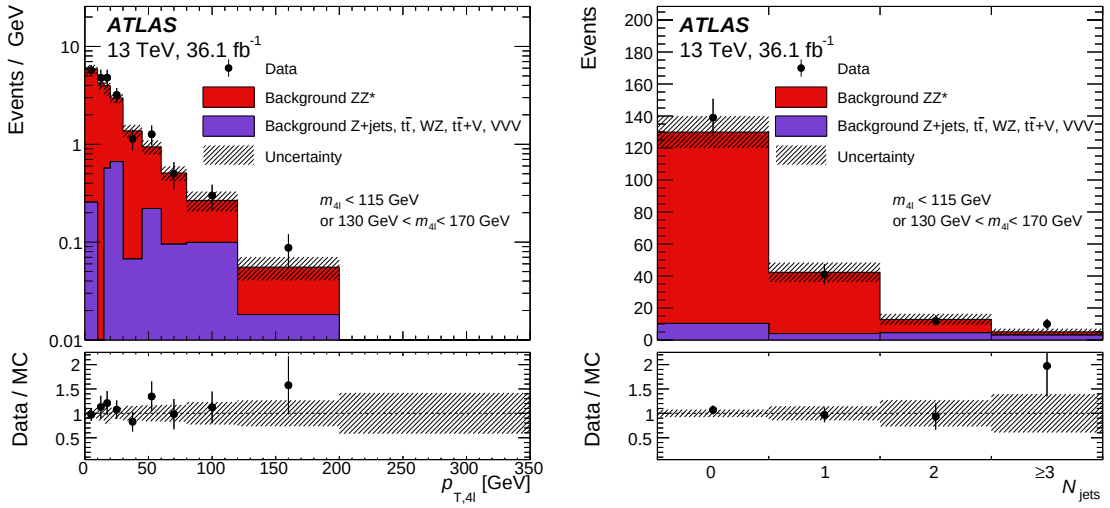

Figure 63: Reco data events compared to Monte Carlo truth reco events in an irreducible background control region. Defined by an event selection where the mass window cut is replaced by $m_{4\ell} < 115$ GeV or 130 GeV$< m_{4\ell} <$ 170 GeV.

6.2 Reducible Background

The reducible backgrounds contain at least one jet, photon, or a non-isolated lepton that is misidentified as a prompt lepton from the hard scatter. Z+jets, $t\bar{t}$ and WZ can all create candidates that might be mis-identified, as seen in Figure 65. Z+jet is the general term for $Z + bb$ and Z+light flavor together. Z+jets contributes the most reducible background events, though at a much lower rate than $q\bar{q}ZZ$, as seen in Table 64.

Higgs	Z+jets	$t\bar{t}$	WZ
55.91	4.60	0.35	0.16

Figure 64: Expected Higgs and expected reducible background events (gotten from MC) at 36.1fb^{-1}. Z+jets contributes the most. $t\bar{t}$ and WZ are minor.

The selection cuts are extremely good at cutting out the reducible backgrounds due to the low probability of jets faking two leptons at the same time. The low selection efficiency makes generating enough Monte Carlo events for background modeling difficult, so data driven methods are used instead. The data driven methods work by first defining control regions by either inverting or relaxing a cut of the standard event selection. These inverted/relaxed cuts have relatively high

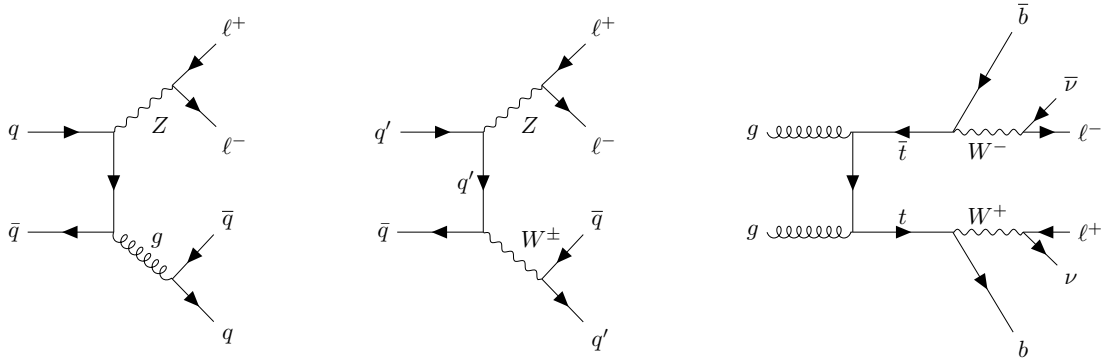

Figure 65: Reducible background contributions. Z+jets contributes the most, through both heavy and light quark jets. Others include WZ and $t\bar{t}$ (where the b-jets semileptonically decay).

efficiency for the backgrounds, allowing enough Monte Carlo events to pass for modeling. These models are fit to data, and then transfer or efficiency factors are calculated to extrapolate the number of data events found in the control region to the signal region.

Low p_{T} fake leptons come from different sources depending on whether they are an electron or muon, so different methods are used for the $\ell\ell\mu\mu$ and $\ell\ell ee$ backgrounds. Many $\ell\ell\mu\mu$ events come from heavy flavor hadron decays of $Z + bb$ and $t\bar{t}$ all-leptonic, where the jets have a b-jet that semileptonically decays to a muon. Z+light jets can also contribute through π/K decays. $\ell\ell ee$ events come mostly from light jets misreconstructed as electrons, though sometimes they come from photon conversions or heavy flavor hadron decay.

6.3 Reducible $\ell\ell + \mu\mu$ Background

As mentioned in Section 6.2, The $\ell\ell\mu\mu$ background consists mainly of three processes, $Z + bb$, Z+light jets, and $t\bar{t}$. To estimate the muon background, we define three control regions (CR) which are enhanced in each of these backgrounds. Each of these control regions is orthogonal to each other and to the signal region (SR), so an event found in one CR should not appear in any other region. The background estimation is done through a data-driven method, meaning that the number of reducible background events in the SR will be extrapolated from using data events found in the CRs, rather than using the number of expected Monte Carlo events in the SR.

6.3.1 $\ell\ell\mu\mu$ Control Regions

The three CRs enhanced in background events are defined as follows.

1. **Inverted d_0 CR (enhanced in heavy flavor ($Z+bb$ and $t\bar{t}$))** . Heavy flavor jets are known for having a displaced secondary vertex, so this control region is built to select for such events. The leading lepton pair cuts are applied as normal to select for an on-shell Z boson, but the vertex cut is not applied, and at least one subleading lepton is required to pass an inverted d_0 cut, specifically to find displaced leptons. Isolation cuts (meant to supress background) are also not applied. This control region enhances the $Z+bb$ and $t\bar{t}$ backgrounds which often have heavy flavor jets in their events.

2. **$e\mu$+$\mu\mu$ CR (enhanced in $t\bar{t}$)** . An event with a real Z boson will always produce an opposite sign, same flavor lepton pair. By requiring the leading lepton pair to be an opposite sign, opposite flavor pair, one can guarantee that the leading pair did not come from a Z boson. The vertex cut is not applied to the event, and all the background rejection cuts (d_0 and isolation) are not applied to the subleading lepton pair. This CR is predominantly made up of $t\bar{t}$ background.

3. **Inverted isolation CR (enhanced in Z+light)** . Non-isolated leptons often are surrounded by the jet they came from. By imposing the d_0 and vertex cuts but inverting the isolation cuts, one can eliminate many of the heavy flavor jets while leaving the light flavor ones. In this CR, the leading lepton pair cuts are applied as normal to select for an on-shell Z boson, and the vertex and d_0 cut are left in, but the isolation cut is inverted to specifically gather events with non-isolated leptons. This CR has contributions from all background, but should have an enhanced component of Z+light background.

There is an additional fourth CR known as the **Relaxed CR** which is not orthogonal to the three other CRs and the SR, but is replete with events in all backgrounds. In this CR, the the leading lepton pair cuts are applied as normal to select for an on-shell Z boson, but no background cuts are applied to the subleading lepton pair, i.e. the vertex, d_0, and isolation cuts are not applied. Fits in the previous three CR are used to extract the proportion of each background source in this Relaxed CR. Then, $N_{\text{data},i}^{\text{Relax CR}}$ (for each of the i backgrounds) is extrapolated to the signal region with a transfer factor. The following formula is used to calculate the number of background events in the SR:

$$N_{\text{data},i}^{\text{SR}} = \mathcal{F}_i \times N_{\text{data},i}^{\text{Relax CR}} \tag{6.1}$$

Where $i = Z + bb$, Z+light, or $t\bar{t}$, $\mathcal{F}_i$ is the transfer factor, and $N_{\text{data},i}^{\text{Relax CR}}$ is the number of data events for the i^{th} background in the Relaxed CR. The transfer factors are obtained from Monte Carlo by taking the ratio of the events from the SR and dividing by the events in the Relaxed CR.

$$\mathcal{F}_i = \frac{N_{\text{MC},i}^{\text{SR}}}{N_{\text{MC},i}^{\text{Relax CR}}} \tag{6.2}$$

Systematics on the transfer factors are obtained from data-Monte Carlo discrepancies. Table 61 gives the transfer factors for each of the backgrounds.

Type	Transfer factor
$Z + bb$	0.0075 ± 0.0009
$t\bar{t}$	0.0025 ± 0.0003
Z+light	0.030 ± 0.0040

Table 61: Transfer factor calculated from Monte Carlo simulations in SR and Relaxed CR. The shown errors on the transfer factors are statistical only. The systematics are on the transfer factors are shown in Section 8.2.

Getting $N_{\text{data},i}^{\text{Relax CR}}$ for each background is done through a two step process.

6.3.2 Step 1. Fit for $Z + bb$ and $t\bar{t}$

The first step is to do an unbinned maximum likelihood fit simultaneously on the inverted d_0 CR as well as the $e\mu$+$\mu\mu$ CR using the m_{12} variable to estimate $N_{\text{data},Z+bb}^{\text{Relax CR}}$ and $N_{\text{data},t\bar{t}}^{\text{Relax CR}}$. The m_{12} provides good separation between the backgrounds, as the $Z + bb$ will have a resonant Z boson peak while $t\bar{t}$ will be non-resonant. The $e\mu$+$\mu\mu$ CR should be entirely $t\bar{t}$, while the inverted d_0 CR should have a mix of both. Both regions will have a few events from ZZ^* and WZ, which will not be fit to, but constrained to the yields taken from Monte Carlo. Figure 66 shows the two control regions with the expected yields from Monte Carlo for all backgrounds, as well as the data. As you can see, the Monte Carlo does not model the data yields well.

To calculate $N_{\text{data},t\bar{t}}^{\text{Relax CR}}$ and $N_{\text{data},Z+bb}^{\text{Relax CR}}$ using the two orthogonal CRs, we use the following unbinned likelihood function and maximize it in the two CRs simultaneously:

$$L(N_{\text{data},t\bar{t}}^{\text{Relax CR}}, N_{\text{data},Z+bb}^{\text{Relax CR}} | m_{12}) = \prod_{i}^{\substack{\text{events in} \\ d_0\text{CR}}} \mathcal{F}_{d_0}(m_{12}^i) \prod_{j}^{\substack{\text{events in} \\ e\mu\mu\mu\text{CR}}} \mathcal{F}_{e\mu+\mu\mu}(m_{12}^j) \tag{6.3}$$

$$\mathcal{F}_{d_0}(m_{12}^i) = N_{\text{data},t\bar{t}}^{\text{Relax CR}} \cdot f_{t\bar{t}}^{d_0} \cdot \mathcal{M}_{t\bar{t}}(m_{12}^i) + N_{\text{data},Z+bb}^{\text{Relax CR}} \cdot f_{Z+bb}^{d_0} \cdot \mathcal{M}_{Z+bb}(m_{12}^i) + N_{ZZ+WZ}^{\text{MC}} \tag{6.4}$$

$$\mathcal{F}_{e\mu+\mu\mu}(m_{12}^j) = N_{\text{data},t\bar{t}}^{\text{Relax CR}} \cdot f_{t\bar{t}}^{e\mu} \cdot \mathcal{M}_{t\bar{t}}(m_{12}^j) + N_{\text{data},Z+bb}^{\text{Relax CR}} \cdot f_{Z+bb}^{e\mu} \cdot \mathcal{M}_{Z+bb}(m_{12}^j) + N_{ZZ+WZ}^{\text{MC}} \tag{6.5}$$

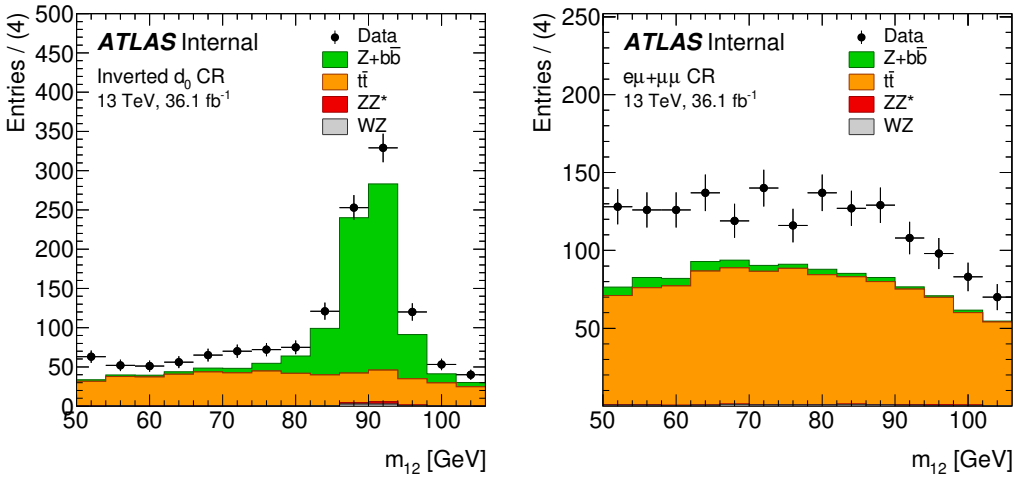

Figure 66: The m_{12} distributions for data and MC-simulated events in the inverted d_0 CR (left) and the $e\mu$+$\mu\mu$ CR (right).

f_i^{CR} is the ratio of the i^{th} background between the CR and the Relaxed CR as calculated from Monte Carlo, i.e. $N_{\text{MC},i}^{\text{CR}}/N_{\text{MC},i}^{\text{Relax CR}}$. It is essentially a transfer factor from the Relaxed CR to the CR. The $\mathcal{M}_i$ are the models for the i^{th} background, described by analytic functions. The models have the same shape in all CRs. The $t\bar{t}$ background shape is modeled by a 2nd order Chebyshev polynomial, described by two parameters, c_0 and c_1. $Z + bb$ is modeled by a Breit-Wigner function convolved with a Crystal Ball function, described by 6 parameters (μ_{CB}, α_{CB}, η_{CB}, σ_{CB}, m_Z, and σ_{BW}). The values for these model parameters are also taken from Monte Carlo. The ZZ^* and WZ backgrounds are taken to be the same as the Z+bb shape (since they also contain a Z resonance), with their N constrained to their Monte Carlo values.

During the fit, the two $N_{\text{data}}^{\text{Relax CR}}$ terms will be fit for, while the four transfer factors, eight model parameters, and ZZ^* and WZ yields are treated as nuisance parameters in the fit, constrained to their MC fitted values within the MC fit error, using gaussian constraints. Figure 67 shows the results of the fit. The χ^2/NDF value of the simultaneous fit is $21.63/24 = .90$.

6.3.3 Step 2. Fit for Z+light

The next step is to do an unbinned maximum likelihood fit on the inverted isolation CR, again using the m_{12} variable, to estimate $N_{\text{data},Z+\text{light}}^{\text{Relax CR}}$. The Monte Carlo for Z+light does not describe the shape of the background very well, due to the fact that light jets fakes are not modeled by the Monte Carlo generators, but are phenomena of the detector mis-reconstruction. Instead the

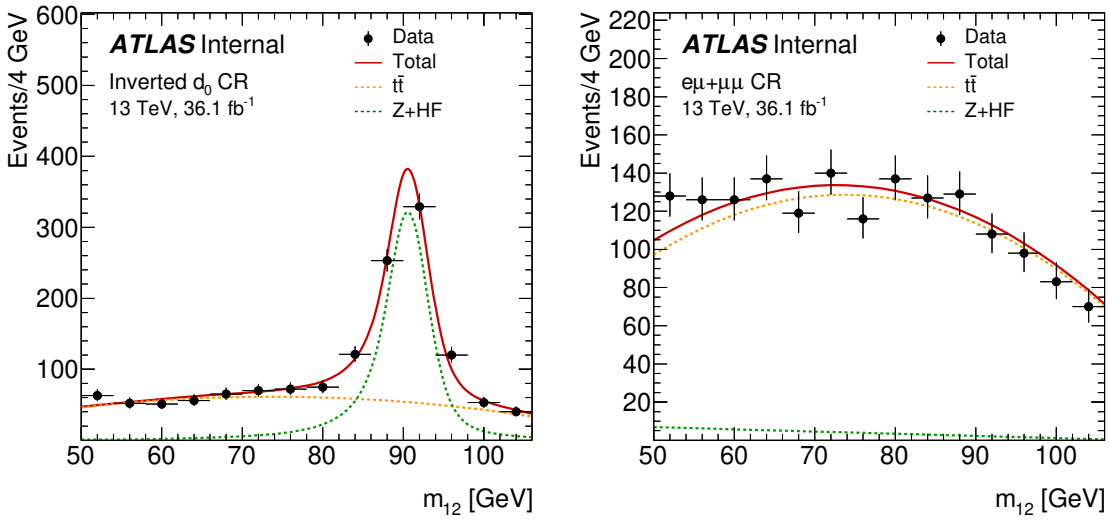

Figure 67: Distributions of m_{12} in the CRs. The data are fitted simultaneously in the the inverted d_0 (left) and the $e\mu$+$\mu\mu$ (right) CRs and the result of the fit is shown with the continuous line. The dashed lines correspond to the $Z + bb$ and $t\bar{t}$ components of the fit.

fit is done is a completely data driven way, where the other backgrounds are constrained to their estimated values, and the Z+light estimate is fit to whatever events are left over. Figure 68 shows the CR with the expected yields from Monte Carlo for all backgrounds (except Z+light because it is not simulated well), as well as the data.

The model shape for Z+light is also assumed to have the Z-peak shape of the Crystal Ball convoluted with Breit-Wigner, like the other resonant backgrounds. ZZ^* and WZ yields in this CR are taken from MC simulation, while the $Z + bb$ and $t\bar{t}$ yields are taken from the results in Step 1. All the shape and normalisation parameters are constrained to their values with Gaussian errors. Only Z+light normailzation is free. The result of the fit in this CR is shown in Figure 68, and no Z+light events were found. The χ^2/NDF value of the fit is $13.65/12 = 1.14$.

6.3.4 $\ell\ell\mu\mu$ Results

Using the formula in Equation 6.1, we can now calculate our reducible background events for $\ell\ell\mu\mu$ events. The results are listed in Table 62.

For the differential distributions, the shapes of the Z+jets and $t\bar{t}$ backgrounds are taken from simulation and normalized using the inclusive data-driven estimate. Cross checks on the results are done by plotting the diffential variables in the Relaxed CR, with the Higgs mass window cut inverted

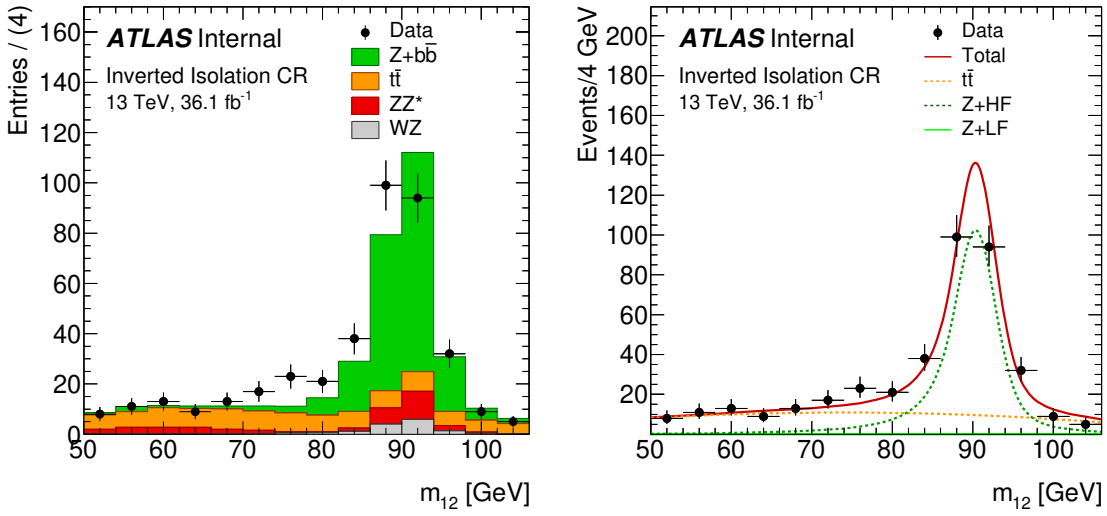

Figure 68: The left plot shows the m_{12} distributions for data and MC-simulated events from different background sources in the inverted isolation control region. The right plot shows the m_{12} distributions for data and the final fit to different background sources in the inverted isolation control region. The fits use the analytic functions of the background shapes. No Z+light background yield is found from the fit.

Type	Data fit	Transfer factor [%]	SR yield
$Z + bb$	928 ± 50	0.75 ± 0.09	$6.96 \pm 0.37 \pm 1.19$
$t\bar{t}$	934 ± 23	0.25 ± 0.03	$2.33 \pm 0.06 \pm 0.44$
Z+light	0 ± 16	3.0 ± 0.40	$0 \pm 0.49 \pm 0.25$
WZ	(MC-based estimation)		0.91 ± 0.50

Table 62: Estimate of the reducible $\ell\ell\mu\mu$ event yields. The statistical uncertainties are obtained from the fit to the CRs and the systematic uncertainties take into account the efficiency differences in the CR cuts between data and Monte Carlo.

in order to suppress the signal events, $110 < m_{4\ell} < 118\,\text{GeV}$ and $129 < m_{4\ell} < 170\,\text{GeV}$. Figure 69 shows the comparison between data and data-driven backgrounds for $p_T^{4\ell}$ and N_{jets}, demonstrating good agreement.

6.4 Reducible $\ell\ell + ee$ Background

The $\ell\ell ee$ background consists mainly of events with Z+light quark jets being mis-reconstructed as electrons, also known as fakes (f). The probability of Z+light jets faking a signal event in the signal region (SR) is very small, giving too few statistics in Monte Carlo (even with millions of simulated

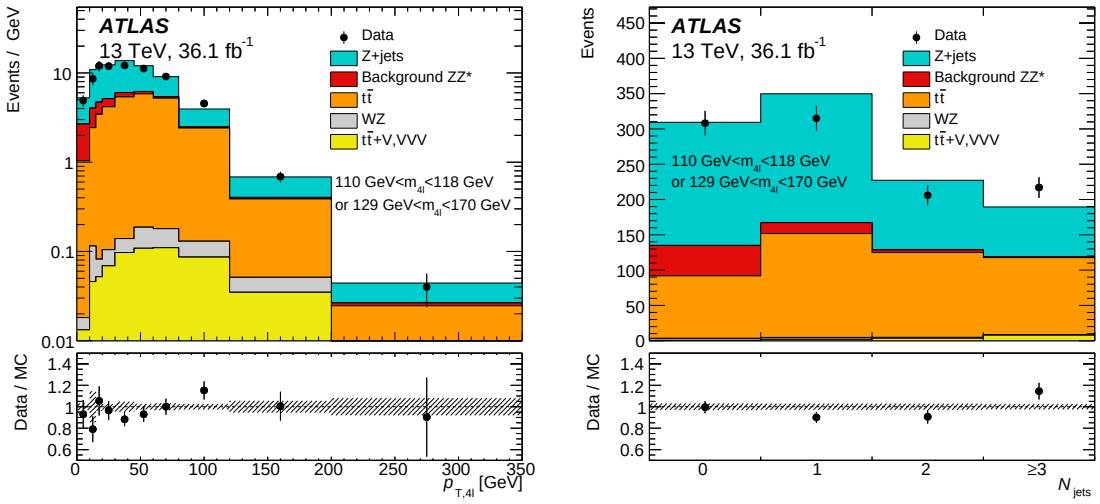

Figure 69: $\ell\ell + \mu\mu$ Relaxed CR plots for $p_T^{4\ell}$ (left) and N_{jets} (right). Background yields are taken from the data driven method for Z+jets and $t\bar{t}$ while ZZ^*,WZ, and Triboson are taken from Monte Carlo.

Z+light events) to model the background well. In addition, the fakes are difficult to simulate in Monte Carlo, as they are due to how effects like π/K decays, charged pions in the caloriemter, and hard bremsstrahlung with pair production are treated within the GEANT4 detector simulation, and are not as simple as leptons from semileptonic decay from a heavy jet. Other sources of $\ell\ell ee$ background are electrons from photon (γ) conversions, and a small amount of backgrounds also come from heavy jet semileptonic decays to electrons (q). We define control regions (CR) which relax the cuts for the signal selection to enhance the amount of background events. The background estimation is done through a data-driven method, meaning that the number of reducible background events in the SR will be extrapolated from using data events found in the CRs, rather than using the number of expected Monte Carlo events in the SR.

6.4.1 $\ell\ell ee$ Control Regions

The CRs, which are enhanced in background events, are defined as follows

1. $3\ell + X$ **CR (Enhanced in f and γ)**. This CR is used for the fit to data. The first three leptons of the quadruplet have the standard signal selection cuts applied. The leading lepton pair should reconstruct to a Z boson and the higher E_{T} lepton of the subleading pair should pass all the electron cuts. The lower E_{T} lepton of the subleading pair is the X electron

candidate, and must only pass a few electron ID cuts, namely the track quality cut of at least 1 Pixel + 7 Si hits, and the d_0 significance cut. The other *Loose* ID cuts and isolation cuts are not applied. The vertex cut is applied to the quadruplet to reduce heavy flavor contamination, and the subleading lepton pair is required to have the same sign, to reduce ZZ^* irreducible background contamination.

2. $Z+X$ **CR (Enhanced in f and γ)**. This CR is a huge sample of Z boson events associated with an electron candidate. The large amount of statistics is necessary to calculate efficiencies and templates for the f and γ background. The two leading leptons have the standard selection applied in order to find a real Z boson. For the X electron candidate, the selection only uses the track quality cut the d_0 significance cut. The *Loose* likelihood cut, the vertex cut, and the isolation cut are not applied. The X electrons must be well separated from the Z leptons, with $\Delta R > 0.2$ for diferent flavor, and $\Delta R > 0.1$ for same flavor.

3. $Z + X(\gamma)$ **CR (Enhanced in γ)**. This CR is exactly like the $Z + X$ CR except with an additional $n_{\text{InnerPix}} = 0$ cut to purify the sample in γ. n_{InnerPix} is the number of IBL hits, except if there is a dead area of the IBL, in that case, the number of hits on the next-to-innermost pixel layer is used instead. After this cut, the X in this sample will be 90% γ according to Monte Carlo simulation.

4. $Z + X(f)$ **CR (Enhanced in f)**. This CR is exactly like the $Z + X$ CR except with an additional $n_{\text{InnerPix}} > 0$ cut to purify the sample in f. After this cut, the X in this sample will be 98% f according to Monte Carlo simulation.

6.4.2 The n_{InnerPix} fit in $3\ell + X$

To calculate the number of background events in the SR, the following formula is used separately for both f and γ (q is estimated from Monte Carlo):

$$N^{\text{SR}}_{\text{data},i} = \sum_{j}^{\substack{p_{\text{T}} \\ \text{bins}}} \mathcal{S}_{ij} \sum_{k}^{\substack{N_{\text{jets}} \\ \text{bins}}} \varepsilon_{ijk} \times N^{3\ell+X}_{\text{data},ijk} \tag{6.6}$$

$i = f$ or γ, j is the p_{T} bin of the X electron candidate, and k is the N_{jets} in the event. ε_{ijk} is the efficiency of a f or γ background object to pass the standard signal electron cuts with full electron indentification and isolation requirements (as a function of p_{T} and N_{jets}). $\mathcal{S}_{ij}$ is the scale factor for correcting the efficiency discrepancies between data and Monte Carlo (as a function of p_{T}). $N^{3\ell+X}_{\text{data},ijk}$

is the number of data events for the i^{th} background in the $3\ell+X$ CR (as a function of p_{T} and N_{jets}). ε_{ijk} is derived solely from Monte Carlo, while $\mathcal{S}_{ij}$ uses both data and Monte Carlo. The following sections will explain how each term is calculated.

6.4.2.1 Events in the CR, $N^{3\ell+X}_{\mathbf{data},ijk}$

To get the number of f and γ events in the $3\ell + X$ CR, first we separate the events into 2D bins of p_{T}-N_{jets}. For each bin, we plot the X electron candidates as a function of n_{InnerPix}. n_{InnerPix} is an integer quantity and is the number of IBL hits associated with the X electron track, except if there is a dead area of the IBL, where in that case, the number of hits on the next-to-innermost pixel layer is used instead.

Before fitting to the data in the CR, it is necessary to get the templates for the f and γ shapes. The templates are obtained from the Monte Carlo in the $Z + X$ CR. `MCTruthClassifier` is used to identify the origin of the X object as being either f, γ, or q. The templates are plotted in Figure 610. As you can see, the f and q templates have a very similar shapes, so the f template is used for both.

Once the shape templates have been extracted, we use them in the fit to n_{InnerPix} in the $3\ell + X$ CR from data. The q and ZZ^* events in the sample are estimated directly from their Monte Carlo numbers and subtracted out. The fit is done in 2D data bins of p_{T} and N_{jets}. The sPlot method is used to do the fit [138]. The sPlot tool in ROOT returns a covariance-weighted value, $sWeight_i$, for each X candidate, for both f and γ. The $N^{3\ell+X}_{\text{data},ijk}$ for each background is obtained by summing up the $sWeight_i$ from all events in the specific p_{T}-N_{jets} bin. The inclusive $N^{3\ell+X}_{\text{data},i}$ is obtained by summing all the bins together. The inclusive results of the fit are shown in Figure 610.

6.4.2.2 Efficiency, ε_{ijk}

The efficiency is the fraction of the X electrons that pass the complete signal electron selection, which means also passing the full *Loose* electron ID and the isolation cuts. These efficiency numbers are calculated from $Z+X$ CR Monte Carlo for the f and γ objects identified by `MCTruthClassifier` in 2D bins of p_{T}-N_{jets}. The efficiencies are used to extrapolate from the f and γ yields obtained from the fit in the $3\ell + X$ CR to the SR.

$$\varepsilon_{ijk} = \frac{N^{\text{pass},i}_{\text{MC}}(j,k)}{N^{i}_{\text{MC}}(j,k)} \tag{6.7}$$

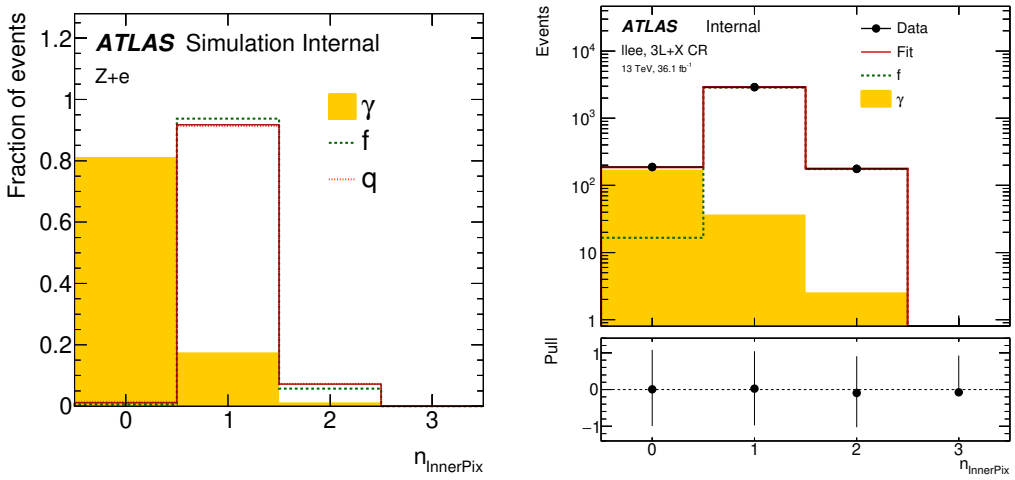

Figure 610: (Left) Templates used in the 3ℓ+X fit to n_{InnerPix} for the γ and f backgrounds, obtained from MC simulation in the Z+X control sample. q is very similar in shape to f and f is used for both when needed. (Right) Data 3ℓ+X events and result of the fit to n_{InnerPix} with q estimated from MC and subtracted out.

Where $i = f$ or γ and (j, k) is the $(p_{\text{T}}, N_{\text{jets}})$ bin. These efficiencies have to be corrected to match the efficiencies in data, which is done through the use of scale factors, $\mathcal{S}_{ij}$, explained in the next section.

6.4.2.3 Scale Factor, $\mathcal{S}_{ij}$

To correct for the mismodeling of the Monte Carlo, scale factors are derived to go from the efficiencies calculated from Monte Carlo to the efficiencies in actual data. These factors depend on the p_{T} of the X electron candidate and show little dependence on N_{jets}, so the scale factors are binned in just the p_{T} variable. The scale factor is defined as

$$\mathcal{S}_{ij} = \frac{\varepsilon_{ij}^{\text{data}}}{\varepsilon_{ij}^{\text{MC}}} = \frac{s_{ij}^{\text{pass}}}{s_{ij}} \tag{6.8}$$

Where i is the background, and j is the p_{T} bin. s_{ij} is the scale factor of the i^{th} background yield in the CR, and s_{ij}^{pass} is the scale factor of the i^{th} background yield for electrons that have passed the standard selection cuts in the CR. s_{ij} and s_{ij}^{pass} are obtained by using CRs that are as pure as possible in the background of interest. Through Monte Carlo studies, the $Z + X(\gamma)$ CR and $Z + X(f)$ CR have 90% and 98% purity in their respective backgrounds. Calculating the s_{ij} is done

in an iterative way. First we calculate s_γ (for a p_{T} bin), then use that result to calculate s_f, and then use that result to calculate s_γ again, and repeat until the result converges.

To begin, we use the $Z + X(\gamma)$ CR to calculate the scale factor for the γ yield with the following equation

$$s_\gamma = \frac{N_{\mathrm{data}} - N_q - N_f}{N_\gamma} \tag{6.9}$$

N_{data} is the number of data events in $Z + X(\gamma)$ CR. N_q,N_f, and N_γ are the Monte Carlo events in the $Z + X(\gamma)$ CR. Next we use the $Z + X(f)$ CR and s_γ to calculate the scale factor for the f yield with the following equation

$$s_f = \frac{N_{\mathrm{data}} - N_q - s_\gamma \cdot N_\gamma}{N_f} \tag{6.10}$$

The calculated s_f is then plugged back into the s_γ equation, replacing $N_f \to s_f \cdot N_f$, and a new s_γ is computed. The iterations is done three times before convergence is reached. The same thing is done to calculate s_γ^{pass} and s_f^{pass} with the X electrons in the CRs having to pass the standard isolation and *Loose* ID selection. Finally, $\mathcal{S}_{ij}$ is calculated according to Equation 6.8. Scale factor results in bins of p_{T} are listed in Table 63.

p_{T} [GeV]	scale factor [%]
light-flavour jets (f)	
$[7, 10]$	1.42 ± 0.09
$[10, 15]$	2.57 ± 0.27
$[15, 70]$	4.38 ± 0.63
photon conversions (γ)	
$[7, 10]$	1.01 ± 0.04
$[10, 15]$	1.18 ± 0.07
$[15, 70]$	1.91 ± 0.12

Table 63: Data/MC scale factors for f and γ calculated from their respective enriched $Z + X$ CR. Errors shown are statistical only.

6.4.3 $\ell\ell ee$ Result

We can now use Equation 6.6 to calculate the background yield in the SR. Table 64 shows the fit results $N_{\mathrm{data},i}^{3\ell+X}$, the yields in the 3ℓ+X CR, with statistical errors. Also shown is the q contamination in the CRs, and the scale factor times efficiency used to extrapolate the yields to the SR. The SR yields for the f and γ backgrounds are quoted with statistical uncertainty as returned from the data

fit, and systematic uncertainty of the scaled efficiency for the fit. The q component is not fitted to the data, so the SR yield is taken directly from MC simulation.

Type	Data fit	q cont.	$\mathcal{S} \cdot \varepsilon$ [%]	SR yield
f	3075 ± 56	280 ± 6	0.20 ± 0.04	$5.68 \pm 0.36 \pm 1.19$
γ	208 ± 17	19.4 ± 0.5	0.71 ± 0.14	$1.34 \pm 0.35 \pm 0.27$
q	(MC-based estimation)			6.34 ± 1.93

Table 64: Estimate of the reducible $\ell\ell ee$ event yields. The statistical uncertainties are obtained from the fit to the CRs and the systematic uncertainties take into account the efficiency differences in the CR between data and Monte Carlo.

Chapter 7

Unfolding

7.1 Introduction

The production of the Higgs boson is an inherently statistical process. For a given integrated luminosity, the number of Higgs bosons produced in collisions in ATLAS follow a Poisson distribution, where the expected number produced is determined by the inclusive Higgs cross section, whose value is predicted by the Standard Model. The kinematic properties of the Higgs, like its transverse momentum (p_T^H) or rapidity ($|y^H|$), are also random variables that follow their own probability distribution functions (p.d.f.'s). Measuring the Higgs properties at ATLAS is a process of constantly sampling the p.d.f.'s of each of the properties of interest to determine their shape. Our Monte Carlo simulations (after a very large number of generated events) give predictions of the shapes of the p.d.f.'s. We call these distributions from simulation the "truth" distributions of the Higgs, $f_{\text{truth}}(x)$, where x might be p_T^H, $|y^H|$ or another variable. If we had a perfect detector with infinite resolution, then after collecting many, many events to the point that the variance of the Poisson statistics was negligible, we would expect the shape of the measured distributions to match the shape of the truth distribution (if the truth distribution indeed described the real physics).

Of course in reality ATLAS does not have infinite resolution, and the detector does not measure the Higgs itself but its stable decay products. Rather than sampling the Higgs directly, we are reconstructing $H \to ZZ^* \to 4\ell$ events by taking the physical detector hits and turning them into physics objects (e.g. electrons and muons) and calculating the four vector of the 4ℓ system. We are not actually sampling the distribution $f_{\text{truth}}(x)$ when we collect events, but the related distribution $f_{\text{reco}}(x^{4\ell})$, where "reco" stands for reconstructed.

$f_{\text{truth}}(x)$ is a distribution inherent to the Higgs bosons coming from colliding protons at 13 TeV.

A Higgs coming from protons colliding in space at 13 TeV would still have its properties follow this distribution. $f_{\text{reco}}(x^{4\ell})$ is a distribution unique to the context of the ATLAS detector. CMS, or any other experiment, would have its own reco distribution as well, separate from ATLAS. When we measure the p.d.f.'s of the properties of the Higgs from our collected data, we are making statements based on $f_{\text{reco}}(x^{4\ell})$. In order to compare results between experiments in a straight-forward way, it is useful to present our results by taking our samples of $f_{\text{reco}}(x^{4\ell})$ and transform them to our best estimate of samples from $f_{\text{truth}}(x)$.

The process of "unfolding" measured data from a variable that follows $f_{\text{reco}}(x^{4\ell})$ to a variable that follows $f_{\text{truth}}(x)$ is like sharpening a grainy or blurry photograph, where the blurring was caused by the finite resolution of the camera. To unfold, what's required is a good model of the resolution of the measuring instrument as well as a model of what the underlying "truth" distribution looks like. Unfolding mainly attempts to correct for the following things:

1. Smearing effects due to limited resolution, which will cause migration across bins and turn sharp peaks into soft hills.

2. Acceptance and efficiency effects due to the instrument reconstructing the data improperly or not at all, causing a reduced number of events in the bin.

3. Non-linear transformations of the events due to detector response effects.

7.2 Acceptance factors

To create our model $f_{\text{truth}}(x^H)$, we create a large sample of Monte Carlo simulted Higgs events. These are generated using the latest predictions from the Standard Model, and we simulate large samples in order to reduce any errors in the distribution due to statistical fluctuations. The distribution is normalized to unity to create the p.d.f.

We can use $f_{\text{truth}}(x^H)$ to create a histogram of expected events $\vec{N}_{\text{truth}} = \{N^1_{\text{truth}}, \dots N^i_{\text{truth}}, \dots\}$ normalized to a desired integrated luminosity with the following equation:

$$N^i_{\text{truth}} = \mathcal{L}_{\text{int}} \cdot \sigma_H \cdot \int_{\text{bin } i} f_{\text{truth}}(x)\,\mathrm{d}x \tag{7.1}$$

In a fiducial analysis, we are interested in a related distribution called $f_{\text{fid}}(x^{4\ell})$. In this distribution, the Higgs events are decayed through the $H \to ZZ^* \to 4\ell$ channel and fiducial level cuts are applied to the decay products (see Section 5.3). A four-vector of the 4ℓ system is built from the decay prodcuts and is used to populate distributions of any desired Higgs property. We are interested

in these fiducial distributions because they are the distributions that can actually be measured by our detector. ATLAS can only measure the stable decay prodcuts of the Higgs, and the fiducial cuts are meant to model the detector acceptance, which is low at high η regions where the detector material is sparse, and with low p_{T} particles that may not be reconstructed at all.

The total N_{fid} will be lower than the total $N_{\mathrm{truth}} = \sigma_H \cdot \mathcal{L}_{\mathrm{int}}$ due to two effects

1. The decay to 4ℓ reduces the yield by the branching fraction.
2. The fiducial cuts reduce the phase space of the Higgs decay.

The effect of the phase space reduction can be represented by an acceptance function $\alpha(x)$ that gives the fraction of truth events found in the fiducial space.

You can define an acceptance factor, $\mathcal{A}_i$, for bin i in the following way

$$\mathcal{A}_i = \frac{\int_{\mathrm{bin}\,i} \alpha(x) f_{\mathrm{truth}}(x)\,\mathrm{d}x}{\int_{\mathrm{bin}\,i} f_{\mathrm{truth}}(x)\,\mathrm{d}x} \tag{7.2}$$

We can use $\mathcal{A}_i$ (or $\alpha(x)$) to create a histogram $\vec{N}_{\mathrm{fid}} = \{N^1_{\mathrm{fid}}, \dots N^i_{\mathrm{fid}}, \dots\}$ normalized to a desired integrated luminosity with the following equation:

$$\begin{aligned} N^i_{\mathrm{fid}} &= \mathcal{L}_{\mathrm{int}} \cdot \sigma_H \cdot \mathrm{BR}(H \to 4\ell) \cdot \int_{\mathrm{bin}\,i} \alpha(x) f_{\mathrm{truth}}(x)\,\mathrm{d}x \\ &= \mathrm{BR}(H \to 4\ell) \cdot \mathcal{A}_i \cdot N^i_{\mathrm{truth}} \end{aligned} \tag{7.3}$$

$$f_{\mathrm{fid}}(x) = \frac{\alpha(x) \cdot f_{\mathrm{truth}}(x)}{\int \alpha(y) f_{\mathrm{truth}}(y)\,\mathrm{d}y} \tag{7.4}$$

One can calculate $\mathcal{A}_i$ from Monte Carlo by simulating a Higgs sample that has $\mathrm{BR}(H \to 4\ell) = 1$ and then applying the fiducial selection to that sample to calculate

$$\mathcal{A}_i = \frac{N^i_{\mathrm{fid,MC}}}{N^i_{\mathrm{truth,MC}}} \tag{7.5}$$

The inclusive $\mathcal{A}$ factors for each Higgs production mode and 4ℓ decay channel are shown in Fig. 71. The total inclusive $\mathcal{A}$ factor is calculated to be 42.16%. This means that of the total number of $H \to ZZ^* \to 4\ell$ events predicted to be produced at the LHC, our fiducial analysis is expected to only see 42.16% of them. Even though all 4 of the the 4ℓ decay channels have equal predicted rates of happening, our fiducial event selection has looser cuts on $\mu\, p_{\mathrm{T}}$ than on $e\, p_{\mathrm{T}}$ (Sec. 5.3), leading to a higher acceptance of 4μ events than $4e$ events. After 4μ is the $2e2\mu$ channel in terms of

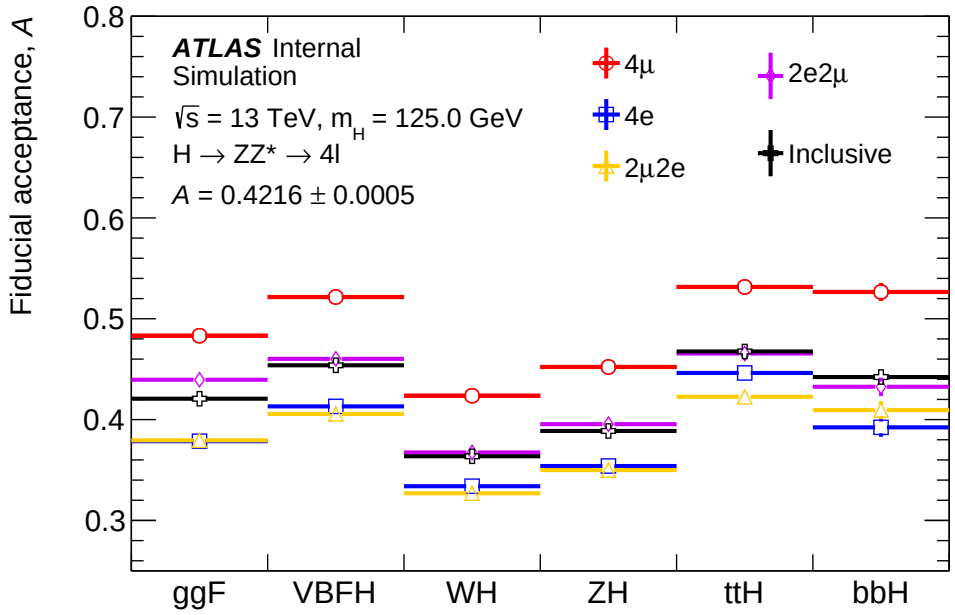

Figure 71: Acceptance factors for $\sqrt{s} = 13\,\text{TeV}$ and 125.0 GeV. $\mathcal{A}$ is obtained by a weighed average of the extracted values of all production modes and the four final states. The weight is determined by the production cross section of each mode as predicted by the SM and evaluated in the YR4. Uncertainties are statistical only.

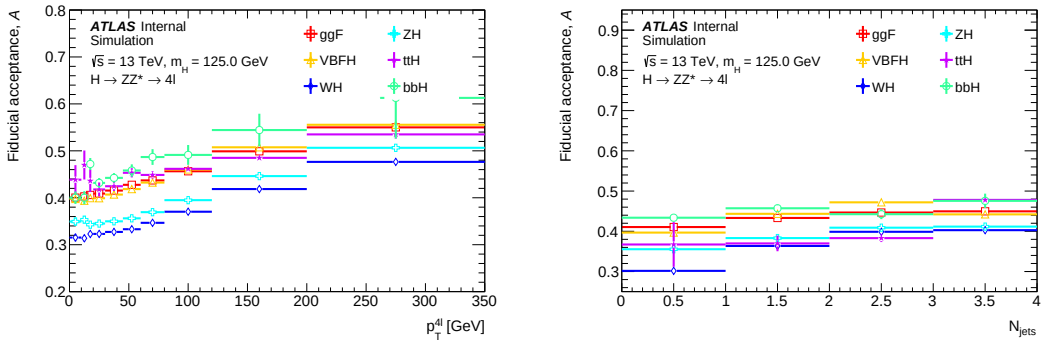

Figure 72: Values of $\mathcal{A}$ as a function of $p_T^{4\ell}$ and N_{jets}.

acceptance, since the leptons of the off-shell Z boson have on average lower momentum, so it brings up the acceptance when we use the more loosely cut μ's to build the off-shell Z. As for differences in production mode, VBF and $t\bar{t}H$ events produce a boosted Higgs due to the associated jets and so on average have higher p_{T} leptons than ggF. While the WH/ZH production modes also have a

boosted Higgs, the associated W/Z can also decay into charged leptons, and sometimes the fiducial analysis cuts may mis-reconstruct the on-shell Z with one of the associated leptons, causing the fiducial selection to fail at a later step when trying to reconstruct the full 4ℓ four-vector.

Differential $\mathcal{A}_i$ factors were also made for each variable of interest. The factors for the $p_T^{4\ell}$ and N_{jets} variables for each Higgs production mode are shown in Fig. 72. The production modes follow the same trends as the inclusive $\mathcal{A}$ fators for the most part. The $p_T^{4\ell}$ spectrum on average increases in acceptance due to the higher average p_{T} of the constiuent leptons. It is a similar story for the N_{jets} variable. More jets in an event can lead to a more boosted Higgs, which increases the average p_{T} of the leptons, which leads to higher acceptance.

Bias

These $\mathcal{A}_i$ factors can be used to extrapolate back to the truth Higgs distributions from the fiducial distribution to get a more detector-independent measurement at the cost of introducing more model-dependence. The final result will be systematically biased to the degree that the underlying truth and fiducial model used to generate the Monte Carlo does not describe the fiducial physics data.

$$\text{bias} = N^i_{\text{truth}} - \frac{E[N^i_{\text{data,fid}}]}{\mathcal{A}_i \cdot \text{BR}(H \to 4\ell)} = E[N^i_{\text{data,fid}}] \left(\frac{N^i_{\text{truth}}}{E[N^i_{\text{data,fid}}]} - \frac{N^i_{\text{truth,MC}}}{N^i_{\text{fid,MC}} \cdot \text{BR}(H \to 4\ell)} \right) \tag{7.6}$$

Where $E[N^i_{\text{data,fid}}]$ is the expectation value of the measured fiducial events. Systematic errors on the $\mathcal{A}_i$ factors are calculated in Section 8.3.

7.3 Correction factors

We are not actually probing the distribution $f_{\text{fid}}(y)$ either when we collect events in ATLAS. Detector resolution and misidentification of particles will also play a role, so the sampling distribution is actually $f_{\text{reco}}(x)$. To state a fiducial measurement in our results, we need to be able to correct for these detector effects.

The following unfolding procedure is meant to take data sampled from the distribution after reconstruction, $f_{\text{reco}}(x)$, to the fiducial distribution of the decay products, $f_{\text{fid}}(y)$. Detector resolution effects (e.g. migrations in energy) and muon, electron, and jet identification and efficiencies are all taken into account. The effects of can be split into an efficiency function, $\epsilon(x)$, the fraction of fiducial events that are reconstructed as a reco event, and a response function, $s(x|y)$, a conditional p.d.f. for

the reco value being x, given that the fiducial value was y [139]. We can use $f_{\text{fid}}(y)$ and our efficiency and response functions to create a histogram of expected reco events $\vec{N}_{\text{reco}} = \{N^1_{\text{reco}}, \dots N^i_{\text{reco}}, \dots\}$

$$N^i_{\text{reco}} = N^{\text{total}}_{\text{fid}} \int_{\text{bin } i} \mathrm{d}x \int s(x|y)\epsilon(x) f_{\text{fid}}(y)\, \mathrm{d}y \tag{7.7}$$

We can discretize the above equation in the following way

$$N^i_{\text{reco}} = \sum_j R_{ij} \cdot \mathcal{C}_j \cdot N^j_{\text{fid}} \tag{7.8}$$

Where $\mathcal{C}_j$ is the correction factor, the efficiency for reconstructing a fiducial event in bin j, and R_{ij} is the response matrix, a probability matrix for an event in the fiducial bin j ending up in reco bin i.

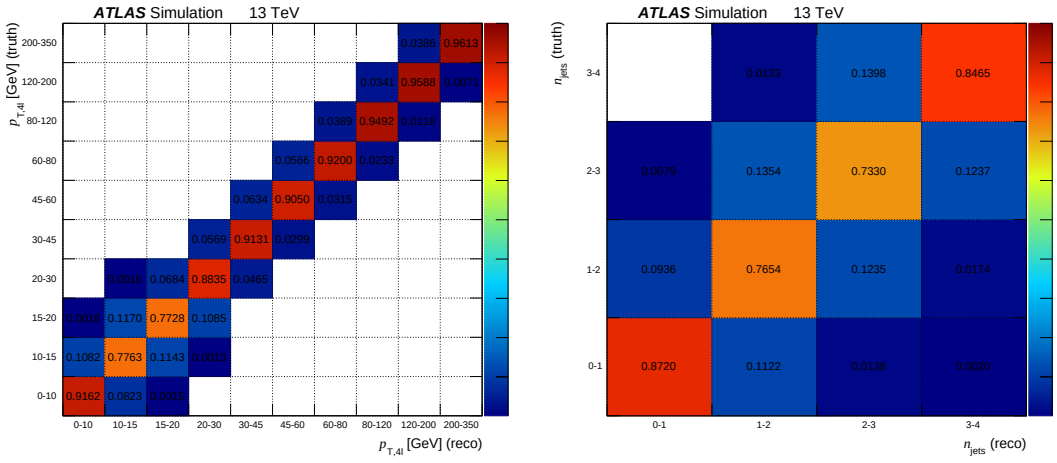

Figure 73: Response matrices evaluated using signal MC at $m_H = 125\,\text{GeV}$ (summing over all production modes) for $p_T^{4\ell}$ (a) and N_{jets} (b). Only the events that pass both fiducial and reco selection cuts have been included.

When the chosen binning is greater than the resolution of the detector, the response matrix will become more diagonal. There can still be off-diagonal elements from other detector effects, but if the systematic errors are deemed tolerable (due to larger statistical errors in the bins) one can approximate Eq. 7.8 as

$$N^i_{\text{reco}} \approx \mathcal{C}_i \cdot N^i_{\text{fid}} \tag{7.9}$$

And subsequently calculate $\mathcal{C}_i$ from Monte Carlo.

7.3.1 Bin-by-bin correction factors

The correction factor $\mathcal{C}_i$ can be calculated from Monte Carlo in the following way

$$\mathcal{C}_i = \frac{N^i_{\text{reco,MC}}}{N^i_{\text{fid,MC}}} \tag{7.10}$$

While it looks very similar to the definition of the $\mathcal{A}$ factor (Eq. 7.5), is meant to be less model dependent, as it is only supposed to deal with the detector efficiency, and the effects from physics modeling cancel out between the numerator and denominator (though will still have some effect). The model independence can depend a lot of how well the fiducial cuts match the reco cuts. The discrepancy between the two can be quantified by the the fiducial leakage, explained in Section 7.4. Fig. 74 shows the $\mathcal{C}$ factors for all Higgs production modes for each of the 4ℓ decay channels.

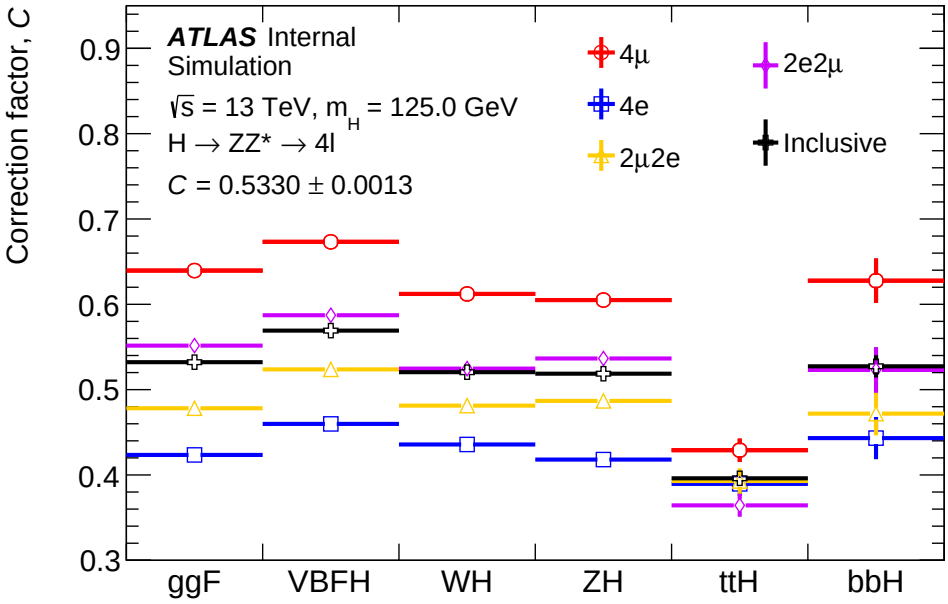

Figure 74: Correction factors for $\sqrt{s} = 13\,\text{TeV}$ and $125.0\,\text{GeV}$. $\mathcal{C}$ is obtained by a weighed average of the extracted values of all production modes and the four final states. The weight is determined by the production cross section of each mode as predicted by the SM and evaluated in the YR4. Uncertainties are statistical only.

The inclusive $\mathcal{C}$ factors for each Higgs production mode and 4ℓ decay channel are shown in Fig. 74. The total inclusive $\mathcal{C}$ factor is calculated to be 53.30%. This means that of the fiducial $H \to ZZ^* \to 4\ell$ events ATLAS even has a chance of seeing, due to detector efficiency, we only expect

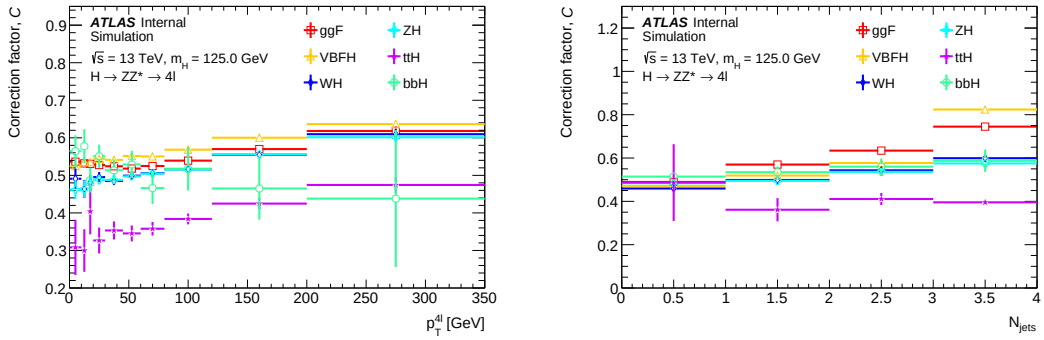

Figure 75: Values of $\mathcal{C}$ as a function of $p_T^{4\ell}$ and N_{jets}.

to reconstruct 53.30% of those fiducial events. That means that out of all the truth $H \to ZZ^* \to 4\ell$ Higgs events predicted to be produced in ATLAS, we only expect to see $\mathcal{A} \times \mathcal{C} = 22.47\%$ of them.

We are also better at identifying and reconstructing muons than electrons (Chp. 4), leading to more than 60% of 4μ events being reconstructed, compared to less than 45% of $4e$ events. After 4μ is the $2e2\mu$ channel in terms of efficiency, since the leptons of the off-shell Z boson have on average lower momentum, so there is a better chance of actually reconstructing the off-shell Z if it is made from μ's. The factors are mostly flat across production modes, demonstrating the model independence of the of the reconstruction. The reduced $\mathcal{C}$ factor in $t\bar{t}H$ is the result of the lepton isolation requirements in the reco event selection. The reconstructed leptons are less isolated because of the presence of the additional jets from the $t\bar{t}$ decays, while no isolation requirements are imposed on the fiducial cuts.

Differential $\mathcal{C}_i$ factors were also made for each variable of interest. The factors for the $p_T^{4\ell}$ and N_{jets} variables for each Higgs production mode are shown in Fig. 72. The production modes follow the same trends as the inclusive $\mathcal{C}$ fators for the most part. The $p_T^{4\ell}$ spectrum on average increase in efficiency due to the higher average p_{T} of the constiuent leptons. It is a similar story for the N_{jets} variable. More jets in an event can lead to a more boosted Higgs, which increases the average p_{T} of the leptons, which leads to higher efficiency.

Bias

There are two sources of systematic bias when using the bin-by-bin correction factors [139]

1. The degree to which the underlying $f_{\text{fid}}(x)$ and $f_{\text{reco}}(x)$ distributions used to generate the MC do not describe the physics data.

2. The size of the off-diagonals in the response matrix.

Assuming the response matrix is perfectly diagonal, the first source of bias takes the same form as the $\mathcal{A}$ factor bias (Equation 7.6), and is

$$\text{bias} = N^i_{\text{fid}} - \frac{E[N^i_{\text{reco,data}}]}{\mathcal{C}_i} = E[N^i_{\text{reco,data}}] \left(\frac{N^i_{\text{fid}}}{E[N^i_{\text{data,reco}}]} - \frac{N^i_{\text{fid,MC}}}{N^i_{\text{reco,MC}}} \right) \tag{7.11}$$

The next large source of systematic bias comes from the size of the off diagonal elements of the response matrix [139]

$$\text{bias} = N^i_{\text{reco}} \times \sum_{i \neq j} R^{-1}_{ij} \left(\frac{N^j_{\text{reco}}}{N^i_{\text{reco}}} - E\left[\frac{N^j_{\text{reco,data}}}{N^i_{\text{reco,data}}} \right] \right) \tag{7.12}$$

Therefore, the size of this bias goes to zero as the response matrix becomes diagonal. Systematic errors on the $\mathcal{C}_i$ factors are calculated in Section 8.3.

If the size of the bias from the off-diagonal elements of the response matrix is considered too large (c.f. $p_T^{4\ell}$ vs N_{jets} in Fig. 73) there are alternatives to the bin-by-bin correction factors. One alternative is to simply invert the response matrix. This will eliminate the bias due to the off-diagonal elements, but the trade off is that the statistical variance will increase, as any noise in $N_{\text{reco,data}}$ will be unfolded as if it were signal. If the response matrix smears out peaks in data, then applying the inverse will create peaks from smears. Unfolding the noise creates a large amount of fine-structure where there isn't any, and results in large statistical errors. Due to the low statistics in the standard 4ℓ analysis, adding more statistical error is undesireable, so we stay with the bin-by-bin unfolding and take into account the corresponding systematic error from the bias.

7.4 Fiducial Leakage and Purity

Fiducial leakage is defined as follows:

$$\text{Leakage} = \frac{N_{\text{reco}} - N_{\text{reco \& fid}}}{N_{\text{reco}}} \, . \tag{7.13}$$

The leakage is the fraction of reco events that do not also pass the fiducial selection. This is used to determine if the fiducial region is well defined, where the closer to 0 the leakage is, the more well defined the fiducial region is. The fiducial leakage is expected to be non-zero due to detector and reconstruction effects, causing event migration at the edge of the fiducial region. Leakage events are being produced by signal processes but are considered background as they are outside

the fiducial region. Therefore, reductions in the fiducial leakage are highly desirable, as we get to turn background into signal events.

N is the number of fiducial and/or reconstructed events that pass the respective selections in the MC sample. Table 71 shows the fiducial leakage using three truth lepton definitions, born, dressed, and bare, whose definitions are discussed in Section 5.3. Born leptons are more a benchmark, since they are not used in the defintion of the fiducial selection because born leptons are not stable, final state particles. Dressing decreases the p_{T} of leptons relative to the born leptons due to some loss from far FSR photons not caught in the dressing algorithm. This will push the dressed lepons out of the fiducial region more often, relative to born. Bare leptons do no FSR recovery and so perform the worst.

Comparing the number of events that pass the fiducial cuts when using born versus dressed leptons, we see a decrease of around 5% from born to dressed. This shows up in the $\mathcal{A}$ and $\mathcal{C}$ factors as an increase of 5.05% in the $\mathcal{C}$ factor and a decrease of -4.81% in the $\mathcal{A}$.

Fig. 76 shows a related quantity called the purity for the differential varaibles $p_T^{4\ell}$ and N_{jets}, where

$$\text{Purity} = 1 - \text{Leakage} = \frac{N_{\text{reco \& fid}}}{N_{\text{reco}}} \,. \tag{7.14}$$

This is eseentially a measure of how many reco events in a given bin actually came from that bin. The higher the purity, the less bias there will be when using the bin-by-bin correction factors. When determining the binning used for the differential variables, the bin purity was a factor (along with the significance) is choosing the bin limits, with a goal of having above 70% purity in each bin.

Fiducial Leakage [%]			
Decay Channel	Born	Dressed	Bare
4μ	0.63	1.30	2.28
4e	2.45	3.17	10.09
4ℓ	1.35	2.09	5.66

Table 71: The fiducial leakage on a $m_H = 125\,\mathrm{GeV}$ ggF sample using the born, dressed, and bare truth lepton defintions.

7.5 Alternative Models

To demonstrate the effect of how the underlying Monte Carlo model affects the $\mathcal{A}$ and $\mathcal{C}$ factors, we used the ggF Higgs signal sample from multiple generators to study the model dependence.

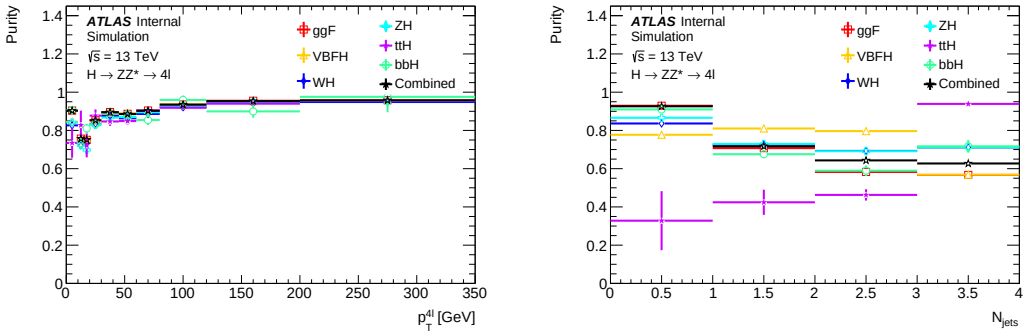

Figure 76: Purity of production modes for variables $p_T^{4\ell}$ (a) and N_{jets} (b) in each bin. A SM Higgs with $m_H = 125.0\,\text{GeV}$ has been assumed.

Our baseline generator and nominal factors are made from ggF Powheg, which has had its Higgs p_T distribution reweighed to account for NLO QCD corrections. For comparison we used the ggF MadGraph5 generator, and within MadGraph5, we used both SM and various EFT samples to do the comparison. Studies for $p_T^{4\ell}$ and N_{jets} are shown in Fig. 77 and Fig. 78.

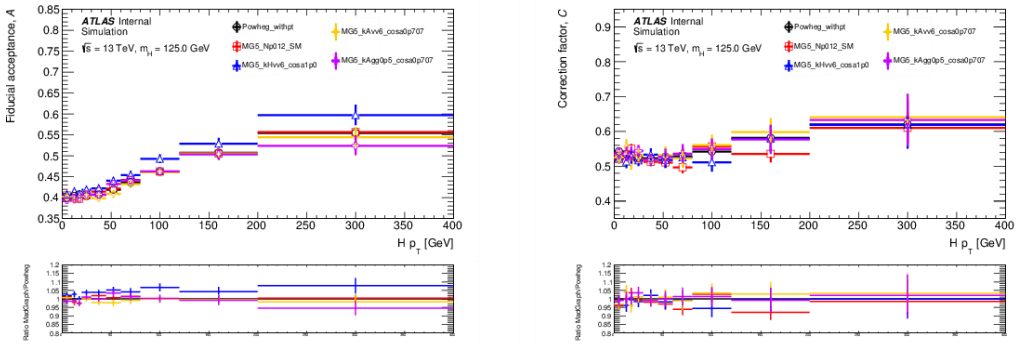

Figure 77: ggF values of $\mathcal{A}$ and $\mathcal{C}$ as a function of $p_T^{4\ell}$ for Powheg (nominal) and MadGraph SM and EFT samples.

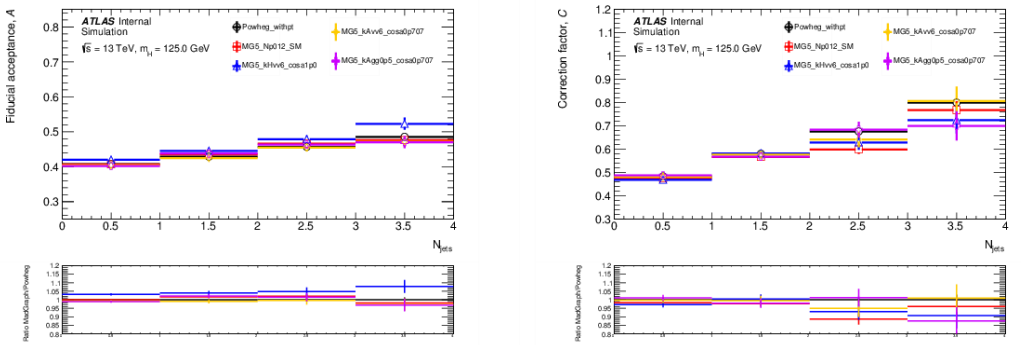

Figure 78: ggF values of $\mathcal{A}$ and $\mathcal{C}$ as a function of N_{jets} for Powheg (nominal) and MadGraph SM and EFT samples.

Chapter 8

Systematic Uncertainties

This chapter explains the uncertainties in the analysis due to non-statistical effects. Any systematic uncertainty can be broadly fit into one of two classes: either it is due to experimental uncertainties in the reconstruction/identification of physics objects, or due to theoretical uncertainties or mismodeling in the Monte Carlo models.

Section 8.1 lists the systematics that affect the measured electrons, muons, and jets in an event. 8.2 lists the systematics that affect the background selection, yields, and modeling. Section 8.3 lists the systematics that affect the unfolding procedure. For the experimental systematics, the usual method to constrain the uncertainty is either to vary some parameter by $\pm 1\sigma$ and generate new Monte Carlo to see how it affects the yields of the selection, or to compare the yields between completely different Monte Carlo generators. For the theoretical systematics, the uncertainty usually comes from unknown effects of higher order terms in the perturbative part of the interaction, or uncertainty in the Parton Distribution Functions that model the non-perturbative part of the interaction. The results of these systematics are used as Gaussian nuisance parameters in the maximum likelihood fit when extracting the final cross section, and have the effect of widening the error bars on the final measurement, as explained in Chapter 9.

8.1 Event Systematics

Two experimental uncertainties that affect all events are `LUMI` and `PRW_DATASF`.

`LUMI` is the uncertainty on the integrated luminosity, which is a measured of the total number of proton-proton collisions ATLAS collected over 2015 and 2016. The uncertainty was 2.1% for the 2015 dataset and 3.4% for the 2016 dataset, resulting in a $\pm 3.2\%$ uncertainty for the full 36.1fb^{-1}

of integrated luminosity. PRW_DATASF is essentially an uncertainty on $\langle\mu\rangle$ i.e. the average number of inelastic collisions in a single bunch crossing, and stands for "Pile-up reweighting data scale factor". All Monte Carlo are generated with a fixed pile-up distribution which is usually different from real data, so scale-factors have to be applied to reweight the Monte Carlo. The uncertainty on the scale factor is given by PRW_DATASF and was about ±1.2%.

8.1.1 Electron uncertainties

Effects of the electron systematics on event yields for demonstrative variables is shown in Figure 81. Section 4.2 explains the reconstruction. Electron systematics include

- The reconstruction and identification uncertainty of the physics objects:
  - EL_EFF_Reco_TOTAL_1NPCOR_PLUS_UNCOR,
  - EL_EFF_ID_TotalCorrUncertainty,
  - EL_EFF_ID_CorrUncertaintyNP (0 to 14) and
  - EL_EFF_ID_SIMPLIFIED_UncorrUncertaintyNP (0 to 15).
- The energy scale and resolution uncertainty:
  - EG_RESOLUTION_ALL,
  - EG_SCALE_ALLCORR,
  - EG_SCALE_E4SCINTILLATOR,
  - EG_SCALE_LARTEMPERATURE_EXTRA2015PRE,
  - EG_SCALE_LARTEMPERATURE_EXTRA2016PRE and
  - EG_SCALE_LARCALIB_EXTRA2015PRE.
- The isolation uncertainty:
  - EL_EFF_Iso_TOTAL_1NPCOR_PLUS_UNCOR.

8.1.2 Muon uncertainties

Effects of the muon systematics on event yields for demonstrative variables is shown in Figure 82. Section 4.3 explains the reconstruction. Muon systematics include

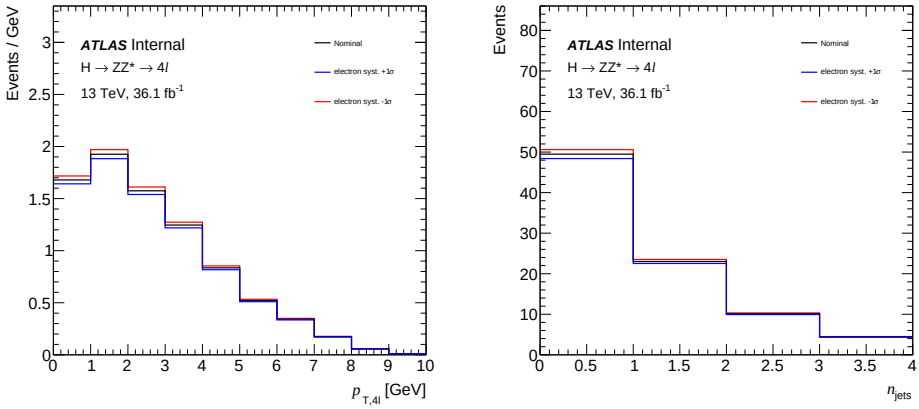

Figure 81: Effect of the electron systematics on the (left) $p_T^{4\ell}$ and (right) N_{jets} yields. The nominal distribution (black) is compared with up (red) and down (blue) variations.

- The reconstruction and identification uncertainty of the physics objects:
  - `MUON_EFF_STAT` and `MUON_EFF_SYS`, and
  - `MUON_EFF_STAT_LOWPT` and `MUON_EFF_SYS_LOWPT` (for muons with $p_{\text{T}} < 15$)
- The energy scale and resolution uncertainty, which are separated between the Inner Detector and Muon System, as well as the uncertainty associated with the track correction:
  - `MUONS_SCALE`,
  - `MUONS_ID`, `MUONS_MS`,
  - `MUON_SAGITTA_RESBIAS` and `MUON_SAGITTA_RHO`.
- The uncertainty of an additional correction for the efficiency of the muon track-to-vertex association (TTVA) cuts:
  - `MUON_TTVA_STAT` and `MUON_TTVA_SYS`.
- The isolation uncertainty:
  - `MUON_ISO_STAT` and `MUON_ISO_SYS`.

8.1.3 Jet uncertainties

Effects of the jet systematics on event yields for demonstrative variables is shown in Figure 83. Section 4.4 explains the reconstruction. Jet systematics include

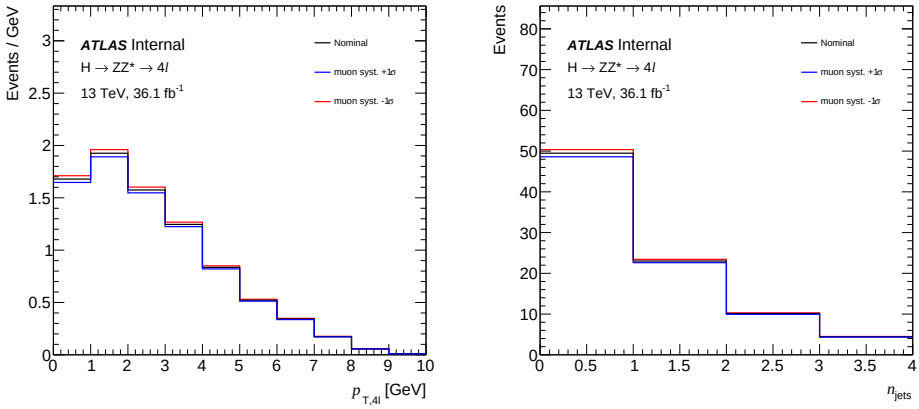

Figure 82: Effect of the muon systematics on the (left) $p_T^{4\ell}$ and (right) N_{jets} yields. The nominal distribution (black) is compared with up (red) and down (blue) variations.

- The jet energy scale uncertainties, explained in detail in [127]:
  - `JET_EtaIntercalibration_Modelling`,
  - `JET_EtaIntercalibration_TotalStat`,
  - `JET_EtaIntercalibration_NonClosure`,
  - `JET_PunchThrough_MC15`,
  - `JET_EffectiveNP` (1 to 8),
  - `JET_SingleParticle_HighPt`,
  - `JET_RelativeNonClosure_MC15`,
  - `JET_BJES_Response`,
  - `JET_Flavor_Composition and JET_Flavor_Response`.
- The jet energy resolution uncertainty:
  - `JET_JER_SINGLE_NP`

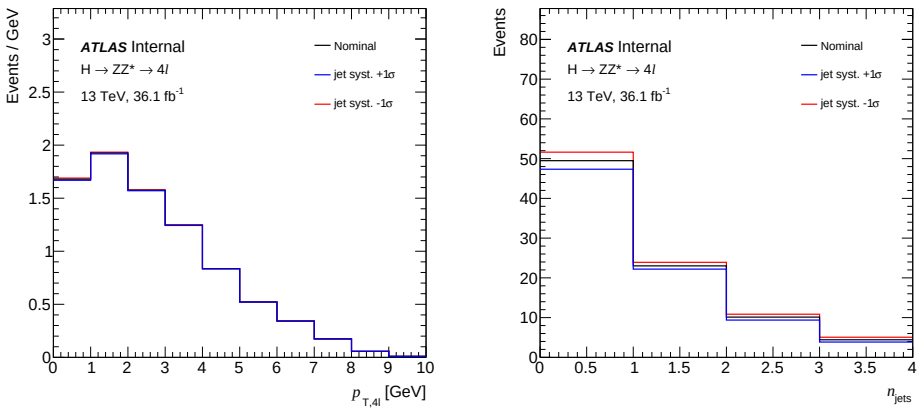

Figure 83: Effect of the jet systematics on the (left) $p_T^{4\ell}$ and (right) N_{jets} yields. The nominal distribution (black) is compared with up (red) and down (blue) variations.

8.2 Background Systematics

Besides the systematics that affect all measured events, there are uncertainties that affect the background events specifically. For the irreducible background (Section 6.1) the major systematics are from the theory predictions for the theory preductions that are modeled with Monte Carlo. For the reducible background (Section 6.2) the major systematics are from the uncertainty on the extrapolation and efficiency factors from the data driven techniques.

See Table 81 for the relative uncertainty each of the systematics has on the backgrounds.

- **Renormalisation and factorisation scales**.

  The irreducible ZZ^* background is simulated with Sherpa2.2 and has NLO accuracy in QCD for zero and one-jet final states, and LO accuracy for two and three-jet final states. In order to take into account missing information from higher order terms, the renormalisation (μR) and factorisation (μF) scales are obtained by varying μR and μF simultaneously between 0.5 and 2 times their nominal value. The uncertainty bands are shown in Fig. 84 for two demonstrative variables. The envelope of all the variations is taken as the final uncertainty.

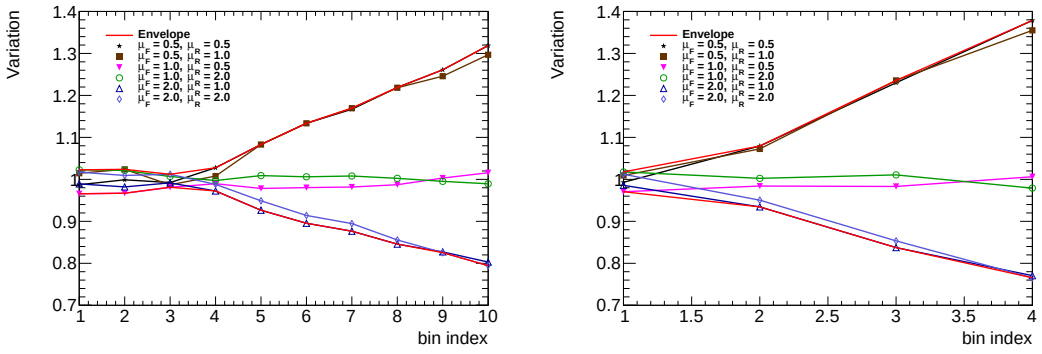

Figure 84: $p_T^{4\ell}$ (left) and N_{jets} (right) scale uncertainties due to missing higher terms in the ZZ^* Monte Carlo. The envelope of the scale variations determines the final uncertaintity.

- **Alternative parton distribution functions**.

  The irreducible ZZ^* background is simulated with Sherpa2.2 with a nominal Parton Distribution Function of NNPDF3.0 NNLO PDF. Uncertainties related to the choice of PDF set are evaluated by taking the Hessian error of the PDF4LHC variations, which is a combination of the eigenvector variations of the baseline NNPDF3.0 set and the central values of alternative (MMHT2014 and CT14) PDF sets. The uncertainty bands are shown in Fig. 84 for

two demonstrative variables. The envelope of the central values of the alternative sets with the Hessian of the variations of the baseline set is taken as the final uncertainty. The Hessian error is given by

$$\Delta X = \sqrt{\sum_i \left(X_{i+} - X_{i-}\right)^2}\,, \tag{8.1}$$

Where X are the up and down PDF variations in the set.

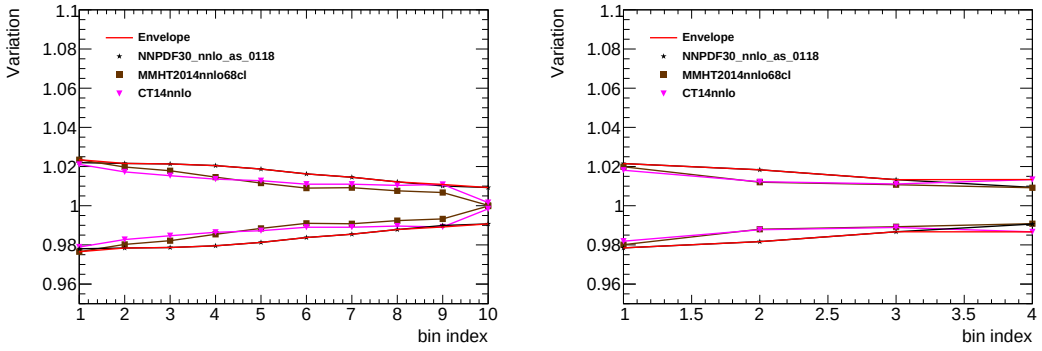

Figure 85: $p_T^{4\ell}$ (left) and N_{jets} (right) PDF theory variations due to alternative choices of Parton Distribution Function in the Monte Carlo. The envelope of the variations determines the final uncertaintity.

- **Reducible background modeling**.

  Systematics from the reducible background yields come from impurities in the sample CRs (e.g. contamination from q in the case of $\ell\ell ee$) as well as Monte Carlo mismodeling.

  For $\ell\ell\mu\mu$, the transfer factors are completely Monte Carlo based, but there are differences in the efficiencies of the inverted d_0 and relaxed isolation control region cuts between data and Monte Carlo. These differences are studied in a dedicated high stats $Z+\mu$ control region, and the difference between data and Monte Carlo is seen to be around 12%, which is taken as the systematic error.

  For $\ell\ell ee$, modeling systematics are taken from calculating the scaled efficiencies $\mathcal{S}_{ij} \cdot \varepsilon_{ij}$ from different generators, in this case Sherpa and MadGraph, and taking their difference. Comparisons between generators are shown in Figure 86. Sherpa is the baseline. The scale factors have a difference of 23% between the two generators, and this is the biggest uncertainity on the final N^{SR}.

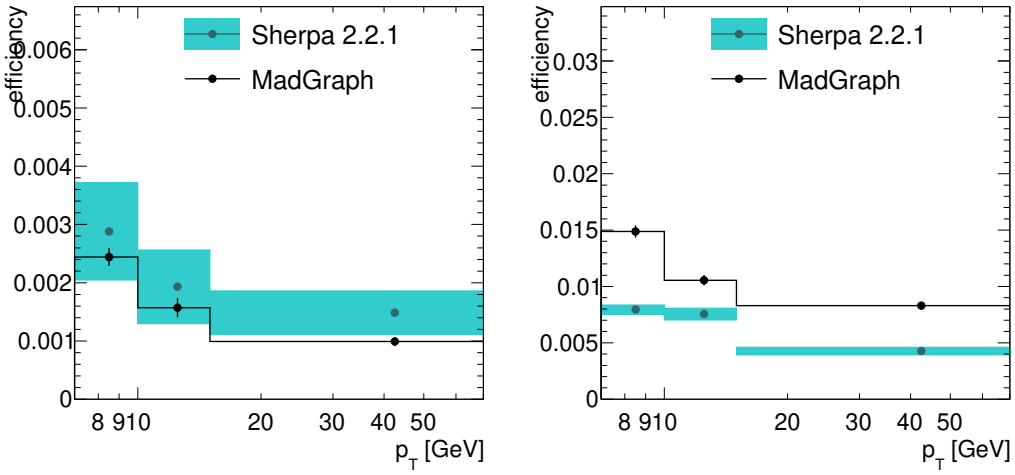

Figure 86: Comparison of scaled efficiencies $\mathcal{S}_{ij} \cdot \varepsilon_{ij}$ obtained from Sherpa 2.2.1 and MadGraph for the f (left) and γ (right) background components. The blue band around Sherpa represents uncertainty from q contamination.

Table 81: Summary of the systematic uncertainties on the inclusive irreducible and reducible backgrounds.

Systematic Uncertainties [%]	Up	Down
ZZ^* μR and μF Scale	4.60	4.60
ZZ^* Alternative PDFs	2.00	2.00
$\ell\ell\mu\mu$ Reducible	6.47	6.47
$\ell\ell ee$ Reducible	12.3	12.3

8.3 Unfolding Systematics

After selecting our $H \to ZZ^* \to 4\ell$ signal events in ATLAS, the $\mathcal{C}$ factors are meant to correct the measured distributions for detector inefficiencies, and the $\mathcal{A}$ factors for the kinematic and geometric acceptance of the detector (See Chapter 7). These factors necessarily contain theoretical assumptions about how the Higgs is modeled. The factors are calculated by using Monte Carlo simulations that encode the Higgs theory assumptions (Section 2.4), so any deviation of the $f_{\text{truth}}(x)$, $f_{\text{fid}}(x)$, and $f_{\text{reco}}(x)$ distributions used by the Monte Carlo from the real $f_{\text{truth}}(x)$, $f_{\text{fid}}(x)$, $f_{\text{reco}}(x)$ in data will introduce a systematic bias.

By modifying the parameters of the underlying models and regenerating the Monte Carlo (or calculating new weights to multiply the Monte Carlo events by) we can measure how much these changes shift the factors up or down. If a variation changes the distribution used in the numerator and denominator in the same way, we expect the resulting uncertainty to be small. For example, $\mathcal{C}$

factors are more model-independent since they only deal with the changes due to reconstruction and not the underlying theory. Any theory assumptions should cancel out between the numerator and denominator, thus making the theory uncertainty small. However the uncertainty from the detector effects will be relatively larger, as they affect the numerator but not the denominator.

See Table 82 for the relative uncertainty each of the systematics has on the nominal unfolding factors.

- **Renormalisation and factorisation scales**.

  The effect due to the imperfect knowledge on the renormalisation (μR) and factorisation (μF) scales is obtained by varying μR and μF simultaneously between 0.5 and 2 times their nominal value. There are 8 total variation, as shown in Fig. 87 and Fig. 88 . The envelope of all the variations is taken as the final uncertainty.

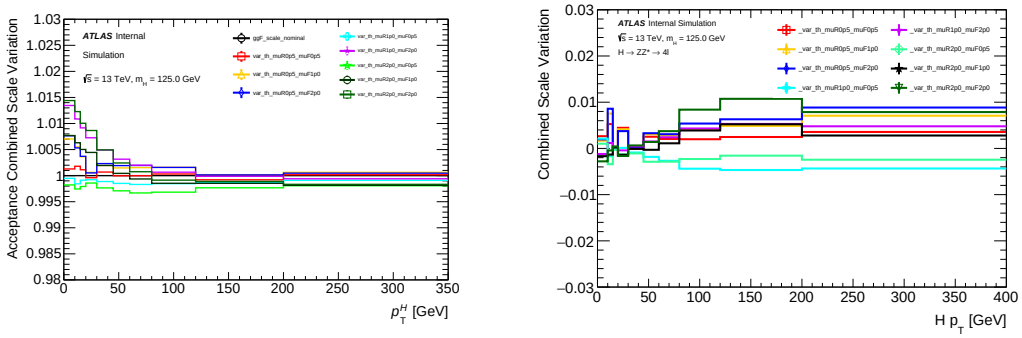

Figure 87: Renormalization (stylized `muR` in the plots) and Factorization (`muF`) scale uncertainties on the Acceptance (left) and Correction (right) factor are shown for variable $p_T^{4\ell}$. The envelope of the 8 scale variations determines the final uncertaintity.

- **Alternative PDFs**.

  Uncertainties related to the choice of PDF set are evaluated by taking the Hessian error of the PDF4LHC variations, which is a combination of the eigenvector variations of the baseline NNPDF3.0 set and the central values of alternative (MMHT2014 and CT14) PDF sets. The uncertainty bands are shown in Fig. 89 and Fig. 810 for the $\mathcal{A}$ and $\mathcal{C}$ factors. The envelope of the central values of the alternative sets with the Hessian of the variations of the baseline set is taken as the final uncertainty. The Hessian error is given by

$$\Delta X = \sqrt{\sum_i \left(X_{i+} - X_{i-}\right)^2}\,, \tag{8.2}$$

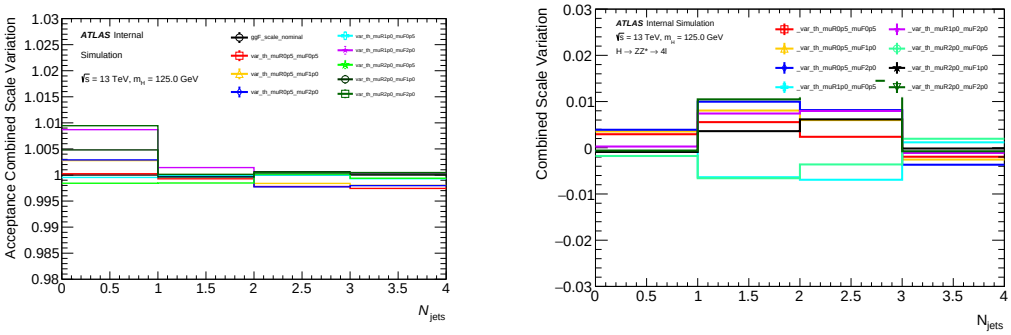

Figure 88: Renormalization (stylized `muR` in the plots) and Factorization (`muF`) scale uncertainties on the Acceptance (left) and Correction (right) factor are shown for variable N_{jets}. The envelope of the 8 scale variations determines the final uncertaintity.

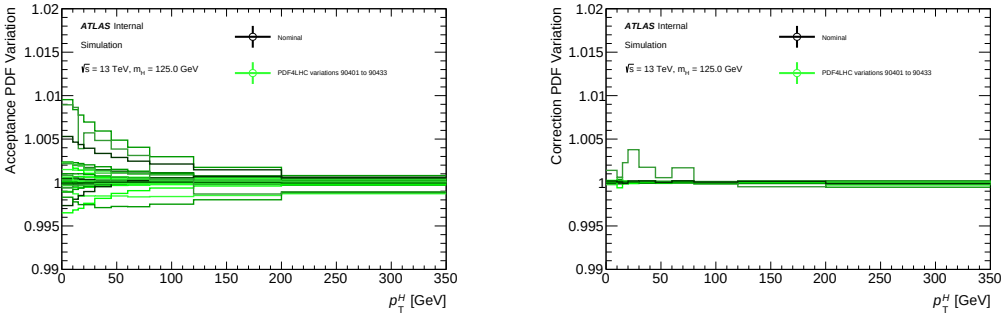

Figure 89: Uncertainties due to the variation of the PDF sets on the Acceptance (left) and Correction (right) factor for variable $p_T^{4\ell}$. Each plot is one of the 32 PDF4LHC variations.

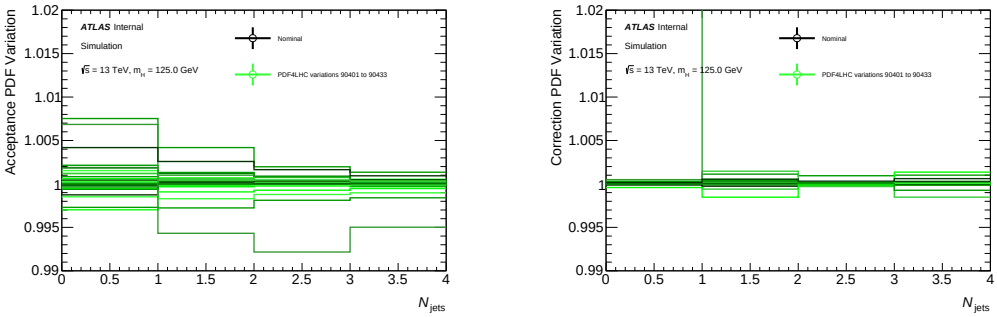

Figure 810: Uncertainties due to the variation of PDF sets on the Acceptance (left) and Correction (right) factor for variable N_{jets}. Each plot is one of the 32 PDF4LHC variations.

- **Higgs mass**.

  The effect of the uncertainty of the Higgs mass on the $\mathcal{A}$ and $\mathcal{C}$ factors is evaluated by shifting the nominal values m_H to the ± 1 σ experimental uncertainty on m_H [35] ($\pm$240 MeV) and re-evaluating the factors.

- **Uncertainties due to detector performance**.

  This uncertainty only applies to $\mathcal{C}$. The effect of the imperfect knowledge on the detector lepton (and jet) identification efficiency, reconstruction efficiency and resolution on the $\mathcal{C}$ factor is estimated as described in Section 10.2 of the event selection and background estimation note [140]. The effect of each component is propagated to the detector correction factor by the corresponding change in N_{reco}.

- **Signal composition.**

  The signal composition uncertainty has to do with the relative fraction of each production mode of the Higgs. Assuming a Standard Model Higgs, the relative fraction has been constrained from recent cross section measurements from ATLAS and CMS. The uncertainties are taken from the measured ratios and correlations between the ggF and the VBF, WH, ZH, $t\bar{t}H$ production modes in Table 9 of reference [141]. This uncertainty applies to the proportion of each production mode within the decay channel, denoted by r_p, where p stands for the production mode.

$$r_p = \frac{\sigma_p}{\sigma_{\text{total}}}, \qquad p = gg\text{F}, \text{VBF}, WH, ZH, t\bar{t}H, b\bar{b}H. \tag{8.3}$$

  The covariance matrix of the errors is $C_{ij} = \sqrt{\Delta\left(\frac{\sigma_i}{\sigma_{gg\to H}}\right)\Delta\left(\frac{\sigma_j}{\sigma_{gg\to H}}\right)}\,\rho_{ij}$. ρ_{ij} are the correlations, and $\Delta\left(\frac{\sigma_i}{\sigma_{gg\to H}}\right)$ are the measured errors [141]. One can then find the eigenvectors of C and use them to turn C into a diagonal matrix where the errors are uncorrelated, and the variances are given by the eigenvalues of C. One can then use the eigenvalue and eigenvectors, with the vector of measured ratios, to get the 68% errors on the r factors.

$$\nu_1 = \left(\vec{\sigma} - \left(\sqrt{\text{Eigenvalues}(C)_1}, 0, 0, 0\right) \times \text{Eigenvectors}(C)^T\right) / \vec{\sigma}_{\text{SM}} \tag{8.4}$$

$$= (1.453, 0.6354, 4.617, 3.408) \tag{8.5}$$

$$\nu_2 = \left(\vec{\sigma} - \left(0, \sqrt{\text{Eigenvalues}(C)_2}, 0, 0\right) \times \text{Eigenvectors}(C)^T\right) / \vec{\sigma}_{\text{SM}} \tag{8.6}$$

$$= (0.9989, 0.4674, 3.293, 3.149) \tag{8.7}$$

$$\nu_3 = \left(\vec{\sigma} - \left(0, 0, \sqrt{\text{Eigenvalues}(C)_3}, 0\right) \times \text{Eigenvectors}(C)^T\right) / \vec{\sigma}_{\text{SM}} \tag{8.8}$$

$$= (1.447, 0.2426, 2.694, 3.287) \tag{8.9}$$

$$\nu_4 = \left(\vec{\sigma} - \left(0, 0, 0, \sqrt{\text{Eigenvalues}(C)_4}\right) \times \text{Eigenvectors}(C)^T\right) / \vec{\sigma}_{\text{SM}} \tag{8.10}$$

$$= (1.332, 0.8391, 3.06, 2.331) \tag{8.11}$$

ν_i are the eigenvector variations, while $\vec{\sigma} = \left(\frac{\sigma_{\text{VBF}}}{\sigma_{gg\to H}}, \frac{\sigma_{WH}}{\sigma_{gg\to H}}, \frac{\sigma_{ZH}}{\sigma_{gg\to H}}, \frac{\sigma_{ttH}}{\sigma_{gg\to H}}\right)$, and $\vec{\sigma}_{\text{SM}}$ are the corresponding vectors of the measured (SM) ratios, respectively. $\vec{\sigma}/\vec{\sigma}_{\text{SM}}$ is the element by element normalization of the measured ratios to the SM ratios.

The symmetric up and down variations on the r factors per production mode, r_{ip}, are then calculated by

$$r_{ip+} = \frac{\sigma_p \times \nu_{ip}}{\sum_j \sigma_j \times \nu_{ij}}, \qquad r_{ip-} = 2r_p - \frac{\sigma_p \times \nu_{ip}}{\sum_j \sigma_j \times \nu_{ij}}, \tag{8.12}$$

where i is one of the four eigenvector variation, and p is the production mode ggF, VBF, WH, ZH, $t\bar{t}H$, or $b\bar{b}H$. For gg$F$ and $b\bar{b}H$, $\nu_{ip} = 1.0$ always. r_p is the nominal SM fraction of the production mode as determined by YR4.

To calculate the effect of the variations on the $\mathcal{A}$ and $\mathcal{C}$ factors, the formula to use is

$$\mathcal{F}_i = \sum_p \mathcal{F}_p \times r_{ip} \qquad \Delta\mathcal{F} = \sqrt{\sum_i \left(\frac{\mathcal{F}_i - \mathcal{F}}{\mathcal{F}}\right)^2} \tag{8.13}$$

Where $\mathcal{F}$ and $\mathcal{F}_p$ is the nominal $\mathcal{A}$ or $\mathcal{C}$ factor for the the sum of production modes and each production mode p, respectively. $\mathcal{F}_i$ is one of the four variations of the factor.

Table 82: Summary of the systematic uncertainties on the inclusive $\mathcal{A}$ and $\mathcal{C}$ factors for the fiducial analysis.

Systematic Uncertainties [%]		
	Up	Down
Detector correction factors, $\mathcal{C}$		
Experimental, muons	2.74	2.24
Experimental, electrons	3.15	2.65
Higgs boson mass	0.04	0.04
Signal composition	1.20	1.20
μR and μF Scale	0.13	0.14
Alternative PDFs	0.07	0.07
MC stats	0.18	0.18
Acceptance factors, $\mathcal{A}$		
Higgs boson mass	0.62	0.62
Signal composition	0.57	0.57
μR and μF Scale	0.32	0.47
Alternative PDFs	0.66	0.66
MC stats	0.06	0.06

Chapter 9

Statistical Methods

The number of Higgs bosons produced for a given integrated luminosity is N_s, a random variable that follows a Poisson distribution, $\text{Pois}(N_s|N_{\text{truth}})$. The expected number of Higgs events is $N_{\text{truth}} = \langle N_s \rangle = \sigma \times \mathcal{L}_{\text{int}}$, where σ is the total Higgs cross section, and $\mathcal{L}_{\text{int}}$ is the integrated luminosity. As explained in Section 7.1, ATLAS does not directly sample N_s due to efficiency and acceptance effects, so the number of expected signal events in ATLAS is actually $N_{\text{reco}} = N_{\text{truth}} \times \text{BR}(H \to 4\ell) \times \varepsilon$, where $\text{BR}(H \to 4\ell)$ is the branching ratio to the 4ℓ final state, and ε is the efficiency and acceptance of ATLAS in the final state.

In this chapter, we describe the method used to extract the best estimate for σ as well as the 68% confidence interval on that estimate after having collected the data N, which is the number of signal and background events. The method uses the maximum likelihood estimator, which calculates the value of σ that maximizes the likelihood function $L(N|\sigma)$ given the measured events N, where N is the sum of the signal events N_s and background events N_b. In the following chapter, uppercase variables will usually represent observables, while lowercase variables will represent parameters. A hat over a parameter, e.g. $\widehat{\sigma}$, represents an estimate of the parameter.

Section 9.1 describes how to calculate the maximum likelihood estimator in a simple example, while Section 9.2 describes the method after including backgrounds and nuisance parameters. Sections 9.3 and 9.4 describe how the analysis extracts the inclusive and differential cross section estimate from data, both fiducially and totally. Finally Section 9.5 uses simulated Asimov data [145] to calculate the expected cross section uncertainties. Results using actual data are presented in Chapter 10.

9.1 Simple Example

If we could measure the total number of Higgs events produced at ATLAS with no systematic uncertainties, no background, and no acceptance and efficiency loss, then N would equal N_s, and the likelihood function would be very simple.

$$L(N_s|\sigma) = \text{Pois}(N_s|\sigma) = \frac{e^{-\sigma\mathcal{L}_{\text{int}}}(\sigma\mathcal{L}_{\text{int}})^{N_s}}{N_s!} \tag{9.1}$$

Often in the analysis, rather than maximizing the likelihood, we will minimize the negative log likelihood. This will give the same result, since $\ln(x)$ is monotonically increasing with x and whatever is the maximum of the likelihood function will be the minimum of the negative log likelihood function. Why we would want to do this transformation will become clear when we start computing confidence intervals. For now we will stick with the standard likelihood. The best estimate for σ by maximizing L is:

$$\frac{-\partial \ln L}{\partial\sigma}\Big|_{\widehat{\sigma}} = 0 \rightarrow \frac{\partial}{\partial\sigma}\left(\sigma\mathcal{L}_{\text{int}} - N_s \ln \sigma\mathcal{L}_{\text{int}} + \ln N_s!\right) = 0$$
$$\widehat{\sigma} = \frac{N_s}{\mathcal{L}_{\text{int}}}$$

Since N_s is a random variable, our calculated $\widehat{\sigma}$ is a random variable as well (since it is a function of N_s). Any one $\widehat{\sigma}$ we calculate is probably not going to be the true Higgs cross section σ. To demonstrate, imagine a world without measurement error where $\sigma = 55.6\text{pb}$ and $\mathcal{L}_{\text{int}} = 36.1\text{fb}^{-1}$ exactly. That would give an expected mean of $\langle N_s\rangle = 2,007,160$. The probably of getting this number of events exactly from a measurement is only 0.028%.

In addition to the best fit value then, we need to quote the confidence interval around the measurement. A 68% confidence interval (CI) in the frequentist sense means that 68% of the intervals we construct from repeated estimates $\widehat{\sigma}$ at the given $\mathcal{L}_{\text{int}}$ are expected to contain the true value of σ. The interval itself is a random variable, just like $\widehat{\sigma}$. There are many ways of constructing the confidence interval, as well as approximating it. The most popular way in particle physics of calculating a confidence interval is through the Feldman-Cousins method based on Neyman Construction using pseudo-experiments [142, 143] as explained in the citation, but as our Monte Carlo resources are limited, we approximate confidence intervals using some asymptotic assumptions.

The approximation depends on the properties of the maximum likelihood estimator (MLE) $\widehat{\sigma}$ defined above, specifically its unbiased asymptotic normality. What this means is that in the limit

of large N_s (asymptotic), the probability distribution function of $\widehat{\sigma}$ will approach a Gaussian distribution (normality) with the mean centered at the true σ (unbiased). The variance of $\widehat{\sigma}$ will also approach $\left(-E\left[\frac{\partial^2 \ln L}{\partial \sigma^2}\right]\right)^{-1}$, where $-E\left[\frac{\partial^2 \ln L}{\partial \sigma^2}\right]$ is the negative expectation value of the second derivative of the log likelihood function. This value is known as the Hessian, H. When doing negative log likelihood minimization with ROOT `MINUIT` [144], calling `HESSE` to calculate the errors returns the Hessian evaluated at the global minimum. So using this assumption of normality around the global minimum, the confidence interval is

$$\widehat{\sigma} \pm \frac{1}{\sqrt{-\frac{\partial^2 \ln L}{\partial \sigma^2}\Big|_{\widehat{\sigma}}}} = \widehat{\sigma} \pm \sqrt{H(\widehat{\sigma})^{-1}} \tag{9.2}$$

And for the example of a Poisson distributed random variable above, the approximate 68% confidence interval will be

$$\frac{\partial^2 \ln L}{\partial \sigma^2}\Big|_{\widehat{\sigma}} = \frac{-N_s}{\widehat{\sigma}^2} \qquad so \qquad \widehat{\sigma} \pm \frac{\widehat{\sigma}}{\sqrt{N_s}}$$
$$\mathrm{CI}(\widehat{\sigma}) = \frac{N_s}{\mathcal{L}_{\mathrm{int}}} \pm \frac{\sqrt{N_s}}{\mathcal{L}_{\mathrm{int}}}$$

9.2 Signal Extraction with Backgrounds and Nuisance Parameters

The presence of backgrounds means that the measured number events of $N \neq N_s$, but rather $N = N_s + \sum_i N_b^i$. The addition of a background process adds a new, distinct class of events to the analysis besides the signal event class. Each background N_b^i is a random variable with its own Poisson probability distribution, with expected value $n_{b,i}$, with its own distributions for the observables. The fact that the signal and background classes have different shapes for their invariant mass distributions provides a way for the number of events in each class to be extracted by the maximum likelihood method. For simplicity of notation let's also call the expected number of signal events n_s and define the expected number of total events to be $n = n_s + \sum_i n_{b,i}$. The likelihood changes in the following way

$$L(N, m_{4\ell}|n_s, n_{b,i}) = \mathrm{Pois}(N|n) \prod_j^{\mathrm{events}} \left(\frac{n_s}{n} F_s(m_{4\ell}^j) + \sum_i \frac{n_{b,i}}{n} F_{b,i}(m_{4\ell}^j) \right) \tag{9.3}$$

Where F_s and $F_{b,i}$ are the probability distribution functions (PDFs) for the $m_{4\ell}$ shape of both the signal and the background. F_s will have a resonance at 125 GeV while all the backgrounds shapes

will not. If we continue to imagine that we had no systematic uncertainties and no acceptance and efficiency loss, then $n_s = \sigma\mathcal{L}_{\text{int}}$ still, and is the only parameter we care to extract. Though the likelihood depends on the background parameters, all of the $n_{b,i}$ are considered nuisance parameters, which are parameters we are not interested in extracting but which add additional degrees of freedom to the analysis. The background parameters are not completely free parameters either, but are constrained to float between certain values, as will be explained later. To deal with the nuisance parameters when extracting the best fit value and confidence interval for n_s, we will use the profile likelihood ratio fit [145].

The profile likelihood ratio is defined as

$$\lambda(n_s) = \frac{L(N, m_{4\ell}|n_s, \widehat{\widehat{n_{b,i}}})}{L(N, m_{4\ell}|\widehat{n_s}, \widehat{n_{b,i}})} \tag{9.4}$$

The denominator is the likelihood function at the global maximum where all the parameters have been set to their maximum likelihood estimate (MLE). In the numerator, $\widehat{\widehat{n_{b,i}}}$ are the MLEs of the nuisance parameters for a given value of n_s, i.e. for each different value of n_s, the likelihood is re-maximized at that point to find the MLE of the nuisance parameters. $\lambda(n_s)$ is now a function of one variable, equal to 1 at the global maximum and $1 > \lambda \geq 0$ at any other other value of n_s. In order to make good use of some asymptotic properties of the profile likelihood ratio, we will transform the variable to the -2 log likelihood, $-2\ln\lambda(n_s)$.

Minimizing $-2\ln\lambda(n_s)$ will find the best estimate for $\widehat{\sigma} = \frac{\widehat{n_s}}{\mathcal{L}_{\text{int}}}$, while getting the confidence interval requires calculating an approximation of the PDF of $-2\ln\lambda(n_s)$. $-2\ln\lambda(n_s)$ is a random variable, since it is a function of the random variables N and $m_{4\ell}$. To approximate the PDF, we use Wilk's Theorem [136] which states that in the limit of large N, the variable $-2\ln\lambda(n_s)$ will be distributed like a χ^2 variable with one degree of freedom. For a χ^2 distributions, $\chi^2 = 1$ corresponds to a confidence level of 68.3% while $\chi^2 = 4$ corresponds to a confidence level of 95.5%.

In order to calculate the 68% confidence interval then, it is necessary to find the values of n_s^* such that $-2\ln\lambda(n_s^*) + 2\ln\lambda(\widehat{n_s}) = 1$. When doing profile likelihood ratio minimization with ROOT `MINUIT` [144], calling `MINOS` will find the n_s^* (both the lower and upper bound) which return $-2\ln\lambda_{\text{min}} + 1$. `MINOS` follows the $-2\ln\lambda(n_s)$ function out from the global minimum to find where it crosses +1 value, instead of using the curvature at the global minimum and assuming a parabolic shape, like with `HESSE`.

9.2.1 Adding Systematic Uncertainties

When calculating the estimate of the cross section, we have to divide out the integrated luminosity from $\widehat{n_s}$. The integrated luminosity is not a constant, but a measured quantity with its own uncertainty. To take into account the uncertainty of the luminosity, we add a Gaussian constraint to the likelihood in the form of

$$L(N, m_{4\ell}|n_s, n_{b,i}, \theta_{\mathcal{L}}) = \text{Pois}(N|n) \times P(m^j_{4\ell}|s, n_{b,i}) \times \text{Gaus}(\Theta_{\mathcal{L}}|\theta_{\mathcal{L}}, \alpha_{\mathcal{L}}) \tag{9.5}$$

$$P(m^j_{4\ell}|s, n_{b,i}) = \prod_j^{\text{events}} \left(\frac{s}{n} F_s(m^j_{4\ell}) + \sum_i \frac{n_{b,i}}{n} F_{b,i}(m^j_{4\ell}) \right) \tag{9.6}$$

$\Theta_{\mathcal{L}}$ is a Gaussian random variable with mean $\theta_{\mathcal{L}}$ and standard deviation $\alpha_{\mathcal{L}}$. $\Theta_{\mathcal{L}}$ represents the percent deviation from the measured value of the luminosity, and so in the likelihood is $\Theta_{\mathcal{L}} = 0$. During the fit, the parameter $\theta_{\mathcal{L}}$, the mean deviation, is allowed to float in order to find the global best fit, and may not necessarily be 0. It also acts as a constraint when doing a maximum likelihood fit, as values too far away from 0 become excessively 'unlikely'. $\alpha_{\mathcal{L}}$ is always fixed and is gotten from experimental measurements. The number of expected signal events in the likelihood are now constructed as

$$s = n_s(1 + \theta_{\mathcal{L}} \cdot \alpha_{\mathcal{L}}) = \sigma \mathcal{L}_{\text{int}}(1 + \theta_{\mathcal{L}} \cdot \alpha_{\mathcal{L}}) \tag{9.7}$$

n_s is the nominal number of expected signal events, and s is the expected number of signal events taking into account variation due to the uncertainty on the luminosity. The notation change in the likelihood from $n_s \to s$ reflects this difference. The value of $\mathcal{L}_{\text{int}}$ is fixed while its variation is taken care of by the parameter $\theta_{\mathcal{L}}$. When doing the profile likelihood ratio fit, $\theta_{\mathcal{L}}$ and $n_{b,i}$ are the nuisance parameters which are constrained by experimental data, while σ is the parameter of interest to be estimated. Adding more nuisance parameters has the tendency to widen the confidence interval gotten from the profile fit.

9.3 Inclusive Cross Section Measurement

For the total inclusive cross section, the parameter of interest is

$$\sigma = \frac{n_s}{\mathcal{L}_{\text{int}} \cdot \text{BR}(H \to 4\ell) \cdot \mathcal{A} \cdot \mathcal{C}} \tag{9.8}$$

BR($H \to 4\ell$) is the branching ratio to 4ℓ, $\mathcal{C}$ is a detector correction factor accounting for trigger, reconstruction and identification efficiencies for detecting the final state, and $\mathcal{A}$ is the kinematic and geometric acceptance, as explained in Chapter 7. All of the parameters on the right side of the equation have associated systematics which take into account theory uncertainties and detector/experimental uncertainties as explained in Chapter 8.

The acceptance factor $\mathcal{A}$ cannot be constrained by data since most of the non-fiducial events are not detectable (their leptons are too soft or too forward). The acceptance factor therefore depends fully on the simulations used, which introduces a model dependence. To get a more model independent measurement, we calculate the fiducial inclusive cross section instead, as follows

$$\sigma_{\text{fid}} = \frac{n_s}{\mathcal{L}_{\text{int}} \cdot \mathcal{C}} \tag{9.9}$$

9.3.1 The Likelihood function

The likelihood function for the cross section extraction is

$$L = \text{Pois}(N|s + \sum_i b_i) \times P(m^j_{4\ell}|s, b_i) \times \prod_{i=1}^{\text{bkgs}} \text{Gaus}(N_{b,i}|n_{b,i}, \alpha_i) \times \prod_{k=1}^{\text{syst}} \text{Gaus}(\Theta_k|\theta_k, \alpha_k) \tag{9.10}$$

$$P(m^j_{4\ell}|s, b_i) = \prod_j^{\text{events}} \left(\frac{s}{n} F_s(m^j_{4\ell}) + \sum_i \frac{b_i}{n} F_{b,i}(m^j_{4\ell}) \right) \tag{9.11}$$

$$s = n_s \prod_{k=0}^{\text{syst}} (1 + \alpha_{s,k} \cdot \theta_{s,k}) \qquad b_i = n_{b,i} \prod_{k=0}^{\text{syst}} (1 + \alpha_{i,k} \cdot \theta_{i,k}) \tag{9.12}$$

$$\tag{9.13}$$

The first term of the likelihood function is a Poisson function that gives the probability to observe N data events given an expectation of $s + \sum_i b_i$ events (after selection within the mass window $115.0 < m_{4\ell} < 130.0\,\text{GeV}$).

The second term is the signal and background fraction extraction. It is used to fit the N data events to the respective fraction of signal and background events. The invariant mass PDFs F_s and $F_{b,i}$ (for the Higgs boson signal and the background processes, respectively) are fit to the $m_{4\ell}$ distribution in data. The signal shape and most of the background shapes are obtained from the simulated samples described in Chapter 2, while some of the backgrounds in the $\ell\ell + ee$ channel are derived from control regions in data, as described in Section 6.4.

The third term imposes Gaussian constraints on the normalizations of the backgrounds. These constraints come from measurements of $N_{b,i}$ from control region fits calculated in Chapter 6.

The fourth term adds systematic uncertainties as described in Chapter 8. These include luminosity and branching ratio uncertainties, detector reconstruction and identification uncertainties, model and theory uncertainties, background shape uncertainties, transfer factor uncertainties, and $\mathcal{A}/\mathcal{C}$ factor uncertainties. Equations 9.12 and 9.13 show how the θ_k parameters affect the expected number of events. Some θ_k only modify n_s, and other θ_k only modify the background events, $n_{b,i}$.

9.3.2 Parameter Estimation

We use the log likelihood method to estimate σ_{fid}. The fiducial measurement is explained in this section, and the total measurement is explained in Section 9.6.

First, we need to rewrite n_s in Equation 9.10 in terms of our parameter of interest. For the fiducial inclusive cross section

$$n_s = \sigma_{\text{fid}} \cdot \mathcal{L}_{\text{int}} \sum_p r_p^{\text{fid}} \cdot \mathcal{C}_p \tag{9.14}$$

p is the production mode of the Higgs, which in this case can be ggF, VBF, WH,ZH,$t\bar{t}H$, or $b\bar{b}H$. r_p is the fraction of the Higgs cross section from that production mode i.e. $r_p = \frac{\sigma_p}{\sigma}$ and is calculated using the latest theory predictions from the YR4 [17]. $\mathcal{C}_p$ is the correction factor calculated only using the Monte Carlo events of the production mode p. Figure 74 shows $\mathcal{C}_p$ for each production mode and decay channel.

From the likelihood equation 9.10, we then build the profile likelihood function to find the best fit value for the fiducial cross section, as well as the confidence interval.

$$-2\ln\lambda\left(\sigma_{\text{fid}}\right) = -2\ln\frac{L\left(N, N_{b,i}, m_{4\ell}|\sigma_{\text{fid}}, \widehat{\widehat{n_{b,i}}}, \widehat{\widehat{\theta}}_k\right)}{L\left(N, N_{b,i}, m_{4\ell}|\widehat{\sigma}_{\text{fid}}, \widehat{n_{b,i}}, \widehat{\theta}_k\right)} \tag{9.15}$$

Where all $n_{b,i}$ and θ_k are nuisance parameters. The result for the cross section measurement is the best fit estimate, $\widehat{\sigma}_{\text{fid}}$, which minimizes $-2\ln\lambda\left(\sigma_{\text{fid}}\right)$. The result is found by using ROOT's `MINUIT MIGRAD` [144] function, which uses gradient descent to numerically minimize Equation 9.15. The 68% confidence interval is calculated by assuming that $-2\ln\lambda\left(\sigma_{\text{fid}}\right)$ follows a χ^2 distribution with one degree of freedom (due to Wilk's Theorem[136]). We use ROOT's `MINUIT MINOS` to crawl out from the global minimum of $-2\ln\lambda_{\text{min}}$ to find at what value of σ_{fid} it crosses $-2\ln\lambda_{\text{min}} + 1$, which corresponds to the 68% confidence level of a χ^2 distribution.

Section 9.5 shows the above method extracting a cross section and its confidence interval on simulated Asimov data. The results for the inclusive cross section from real data is shown in Chapter 10.

9.4 Differential Cross Section Measurement

For the differential cross section measurements, the fiducial measurement is explained in this section, and the total measurement is explained in Section 9.6.

When estimating the fiducial differential cross section, the method is almost exactly the same as for the fiducial inclusive cross section measurement as explained in Section 9.3. For every differential variable, the number of cross section parameters to estimate is equal to the number of bins. Each bin gets its own likelihood function, and each likelihood function has the same form as Equation 9.10. Rather than using all N events that pass the event selection as input to the likelihood, only the events that fall within the bin are used. The number of background events calculated from control regions must also be calculated per bin, as well as all the uncertainties that will be included as nuisance parameters.

The number of expected events for each bin i is

$$n_s^i = \sigma_{\text{fid},i} \cdot \mathcal{L}_{\text{int}} \cdot \sum_p r_{p,i}^{\text{fid}} \cdot \mathcal{C}_{p,i} \tag{9.16}$$

$\sigma_{\text{fid},i}$ is the fiducial cross section in bin i (as well as our parameter of interest), and $r_{p,i}^{\text{fid}}$ and $\mathcal{C}_{p,i}$ are the production mode fractions and correction factors for bin i. All factors are calculated from Higgs Monte Carlo samples. Figures 91, 92 show the $r_{p,i}^{\text{fid}}$ factors for all differential variables, and Figures 93, 94 show the $\mathcal{C}_{p,i}$ for all differential variables.

To extract the cross section for each bin, the profile-likelihood-ratio $\lambda(\sigma_{\text{fid},i})$ is formed and $-2\ln\lambda\left(\sigma_{\text{fid},i}\right)$ is minimized. Section 9.5 shows the expected results for each bin using Asimov simulations. The results for the differential cross section from real data are shown in Chapter 10.

9.5 Tests on Asimov Data

To estimate the expected cross section and its uncertainty in each bin, one can simulate many pseudo-experiments, find the best fit cross section, $\widehat{\sigma_{\text{fid}}}$, for each pseudo-experiment, and then plot the values in a histogram. The mean of $\widehat{\sigma_{\text{fid}}}$ would be the expected cross section, and the 68% confidence interval would be constructed by taking 68% of the experiments around the median of

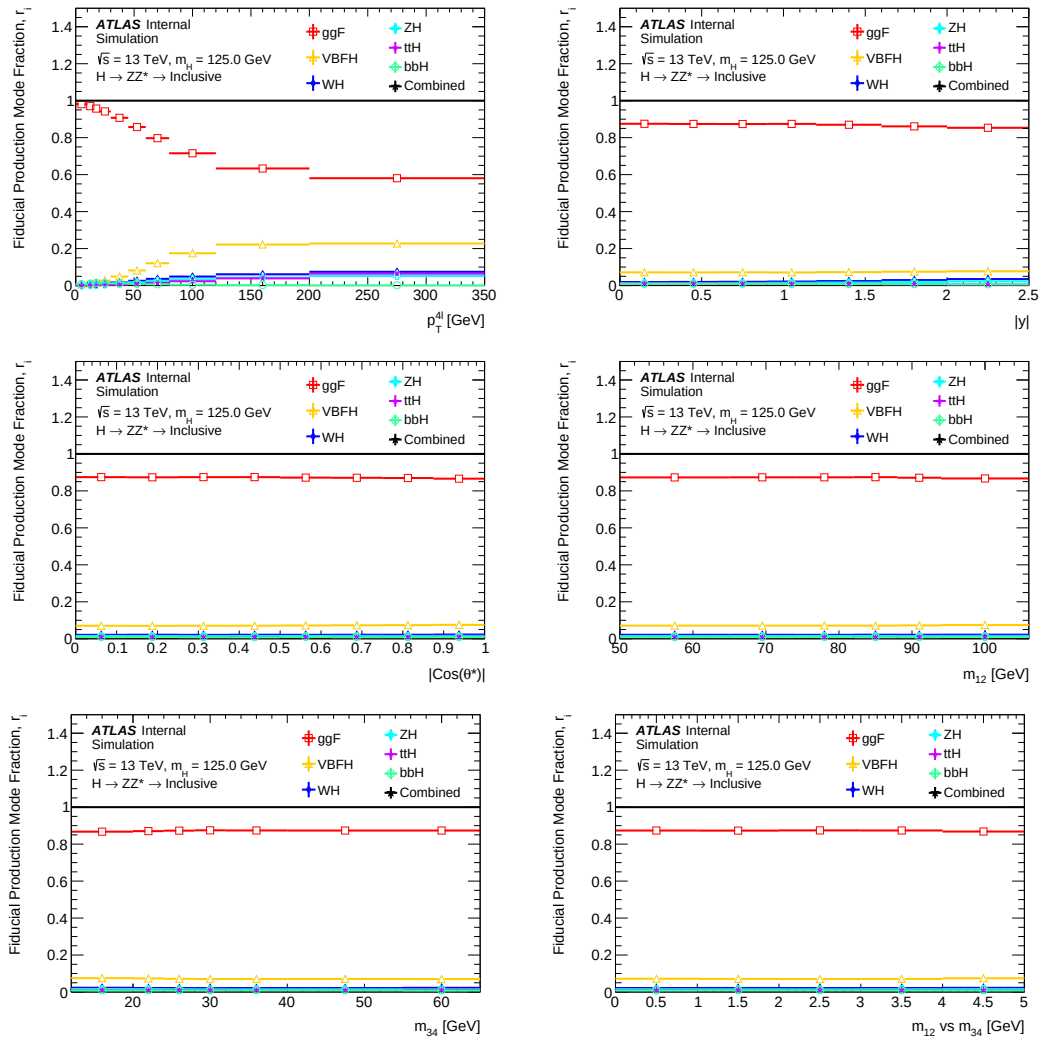

Figure 91: Higgs boson production mode fractions as a function of variables p_T (a), $|y|$ (b), $|cos(\theta^*)|$ (c), m_{12} (d), m_{34} (e), and m_{12}vs.m_{34} (f). A SM Higgs with $m_H = 125.0\,\text{GeV}$ has been assumed.

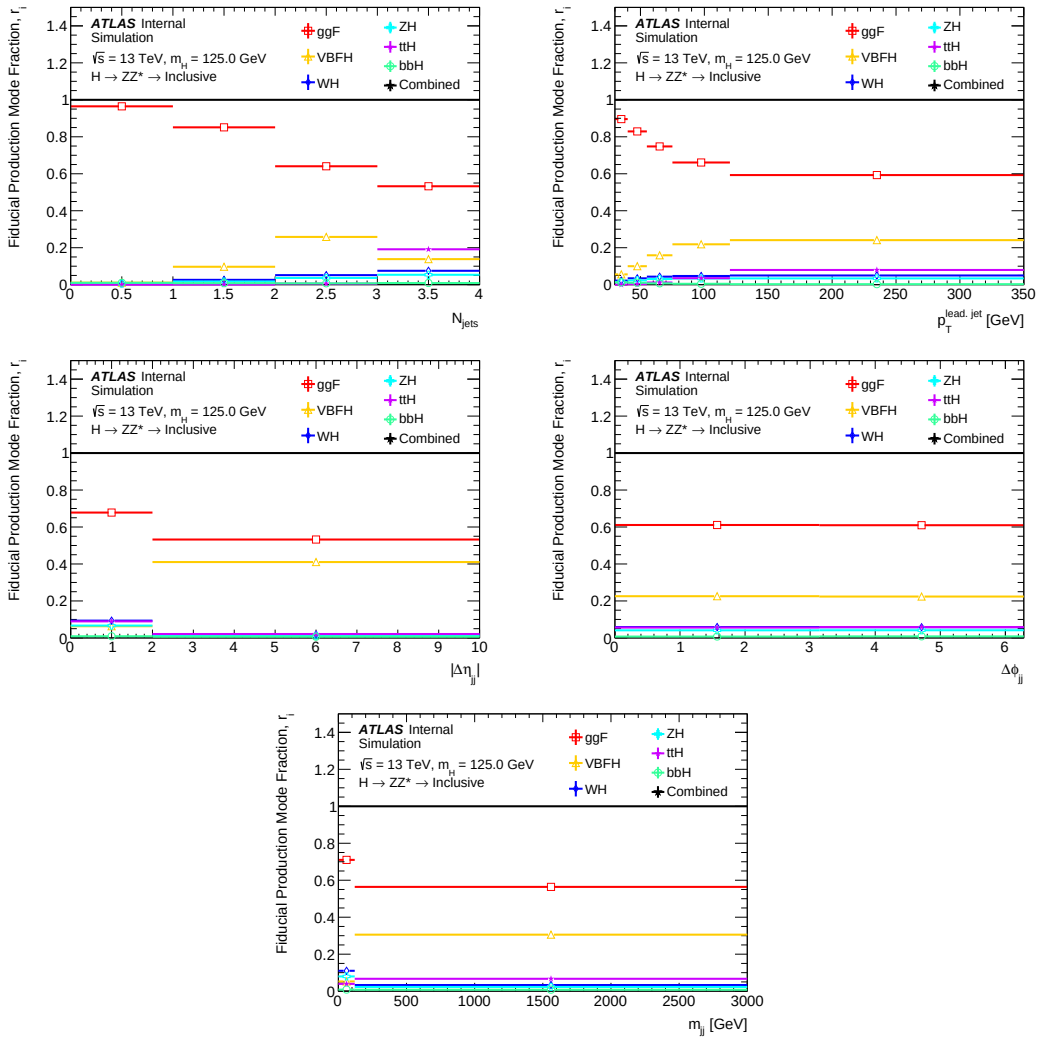

Figure 92: Higgs boson production mode fractions as a function of variables N_{jets} (a), $p_T^{\text{lead. jet}}$ (b), $\Delta\eta_{jj}$ (c), $\Delta\phi_{jj}$ (d), m_{jj} (e). A SM Higgs with $m_H = 125.0\,\text{GeV}$ has been assumed.

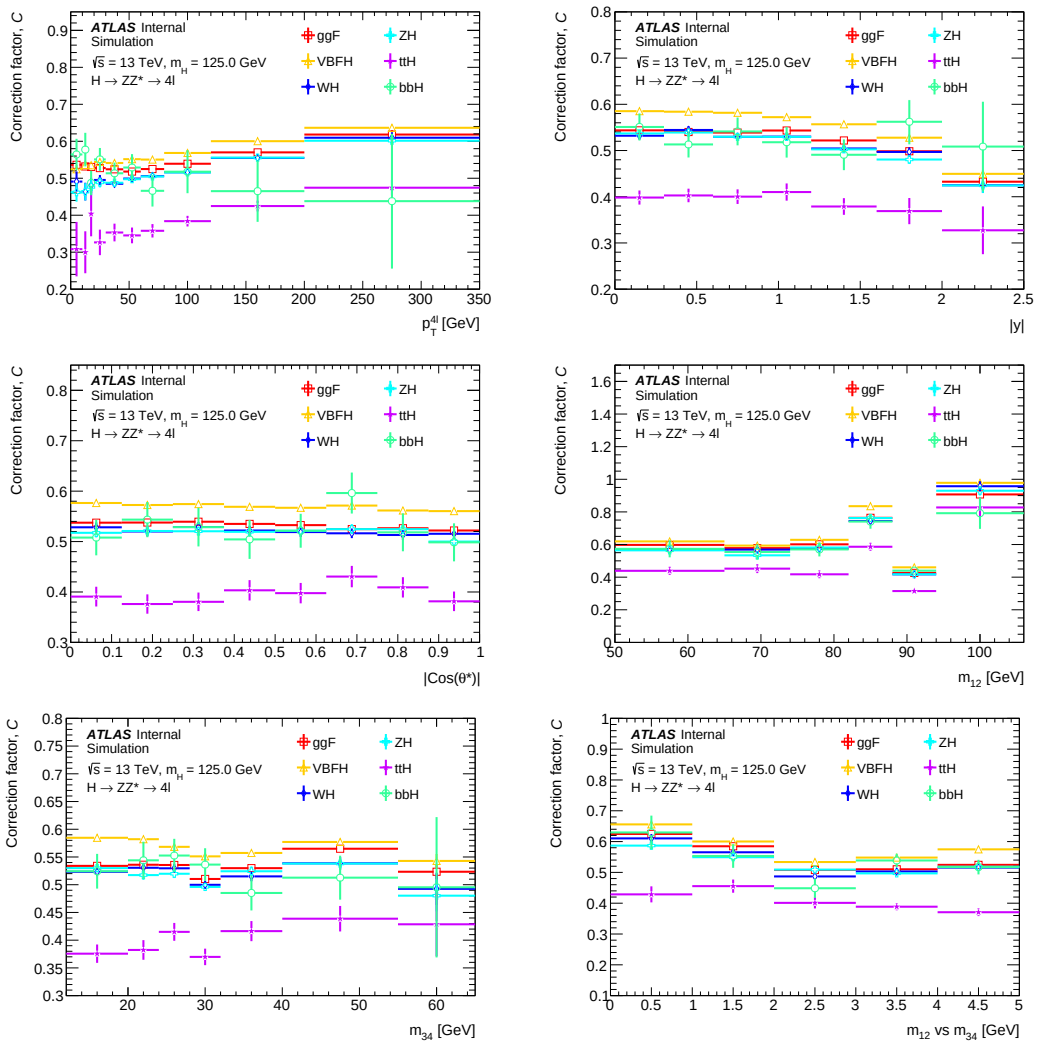

Figure 93: Differential $\mathcal{C}$ factors for variables p_T (a), $|y|$ (b), $|cos(\theta^*)|$ (c), m_{12} (d), m_{34} (e) and m_{12}vs.m_{34} (f) in each bin. A SM Higgs with $m_H = 125.0\,\text{GeV}$ has been assumed.

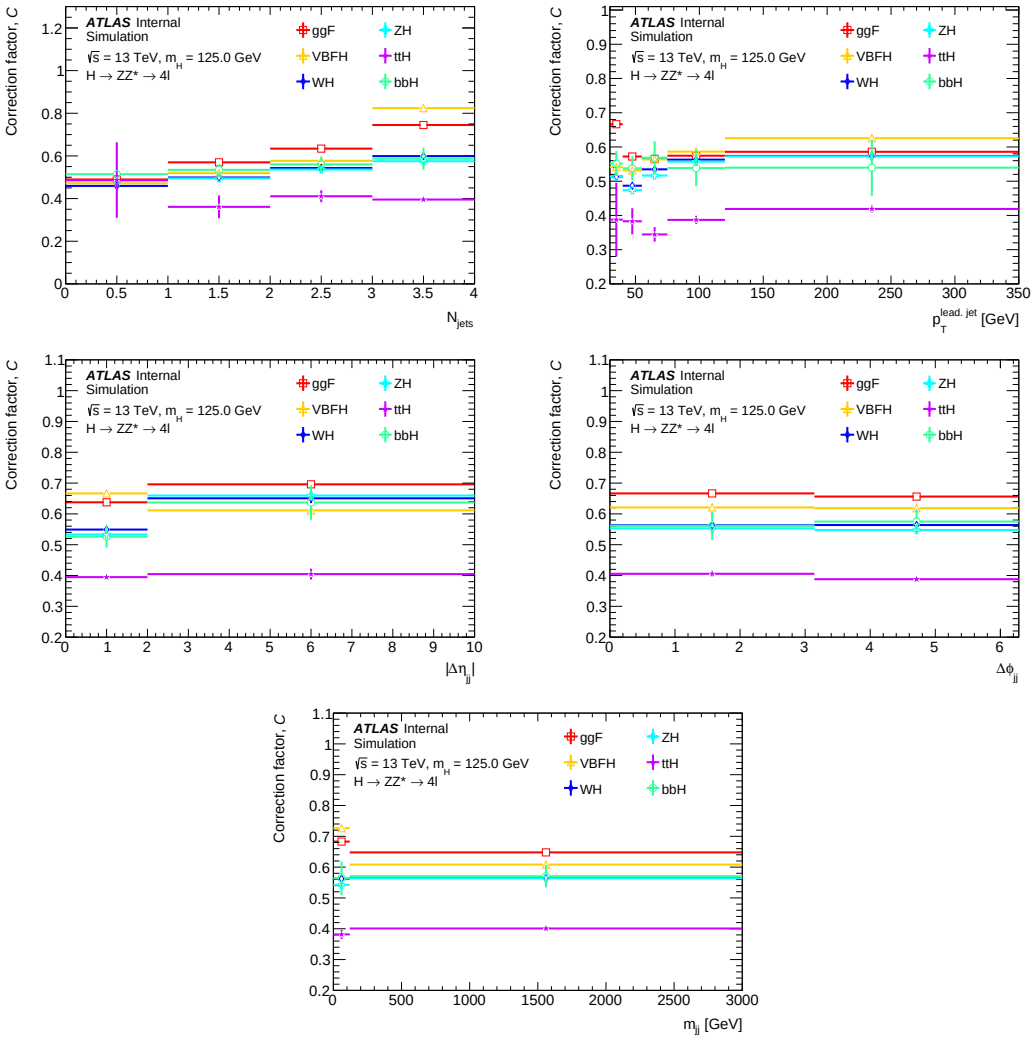

Figure 94: Differential $\mathcal{C}$ factors for N_{jets} (a), $p_T^{\text{lead. jet}}$ (b), $\Delta\eta_{jj}$ (c), $\Delta\phi_{jj}$ (d), m_{jj} (e) in each bin. A SM Higgs with $m_H = 125.0\,\text{GeV}$ has been assumed.

$\widehat{\sigma_{\text{fid}}}$. The mean of $\widehat{\sigma_{\text{fid}}}$, in the asymptotic limit, should be the "truth" σ_{fid} used to generate the samples, unless the method used to compute $\widehat{\sigma_{\text{fid}}}$ is biased.

To save time and computer resources, we instead use the "Asimov dataset" [145] to calculate the expected cross section uncertainty in each bin. The Asimov dataset assumes that the asymptotic assumptions are true, and automatically sets the PDF of $\widehat{\sigma_{\text{fid}}}$ to be its asymptotic distribution. This means that the PDF of $-2\ln\lambda(\sigma_{\text{fid}})$ will behave as a χ^2 distribution with one degree of freedom, and that the minimum value of $-2\ln\lambda(\sigma_{\text{fid}})$ will be the "truth" σ_{fid}.

The Asimov data are generated assuming SM expectation for the Higgs ($m_H = 125\,\text{GeV}$), ZZ^* background ($qq + gg$) and reducible background (Z+jets, $t\bar{t}$, $t\bar{t}+V$, and VVV). All the nuisance parameters are set to zero. Figure 95 shows the scan of the -2 Log Likelihood of the fitted cross section from Asimov dataset. The table next to it shows the expected cross section from Monte Carlo, the fitted cross section from the Asimov data, and the expected relative errors with and without including the systematic uncertainties. The expected statistical error on the cross section is $\sim 16\%$ with an integrated luminosity of 36.1fb^{-1}.

Figure 97 shows the scans of the -2 Log Likelihood in each bin of $p_T^{4\ell}$ using the Asimov dataset. Table 91 shows the expected cross section values as well as their relative errors. Figure 98 and Table 92 show the same thing for N_{jets}.

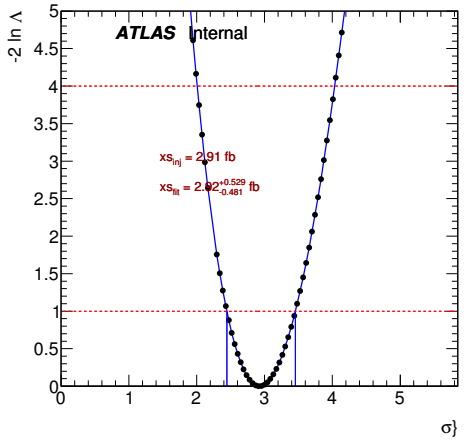

Parameter	XS_{exp}	XS_{fit}	Rel. Error
σ_{fid} [fb] (stat)	2.91	$2.92^{+0.489}_{-0.451}$	$^{+16.7\%}_{-15.4\%}$
σ_{fid} [fb] (stat+sys)	2.91	$2.92^{+0.521}_{-0.481}$	$^{+17.8\%}_{-16.4\%}$

Figure 95: Expected and fitted cross section for the fiducial inclusive cross section using Asimov data and assuming an integrated luminosity of 36.1fb^{-1}. The table shows cross section uncertainty with and without systematics included.

Parameter	XS_{exp}	XS_{fit}	Rel. Error
σ_{bin0} [fb]	0.0389	$0.0387^{+0.0212}_{-0.0175}$	$^{+54.8\%}_{-45.2\%}$
σ_{bin1} [fb]	0.0553	$0.055^{+0.034}_{-0.0267}$	$^{+61.9\%}_{-48.5\%}$
σ_{bin2} [fb]	0.052	$0.0517^{+0.0321}_{-0.0248}$	$^{+62.1\%}_{-47.9\%}$
σ_{bin3} [fb]	0.0426	$0.0423^{+0.0198}_{-0.0162}$	$^{+46.8\%}_{-38.2\%}$
σ_{bin4} [fb]	0.0306	$0.0305^{+0.0133}_{-0.0109}$	$^{+43.7\%}_{-35.7\%}$
σ_{bin5} [fb]	0.0207	$0.0206^{+0.011}_{-0.00852}$	$^{+53.3\%}_{-41.4\%}$
σ_{bin6} [fb]	0.0135	$0.0135^{+0.00764}_{-0.00583}$	$^{+56.6\%}_{-43.3\%}$
σ_{bin7} [fb]	0.00719	$0.00718^{+0.00377}_{-0.0029}$	$^{+52.6\%}_{-40.4\%}$
σ_{bin8} [fb]	0.00243	$0.00243^{+0.00149}_{-0.00108}$	$^{+61.4\%}_{-44.5\%}$
σ_{bin9} [fb]	0.000319	$0.000319^{+0.193}_{-0.000206}$	$^{+6.06e+04\%}_{-64.5\%}$
Parameter	XS_{fit}	XS_{fit}	Rel. Error
σ_{bin0} [fb]	0.0389	$0.0387^{+0.0128}_{-0.00711}$	$^{+33\%}_{-18.4\%}$
σ_{bin1} [fb]	0.0553	$0.055^{+0.0344}_{-0.0144}$	$^{+62.5\%}_{-26.2\%}$
σ_{bin2} [fb]	0.052	$0.0517^{+0.0191}_{-0.0145}$	$^{+37\%}_{-28.1\%}$
σ_{bin3} [fb]	0.0426	$0.0423^{+0.0172}_{-0.00775}$	$^{+40.6\%}_{-18.3\%}$
σ_{bin4} [fb]	0.0306	$0.0305^{+0.0135}_{-0.00497}$	$^{+44.2\%}_{-16.3\%}$
σ_{bin5} [fb]	0.0207	$0.0206^{+0.00957}_{-0.00497}$	$^{+46.5\%}_{-24.2\%}$
σ_{bin6} [fb]	0.0135	$0.0135^{+0.00772}_{-0.00378}$	$^{+57.3\%}_{-28.1\%}$
σ_{bin7} [fb]	0.00719	$0.00718^{+0.00382}_{-0.00187}$	$^{+53.2\%}_{-26.1\%}$
σ_{bin8} [fb]	0.00243	$0.00243^{+0.00146}_{-0.000868}$	$^{+60.2\%}_{-35.8\%}$
σ_{bin9} [fb]	0.000319	$0.000319^{+0.196}_{-0.000206}$	$^{+6.13e+04\%}_{-64.5\%}$

Table 91: Expected and fitted cross sections in each category of p_T using the Asimov dataset (top) without systematics and (bottom) with systematics.

Parameter	XS_{exp}	XS_{fit}	Rel. Error
σ_{bin0} [fb]	1.62	$1.61^{+0.398}_{-0.358}$	$^{+24.7\%}_{-22.2\%}$
σ_{bin1} [fb]	0.82	$0.818^{+0.247}_{-0.213}$	$^{+30.2\%}_{-26.1\%}$
σ_{bin2} [fb]	0.363	$0.362^{+0.158}_{-0.127}$	$^{+43.7\%}_{-35.2\%}$
σ_{bin3} [fb]	0.141	$0.14^{+0.0953}_{-0.0677}$	$^{+67.9\%}_{-48.2\%}$

Parameter	XS_{exp}	XS_{fit}	Rel. Error
σ_{bin0} [fb]	1.62	$1.61^{+0.437}_{-0.383}$	$^{+27.2\%}_{-23.8\%}$
σ_{bin1} [fb]	0.82	$0.817^{+0.256}_{-0.222}$	$^{+31.4\%}_{-27.2\%}$
σ_{bin2} [fb]	0.363	$0.362^{+0.166}_{-0.132}$	$^{+46\%}_{-36.6\%}$
σ_{bin3} [fb]	0.141	$0.14^{+0.102}_{-0.0698}$	$^{+72.7\%}_{-49.8\%}$

Table 92: Expected and fitted cross sections in each category of N_{jets} using the Asimov dataset (left) without systematics and (right) with systematics.

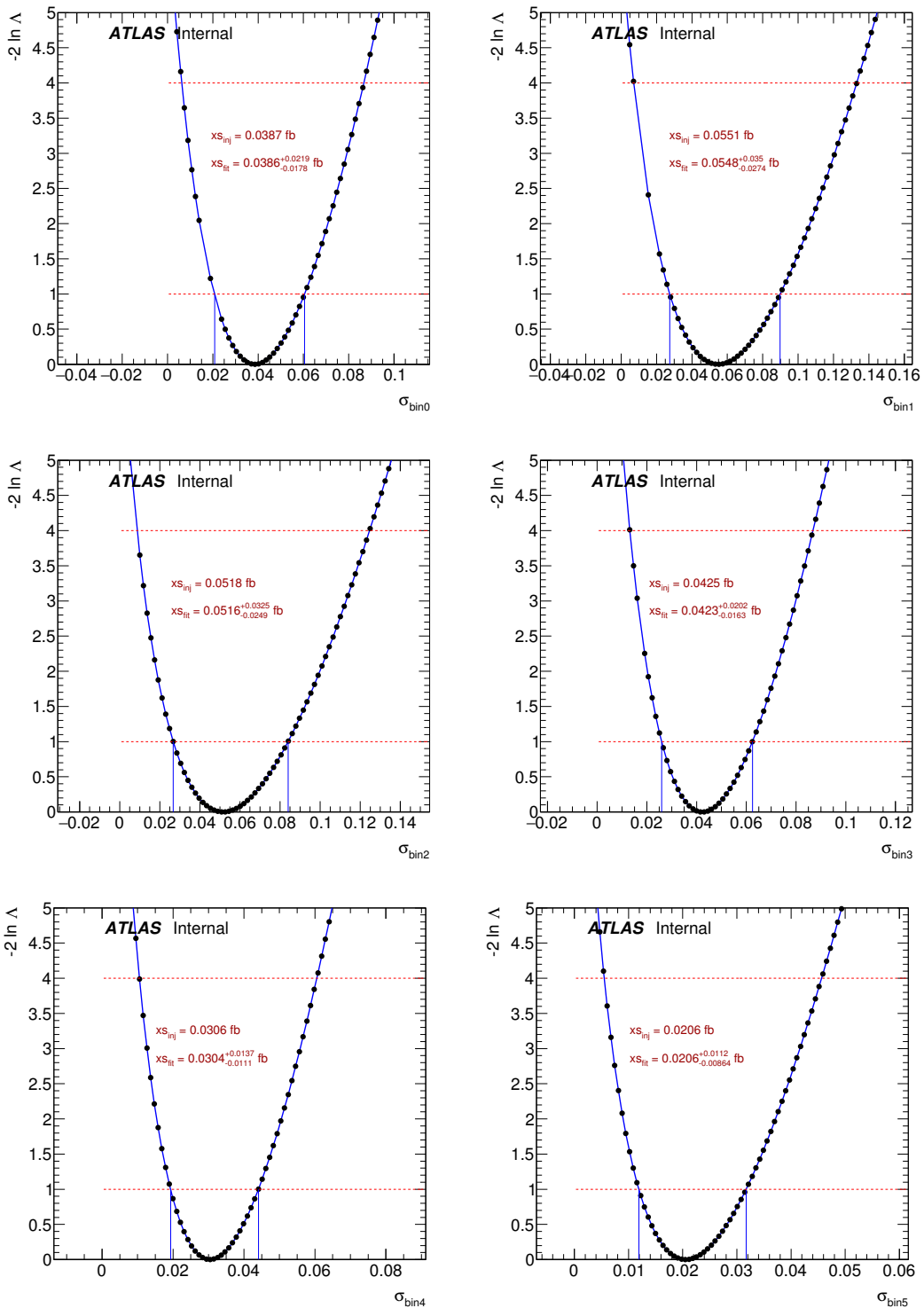

Figure 96: Cross sections fit in bins 0 through 5 of p_T distribution ($\sigma_{p_T,\,i}$) using the Asimov dataset. Systematic uncertainties are included.

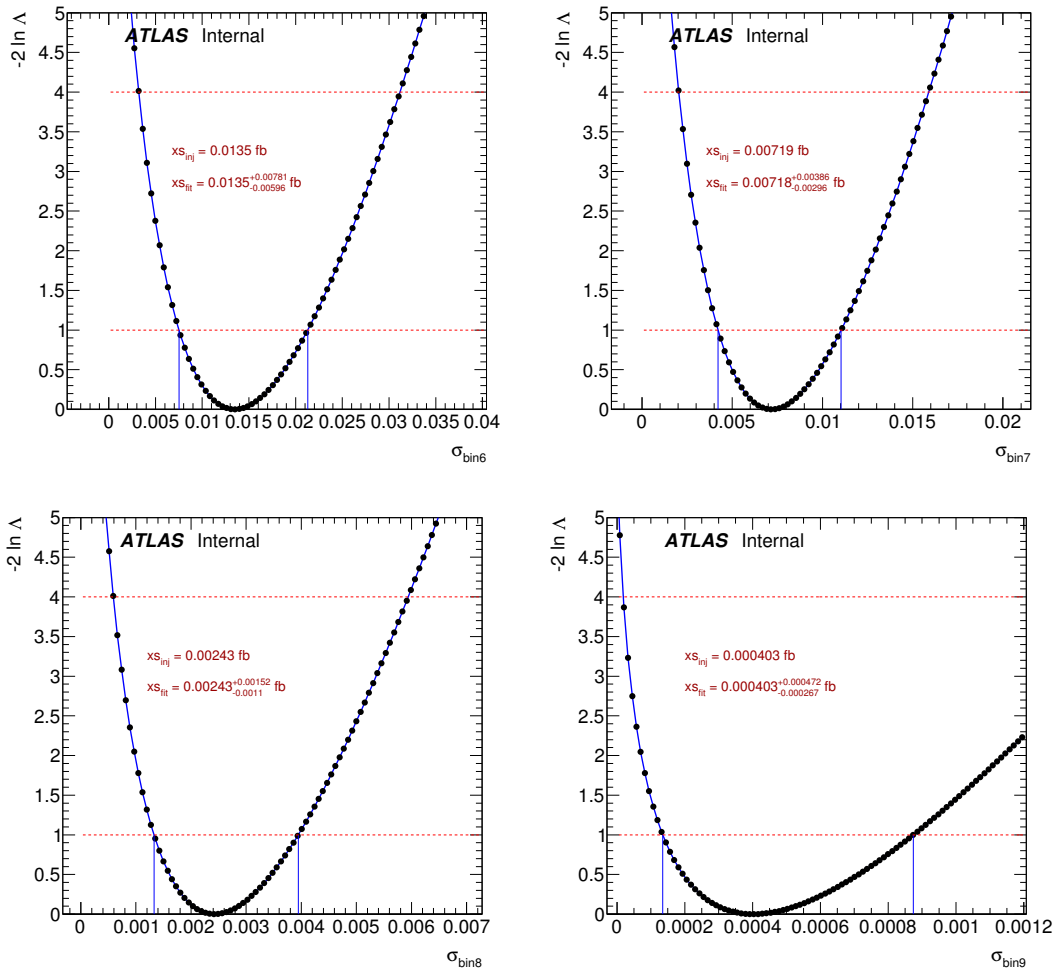

Figure 97: Cross sections fit in bins 6 through 9 of p_T distribution ($\sigma_{p_T,\,i}$) using the Asimov dataset. Systematic uncertainties are included.

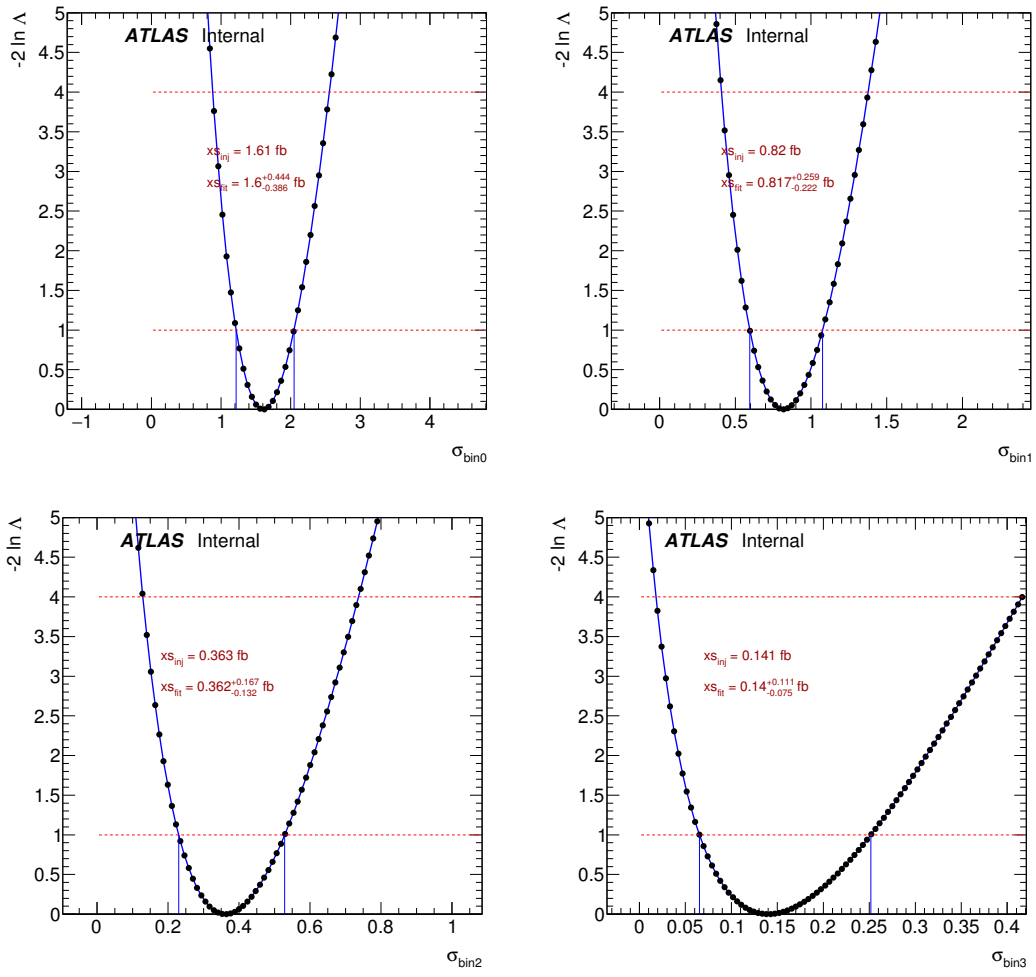

Figure 98: Cross sections fit in each bin of N_{jets} distribution ($\sigma_{N_{\text{jets}},\,i}$) using the Asimov dataset. Systematic uncertainties are included.

9.6 Combination with $H \to \gamma\gamma$

The total inclusive and differential cross sections for the Higgs in the full phase space are also extracted using a combination of the $H \to ZZ^* \to 4\ell$ and $H \to \gamma\gamma$ analyses. The observables in the differential analysis must be common to both channels, which includes p_T^H, $|y^H|$, N_{jets}, and $p_T^{\text{lead. jet}}$. The cross sections are obtained by using the yields from the two channels, combining them while also taking into account the two sets of detector efficiencies, acceptances, branching fractions, and uncertainties. This section will not go into the derivations of the signal, background, and systematics modeling of the $H \to \gamma\gamma$ channel, but those interested are invited to read the $\gamma\gamma$ fiducial measurement paper[12] for those details. The details of this section will focus on how to move from a fiducial measurement in the two channels to one total measurement.

Extrapolating to the common phase space of the two channels increases the degree of model dependence compared to the individual fiducial measurements since systematics on both the branching ratios and the acceptance factors now have to be included. Despite the additional systematic uncertainties, the combination significantly reduces the measurement uncertainty compared to the results in the individual decay channels.

9.6.1 Acceptance Factors for Full Phase Space

Since we combine two different decay channels with different objects in the final state, it is not possible to define a common fiducial region based on the kinematics of the decay products. Instead we extrapolate from each channel's fiducial phase space to the full phase space of the Higgs boson. The full phase space means that there are no cuts on the kinematics of the Higgs boson and the distributions for the differential cross sections are determined by the probability distributions f_{truth}. $\mathcal{A}$ factors are defined in Section 7.2 and are used to do the extrapolation to the full phase space from the fiducial phase space. Two acceptance factors are needed for each variable and bin, one for each decay channel.

The fiducial definition for the $H \to ZZ^* \to 4\ell$ channel is defined in Section 5.3 while the fiducial definition for $H \to \gamma\gamma$ is summarized in Table 93. Jet definitions are changed to be independent of the Higgs decay products, and are reconstructed using the anti-k_t algorithm [123] with distance parameter $\Delta R = 0.4$, and are required to have $p_{\text{T}} > 30\,\text{GeV}$ and $|y| < 4.4$. Systematics on the $\mathcal{A}$ factors due to model and theory uncertainties in the $H4\ell$ channel are discussed and enumerated in Section 8.3.

The inclusive acceptance factors are 50% for the $H \to \gamma\gamma$ channel and 42% for the $H \to ZZ^* \to$

Table 93: Summary of particle level fiducial definitions in the $H \to \gamma\gamma$ analysis. The particle photon isolation $p_{\mathrm{T}}^{\mathrm{iso},0.2}$ is defined analogously to the track isolation of reconstructed objects as the transverse momentum of the system of charge truth particles within $\Delta R < 0.2$ of the photon.

Objects	Definition
Photons	$\lvert\eta\rvert < 1.37$ OR $1.52 < \lvert\eta\rvert < 2.37$, $p_{\mathrm{T}}^{\mathrm{iso},0.2}/p_{\mathrm{T}}^{\gamma} < 0.05$
Jets	anti-k_t, $R = 0.4$, $p_{\mathrm{T}} > 30\,\mathrm{GeV}$, $\lvert y\rvert < 4.4$
Event selection	Definition
Diphoton fiducial	$N_\gamma \geq 2$, $p_{\mathrm{T}}^{\gamma_1} > 0.35\,m_{\gamma\gamma}$, $p_{\mathrm{T}}^{\gamma_2} > 0.25\,m_{\gamma\gamma}$

4ℓ channel. The acceptance is lower for 4ℓ than $\gamma\gamma$ since it is less likely for four leptons to fulfill the fiducial requirements. Figure 99 and Tables 94, 95 show the acceptance factors used for the differential observables and their systematic uncertainties. The fiducial acceptance falls off steeply as the Higgs boson rapidity increases, as both fiducial definitions include pseudorapidity requirements on the Higgs boson decay products.

Table 94: Acceptance factors and total systematic errors for the $H \to ZZ^* \to 4\ell$ channels.

$H \to ZZ^* \to 4\ell$ **acceptance factors and systematic error** [%]										
Variable	Bin 1	Bin 2	Bin 3	Bin 4	Bin 5	Bin 6	Bin 7	Bin 8	Bin 9	Bin 10
p_T	$40.00\ ^{+2.98}_{-2.85}$	$40.23\ ^{+2.25}_{-2.11}$	$40.60\ ^{+2.64}_{-2.56}$	$40.76\ ^{+2.07}_{-1.97}$	$41.29\ ^{+2.07}_{-2.05}$	$42.33\ ^{+1.88}_{-1.88}$	$43.18\ ^{+1.93}_{-1.94}$	$45.10\ ^{+1.86}_{-1.87}$	$49.36\ ^{+1.73}_{-1.73}$	$54.36\ ^{+1.30}_{-1.30}$
$\lvert y\rvert$	$57.46\ ^{+1.47}_{-1.47}$	$57.30\ ^{+1.76}_{-1.76}$	$56.22\ ^{+1.46}_{-1.46}$	$54.14\ ^{+1.32}_{-1.36}$	$46.75\ ^{+1.20}_{-1.20}$	$30.64\ ^{+1.77}_{-1.72}$	$9.23\ ^{+3.34}_{-3.48}$			
N_{jets}	$41.10\ ^{+1.65}_{-1.54}$	$43.21\ ^{+1.98}_{-1.97}$	$43.85\ ^{+1.59}_{-1.59}$	$45.06\ ^{+5.18}_{-5.18}$						
$p_T^{\text{lead. jet}}$	$41.10\ ^{+1.65}_{-1.54}$	$41.15\ ^{+3.81}_{-3.80}$	$42.03\ ^{+3.10}_{-3.11}$	$43.11\ ^{+2.15}_{-2.16}$	$45.33\ ^{+1.67}_{-1.67}$	$49.13\ ^{+2.28}_{-2.28}$				

Table 95: Acceptance factors and total systematic errors for the $H \to \gamma\gamma$ channels.

$H \to \gamma\gamma$ **acceptance factors and systematic error** [%]										
Variable	Bin 1	Bin 2	Bin 3	Bin 4	Bin 5	Bin 6	Bin 7	Bin 8	Bin 9	Bin 10
p_T	$50.40\ ^{+1.15}_{-1.15}$	$52.00\ ^{+1.28}_{-1.28}$	$51.36\ ^{+0.98}_{-0.99}$	$50.17\ ^{+0.77}_{-0.77}$	$48.78\ ^{+0.72}_{-0.73}$	$47.92\ ^{+1.32}_{-1.32}$	$47.00\ ^{+0.63}_{-0.64}$	$51.06\ ^{+0.76}_{-0.77}$	$62.60\ ^{+0.58}_{-0.58}$	
$\lvert y\rvert$	$71.58\ ^{+0.34}_{-0.34}$	$71.22\ ^{+0.88}_{-0.88}$	$69.88\ ^{+1.49}_{-1.49}$	$67.23\ ^{+0.35}_{-0.35}$	$65.09\ ^{+1.07}_{-1.07}$	$62.93\ ^{+0.60}_{-0.60}$	$59.63\ ^{+0.56}_{-0.56}$	$54.16\ ^{+1.42}_{-1.42}$	$28.41\ ^{+0.82}_{-0.82}$	
N_{jets}	$51.77\ ^{+1.04}_{-1.04}$	$48.99\ ^{+0.76}_{-0.77}$	$47.89\ ^{+1.49}_{-1.49}$	$48.27\ ^{+1.38}_{-1.37}$						
$p_T^{\text{lead. jet}}$	$51.77\ ^{+1.04}_{-1.04}$	$47.93\ ^{+0.89}_{-0.86}$	$47.57\ ^{+0.59}_{-0.59}$	$48.12\ ^{+0.80}_{-0.79}$	$53.19\ ^{+1.22}_{-1.20}$					

9.6.2 Combination Likelihood Function

Like the fiducial measurement, the combination is performed using a profile likelihood ratio fit. The likelihood function includes the branching fraction to each channel, the signal extraction, the correction to particle level, and the extrapolation to the total phase space. It also includes shape and normalization uncertainties of all components and their correlations.

The likelihood for an observable is

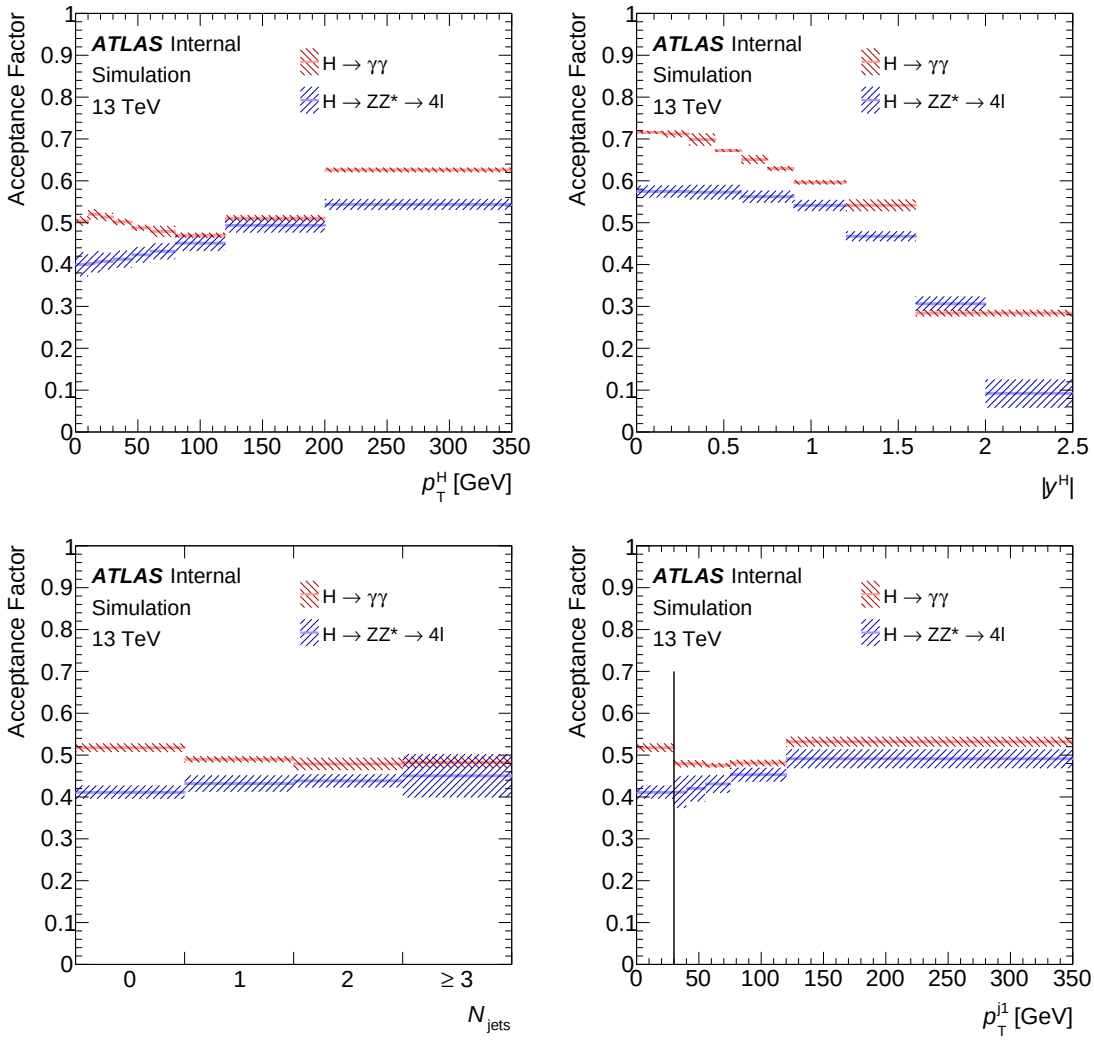

Figure 99: Acceptance factors and total uncertainties for a 125.0 GeV Higgs at $\sqrt{s} = 13$ TeV in the $H \to ZZ^* \to 4\ell$ and $H \to \gamma\gamma$ channels. Plots show acceptance factors for p_T^H, $|y^H|$, N_{jets}, and $p_T^{\text{lead. jet}}$. The first bin of $p_T^{\text{lead. jet}}$ is the same as the 0-jet bin in N_{jets}, as indicated by the black vertical line

$$L = \prod_{j=0}^{\text{decay chan.}} \prod_{i=0}^{\text{bins}} \text{Pois}(N_{ij}|n_{ij}) P(m_{ij}^{H}|s_{ij}, b_{ij}) \times \prod_{k=1}^{\text{syst}} \text{Gaus}(0|\theta_k, \alpha_k) \tag{9.17}$$

$$s_{ij} = \sigma_i \cdot \mathcal{L}_{\text{int}} \cdot \text{BR}_j \cdot \mathcal{A}_{ij} \cdot \mathcal{C}_{ij} \times \prod_{k=0}^{\text{syst}} (1 + \alpha_{ijk} \cdot \theta_{ijk}) \tag{9.18}$$

$$b_{ij} = N_{b,ij} \times \prod_{k=0}^{\text{syst}} (1 + \alpha_{ijk} \cdot \theta_{ijk}) \qquad n_{ij} = s_{ij} + b_{ij} \tag{9.19}$$

Here, i is bin of the observable, j is either the $H4\ell$ or $H\gamma\gamma$ channel, and k is the systematic uncertainties. s_{ij} is the expected number of signal events in a bin and channel, and b_{ij} is the expected number of background events. $\mathcal{A}_{ij}$ and $\mathcal{C}_{ij}$ are the acceptance and correction factors and have been introduced in Section 9.3, and BR_j is the branching fraction for the decay channel. The branching fraction for a Higgs at $m_H = 125.09\,\text{GeV}$ is $(0.227 \pm 0.007)\%$ for $H \to \gamma\gamma$ and $(0.0125 \pm 0.0003)\%$ for $H \to ZZ^* \to 4\ell$ [17]. σ_i is the total cross section in bin i, and is the parameter of interest.

The first term in the likelihood is the Poisson function that calculates the probability to observe N_{ij} data events given the $s_{ij} + b_{ij}$ expected number of events.

The second term contains the invariant mass PDFs for the signal and background events. The shape templates are used to extract the fraction of signal and background events in the bin. This term also contains constraints on the number of background events, $N_{b,ij}$, calculated from background fits in control regions.

The third term contains the Gaussian constraints that encode the systematics of the measurement. The shape and normalization uncertainties of all components are represented as nuisance parameters θ_k. This allows the uncertainties to be correlated between bins, decay channels, and correction and acceptance factors. Correlated uncertainties between the channels include the predicted branching ratios. Correlations between the decay channel acceptance and correction factors include the production mode variations, higher order scale effects, and parton distribution variations. Experimental uncertainties like the luminosity measurement and pileup modeling are also correlated.

To extract the cross section for each bin, the profile-likelihood-ratio is formed

$$\lambda(\sigma_i) = \frac{L(N_{ij}, N_{b,ij}, m_{ij}^{H}|\sigma_i, \widehat{\widehat{b_{ij}}}, \widehat{\widehat{\theta_k}})}{L(N_{ij}, N_{b,ij}, m_{ij}^{H}|\widehat{\sigma_i}, \widehat{b_{ij}}, \widehat{\theta_k})} \tag{9.20}$$

and $-2\ln\lambda(\sigma_i)$ is minimized. The results for the total cross section are shown in Chapter 10.

Chapter 10

Cross Section Results

This chapter describes the results of the analysis. Section 10.1 shows the events passing the $H \to ZZ^* \to 4\ell$ selection from 36.1fb^{-1} of integrated luminosity collected in 2015 and 2016. Section 10.2 shows the extracted fiducial inclusive and differential cross section from those events, as well as comparisons to theory predictions. Section 10.3 shows the extracted total inclusive and differential cross section using the combined data from the $H \to ZZ^* \to 4\ell$ and $H \to \gamma\gamma$ channel and comparisons to theory predictions. Section 10.4 explains an interpretation of the cross section results in the framework of pseudo observables.

10.1 Events Measured

This section illustrates the events obtained from the $H \to ZZ^* \to 4\ell$ selection. Figure 101 shows the invariant mass of the four lepton system ($m_{4\ell}$) overlaying data and expected events from MC simulation. Table 101 shows the number of observed and expected events for the $m_H = 125\,\text{GeV}$ signal hypothesis and the background processes. Figures 102, 103 and 104 show the distribution of all variables of interest when comparing data and the MC simulation. All events were selected in a mass window of $115 < m_{4\ell} < 130\,\text{GeV}$ with an integrated luminosity of 36.1fb^{-1}.

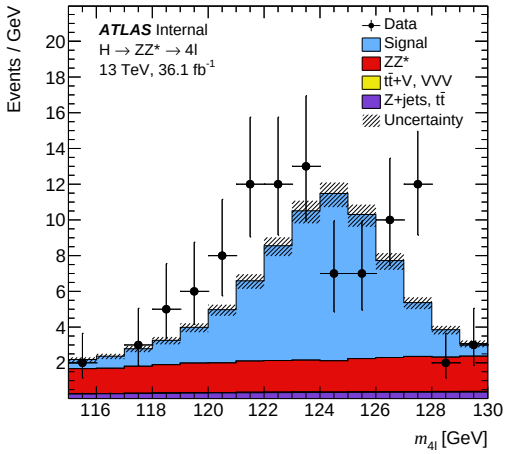

Figure 101: Invariant mass of the four lepton system ($m_{4\ell}$) comparing data and expected events from MC simulation. The black dots represent the data, while the blue, red, violet and yellow areas represent the expected Higgs signal, the ZZ^* background, the reducible background and the other minor backgrounds, respectively. An integrated luminosity of 36.1fb^{-1} has been used.

Final state	Signal	ZZ^*	$Z+$jets, $t\bar{t}$	Expected	S/B	Observed
			WZ, ttV, VVV			
4μ	20.1 ± 2.1	9.8 ± 0.5	1.29 ± 0.28	31.2 ± 2.2	1.8	33
$2e2\mu$	14.2 ± 1.4	7.1 ± 0.4	1.01 ± 0.23	22.3 ± 1.5	1.7	32
$2\mu 2e$	10.8 ± 1.2	4.6 ± 0.4	1.41 ± 0.24	16.8 ± 1.3	1.8	21
$4e$	10.6 ± 1.2	4.4 ± 0.4	1.33 ± 0.23	16.3 ± 1.3	1.8	16
Total	56 ± 6	25.9 ± 1.5	5.0 ± 0.6	87 ± 6	1.8	102

Table 101: The number of events expected and observed for a $m_H = 125\,\text{GeV}$ hypothesis for the four lepton final states in a window of $115 < m_{4\ell} < 130\,\text{GeV}$, using the FSR-corrected $m_{4\ell}$. The columns show the number of expected signal events and the breakdown of irreducible (ZZ^*) and reducible backgrounds events, for an integrated luminosity of 36.1fb^{-1} at $\sqrt{s} = 13\,\text{TeV}$.

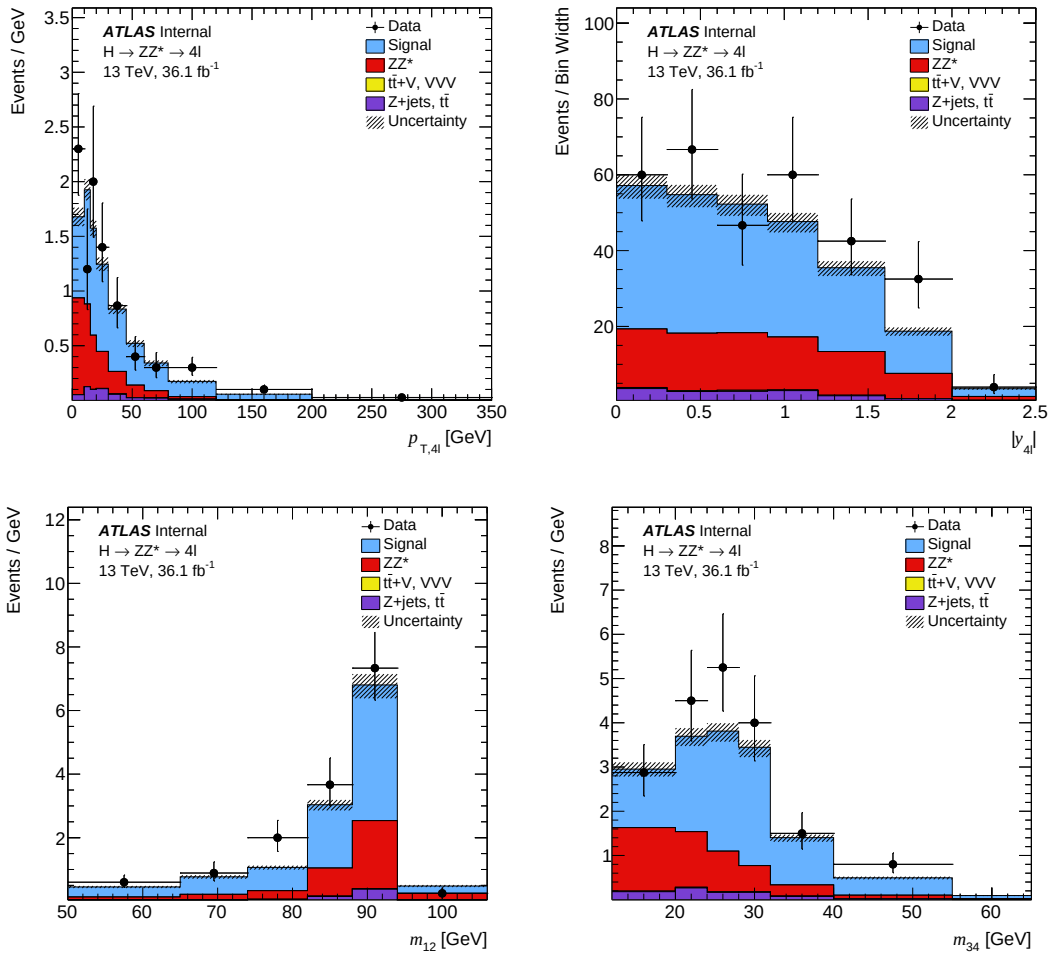

Figure 102: Distribution of p_T (top left), $|y|$ (top right), m_{12} (bottom left) and m_{34} (bottom right) when comparing data and MC simulation. The black dots represent the data, while the blue, red, violet and yellow areas represent the expected Higgs signal, the ZZ^* background, the reducible background and the other minor backgrounds, respectively. An integrated luminosity of $36.1\,\text{fb}^{-1}$ has been used.

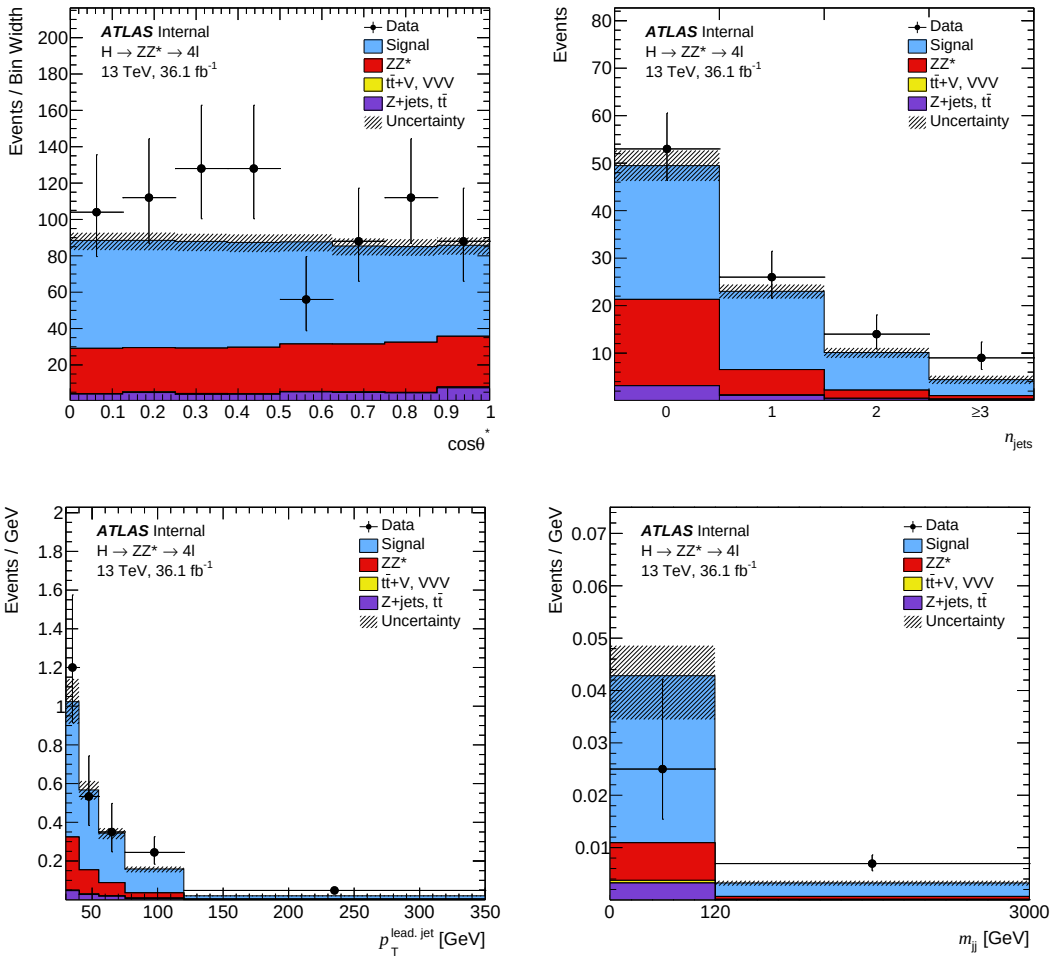

Figure 103: Distribution of $|\cos(\theta^*)|$ (top left), N_{jets} (top right), $p_T^{\text{lead. jet}}$ (bottom left) and m_{jj} (bottom right) when comparing data and MC simulation. The black dots represent the data, while the blue, red, violet and yellow areas represent the expected Higgs signal, the ZZ^* background, the reducible background and the other minor backgrounds, respectively. An integrated luminosity of $36.1\,\text{fb}^{-1}$ has been used.

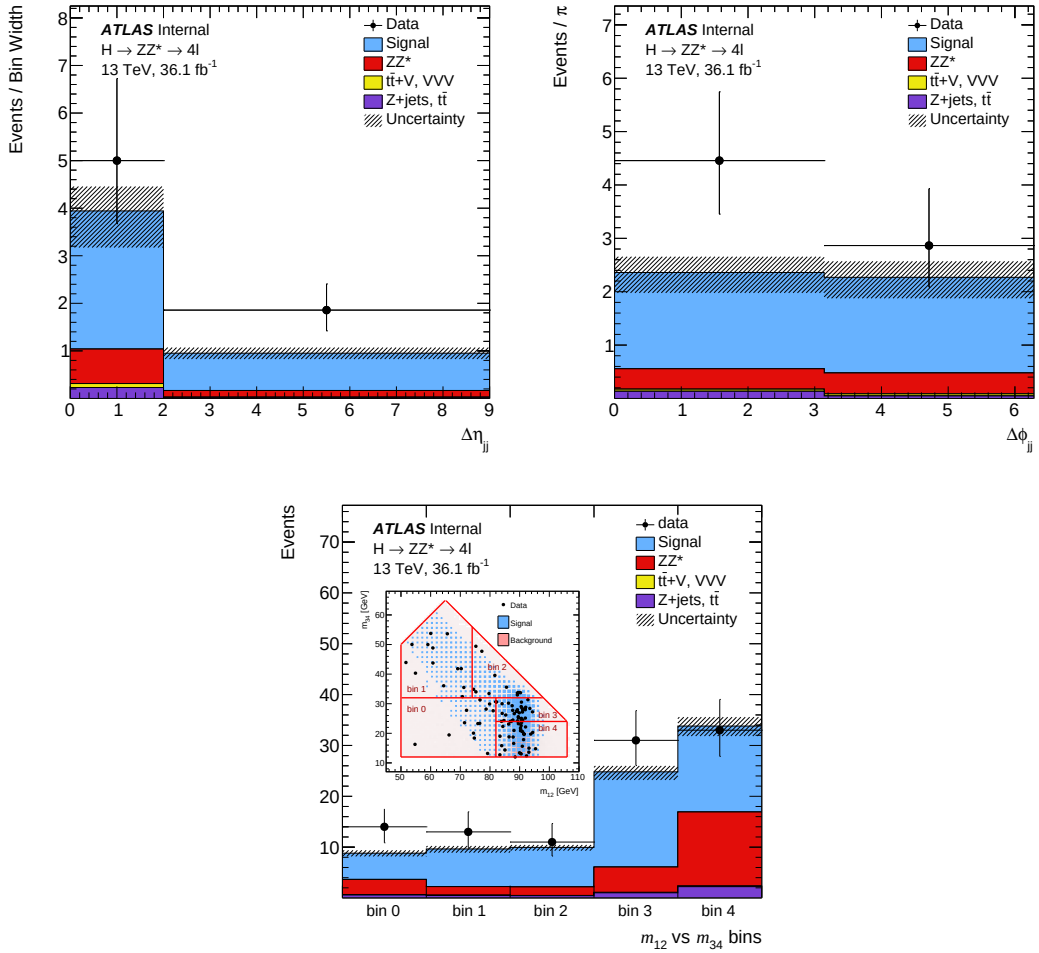

Figure 104: Distribution of $\Delta\eta_{jj}$ (left), $\Delta\phi_{jj}$ (right), and m_{12}vs.m_{34} (bottom) when comparing data and MC simulation. The explanation of the binning of the 2D m_{12}vs.m_{34} variable is shown in the insert, and with more detail in Figure 56. The black dots represent the data, while the blue, red, violet and yellow areas represent the expected Higgs signal, the ZZ^* background, the reducible background and the other minor backgrounds, respectively. An integrated luminosity of 36.1 fb^{-1} has been used.

10.2 Fiducial Cross Sections

This section demonstrates all the results obtained for the fiducial inclusive and differential cross section measurement.

10.2.1 Inclusive Cross Section

The observed fiducial inclusive cross section is

$$\sigma_{\text{fid}} \cdot \text{BR}(H \to 4\ell) = 3.62 \pm 0.50\,(\text{stat})\,^{+0.25}_{-0.20}\,(\text{syst})\ \text{fb} \tag{10.1}$$

This result is consistent with the LHC Cross Section Working Group (LHCXSWG) prediction of $\sigma_{\text{LHC}} = 2.91 \pm 0.13$ fb [17]. The LHCXSWG prediction is accurate to N3LO in QCD for the ggF production mode, and was multiplied by its $\mathcal{A}$ factor to turn it into a fiducial prediction. The compatibility between the prediction and the data is described with a p-value

$$p = \int_{t_{\sigma_{\text{LHC}}}(\widehat{\sigma}_{\text{obs}})}^{\infty} \chi^2(t_{\sigma_{\text{LHC}}}|\,\langle\widehat{\sigma}\rangle = \sigma_{\text{LHC}})\,\mathrm{d}t_{\sigma_{\text{LHC}}} \qquad t_{\sigma_{\text{LHC}}} = -2\ln\frac{L(\sigma_{\text{LHC}}, \widehat{\widehat{\theta}}_k)}{L(\widehat{\sigma}, \widehat{\theta}_k)} \tag{10.2}$$

The p-value of the observed fiducial cross section is 19%, which means there was an 19% chance to have measured the observed cross section (or more extreme), assuming the LHCXSWG value is true. The PDF of $t_{\sigma_{\text{LHC}}}$ is approximated as a χ^2 distribution under asymptotic assumptions, as explained in Chapter 9. Converting the p-value to the equivalent two-sided Z-score of a Gaussian distribution (for illustrative purposes) corresponds to 1.3σ. The threshold for the discovery of new phenomena in particle physics is a significance level of 5σ, which would correspond to getting a p-value of 0.000057% (two-sided).

10.2.2 Differential Cross Section

The $H \to ZZ^* \to 4\ell$ decay channel is useful in that the reconstructed events have the full kinematic information of the Higgs since all four leptons can be measured. The kinematic and jet varibles used in the differential distributions are explained in Section 5.4.2 and 5.4.3. The observed fiducial differential cross sections as a function of these variables are shown in Figures 105, 106 and 107. The data are compared to SM predictions, where the normalization of the distributions is given by the LHCXSWG prediction [17], and the shapes for the ggF distribution are given by NNLOPS [58, 59], MG5_aMC@NLO_FxFx [60, 61], and, for $p_T^{4\ell}$ and $|y^{4\ell}|$, by HRes [62, 63], explained in Section 2.4. The shapes for the other production modes are given by Monte Carlo also discussed in

Table 102: p-values (in percent) indicating the compatibility of the measured differential cross sections and various theory predictions

Prediction p-values [%]	p_T^H	$\lvert y^H \rvert$	m_{12}	m_{34}	m_{12}vs.m_{34}	N_{jets}(excl.)	$p_T^{\text{lead. jet}}$	m_{jj}	$\Delta\phi_{jj}$	$\Delta\eta_{jj}$
NNLOPS	25	65	21	42	41	33	18	1.9	11	11
MADGRAPH5_AMC@NLO_FXFX	42	66	31	44	54	55	37	3.6	20	17
HRES (NNLO+NNLL)	21	64	-	-	-	-	-	-	-	-

Section 2.4. The uncertainty bars on the expected cross section are from the scale and PDF theory uncertainties, while the bars on the data points are the total uncertainty. MG5_AMC@NLO_FXFX only has QCD accuracy at NLO, making its scale uncertainties larger.

The p-values are presented for each variable on their respective plot and in Table 102 for each Standard Model prediction. p-values are calculated using a slightly modified likelihood ratio from Equation 10.2, where the full likelihood is the product of the likelihood of each bin, and $\sigma_{\text{LHC},i}$ in each bin is fixed to the cross sections predicted by theory. Under the asymptotic assumption, $-2\ln\lambda\left(\sigma_{\text{LHC},i}\right)$ behaves as a χ^2 with the number of degrees of freedom equal to the number of bins.

All differential cross section results are compatible with the Standard Model, and m_{34} and $|\cos\theta^*|$ are consistent with measurements that show the Higgs boson is a even parity scalar particle [146]. $p_T^{4\ell}$ and $p_T^{\text{lead. jet}}$ have larger momentum than expected, and N_{jets} also has greater jet multiplicity than expected, similar to what was seen in the Run 1 analysis [147, 1], though neither analysis has excesses that are significant at a 2.5σ level (let alone 5σ). m_{jj}, $\Delta\eta_{jj}$, and $\Delta\phi_{jj}$ have the largest significances at $\sim 2.3\sigma$, $\sim 1.6\sigma$, and $\sim 1.6\sigma$ respectively in NNLOPS. These variables have better agreement in MG5_AMC@NLO_FXFX, as it describes the jet variables better than NNLOPS.

The measurement uncertainties are statistics dominated, usually within 21%–60% uncertainty depending on the bin, but with some bins as high as 150%. Uncertainty in the measured luminosity was the largest systematic uncertainty for most variables (except for the jet variables), ranging from 3%–5% depending on the bin. Experimental jet systematics like the jet energy scale and resolution dominated for the jet variables, from 3%–24% depending on bin. For bins with high proportion of $t\bar{t}H$ events, the uncertainty in the proportion of the production modes of the Higgs becomes relevant, especially for the last bin of N_{jets} where the fraction of $t\bar{t}H$ is theorized to be about 19% (see Figure 92). For $N_{\text{jets}} \geq 3$ the systematic due to production mode fraction by itself accounts for 20% uncertainty.

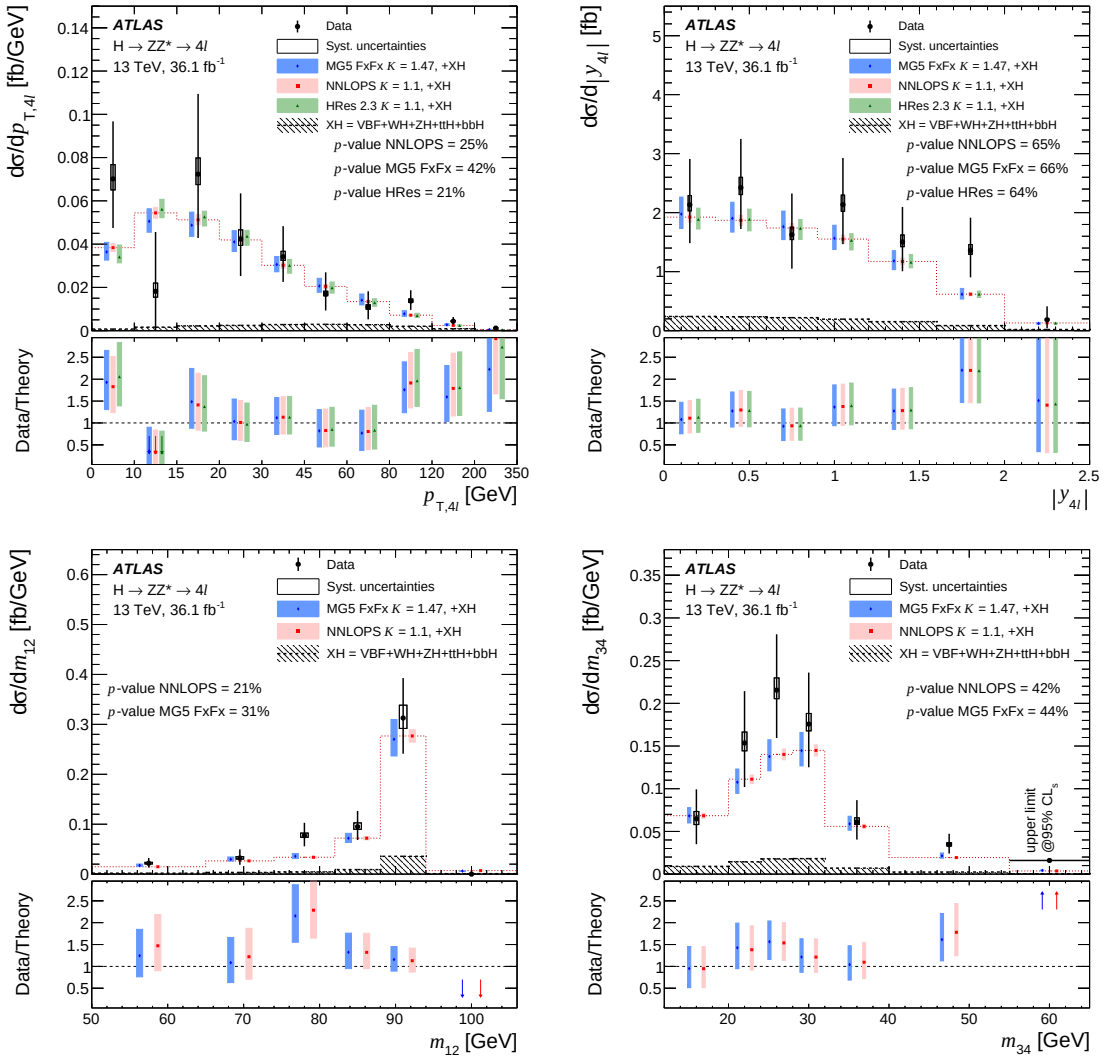

Figure 105: Differential fiducial cross sections, for (top left) the transverse momentum $p_T^{4\ell}$ of the Higgs boson, (top right) the absolute value of the rapidity $|y^{4\ell}|$ of the Higgs boson, (bottom left) the invariant mass of the leading lepton pair m_{12}, (bottom right) the invariant mass of the subleading lepton pair m_{34}. The measured cross sections are compared to ggF predictions by NNLOPS, MG5_aMC@NLO_FxFx, and for $p_T^{4\ell}$ and $|y^{4\ell}|$, by HRes, all normalized to the N3LO cross section with the listed K-factors. Predictions for all other Higgs boson production modes XH are shown in grey. The error bars on the data points show the total uncertainties, while the systematic uncertainties are indicated by the boxes. The shaded bands on the expected cross sections indicate the PDF and scale uncertainties. The p-values indicating the compatibility of the measurement and the SM prediction are shown as well. They do not include the systematic uncertainty in the theoretical predictions.

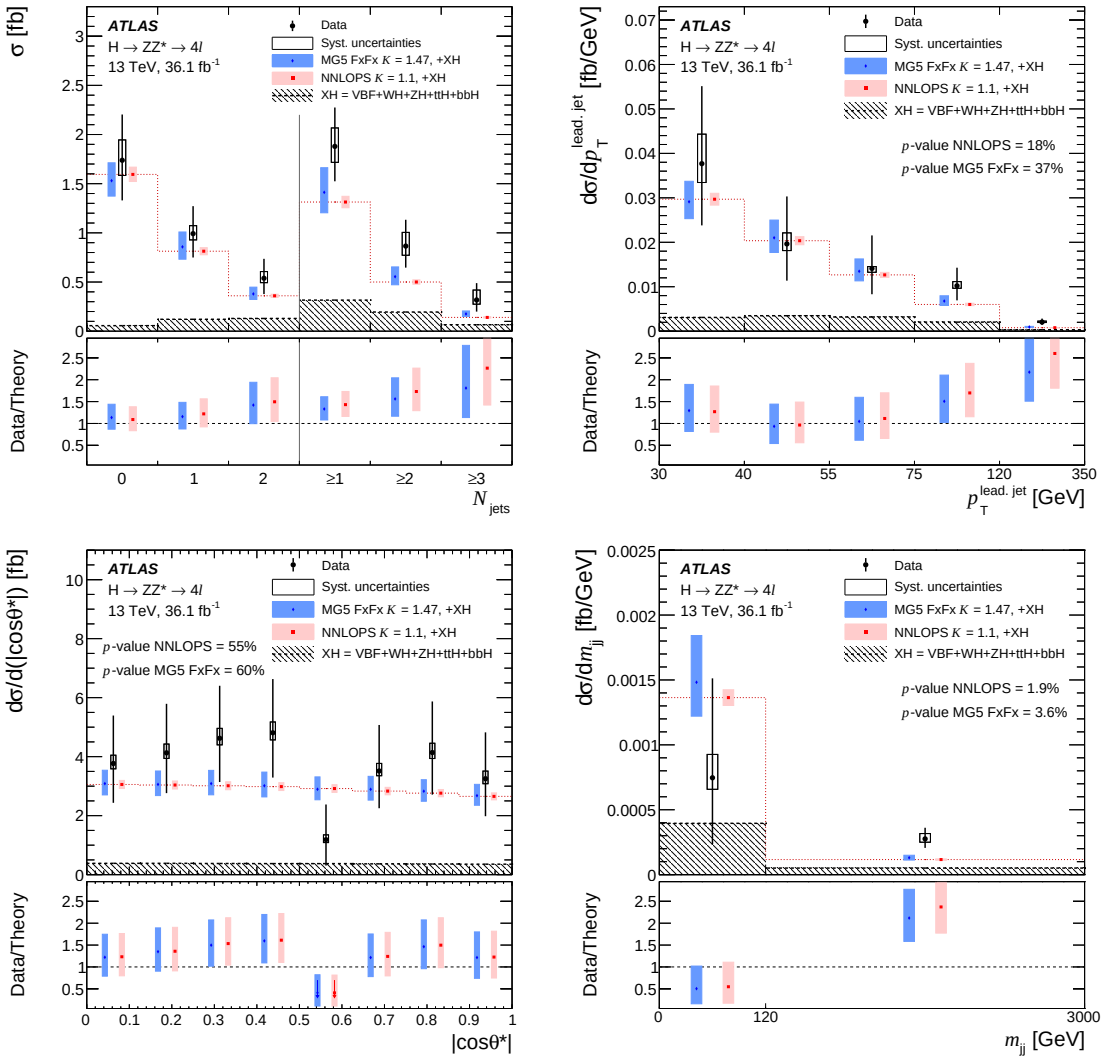

Figure 106: Differential fiducial cross sections, for (top left) the number of jets N_{jets}, (top right) the transverse momentum of the leading jet $p_T^{\text{lead. jet}}$, (bottom left) the magnitude of the cosine of the decay angle of the leading lepton pair in the four lepton rest frame with respect to the beam axis $|\cos\theta^*|$, and (bottom right) the invariant mass of the two leading jets m_{jj}. The measured cross sections are compared to ggF predictions by NNLOPS and MG5_aMC@NLO_FxFx, all normalized to the N3LO cross section with the listed K-factors. Predictions for all other Higgs boson production modes XH are shown in grey. The error bars on the data points show the total uncertainties, while the systematic uncertainties are indicated by the boxes. The shaded bands on the expected cross sections indicate the PDF and scale uncertainties. The p-values indicating the compatibility of the measurement and the SM prediction are shown as well, though for N_{jets} the p-value was only calculated for the exclusive jet multiplicity, and is shown in Table 102. They do not include the systematic uncertainty in the theoretical predictions.

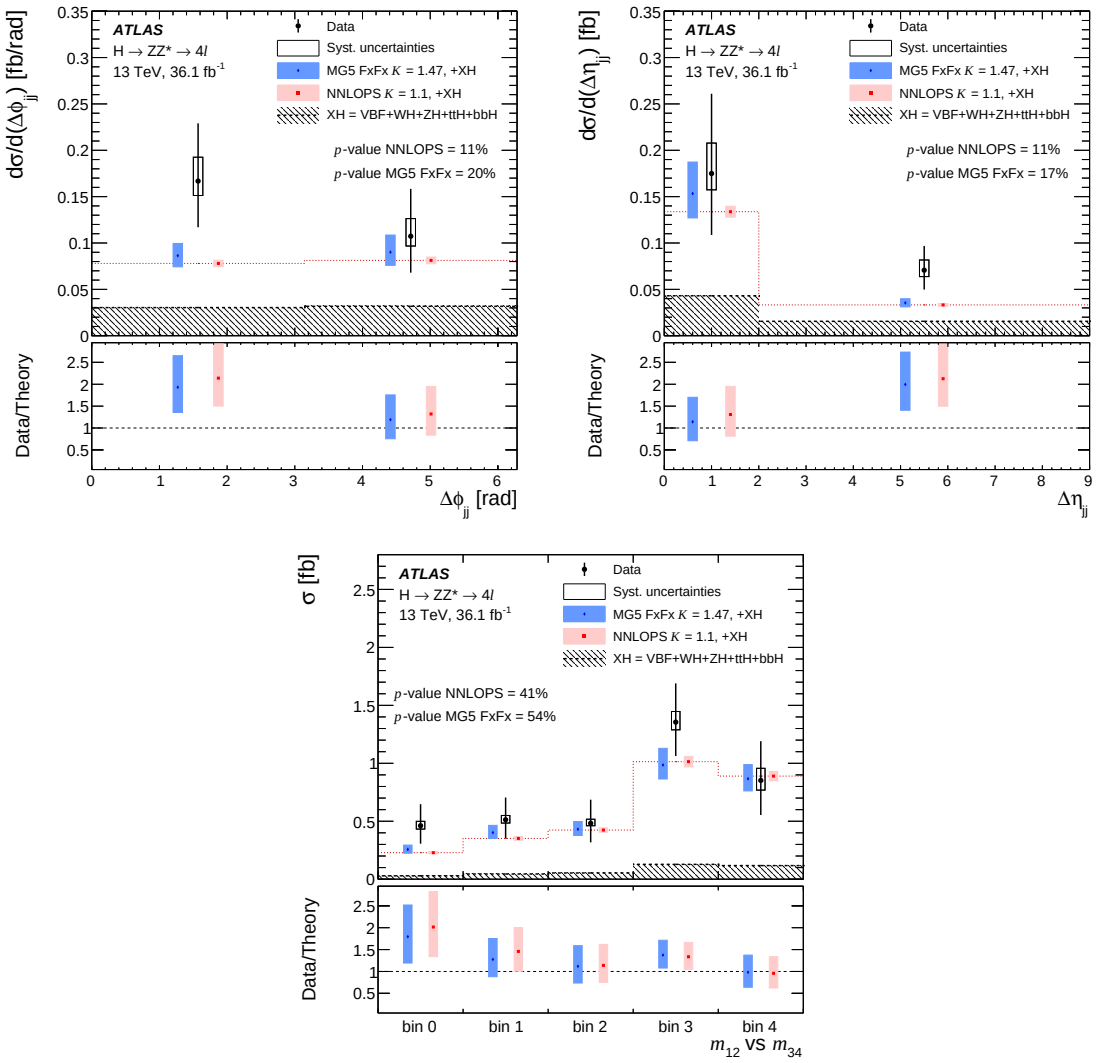

Figure 107: Differential fiducial cross sections, for (top left) the angle between the two leading jets in the transverse plane $\Delta\phi_{jj}$, (top right) the difference in pseudorapidity between the two leading jets in the transverse plane $\Delta\eta_{jj}$, and (bottom) the invariant mass of the leading lepton pair vs that of the subleading pair m_{12}vs.m_{34}, where the binning of this 2D variable is shown in Figure 56. The measured cross sections are compared to ggF predictions by NNLOPS and MG5_aMC@NLO_FxFx, all normalized to the N3LO cross section with the listed K-factors. Predictions for all other Higgs boson production modes XH are shown in grey. The error bars on the data points show the total uncertainties, while the systematic uncertainties are indicated by the boxes. The shaded bands on the expected cross sections indicate the PDF and scale uncertainties. The p-values indicating the compatibility of the measurement and the SM prediction are shown as well. They do not include the systematic uncertainty in the theoretical predictions.

10.3 Total Cross Sections

This section demonstrates all the results obtained for the total inclusive and differential cross section in the $H \to ZZ^* \to 4\ell$ and $H \to \gamma\gamma$ combination.

10.3.1 Inclusive Cross Section

The observed total inclusive cross section is

$$\sigma = 57.0\ ^{+6.0}_{-5.9}\,(\text{stat})\ ^{+4.0}_{-3.3}\,(\text{syst})\ \text{pb} \tag{10.3}$$

$$\sigma_{\gamma\gamma} = 47.9\ ^{+9.1}_{-8.6}\ \text{pb} \qquad \sigma_{4\ell} = 68\ ^{+11}_{-10}\ \text{pb} \tag{10.4}$$

This result is consistent with the LHC Cross Section Working Group (LHCXSWG) prediction of $\sigma_{\text{LHC}} = 55.6 \pm 2.5\text{pb}$ [17]. The LHCXSWG prediction is accurate to N3LO in QCD for the ggF production mode. The compatibility between the Standard Model prediction and the data is described with a p-value as described in Equation 10.2, and has $p = 84\%$. The compatibility between the two channels can be calculated by constructing a profile likelihood ratio of $\sigma_{\gamma\gamma} - \sigma_{4\ell}$ and measuring its consistency with 0. The compatibility between the two channels is measured to be $p = 14\%$.

10.3.2 Differential Cross Section

The observed fiducial differential cross section are shown in Figure 108. The data are compared to various Standard Model predictions, most of which were also used in the fiducial measurement in Section 10.2, but some, like SCETlib (Soft-Collinear Effective Theory library) [148] and RadISH (Radiation of Initial State Hadrons) [149] are introduced here. SCETlib improves the perturbative convergence of ggF by applying a resummation of the virtual corrections to the gluon form factor [150]. RadISH gives QCD NNLO-accurate predictions for the Higgs-plus-jet p_{T} spectrum by taking into account finite mass effects for LO, while using an $m_t \to \infty$ EFT approximation for NLO and NNLO [151].

The NNLOPS and MG5_aMC@NLO_FxFx ggF predictions are normalized to the N3LO LHCXSWG inclusive cross section [17] (their K-factors are noted on the plots), while the other theory predictions are left at their native cross sections. The uncertainty bars on the expected cross sections are from the scale and PDF theory uncertainties, while the bars on the data points are

Table 103: p-values (in percent) indicating the compatibility of the measured differential cross sections and various theory predictions

Prediction p-values [%]	p_T^H	$\lvert y^H \rvert$	N_{jets}(excl.)	$p_T^{\text{lead. jet}}$
NNLOPS	29	92	43	6
HRes (NNLO+NNLL)	16	-	-	-
RaDISH	30	-	-	-
SCETlib	-	91	-	23
Madgraph5_aMC@NLO	77	91	65	-

the total uncertainty. MG5_aMC@NLO_FxFx only has QCD accuracy at NLO, making its scale uncertainties larger.

The agreement between observation and theory predictions is quantified using p-values calculated from the profile likelihood ratio (Equation 10.2), where the full likelihood is the product of the likelihood of each bin, and $\sigma_{\text{LHC},i}$ in each bin is fixed to the cross sections predicted by theory. Under asymptotic assumptions, $-2\ln\lambda(\sigma_{\text{LHC},i})$ behaves as a χ^2 with the number of degrees of freedom equal to the number of bins. p-values for each variable for various theory predictions are listed in Table 103. We also measure the agreement between both channels by calculating the compatibility of $\sigma_{\gamma\gamma} - \sigma_{4\ell}$ with 0 in each bin. The corresponding p-values are all high, indicating good agreement between the results in the two channels: 58% for p_T^H, 40% for $|y^H|$, 53% for N_{jets} and 67% for $p_T^{\text{lead. jet}}$.

All differential cross section results are compatible with the Standard Model. p_T^H and $p_T^{\text{lead. jet}}$ have larger momentum than expected, and N_{jets} also has greater jet multiplicity than expected, similar to what was seen in the Run 1 analysis [1], though neither analysis has excesses that are significant at a 2.5σ level (let alone 5σ). There is not quite a 2σ excess in $p_T^{\text{lead. jet}}$, caused by the last two p_{T} bins being high. The lower p-value for HRes compared to other theories can be explained by the lower natively computed total cross section, as this prediction is at NNLO + NNLL accuracy.

The measurement uncertainties are statistics dominated, though better than with just the $H \to ZZ^* \to 4\ell$ channel alone. Statistical errors are within 20%–30% uncertainty depending on the bin. Uncertainty in the measured luminosity was the largest systematic uncertainty for many variables, ranging from 3%–5%. Experimental jet systematics like the jet energy scale and resolution dominated for the jet variables, typically 3%–6%, with 10% in the $N_{\text{jets}} \geq 3$ bin. Due to having to extrapolate to the full phase space, there are extra systematic uncertainties due to acceptance factors and branching ratios that are not present in the individual fiducial measurements, but the increase in systematic error is less than the decrease in statistical error overall.

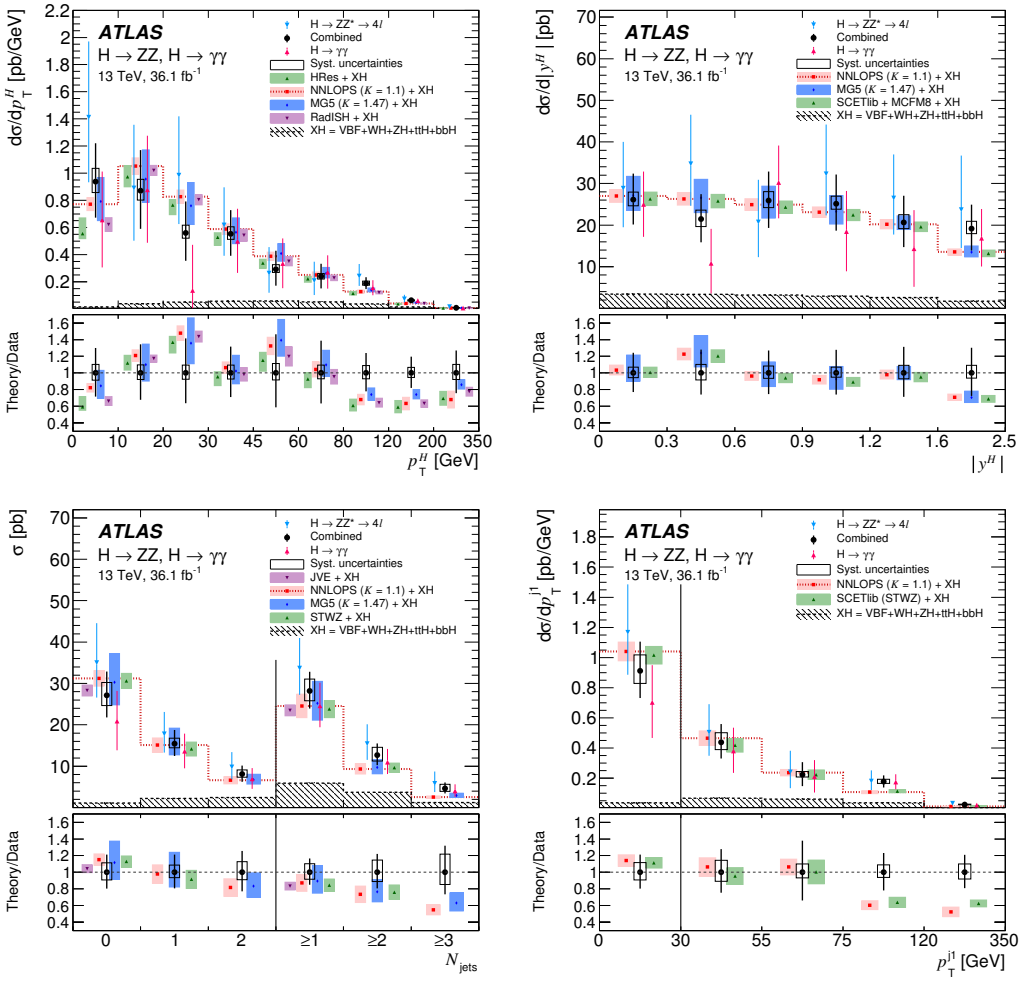

Figure 108: Differential fiducial cross sections, for (top left) the transverse momentum p_T^H of the Higgs boson, (top right) the absolute value of the rapidity $|y^H|$ of the Higgs boson, (bottom left) the number of jets N_{jets}, and (bottom right) the transverse momentum of the leading jet $p_T^{\text{lead. jet}}$. The first bin in the $p_T^{\text{lead. jet}}$ distribution corresponds to the 0-jet bin in the N_{jets} distribution, as indicated by the black vertical line. Different Standard Model predictions are overlaid with the data. NNLOPS and MADGRAPH5_aMC@NLO are scaled to the total N3LO ggF cross section, and their K-factors are given. Other ggF predictions have been left at their natively calculated cross sections. Predictions for all other Higgs boson production modes XH are shown in grey. The dotted red line corresponds to the central value of the NNLOPS ggF prediction, scaled to the total N3LO cross section by the given K-factor, and added to the XH prediction. The data points from the individual $H \to ZZ^* \to 4\ell$ and $H \to \gamma\gamma$ channels are shown in blue and red, respectively. The combined data is shown in black. The error bars on the data points show the total uncertainties, while the systematic uncertainties are indicated by the boxes. The shaded bands on the expected cross sections indicate the PDF and scale uncertainties.

10.4 Limits on Beyond the Standard Model Physics

In the absence of new discoveries that exclude the Standard Model, the next best thing to do is set limits on alternative models. Beyond-the-Standard-Model (BSM) Higgs boson models usually involve new or modified couplings of the Higgs boson. These include things like introducing couplings to new particles produced in association with the Higgs (like a new Z' particle), modifying the HVV coupling or the Higgs self coupling, or adding/removing symmetries to/from the Higgs Lagrangian.

10.4.1 Brief Introduction to Effective Field Theories

Before the discovery of the W, the weak interaction was described with what was essentially an Effective Field Theory (EFT) known as Fermi's theory [152]. Rather than modeling a weak decay as the propagation of a W boson, the theory assumed a contact coupling of the two vector currents, where the coupling constant was called G_F. Equation 10.5 shows the Lagrangian of the Standard Model weak interaction (after EWSB) on the left and the Lagrangian as it would be described by Fermi's theory on the right.

$$\mathcal{L}_{\text{SM}} = \frac{g}{\sqrt{2}} J_+^\mu W_\mu^+ \qquad \mathcal{L}_{\text{EFT}} = \frac{8G_F}{\sqrt{2}} J_+^\mu J_\mu^- \tag{10.5}$$

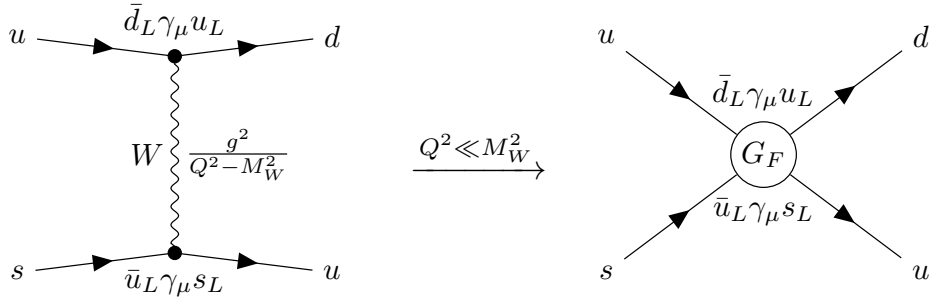

Figure 109: The left diagram shows a $us \to du$ weak decay using the full Standard Model theory where the W carries a momentum Q. The right diagram shows the same diagram in Fermi's Theory, an EFT of the weak interaction. Rather than using the W propagator, the EFT uses a dimension-6 operator made up of the two currents.

The current is defined as $J_+^\mu = \bar{\psi}_L \gamma^\mu \psi'_L$, which means the Fermi operator $J_+^\mu J_\mu^-$ has mass dimension 6, and necessitates G_F having a mass dimension of -2 in order for the total dimension of the Lagrangian to remain 4. Couplings with less than dimension 0 are non-renormalizable. A non-renormalizable theory can still be useful as long as one is aware of the energy scales at which

the theory no longer applies. Figure 109 shows a $us \to du$ decay in both theories. In the limit of $Q^2 << M_W^2$, the matrix element of the SM diagram can be Taylor expanded in the following way

$$\frac{1}{Q^2 - M_W^2} \approx -\frac{1}{M_W^2} + \mathcal{O}\left(\frac{Q^2}{M_W^4}\right) \tag{10.6}$$

Which shows that with a low enough momentum transfer, we can approximate the W propagator as a constant. The matrix element one would get from both diagrams is shown in the following equation:

$$\mathcal{M}_{\text{SM}} = (\bar{d}_L \gamma_\mu u_L)(\bar{u}_L \gamma_\nu s_L) \frac{ig^2}{2(Q^2 - M_W^2)} g^{\mu\nu} \qquad \mathcal{M}_{\text{EFT}} = (\bar{d}_L \gamma_\mu u_L)(\bar{u}_L \gamma_\nu s_L) \frac{-i4G_F}{\sqrt{2}} \tag{10.7}$$

And we can match the Fermi constant with the actual SM weak coupling by using the approximation at low Q^2 to get

$$\frac{G_F}{\sqrt{2}} = \frac{g^2}{8M_W^2} \tag{10.8}$$

We see that the mass dimension of G_F is caused by ignoring the massive W. M_W^2 also sets the energy scale at which the Fermi Theory begins to break down. As soon as the momentum transfer approaches the W mass, the Taylor approximation becomes worse, and more momentum-dependent terms need to be added to the matrix element calculation. Once Q^2 goes on-shell, all bets are off for the EFT.

10.4.2 Parameterizing a BSM model

Different kinds of frameworks can be used to parameterize Higgs boson BSM couplings. One framework is to write down a modified Higgs Lagrangian with the extra couplings and simulate the resulting new matrix elements with a generator like MadGraph to see how it affects the Higgs observables. For example, one can extend the classic Higgs Lagrangian by introducing dimension-6 operators in an Effective Field Theory Lagrangian. The EFT Lagrangian takes the form

$$\mathcal{L}_{\text{EFT}} = \mathcal{L}_{\text{SM}} + \sum_i \frac{1}{\Lambda^2} c_i \mathcal{O}_i \tag{10.9}$$

Where Λ^2 is an energy scale much higher than the current energy scale where the EFT would break down (In Fermi's theory, $\Lambda^2 = M_W^2$). The $\mathcal{O}_i$ terms are dimension-6 operators that respect the SM SU(3)×SU(2)×U(1) gauge invariance and Lorentz invariance, and the c_i are the dimensionless

Wilson coefficients that are a function of the renormalization scale μ^2 (i.e. Q^2), which in this case is the electroweak scale [153]. With the addition of baryon and lepton number conservation, there are 59 independent dimension-6 operators. If one focuses on CP conserving operators of this EFT that would affect the electroweak SU(2)×U(1) gauge couplings, there are a few new Higgs-gauge interactions which introduce momentum dependence into the HVV vertex, and change the shape of the Higgs differential cross section distributions for VBF and WH/ZH production modes [17]. One can then set limits on the c_i from both shape distributions and total cross section data.

Another framework for BSM Higgs couplings is the use of pseudo observables (PO). In the PO framework, one writes down the most general decay amplitude of an on-shell Higgs to 4 leptons, $A[H \to 4\ell]$, that is still Lorentz invariant. Things like assuming the Higgs is part of an $SU(2)_L$ doublet, lepton universality, or CP invariance are not taken for granted [154]. For $H \to 4\ell$, the amplitude takes the form

$$A_{\substack{\text{neutral}\\\text{current}}}[H \to \ell(p_1)\bar{\ell}(p_2)\ell'(p_3)\bar{\ell}'(p_4)] = i\frac{2m_Z^2}{v}\sum_{\ell=\ell_R,\ell_L}\sum_{\ell'=\ell'_R,\ell'_L}(\bar{\ell}\gamma_\rho\ell)(\bar{\ell}'\gamma_\rho\ell')\mathcal{T}^{\rho\sigma}(q_1,q_2) \tag{10.10}$$

$$\mathcal{T}^{\rho\sigma}(q_1,q_2) = F_L^{\ell\ell'}(q_1^2,q_2^2)g^{\rho\sigma} + F_T^{\ell\ell'}(q_1^2,q_2^2)\frac{q_1\cdot q_2 g^{\rho\sigma} - q_2^\rho q_1^\sigma}{m_Z^2} \tag{10.11}$$

$$+ F_{CP}^{\ell\ell'}(q_1^2,q_2^2)\frac{\varepsilon^{\rho\sigma\alpha\beta}q_{V_2\alpha}q_{V_1\beta}}{m_Z^2} \tag{10.12}$$

Where $q_1 = p_1 + p_2$ and $q_2 = p_3 + p_4$.

Pseudo Observable	Description	Modifies	SM value
g_Z^μ, g_Z^e	On-shell coupling between Z and leptons e, μ. Constrained to be very close to the SM from LEP.	F_L,F_T,F_{CP}	$g_Z^{\ell,SM}$
κ_{ZZ}	Effective $H \to ZZ$ signal strength	F_L	1
$\varepsilon_{Z\mu_L}$, ε_{Ze_L}	Contact term between H and Z+left-handed leptons	F_L	0
$\varepsilon_{Z\mu_R}$, ε_{Ze_R}	Contact term between H and Z+right-handed leptons	F_L	0
ε_{ZZ}	Contribution from transverse form factor	F_T	0
ε_{ZZ}^{CP}	Contribution from CP-odd form factor	F_{CP}	0

Table 104: Descriptions of the pseudo observables that affect the $H \to ZZ^* \to 4\ell$ channel.

The form factors $F_L^{\ell\ell'}$, $F_T^{\ell\ell'}$, and $F_{CP}^{\ell\ell'}$ describe the longitudinal, transverse, and CP-odd Lorentz structures of the interaction. In the Standard Model, $F_T^{\ell\ell'}$, and $F_{CP}^{\ell\ell'}$ are 0, while $F_L^{\ell\ell'}$ is only

parameterized by g_Z^ℓ at its SM value. The form factors are Taylor expanded around their physical poles (due to the propagation of the neutral SM electroweak gauge bosons), and the POs are defined from the residues [154]. The expansion is only done out to terms that can also be generated with local EFT operators with dimension 6 or less. Table 104 lists the POs relevant to the 4ℓ analysis. There are also $\gamma\gamma$ and $Z\gamma$ POs that appear in the form factors that are not shown.

10.4.3 Settings limits on Pseudo Observables

Using the results from the $H \to ZZ^* \to 4\ell$ fiducial analysis, we set limits on two simplified PO scenarios:

1. $\varepsilon_{Z\ell_L}$ **vs.** $\varepsilon_{Z\ell_R}$.
   Sets limits on extra contact terms between Higgs and Z+left/right-handed leptons. We keep flavor universality to ensure $\varepsilon_{Z\mu_{L,R}} = \varepsilon_{Ze_{L,R}}$, and keep all the other POs at the their SM values. So κ_{ZZ} is fixed to 1, and all other $\varepsilon = 0$.

2. κ_{ZZ} **vs.** $\varepsilon_{Z\ell_L}$.
   This is a scenario where, working at tree level in the linear EFT, one can be express the POs as linear combinations of the Wilson coefficients of the EFT Lagrangian [155]. $\varepsilon_{Z\ell_R} = 0.48\varepsilon_{Z\ell_L}$. We again keep flavor universality $\varepsilon_{Z\mu_{L,R}} = \varepsilon_{Ze_{L,R}}$, and set all of the other $\varepsilon = 0$.

Since the contact terms $\varepsilon_{Z\ell_L}$ and $\varepsilon_{Z\ell_R}$ are in the F_L form factor, they have the same Lorentz structure as the SM, and so only affect the dilepton invariant mass spectra, and do not affect the lepton angular distributions. We therefore use the difference in χ^2 between the measured and predicted m_{12}vs.m_{34} differential cross section to constrain the possible contributions from the contact terms. Using these constraints, we build a 2D profile likelihood assuming the SM values for all but the two free POs, and then set limits as shown in Figure 1010.

Since the addition of these POs changes the Higgs boson production rate, in principle we could have set limits based on the inclusive Higgs boson cross section alone, but in that case, the contours in the left figure of 1010 would have been a full ellipse. The added information from the invariant mass spectra improves the sensitivity. The shape information in m_{12}vs.m_{34} also improves the limit for the κ_{ZZ} vs $\varepsilon_{Z\ell_R}$ contour.

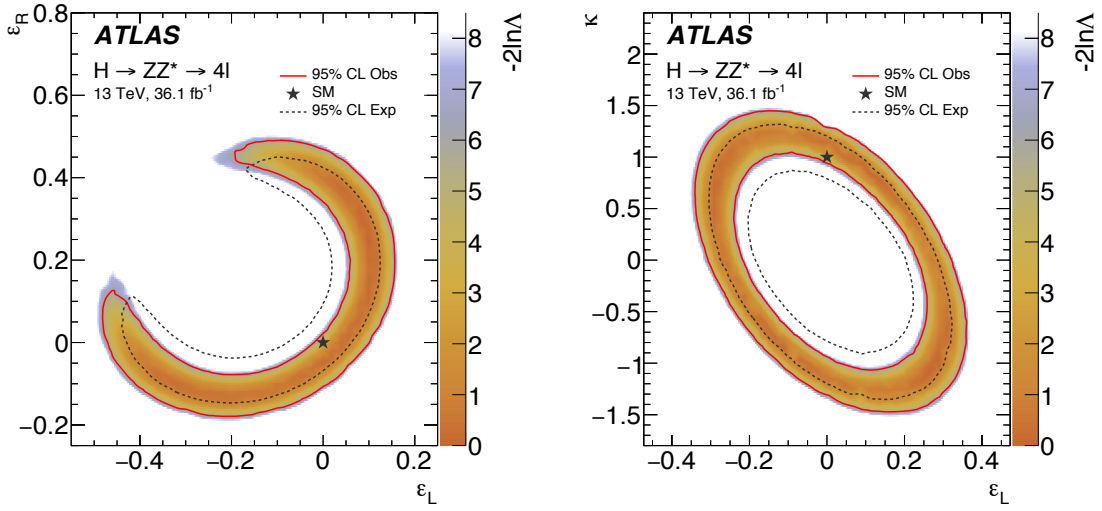

Figure 1010: Limits on pseudo-observables in $H \to 4\ell$ decays. On the left plot, the limits are set for $\varepsilon_{Z\ell_L}$ and $\varepsilon_{Z\ell_R}$, which are contact terms between Higgs boson and Z+left/right-handed leptons. On the right, limits are set on a linear EFT inspired scenario expressed with $\varepsilon_{Z\ell_L}$ and κ_{ZZ}. κ_{ZZ} modifies the strength of the Higgs boson coupling to Z bosons. The 95% confidence contour is surrounded by the red solid line. It is shifted with respect to the Standard Model (the black star and the black dotted line) but there are no significant deviations. The colors indicates the values of $-2\ln\lambda$.

Chapter 11

Conclusion

This thesis has presented results on the Higgs boson inclusive and differential cross sections with the ATLAS detector using proton-proton collisions at $\sqrt{s} = 13\,\text{TeV}$ at the LHC. We have used data collected over the span of 2015 and 2016 totaling to an integrated luminosity of $36.1\,\text{fb}^{-1}$. Two types of cross sections were measured: the fiducial cross sections, limited to the phase space of $H \to ZZ^* \to 4\ell$ and the acceptance of the ATLAS detector, and the total cross sections, measured in the full phase space of the Higgs using data from both $H \to ZZ^* \to 4\ell$ and $H \to \gamma\gamma$ (diphoton) decays. The fiducial cross sections are less model dependent in their measurement, while the total cross sections are more model dependent but benefit from the added statistics of two independent decay channels.

The inclusive cross section result measures the over-all probability of a Higgs boson being produced from a proton-proton collision. The Standard Model (SM) predicted gluon-gluon fusion cross section (which is how 87% of Higgs bosons are produced in pp collisions) was perturbatively calculated to N3LO in QCD, making it the most accurate theory prediction for Higgs boson cross sections to date. In the fiducial analysis, we measured the cross section to be $\sigma_{\text{fid}} \cdot \text{BR}(H \to 4\ell) = 3.62 \pm 0.50$ (stat) +0.25/-0.20 (sys) fb, in agreement with the SM prediction of 2.91 ± 0.13 fb. In the full phase space analysis using the combined data, the cross section was measured to be $\sigma_{\text{tot}} = 57.0$ +6.0/-5.9 (stat.) +4.0/-3.3 (syst.) pb, in agreement with the SM prediction of of 55.6 ± 2.5 pb. Each measurement has a p-value of 19% and 84% respectively. Given this result, the measured cross sections are fully consistent with a Standard Model production of the Higgs boson.

The differential cross section presents the production of the Higgs boson from proton-proton collisions as a function of various observables. An observable like the Higgs transverse momentum, p_T^H, is sensitive to new Higgs couplings to undiscovered particles or modified couplings to known SM

particles, which would show up as more Higgs bosons produced at larger p_T^H. N_{jets} is the number of jets produced in association with the Higgs, and it is sensitive to Higgs production modes, i.e. a Higgs produced via VBF will always be associated with 2 jets while a Higgs produced via ggF is more likely to have no associated jets. Both p_{T} and N_{jets} can provide sensitivity to the couplings of the Higgs. Section 5.4 explains each of the differential variables measured in the analysis and their sensitivity to different properties of the Higgs boson.

To summarize the fiducial and total phase space differential cross section results, we will focus on just p_T^H and N_{jets} and compare them to the baseline NNLOPS theory prediction. We measured in the fiducial analysis a p-value of 25% and 33% for p_T^H and N_{jets} respectively, and in the total phase space analysis a p-value of 29% and 43% for p_T^H and N_{jets} respectively. The measurements both became more compatible with the Standard Model with the additional data from $H \to \gamma\gamma$. While the results overall agree well with coming from the SM, the higher bins of p_T^H and N_{jets}, as seen in Figures 105, 106 for the fiducial result and Figure 108 for the total result, have little sensitivity. The sensitivity in these bins is limited by low statistics, which will improve when the analysis is repeated with the full Run 2 dataset of almost $150\,\text{fb}^{-1}$.

In the absence of any discoveries beyond the Standard Model, limits were also set on alternative models which assume extra couplings between the Higgs boson and SM particles. These alternative models were derived within the framework of pseudo observables (PO). PO models relax certain assumptions that the Standard Model makes about the nature of the Higgs boson such as assuming the Higgs is part of an $SU(2)_L$ doublet, lepton universality, or CP invariance, and creates new parameters that can be fit to with data. Both inclusive and differential distributions can constrain the PO models, and we used the measured m_{12}vs.m_{34} differential cross section to constrain the values of extra contact terms between the Higgs and Z+left/right-handed leptons, as shown in Figure 1010.

Looking Ahead

Given that there is low sensitivity in many distributions at high Higgs and jet p_{T} due to low statistics, the full Run 2 dataset will be able to increase the sensitivity in these bins and reduce the uncertainty of the measurement. In case of revealed excesses from added data, using frameworks like the pseudo observables or dimension-6 Effective Field Theories to parameterize any beyond the Standard Model effects will become more relevant and important. The nature of these excesses would hopefully point to ideas of how to further investigate some of the open questions in particle

physics. Looking towards Run 3, more data will also be able to begin probing rarer properties of the Higgs, such as the Higgs self-coupling term λ with the investigation of di-Higgs production.

The Higgs boson, having only recently been discovered, still has many years of fruitful investigation ahead of it. Better discrimination between production modes will better constrain the strength of its couplings to the fermions and vector bosons and reveal any deviations from the SM. Larger and larger statistics will make rarer decays or deviations more pronounced. The four lepton channel with its strong sensitivity stands to gain deeply from more data, and by the end of Run 3 will have its uncertainties dominated by systematics rather than statistics.

Bibliography

[1] ATLAS Collaboration, *Measurements of the Total and Differential Higgs Boson Production Cross Sections Combining the $H \to \gamma\gamma$ and $H \to ZZ^* \to 4\ell$ Decay Channels at $\sqrt{s} = 8$ TeV with the ATLAS Detector*, Phys. Rev. Lett. **1**15 (2015) 091801, arXiv:1504.05833 [hep-ex]. (document), 10.2.2, 10.3.2

[2] ATLAS Collaboration, *Measurement of inclusive and differential cross sections in the $H \to ZZ^* \to 4\ell$ decay channel in pp collisions at $\sqrt{s} = 13$ TeV with the ATLAS detector*, JHEP **10** (2017) 132, arXiv:1708.02810 [hep-ex]. (document), 1

[3] ATLAS Collaboration, M. Aaboud et al., *Combined measurement of differential and total cross sections in the $H \to \gamma\gamma$ and the $H \to ZZ^* \to 4\ell$ decay channels at $\sqrt{s} = 13$ TeV with the ATLAS detector*, Phys. Lett. **B**786 (2018) 114, arXiv:1805.10197 [hep-ex]. (document), 1

[4] ATLAS Collaboration, *Observation of a new particle in the search for the Standard Model Higgs boson with the ATLAS detector at the LHC*, Phys. Lett. B **7**16 (2012) 1, arXiv:1207.7214 [hep-ex]. 1, 2.3.4

[5] CMS Collaboration, *Observation of a new boson at a mass of 125 GeV with the CMS experiment at the LHC*, Phys. Lett. B **7**16 (2012) 30, arXiv:1207.7235 [hep-ex]. 1

[6] P. W. Higgs, *Broken symmetries, massless particles and gauge fields*, Physics Letters **12** (1964) 132–133. 1, 2.2

[7] P. W. Higgs, *Broken symmetries and the masses of gauge bosons*, Phys. Rev. Lett. **13** (1964) 508–509. 1, 2.2

[8] F. Englert and R. Brout, *Broken symmetry and the mass of gauge vector mesons*, Phys. Rev. Lett. **13** (1964) 321–323. 1, 2.2

[9] ATLAS Collaboration, M. Aaboud et al., *Measurement of the Higgs boson mass in the $H \to ZZ^* \to 4\ell$ and $H \to \gamma\gamma$ channels with $\sqrt{s} = 13$ TeV pp collisions using the ATLAS detector*, Phys. Lett. **B**784 (2018) 345–366, arXiv:1806.00242 [hep-ex]. 1

[10] ATLAS Collaboration, A. Collaboration, *Constraints on off-shell Higgs boson production and the Higgs boson total width in $ZZ \to 4\ell$ and $ZZ \to 2\ell 2\nu$ final states with the ATLAS detector*, Phys. Lett. **B**786 (2018) 223–244, arXiv:1808.01191 [hep-ex]. 1, 2.3.4

[11] ATLAS Collaboration, *Measurement of the Higgs boson coupling properties in the $H \to ZZ^* \to 4\ell$ decay channel at $\sqrt{s} = 13$ TeV with the ATLAS detector*, JHEP **03** (2018) 095, arXiv:1712.02304 [hep-ex]. 1

[12] ATLAS Collaboration, *Measurements of Higgs boson properties in the diphoton decay channel with 36 fb^{-1} of pp collision data at $\sqrt{s} = 13$ TeV with the ATLAS detector*, arXiv:1802.04146 [hep-ex]. 1, 9.6

[13] P. E. R. F.R.S., *The scattering of α and β particles by matter and the structure of the atom*, The London, Edinburgh, and Dublin Philosophical Magazine and Journal of Science **21** (1911) no. 125, 669–688. 1

[14] J. T. F.R.S., *On the structure of the atom: an investigation of the stability and periods of oscillation of a number of corpuscles arranged at equal intervals around the circumference of a circle; with application of the results to the theory of atomic structure*, The London, Edinburgh, and Dublin Philosophical Magazine and Journal of Science **7** (1904) no. 39, 237–265. 1

[15] I. Hertel, *8.2 Differential cross section and Rutherford's scattering experiment*, 2001. http://staff.mbi-berlin.de/hertel/physik3/chapter8/8.2html/01.htm. 11

[16] A. Purcell, *Go on a particle quest at the first CERN webfest. Le premier webfest du CERN se lance à la conquête des particules*, . https://cds.cern.ch/record/1473657. 21

[17] D. de Florian et al., *Handbook of LHC Higgs Cross Sections: 4. Deciphering the Nature of the Higgs Sector*, arXiv:1610.07922 [hep-ph]. 2.1, 2.3.3, 24, 21, 28, 2.3.4, 5.1, 9.3.2, 9.6.2, 10.2.1, 10.2.2, 10.3.1, 10.3.2, 10.4.2

[18] C.-N. Yang and R. L. Mills, *Conservation of Isotopic Spin and Isotopic Gauge Invariance*, Phys. Rev. **96** (1954) 191–195. [,150(1954)]. 2.1

[19] G. 't Hooft and M. Veltman, *Regularization and renormalization of gauge fields*, Nuclear Physics B **44** (1972) 189 – 213. 2.1

[20] M. Y. Han and Y. Nambu, *Three Triplet Model with Double SU(3) Symmetry*, Phys. Rev. **139** (1965) B1006–B1010. [,187(1965)]. 2.1

[21] K. G. Wilson, *Confinement of quarks*, Phys. Rev. D **10** (1974) 2445–2459. 2.1

[22] D. J. Gross and F. Wilczek, *Asymptotically free gauge theories. I*, Phys. Rev. D **8** (1973) 3633–3652. 2.1

[23] D. J. Gross and F. Wilczek, *Asymptotically free gauge theories. II*, Phys. Rev. D **9** (1974) 980–993. 2.1

[24] A. Salam and J. C. Ward, *Electromagnetic and weak interactions*, Phys.Lett. **13** (1964) 168–171. 2.1

[25] S. Weinberg, *A model of leptons*, Phys. Rev. Lett. **19** (1967) 1264–1266. 2.1

[26] S. Glashow, *Partial symmetries of weak interactions*, Nucl.Phys. **22** (1961) 579–588. 2.1

[27] R. P. Feynman, *Mathematical formulation of the quantum theory of electromagnetic interaction*, Phys. Rev. **80** (1950) 440–457. 2.1

[28] C. N. Yang and R. L. Mills, *Conservation of isotopic spin and isotopic gauge invariance*, Phys. Rev. **96** (1954) 191–195. 2.2

[29] G. S. Guralnik, C. R. Hagen, and T. W. B. Kibble, *Global conservation laws and massless particles*, Phys. Rev. Lett. **13** (1964) 585–587. 2.2

[30] J. Ellis, *Higgs Physics*, . https://cds.cern.ch/record/1638469. 52 pages, 45 figures, Lectures presented at the ESHEP 2013 School of High-Energy Physics, to appear as part of the proceedings in a CERN Yellow Report. 22

[31] UA1 Collaboration, *Experimental observation of isolated large transverse energy electrons with associated missing energy at* $\sqrt{s} = 540$ *GeV*, Phys. Lett. B **122** (1983) 103–116. 2.2

[32] UA2 Collaboration, *Observation of single isolated electrons of high transverse momentum in events with missing transverse energy at the CERN pp collider*, Phys. Lett. B **122** (1983) 476–485. 2.2

[33] UA1 Collaboration, *Experimental observation of lepton pairs of invariant mass around 95* GeV/c^2 *at the CERN SPS collider*, Phys. Lett. B **126** (1983) 398–410. 2.2

[34] UA2 Collaboration, *Evidence for* $Z^0 \to e^+e^-$ *at the CERN pp collider*, Phys. Lett. B **129** (1983) 130–140. 2.2

[35] ATLAS and CMS Collaborations, *Combined Measurement of the Higgs Boson Mass in pp Collisions at* $\sqrt{s} = 7$ *and* 8 *TeV with the ATLAS and CMS Experiments*, Phys. Rev. Lett. **1**14 (2015) 191803, arXiv:1503.07589 [hep-ex]. 2.2, 8.3

[36] H. Yukawa, *On the Interaction of Elementary Particles I*, Proc. Phys. Math. Soc. Jap. **17** (1935) 48–57. [Prog. Theor. Phys. Suppl.1,1(1935)]. 2.2

[37] M. E. Peskin and D. V. Schroeder, *An Introduction to Quantum Field Theory*. Addison-Wesley, 1995. 2.3, 2.3.1, 2.3.2

[38] J. C. Collins, D. E. Soper, and G. F. Sterman, *Factorization of Hard Processes in QCD*, Adv. Ser. Direct. High Energy Phys. **5** (1989) 1–91, arXiv:hep-ph/0409313 [hep-ph]. 2.3

[39] L. A. Harland-Lang, A. D. Martin, P. Motylinski, and R. S. Thorne, *Parton distributions in the LHC era: MMHT 2014 PDFs*, The European Physical Journal C **7**5 (May, 2015) 204. https://doi.org/10.1140/epjc/s10052-015-3397-6. 23, 2.3.1

[40] H. Collaboration, *Inclusive deep inelastic scattering at high Q2 with longitudinally polarised lepton beams at HERA*, Journal of High Energy Physics **2**012 (Sep, 2012) 61. https://doi.org/10.1007/JHEP09(2012)061. 2.3.1

[41] V. N. Gribov and L. N. Lipatov, *Deep inelastic e p scattering in perturbation theory*, Sov. J. Nucl. Phys. **1**5 (1972) 438–450. [Yad. Fiz.15,781(1972)]. 2.3.1

[42] G. Altarelli and G. Parisi, *Asymptotic Freedom in Parton Language*, Nucl. Phys. **B**126 (1977) 298–318. 2.3.1

[43] J. Butterworth et al., *PDF4LHC recommendations for LHC Run II*, J. Phys. **G**43 (2016) 023001, arXiv:1510.03865 [hep-ph]. 2.3.1, 2.4.1

[44] S. Dulat, T.-J. Hou, J. Gao, M. Guzzi, J. Huston, P. Nadolsky, J. Pumplin, C. Schmidt, D. Stump, and C. P. Yuan, *New parton distribution functions from a global analysis of quantum chromodynamics*, Phys. Rev. **D**93 (2016) no. 3, 033006, arXiv:1506.07443 [hep-ph]. 2.3.1

[45] R. D. Ball et al., *Parton distributions for the LHC Run II*, JHEP **0**4 (2015) 040, arXiv:1410.8849 [hep-ph]. 2.3.1

[46] S. Actis, G. Passarino, C. Sturm, and S. Uccirati, *NLO Electroweak Corrections to Higgs Boson Production at Hadron Colliders*, Phys. Lett. **B**670 (2008) 12–17, arXiv:0809.1301 [hep-ph]. 2.3.3

[47] M. Kramer, E. Laenen, and M. Spira, *Soft gluon radiation in Higgs boson production at the LHC*, Nucl. Phys. **B**511 (1998) 523–549, arXiv:hep-ph/9611272 [hep-ph]. 2.3.3

[48] M. Bonvini and S. Marzani, *Resummed Higgs cross section at N3LL*, Journal of High Energy Physics **2**014 (Sep, 2014) 7. https://doi.org/10.1007/JHEP09(2014)007. 2.3.3

[49] T. Gleisberg et al., *Event generation with SHERPA 1.1*, JHEP **0**2 (2009) 007, arXiv:0811.4622 [hep-ph]. 29, 2.4.2

[50] S. Agostinelli et al., *GEANT4 - a simulation toolkit*, Nucl. Instrum. Meth. **A**506 (2003) 250–303. 2.4

[51] P. Nason, *A New method for combining NLO QCD with shower Monte Carlo algorithms*, JHEP **1**1 (2004) 040, arXiv:hep-ph/0409146. 2.4.1

[52] S. Frixione, P. Nason, and C. Oleari, *Matching NLO QCD computations with parton shower simulations: the POWHEG method*, JHEP **1**1 (2007) 070, arXiv:0709.2092 [hep-ph]. 2.4.1

[53] S. Alioli, P. Nason, C. Oleari, and E. Re, *A general framework for implementing NLO calculations in shower Monte Carlo programs: the POWHEG BOX*, JHEP **0**6 (2010) 043, arXiv:1002.2581 [hep-ph]. 2.4.1

[54] K. Hamilton, P. Nason, E. Re, and G. Zanderighi, *NNLOPS simulation of Higgs boson production*, JHEP **1**0 (2013) 222, arXiv:1309.0017 [hep-ph]. 2.4.1

[55] P. Nason and C. Oleari, *NLO Higgs boson production via vector-boson fusion matched with shower in POWHEG*, JHEP **0**2 (2010) 037, arXiv:0911.5299 [hep-ph]. 2.4.1

[56] G. Luisoni, P. Nason, C. Oleari, and F. Tramontano, *$HW^{\pm}/HZ$ + 0 and 1 jet at NLO with the POWHEG BOX interfaced to GoSam and their merging within MiNLO*, JHEP **1**0 (2013) 083, arXiv:1306.2542 [hep-ph]. 2.4.1

[57] K. Hamilton, P. Nason, and G. Zanderighi, *MINLO: Multi-Scale Improved NLO*, JHEP **1**0 (2012) 155, arXiv:1206.3572 [hep-ph]. 2.4.1

[58] S. Catani and M. Grazzini, *An NNLO subtraction formalism in hadron collisions and its application to Higgs boson production at the LHC*, Phys. Rev. Lett. **9**8 (2007) 222002, arXiv:hep-ph/0703012 [hep-ph]. 2.4.1, 10.2.2

[59] M. Grazzini, *NNLO predictions for the Higgs boson signal in the $H \to WW \to \ell\nu\ell\nu$ and $H \to ZZ \to 4\ell$ decay channels*, JHEP **0**2 (2008) 043, arXiv:0801.3232 [hep-ph]. 2.4.1, 10.2.2

[60] J. Alwall et al., *The automated computation of tree-level and next-to-leading order differential cross sections, and their matching to parton shower simulations*, JHEP **07** (2014) 079, arXiv:1405.0301 [hep-ph]. 2.4.1, 10.2.2

[61] R. Frederix and S. Frixione, *Merging meets matching in MC@NLO*, JHEP **12** (2012) 061, arXiv:1209.6215 [hep-ph]. 2.4.1, 10.2.2

[62] D. de Florian, G. Ferrera, M. Grazzini, and D. Tommasini, *Higgs boson production at the LHC: transverse momentum resummation effects in the $H \to 2\gamma, H \to WW \to \ell\nu\ell\nu$ and $H \to ZZ \to 4\ell$ decay modes*, JHEP **06** (2012) 132, arXiv:1203.6321 [hep-ph]. 2.4.1, 10.2.2

[63] M. Grazzini and H. Sargsyan, *Heavy-quark mass effects in Higgs boson production at the LHC*, JHEP **09** (2013) 129, arXiv:1306.4581 [hep-ph]. 2.4.1, 10.2.2

[64] A. D. Martin, W. J. Stirling, R. S. Thorne, and G. Watt, *Parton distributions for the LHC*, Eur. Phys. J. **C** 63 (2009) 189–285, arXiv:0901.0002 [hep-ph]. 2.4.1

[65] K. Hamilton, P. Nason, C. Oleari, and G. Zanderighi, *Merging H/W/Z + 0 and 1 jet at NLO with no merging scale: a path to parton shower + NNLO matching*, JHEP **05** (2013) 082, arXiv:1212.4504 [hep-ph]. 2.4.1

[66] H.-L. Lai et al., *New parton distributions for collider physics*, Phys. Rev. D **82** (2010) 074024, arXiv:1007.2241 [hep-ph]. 2.4.1

[67] R. D. Ball et al., *Parton distributions with LHC data*, Nucl. Phys. B **867** (2013) 244–289, arXiv:1207.1303 [hep-ph]. 2.4.1

[68] T. Sjostrand, S. Mrenna, and P. Skands, *A Brief Introduction to PYTHIA 8.1*, Comput. Phys. Commun. **178** (2008) 852–867, arXiv:0710.3820 [hep-ph]. 2.4.1

[69] ATLAS Collaboration, *Measurement of the Z/γ^* boson transverse momentum distribution in pp collisions at $\sqrt{s} = 7$ TeV with the ATLAS detector*, JHEP **09** (2014) 145, arXiv:1406.3660 [hep-ex]. 2.4.1

[70] M. Bahr et al., *Herwig++ Physics and Manual*, Eur. Phys. J. C **58** (2008) 639–707, arXiv:0803.0883 [hep-ph]. 2.4.1

[71] M. H. Seymour and A. Siodmok, *Constraining MPI models using σ_{eff} and recent Tevatron and LHC Underlying Event data*, JHEP **10** (2013) 113, arXiv:1307.5015 [hep-ph]. 2.4.1

[72] A. Bredenstein, A. Denner, S. Dittmaier, and M. M. Weber, *Precise predictions for the Higgs-boson decay $H \to WW/ZZ \to 4$leptons*, Phys. Rev. **D** 74 (2006) 013004, arXiv:hep-ph/0604011. 2.4.1

[73] A. Bredenstein, A. Denner, S. Dittmaier, and M. M. Weber, *Radiative corrections to the semileptonic and hadronic Higgs-boson decays $H \to WW/ZZ \to 4$ fermions*, JHEP **02** (2007) 080, arXiv:hep-ph/0611234. 2.4.1

[74] S. Höche, F. Krauss, M. Schönherr, and F. Siegert, *QCD matrix elements + parton showers. The NLO case*, JHEP **04** (2013) 027, arXiv:1207.5030 [hep-ph]. 2.4.2

[75] S. Schumann and F. Krauss, *A Parton shower algorithm based on Catani-Seymour dipole factorisation*, JHEP **03** (2008) 038, arXiv:0709.1027 [hep-ph]. 2.4.2

[76] B. Biedermann, A. Denner, S. Dittmaier, L. Hofer, and B. Jäger, *Electroweak corrections to $pp \to \mu^+\mu^- e^+ e^- + X$ at the LHC: a Higgs background study*, Phys. Rev. Lett. **116** (2016) no. 16, 161803, arXiv:1601.07787 [hep-ph]. 2.4.2

[77] B. Biedermann, A. Denner, S. Dittmaier, L. Hofer, and B. Jager, *Next-to-leading-order electroweak corrections to the production of four charged leptons at the LHC*, JHEP **01** (2017) 033, arXiv:1611.05338 [hep-ph]. 2.4.2

[78] N. Kauer, C. O'Brien, and E. Vryonidou, *Interference effects for $H \to W\,W \to \ell\nu q\overline{q}'$ and $H \to ZZ \to \ell\bar{\ell}q\bar{q}$ searches in gluon fusion at the LHC*, JHEP **10** (2015) 074, arXiv:1506.01694 [hep-ph]. 2.4.2

[79] F. Caola, K. Melnikov, R. Rontsch, and L. Tancredi, *QCD corrections to ZZ production in gluon fusion at the LHC*, Phys. Rev. **D92** (2015) no. 9, 094028, arXiv:1509.06734 [hep-ph]. 2.4.2

[80] J. M. Campbell, R. K. Ellis, M. Czakon, and S. Kirchner, *Two loop correction to interference in $gg \to ZZ$*, JHEP **08** (2016) 011, arXiv:1605.01380 [hep-ph]. 2.4.2

[81] K. Melnikov and M. Dowling, *Production of two Z-bosons in gluon fusion in the heavy top quark approximation*, Phys. Lett. **B744** (2015) 43–47, arXiv:1503.01274 [hep-ph]. 2.4.2

[82] T. Gleisberg and S. Höche, *Comix, a new matrix element generator*, JHEP **12** (2008) 039, arXiv:0808.3674 [hep-ph]. 2.4.2

[83] F. Cascioli, P. Maierhofer, and S. Pozzorini, *Scattering Amplitudes with Open Loops*, Phys. Rev. Lett. **108** (2012) 111601, arXiv:1111.5206 [hep-ph]. 2.4.2

[84] J. Alwall, M. Herquet, F. Maltoni, O. Mattelaer, and T. Stelzer, *MadGraph 5 : Going Beyond*, JHEP **06** (2011) 128, arXiv:1106.0522 [hep-ph]. 2.4.2

[85] N. Davidson, T. Przedzinski, and Z. Was, *PHOTOS Interface in C++: Technical and Physics Documentation*, arXiv:1011.0937 [hep-ph]. 2.4.2

[86] T. Sjostrand, S. Mrenna, and P. Skands, *PYTHIA 6.4 physics and manual*, JHEP **05** (2006) 026, arXiv:0603175 [hep-ph]. 2.4.2

[87] P. Golonka and Z. Was, *PHOTOS Monte Carlo: A Precision tool for QED corrections in Z and W decays*, Eur. Phys. J. **C** 45 (2006) 97–107, arXiv:hep-ph/0506026. 2.4.2

[88] S. Jadach, Z. Was, R. Decker, and J. H. Kuhn, *The tau decay library TAUOLA: Version 2.4*, Comput. Phys. Commun. **76** (1993) 361–380. 2.4.2

[89] P. Golonka et al., *The tauola-photos-F environment for the TAUOLA and PHOTOS packages, release II*, Comput. Phys. Commun. **174** (2006) 818–835. 2.4.2

[90] L. R. Evans and P. Bryant, *LHC Machine*, JINST **3** (2008) S08001. https://cds.cern.ch/record/1129806. This report is an abridged version of the LHC Design Report (CERN-2004-003). 3.1

[91] J. Haffner, *The CERN accelerator complex. Complexe des accélérateurs du CERN*, . https://cds.cern.ch/record/1621894. General Photo. 31

[92] ATLAS Collaboration, *The ATLAS Experiment at the CERN Large Hadron Collider*, JINST **3** (2008) S08003. 3.1, 3.3, 33

[93] CMS Collaboration, *The CMS experiment at the CERN LHC*, JINST **3** (2008) S08004. 3.1

[94] T. A. Collaboration, *The ALICE experiment at the CERN LHC*, Journal of Instrumentation **3** (2008) no. 08, S08002. http://stacks.iop.org/1748-0221/3/i=08/a=S08002. 3.1

[95] T. L. Collaboration, *The LHCb Detector at the LHC*, Journal of Instrumentation **3** (2008) no. 08, S08005. http://stacks.iop.org/1748-0221/3/i=08/a=S08005. 3.1

[96] P. Grafström and W. Kozanecki, *Luminosity determination at proton colliders*, Progress in Particle and Nuclear Physics **8**1 (2015) 97–148. http://www.sciencedirect.com/science/article/pii/S0146641014000878. 3.2

[97] R. Bruce, R. W. Assmann, and S. Redaelli, *Calculations of safe collimator settings and β^* at the CERN Large Hadron Collider*, Phys. Rev. ST Accel. Beams **1**8 (Jun, 2015) 061001. https://link.aps.org/doi/10.1103/PhysRevSTAB.18.061001. 3.2

[98] J. Pequenao and P. Schaffner, *A computer generated image representing how ATLAS detects particles*, . https://cds.cern.ch/record/1505342. 34

[99] ATLAS Collaboration, *The ATLAS Inner Detector commissioning and calibration*, Eur. Phys. J. C **7**0 (2010) 787, arXiv:1004.5293 [hep-ex]. 3.4

[100] ATLAS Collaboration, *Vertex Reconstruction Performance of the ATLAS Detector at$\sqrt{s} = 13$ TeV*, ATL-PHYS-PUB-2015-026, 2015. https://cds.cern.ch/record/2037717. 3.4

[101] J. Pequenao, *Computer generated image of the ATLAS inner detector*, . https://cds.cern.ch/record/1095926. 35

[102] G. Aad et al., *ATLAS pixel detector electronics and sensors*, JINST **3** (2008) P07007. 3.4.1

[103] ATLAS Collaboration Collaboration, M. Capeans, G. Darbo, K. Einsweiller, M. Elsing, T. Flick, M. Garcia-Sciveres, C. Gemme, H. Pernegger, O. Rohne, and R. Vuillermet, *ATLAS Insertable B-Layer Technical Design Report*, Tech. Rep. CERN-LHCC-2010-013. ATLAS-TDR-19, Sep, 2010. https://cds.cern.ch/record/1291633. 3.4.1

[104] A. Ahmad et al., *The Silicon microstrip sensors of the ATLAS semiconductor tracker*, Nucl. Instrum. Meth. **A**578 (2007) 98–118. 3.4.2

[105] E. Abat et al., *The ATLAS TRT Barrel Detector*, JINST **3** (2008) P02014. 3.4.3

[106] E. Abat et al., *The ATLAS TRT end-cap detectors*, JINST **3** (2008) P10003. 3.4.3

[107] T. A. T. collaboration, *The ATLAS TRT electronics*, JINST **3** (2008) no. 06, P06007. http://stacks.iop.org/1748-0221/3/i=06/a=P06007. 3.4.3

[108] ATLAS Collaboration, *Basic ATLAS TRT performance studies of Run 1*, ATL-INDET-PUB-2014-001, 2014. https://cds.cern.ch/record/1669603. 36

[109] J. Pequenao, *Computer Generated image of the ATLAS calorimeter*, . https://cds.cern.ch/record/1095927. 37

[110] ATLAS Collaboration, *ATLAS liquid-argon calorimeter: Technical Design Report*. CERN, Geneva, 1996. https://cds.cern.ch/record/331061. 3.5.1

[111] ATLAS Collaboration, *ATLAS tile calorimeter: Technical Design Report*. CERN, Geneva, 1996. https://cds.cern.ch/record/331062. 3.5.2

[112] ATLAS Collaboration, *ATLAS muon spectrometer: Technical Design Report*. CERN, Geneva, 1997. https://cds.cern.ch/record/331068. 3.6

[113] J. Pequenao, *Computer generated image of the ATLAS Muons subsystem*, . https://cds.cern.ch/record/1095929. 38

[114] ATLAS Collaboration, *Performance of the ATLAS muon trigger in pp collisions at* $\sqrt{s} = 8$ *TeV*, Eur. Phys. J. C **75** (2015) 120, arXiv:1408.3179 [hep-ex]. 39

[115] ATLAS Collaboration, *Trigger Menu in 2016*, ATL-DAQ-PUB-2017-001, 2017. https://cds.cern.ch/record/2242069. 4.1

[116] ATLAS Collaboration, *Performance of the ATLAS Trigger System in 2015*, Eur. Phys. J. C **77** (2017) 317, arXiv:1611.09661 [hep-ex]. 4.1

[117] ATLAS, *Overview of the ATLAS trigger and data acquisition system in Run-2*, 2017. https://twiki.cern.ch/twiki/bin/view/AtlasPublic/ApprovedPlotsDAQ. 41

[118] R. Fruhwirth, *Application of Kalman filtering to track and vertex fitting*, Nucl. Instrum. Meth. **A262** (1987) 444–450. 4.2.1

[119] ATLAS Collaboration, *Electron efficiency measurements with the ATLAS detector using 2012 LHC proton–proton collision data*, Eur. Phys. J. C **77** (2017) 195, arXiv:1612.01456 [hep-ex]. 4.2.1

[120] ATLAS Collaboration, *Electron efficiency measurements with the ATLAS detector using the 2015 LHC proton–proton collision data*, ATLAS-CONF-2016-024, 2016. https://cds.cern.ch/record/2157687. 43, 4.2.2, 4.2.2, 44

[121] ATLAS Collaboration, *Muon reconstruction performance of the ATLAS detector in proton–proton collision data at* $\sqrt{s} = 13$ *TeV*, Eur. Phys. J. C **76** (2016) 292, arXiv:1603.05598 [hep-ex]. 4.3.1, 4.3.1, 4.3.2

[122] ATLAS Collaboration, *Topological cell clustering in the ATLAS calorimeters and its performance in LHC Run 1*, Eur. Phys. J. C **77** (2017) 490, arXiv:1603.02934 [hep-ex]. 4.4.1

[123] M. Cacciari, G. P. Salam, and G. Soyez, *The anti-*k_t *jet clustering algorithm*, JHEP **04** (2008) 063, arXiv:0802.1189 [hep-ph]. 4.4.1, 5.3.3, 9.6.1

[124] M. Cacciari, G. P. Salam, and G. Soyez, *FastJet user manual*, The European Physical Journal C **72** (Mar, 2012) 1896. https://doi.org/10.1140/epjc/s10052-012-1896-2. 4.4.1, 5.3.3

[125] ATLAS Collaboration, *Pile-up subtraction and suppression for jets in ATLAS*, ATLAS-CONF-2013-083, 2013. https://cds.cern.ch/record/1570994. 4.4.1

[126] M. Cacciari, G. P. Salam, and G. Soyez, *The Catchment Area of Jets*, JHEP **04** (2008) 005, arXiv:0802.1188 [hep-ph]. 4.4.1

[127] ATLAS Collaboration, *Jet energy scale measurements and their systematic uncertainties in proton–proton collisions at* $\sqrt{s} = 13$ *TeV with the ATLAS detector*, Phys. Rev. D **96** (2017) 072002, arXiv:1703.09665 [hep-ex]. 4.4.1, 8.1.3

[128] ATLAS Collaboration, *Monte Carlo Calibration and Combination of In-situ Measurements of Jet Energy Scale, Jet Energy Resolution and Jet Mass in ATLAS*, ATLAS-CONF-2015-037, 2015. https://cds.cern.ch/record/2044941. 4.4.1

[129] ATLAS Collaboration, *Jet Calibration and Systematic Uncertainties for Jets Reconstructed in the ATLAS Detector at* $\sqrt{s} = 13$ *TeV*, ATL-PHYS-PUB-2015-015, 2015. https://cds.cern.ch/record/2037613. 4.4.1

[130] ATLAS Collaboration, *Selection of jets produced in* 13 *TeV proton–proton collisions with the ATLAS detector*, ATLAS-CONF-2015-029, 2015. https://cds.cern.ch/record/2037702. 4.4.2

[131] ATLAS Collaboration, *Characterisation and mitigation of beam-induced backgrounds observed in the ATLAS detector during the 2011 proton–proton run*, JINST **8** (2013) P07004, arXiv:1303.0223 [hep-ex]. 4.4.2

[132] ATLAS Collaboration, *Tagging and suppression of pileup jets with the ATLAS detector*, ATLAS-CONF-2014-018, 2014. https://cds.cern.ch/record/1700870. 4.4.2

[133] ATLAS Collaboration, *Optimisation of the ATLAS b-tagging performance for the 2016 LHC Run*, ATL-PHYS-PUB-2016-012, 2016. https://cds.cern.ch/record/2160731. 4.4.2, 5.2.2, 5.3.3

[134] Stark, Simon Holm, *Measurements of the elastic, inelastic and total pp cross sections with the ATLAS, CMS and TOTEM detectors*, EPJ Web Conf. **141** (2017) 03007. https://doi.org/10.1051/epjconf/201714103007. 5.1

[135] H. Group, *Common supporting note for the* $H \to 4\ell$ *channel: Event selection, background estimates, performance studies, etc.*, Tech. Rep. ATL-COM-PHYS-2015-1277, CERN, Geneva, Oct, 2015. https://cds.cern.ch/record/2058249. 5.2.3

[136] Wilks, S. S., *The Large-Sample Distribution of the Likelihood Ratio for Testing Composite Hypotheses*, Ann. Math. Statist. **9** (03, 1938) 60–62. https://doi.org/10.1214/aoms/1177732360. 5.5, 9.2, 9.3.2

[137] N. Kauer, *Inadequacy of zero-width approximation for a light Higgs boson signal*, Mod. Phys. Lett. **A**28 (2013) 1330015, arXiv:1305.2092 [hep-ph]. 6.1

[138] M. Pivk and F. Le Diberder, *${}_s$Plot: A Quick Introduction*, arXiv:physics/0602023 [physics.data-an]. 6.4.2.1

[139] G. Cowan, *Statistical data analysis*. 1998. 7.3, 7.3.1, 7.3.1

[140] I. e. a. Nomidis, *Event selection and background estimation in the* $H \to ZZ^{(*)} \to 4\ell$ *channel at* $\sqrt{s} = 13$ TeV *- Moriond 2017 Analysis*, Tech. Rep. ATL-COM-PHYS-2016-1599, CERN, Geneva, Nov, 2016. https://cds.cern.ch/record/2231576. 8.3

[141] ATLAS Collaboration, *Measurements of the Higgs boson production and decay rates and coupling strengths using pp collision data at* $\sqrt{s} = 7$ *and* 8 *TeV in the ATLAS experiment*, Eur. Phys. J. C **76** (2016) 6, arXiv:1507.04548 [hep-ex]. 8.3, 8.3

[142] G. J. Feldman and R. D. Cousins, *Unified approach to the classical statistical analysis of small signals*, Phys. Rev. D **57** (Apr, 1998) 3873–3889. https://link.aps.org/doi/10.1103/PhysRevD.57.3873. 9.1

[143] J. Neyman, *Outline of a Theory of Statistical Estimation Based on the Classical Theory of Probability*, Philosophical Transactions of the Royal Society of London. Series A, Mathematical and Physical Sciences **2**36 (1937) no. 767, 333–380. http://www.jstor.org/stable/91337. 9.1

[144] F. James and M. Roos, *Minuit: A System for Function Minimization and Analysis of the Parameter Errors and Correlations*, Comput. Phys. Commun. **1**0 (1975) 343–367. 9.1, 9.2, 9.3.2

[145] G. Cowan, K. Cranmer, E. Gross, and O. Vitells, *Asymptotic formulae for likelihood-based tests of new physics*, Eur. Phys. J. C **7**1 (2011) 1554, arXiv:1007.1727 [physics.data-an]. [Erratum: Eur. Phys. J. C 73 (2013) 2501]. 9, 9.2, 9.5

[146] ATLAS Collaboration, *Study of the spin and parity of the Higgs boson in diboson decays with the ATLAS detector*, Eur. Phys. J. C **7**5 (2015) 476, arXiv:1506.05669 [hep-ex]. 10.2.2

[147] ATLAS Collaboration, *Fiducial and differential cross sections of Higgs boson production measured in the four-lepton decay channel in pp collisions at* $\sqrt{s} = 8$ *TeV with the ATLAS detector*, Phys. Lett. B **7**38 (2014) 234, arXiv:1408.3226 [hep-ex]. 10.2.2

[148] M. A. Ebert et al., *SCETlib: A C++ Package for Numerical Calculations in QCD and Soft-Collinear Effective Theory*, . http://scetlib.desy.de. In preparation. 10.3.2

[149] P. F. Monni, E. Re, and P. Torrielli, *Higgs Transverse-Momentum Resummation in Direct Space*, Phys. Rev. Lett. **1**16 (2016) no. 24, 242001, arXiv:1604.02191 [hep-ph]. 10.3.2

[150] M. A. Ebert, J. K. L. Michel, and F. J. Tackmann, *Resummation Improved Rapidity Spectrum for Gluon Fusion Higgs Production*, JHEP **0**5 (2017) 088, arXiv:1702.00794 [hep-ph]. 10.3.2

[151] X. Chen, J. Cruz-Martinez, T. Gehrmann, E. W. N. Glover, and M. Jaquier, *NNLO QCD corrections to Higgs boson production at large transverse momentum*, Journal of High Energy Physics **2**016 (Oct, 2016) 66. https://doi.org/10.1007/JHEP10(2016)066. 10.3.2

[152] F. L. Wilson, *Fermi's Theory of Beta Decay*, Am. J. Phys. **3**6 (1968) no. 12, 1150–1160. 10.4.1

[153] B. Henning, X. Lu, and H. Murayama, *How to use the Standard Model effective field theory*, Journal of High Energy Physics **2**016 (Jan, 2016) 23. https://doi.org/10.1007/JHEP01(2016)023. 10.4.2

[154] M. Gonzalez-Alonso, A. Greljo, G. Isidori, and D. Marzocca, *Pseudo-observables in Higgs decays*, The European Physical Journal C **7**5 (Mar, 2015) 128. https://doi.org/10.1140/epjc/s10052-015-3345-5. 10.4.2, 10.4.2

[155] M. Gonzalez-Alonso, A. Greljo, G. Isidori, and D. Marzocca, *Electroweak bounds on Higgs pseudo-observables and* $h \to 4\ell$ *decays*, Eur. Phys. J. C **7**5 (2015) 341, arXiv:1504.04018 [hep-ph]. 2